To the Graduate Council:
I am submitting herewith a thesis written by Tyler Poon entitled "DESIGN OF MACHINE TOOL CROSS BEAM USING METAL BIG AREA ADDITIVE MANUFACTURING." I have examined the final paper copy of this thesis for form and content and recommend that it be accepted in partial fulfillment of the requirements for the degree of Master of Science, with a major in Mechanical Engineering.

Tony Schmitz, Major Professor

We have read this thesis
and recommend its acceptance:

Jared Bradley

Uday Vaidya

Accepted for the Council:

Dixie L. Thompson

Vice Provost and Dean of the Graduate School

To the Graduate Council:
I am submitting herewith a thesis written by Tyler Poon entitled "DESIGN OF MACHINE TOOL CROSS BEAM USING METAL BIG AREA ADDITIVE MANUFACTURING." I have examined the final electronic copy of this thesis for form and content and recommend that it be accepted in partial fulfillment of the requirements for the degree of Master of Science, with a major in Mechanical Engineering.

Tony Schmitz, Major Professor

We have read this thesis
and recommend its acceptance:

Jared Bradley

Uday Vaidya

Accepted for the Council:

Dixie L. Thompson

Vice Provost and Dean of the Graduate School

(Original signatures are on file with official student records.)

DESIGN OF MACHINE TOOL CROSS BEAM USING METAL BIG AREA ADDITIVE MANUFACTURING

A Thesis Presented for the

Master of Science

Degree

The University of Tennessee, Knoxville

Tyler Poon

August 2023

© by Tyler Poon, 2023
All Rights Reserved.

I would like to dedicate this thesis to my mother and sister. Without my mother, I would have never been able to pursue the dreams and aspirations that have gotten me to this point in my life and without a doubt my future. And to my sister, for she looks up to me and consequently motivates me to do my best in all aspects of life.

Acknowledgements

I would like to thank my professor Dr. Tony Schmitz for giving me the opportunity to take on the challenge of this thesis. Not only did he provide me with the opportunity to work on a novel project that I am now proud of, but he also provided me the opportunity to work with Emma Betters, Justin West, and the rest of the Machine Tool Research Center. Without these people, I would not have been able to learn and accomplish this project as well as all the additional knowledge that I have gained.

I am also thankful for all the people that I have worked with at the Oak Ridge National Laboratory's Manufacturing and Demonstration Facility, especially everyone in the Intelligent Machine Tools Group and in the Wire Arc Additive Manufacturing Group. This project would not have been possible without their funding, expertise, and patience.

Lastly, I would like to thank Michael Braddock, my mentors, my close friends, and my family for their support in my pursuit of graduate school. Without their encouragement and guidance, I would have never pursued this path. The most valuable aspects of my graduate degree are all the people that have supported me thus far as well as the pride that I have for making a physical part.

"A good plan violently executed now, is better than a perfect plan next week."

-General George S. Patton

Abstract

The modern world would not be what it is now without machine tools. Advances in materials and processes, such as carbon fiber and additive manufacturing (AM), enable the design space for machine tool components to expand. However, machine tool components require accurate geometry, which is not available from parts produced by metal Big Area Additive Manufacturing (mBAAM). This project outlines the process in which a traditionally manufactured machine tool component, a welded box structure on an existing machine tool, was redesigned to be made using mBAAM. The goal was to design a structure that was printable using the MedUSA system at Oak Ridge National Laboratory (ORNL) and measure the dynamic characteristics of the printed part using modal testing for comparison to finite element models.

The MedUSA system consists of three robotic arms that each manipulate a gas metal arc welding (GMAW) torch. The three torches were used to simultaneously deposit the mBAAM replacement for the traditional welded box structure. The print continued for 245 layers before it was stopped due to significant distortion caused by thermal deformation and fixturing failure. However, modal testing was completed on the 77% complete structure to compare with finite element models that simulated bending mode shapes and natural frequencies. It was confirmed that the printed structure dynamics agreed with the numerical model predictions, which demonstrated that it is feasible to model a large-scale mBAAM part and understand its behavior prior to printing. Another significant outcome of this study is that the incomplete

print shows that there remains a knowledge gap for successful mBAAM. The outcome of this project adds to the understanding necessary to enable successful large metal prints in the future.

AM has become a popular technology due to its expanded opportunities for unique geometries and wide design space, but challenges remain. This printed structure, although incomplete, demonstrates ongoing issues with thermal management and residual stress in large parts. Overall, this study demonstrates an example of designing and printing a large-scale metal structure that was validated through modal testing.

Table of Contents

1 Introduction **1**

2 Literature Review **3**

2.1 Machine tools . . . 3

2.1.1 General machine tools . . . 3

2.1.2 Concrete base machine . . . 5

2.1.3 Machine tool design . . . 7

2.2 Additive manufacturing . . . 10

2.2.1 Additive manufacturing technologies . . . 10

2.2.2 mBAAM . . . 12

2.3 Finite element analysis . . . 19

2.4 Modal analysis and impact testing . . . 21

2.4.1 Modal analysis . . . 21

2.4.2 Impact testing . . . 29

3 Weldment Cross Beam **34**

3.1 Weldment design . . . 34

3.1.1 Original design and purpose . . . 34

3.1.2 Dimensions and features . . . 39

3.2 Weldment analysis . . . 45

3.2.1 Digital modeling . . . 45

3.2.2 Finite element simulation of weldment . . . 49

3.2.3 Impact (tap) testing of weldment 80
3.2.4 Comparison of finite element simulation and impact testing . . 92

4 Design of mBAAM cross beam 126
4.1 Machine tool design constraints 126
4.2 mBAAM design constraints 128
4.2.1 MedUSA welding system 128
4.2.2 Capabilities and limitations 128
4.3 Iterative design process 131
4.4 Finalized design 134
4.5 Comparison of weldment and mBAAM cross beam 142

5 Fabrication 156
5.1 mBAAM printing results 156
5.2 Residual stress and fixturing issues 166
5.3 Impact testing 170
5.3.1 Bottom face 185
5.3.2 Front face 204
5.4 Comparison of damping ratios for weldment and mBAAM cross beam 218

6 Conclusions and recommendations 223

A Drawings for weldment cross beam 232

Vita 245

List of Tables

3.1 Material properties for A36 steel 54
3.2 Cutting parameter inputs for calculations 59
3.3 Cutting parameter results after using Equations 3.1 through 3.4 . . . 61
3.4 Break down of deflections due to various forces in various configurations for the simplified weldment 78
3.5 Peak picked values of Mode 1 at 209 Hz at each location of the bottom face normalized to (1,1) and scaled by -25.40 97
3.6 Peak picked values of Mode 2 at 373 Hz at each location of the bottom face normalized to (1,1) and scaled by -25.40 99
3.7 Peak picked values of Mode 3 at 377 Hz at each location of the bottom face normalized to (1,1) and scaled by -25.40 101
3.8 Peak picked values of Mode 4 at 413 Hz at each location of the bottom face normalized to (1,1) and scaled by -25.40 103
3.9 Peak picked values of Mode 5 at 545 Hz at each location of the bottom face normalized to (1,1) and scaled by -25.40 105
3.10 Dynamic mode frequencies from peak-picking and FEA of modes 1-5 for the bottom face in addition to the percent difference 108
3.11 Calculated damping ratio and stiffness values from the five modes of the bottom face through peak-picking 109
3.12 Peak picked values of Mode 1 at 209 Hz at each location of the front face normalized to (1,1) and scaled by -25.40 113

3.13 Peak picked values of Mode 2 at 375 Hz at each location of the front face normalized to (1,1) and scaled by -76.20 115
3.14 Peak picked values of Mode 3 at 529 Hz at each location of the front face normalized to (1,1) and scaled by -76.20 117
3.15 Peak picked values of Mode 4 at 546 Hz at each location of the front face normalized to (1,1) and scaled by -76.20 119
3.16 Peak picked values of Mode 5 at 833 Hz at each location of the front face normalized to (1,1) and scaled by -76.20 121
3.17 Dynamic mode frequencies from peak-picking and FEA of modes 1-5 for the front face in addition to the percent difference 123
3.18 Calculated damping ratio and stiffness values from the five modes of the front face through peak-picking 125

4.1 Material properties for LA-100 steel 143
4.2 Summary of deflections due to various forces in various configurations for the WAAM cross beam 153
4.3 Difference in the magnitude of deflection values of the WAAM cross beam and the weldment where green is acceptable, blue is an improvement, and red is not an improvement 154

5.1 Peak picked values for columns 1 - 10 of Mode 1 at 184 Hz at each location of the bottom face normalized to (1,1) and scaled by -50.80 . 187
5.2 Peak picked values for columns 11 - 19 of Mode 1 at 184 Hz at each location of the bottom face normalized to (1,1) and scaled by -50.80 . 188
5.3 Peak picked values for columns 1 - 10 of Mode 2 at 233 Hz at each location of the bottom face normalized to (1,1) and scaled by -25.40 . 190
5.4 Peak picked values for columns 11 - 19 of Mode 2 at 233 Hz at each location of the bottom face normalized to (1,1) and scaled by -25.40 . 191
5.5 Peak picked values for columns 1 - 10 of Mode 3 at 291 Hz at each location of the bottom face normalized to (1,1) and scaled by 76.20 . 193

5.6 Peak picked values for columns 11 - 19 of Mode 3 at 291 Hz at each location of the bottom face normalized to (1,1) and scaled by 76.20 . 194
5.7 Peak picked values for columns 1 - 10 of Mode 4 at 377 Hz at each location of the bottom face normalized to (1,1) and scaled by -50.80 . 196
5.8 Peak picked values for columns 11 - 19 of Mode 4 at 377 Hz at each location of the bottom face normalized to (1,1) and scaled by -50.80 . 197
5.9 Peak picked values for columns 1 - 10 of Mode 5 at 687 Hz at each location of the bottom face normalized to (1,1) and scaled by -76.20 . 199
5.10 Peak picked values for columns 11 - 19 of Mode 5 at 687 Hz at each location of the bottom face normalized to (1,1) and scaled by -76.20 . 200
5.11 Dynamic mode frequencies from peak-picking and FEA of modes 1-5 for the bottom face of the WAAM print in addition to the percent difference 202
5.12 Calculated damping ratio and stiffness values from the five modes of the bottom face through peak-picking 205
5.13 Peak picked values of Mode 1 at 483 Hz at each location of the front face normalized to (1,2) and scaled by 50.80 207
5.14 Peak picked values of Mode 2 at 486 Hz at each location of the front face normalized to (1,2) and scaled by 50.80 209
5.15 Peak picked values of Mode 3 at 566 Hz at each location of the front face normalized to (1,2) and scaled by -76.20. 211
5.16 Peak picked values of Mode 4 at 610 Hz at each location of the front face normalized to (1,2) and scaled by -50.80. 213
5.17 Peak picked values of Mode 5 at 674 Hz at each location of the front face normalized to (1,2) and scaled by 50.80. 215
5.18 Dynamic mode frequencies from peak-picking and FEA of modes 1-5 for the front face of the WAAM print in addition to the percent difference 217
5.19 Calculated damping ratio and stiffness values from the five modes of the front face through peak-picking 219

5.20 Frequencies and damping ratios of the bottom faces of the weldment and WAAM cross beam 220
5.21 Frequencies and damping ratios of the front faces of the weldment and WAAM cross beam 221

List of Figures

2.1 Haas desktop machine tool which is used for teaching and machine tool introduction [1]. 4
2.2 Large machining center from K&M Machine Fabricating, Inc which is used for large-scale parts [2]. 4
2.3 Printing of polymer mold with rebar and concrete [3]. 6
2.4 Concrete base machine tool components in the isometric orientation. . 8
2.5 Concrete base machine tool components from the YZ-plane. 8
2.6 Concrete base machine tool axes of motion. 9
2.7 Lightweight and fast CNC machine by EEW Protec[4]. 11
2.8 Carbon fiber column within CNC machines produced by map dynamic inside [5]. 11
2.9 Components of the MIG process [6]. 14
2.10 The MedUSA mBAAM system at ORNL consists of three six-axis robotic arms fitted with MIG torches along with the circular build table. 16
2.11 The MedUSA mBAAM print cell at ORNL consists of three six-axis robotic arms fitted with MIG torches along with the circular build table. 17
2.12 MIG torch at the end of one of the robotic arms from the MedUSA cell. 18
2.13 Excavator arm that was printed on the MedUSA system [7]. 20
2.14 Example of a damped free vibration system in the time domain [8]. . 23
2.15 Example of forced vibration magnitude in the frequency domain [8]. . 23

2.16 Example of a magnitude and phase plot for a single degree of freedom system [8]. 27
2.17 Example of a real and imaginary plot for a single degree of freedom [8]. 27
2.18 Large impact hammer used for impact testing with a nylon tip and extended mass. 31
2.19 Large magnetic accelerometer that was used for impact testing. . . . 32
2.20 Representation of direct and cross FRF measurements on an example test system where f_1 is the input force and the x values represent different locations[9]. 32

3.1 Concrete base machine tool with the cross beam supporting the Z-axis and spindle assembly on top of the concrete base. 35
3.2 Front view of cross beam weldment on concrete base machine. 36
3.3 Back right corner view of the cross beam weldment on concrete base machine 36
3.4 Connection of a foot of the cross beam to the concrete base. 37
3.5 Right side view of guideways on the front face of the cross beam. . . . 37
3.6 Left side view of guideways on the front face of the cross beam. . . . 38
3.7 Back right corner view of cross beam weldment on the concrete base machine with cables. 40
3.8 Isometric view of digital weldment cross beam. 40
3.9 Front view of digital weldment cross beam with dimensions in millimeters. 41
3.10 Top view of digital weldment cross beam with dimensions in millimeters. 41
3.11 Front section view of digital weldment cross beam showing the center plate with dimensions in millimeters. 42
3.12 Side view of digital weldment cross beam with dimensions in millimeters. 42
3.13 Bottom view of digital weldment cross beam with dimensions in millimeters showing mounting hole locations and dimensions. 43
3.14 Front view with side and mounting plates with gussets identification. 43

3.15 Top view with front and back plate identification. 44
3.16 Side view with top, bottom, and center plate identification. 44
3.17 Isometric view of simplified cross beam weldment model. 46
3.18 View of modified plate dimensions for the front and back plates while the respective thickness of the plates remained the same. 47
3.19 View of modified plate dimensions of the plate used for the top and bottom which are identical. 47
3.20 Side view of the overlap pattern used for the simplified model where both the top and bottom plates were butted against the front and back plates. 48
3.21 Location of the load bearing region on the rails in the column-centered configuration. 50
3.22 Location of the load bearing region on the rails in the column-offset configuration. 50
3.23 Front isometric view of refined model with weld beads. 51
3.24 Back isometric view of refined model with weld beads. 51
3.25 Isometric view of weld beads on and in the cross beam body. 52
3.26 Isometric view and dimensions of a single weld bead from the refined model. 52
3.27 Isometric view of simplified weldment with fixed metal pads. 54
3.28 Isometric view of one of the two fixed metal pads simulating the mounting location of the concrete base machine (the green arrows represent the fixed condition). 55
3.29 Zoomed in view of the bolt-hole fixed constraint (the green arrows represent the fixed condition). 55
3.30 Spindle assembly (left) and Z-axis assembly (right) of the concrete base machine 56
3.31 Top and side view of a two-flute endmill cutting aluminum for a finishing pass. 58

3.32 Top and side view of a two-flute endmill cutting aluminum for a roughing pass. 58
3.33 Top and side view of a six-flute endmill cutting titanium for a finishing pass. 59
3.34 Top and bottom rails highlighted in red for the centered configuration. 61
3.35 Top and bottom rails highlighted in red for the offset configuration. . 62
3.36 Centered configuration with red gravity vector arrow. 64
3.37 Centered configuration with red gravity vector arrow with the remote mass attached via rigid connections. 64
3.38 Centered continuation with red gravity vector arrow with the too tip attached via rigid connections. 65
3.39 The purple outline highlights the contact interaction between the bottom of the mounting feet and the top of the fixed metal plates. . . 65
3.40 Isometric view of the front of the weldment with its final mesh. . . . 67
3.41 Isometric view of the back of the weldment with its final mesh. 67
3.42 Weldment simulation with gravity, remote mass, and the remote tool tip point. 69
3.43 Simulation of weldment in the centered configuration along with a remote X-cutting force in the -X direction. 69
3.44 Simulation of weldment in the centered configuration along with a remote Y-cutting force in the -Y direction. 70
3.45 Simulation of weldment in the centered configuration along with a remote Z-drilling force in the +Z direction. 70
3.46 Simulation of weldment in the centered configuration along with torque about the Z-axis of the tool tip. 71
3.47 FEA resultant displacement of the weldment in the rails centered configuration with gravity only. 71
3.48 FEA resultant displacement of the weldment in the rails centered configuration with gravity and the remote mass. 72

3.49 FEA resultant displacement of the weldment in the rails centered configuration with gravity, remote mass, and X-cutting force. 72
3.50 FEA resultant displacement of the weldment in the rails centered configuration with gravity, remote mass, and Y-cutting force. 73
3.51 FEA resultant displacement of the weldment in the rails centered configuration with gravity, remote mass, and Z-drilling force. 73
3.52 FEA resultant displacement of the weldment in the rails centered configuration with gravity, remote mass, and torque force. 74
3.53 FEA resultant displacement of the weldment in the rails offset configuration with gravity only. 74
3.54 FEA resultant displacement of the weldment in the rails offset configuration with gravity and the remote mass. 75
3.55 FEA resultant displacement of the weldment in the rails offset configuration with gravity, remote mass, and X-cutting force. 75
3.56 FEA resultant displacement of the weldment in the rails offset configuration with gravity, remote mass, and Y-cutting force. 76
3.57 FEA resultant displacement of the weldment in the rails offset configuration with gravity, remote mass, and Z-cutting force. 76
3.58 FEA resultant displacement of the weldment in the rails offset configuration with gravity, remote mass, and torque force. 77
3.59 Isometric front view of FEA simulation of the first mode shape of the refined weldment. 81
3.60 Isometric back view of FEA simulation of the first mode shape of the refined weldment. 81
3.61 Modal hammer used for impact testing with a nylon tip and extended mass. 82
3.62 Magnetic accelerometer used for impact testing. 82
3.63 MetalMAX data acquisition unit that was used to connect the modal hammer, accelerometer, and computer. 83

3.64 Bottom face of weldment with all of the impact points marked in red dots. 85
3.65 Front face of weldment with all of the impact points marked in red dots. 85
3.66 Bottom face of weldment with dimensions of impact points. 86
3.67 Front face of weldment with dimensions of impact points. 87
3.68 Bottom face of physical weldment with all of the impact points marked in black points. 88
3.69 Front face of physical weldment with all of the impact points marked in black points. 88
3.70 Overhead crane lifting weldment to establish free-free tap testing conditions. 89
3.71 Overhead crane lifting weldment to establish free-free tap testing conditions close up. 90
3.72 Accelerometer location of direct FRF point on the bottom face of the weldment. 90
3.73 Accelerometer location of direct FRF point on the front face of the weldment. 91
3.74 Coordinate locations for the bottom face of the weldment. 93
3.75 Coordinate locations for the front face of the weldment. 93
3.76 Reciprocity check of real and imaginary plots of the bottom face cross FRF points of (1,1) and (1,9) where the blue is for the first measurement and pink for the second. 94
3.77 Reciprocity check of real and imaginary plots of the front face cross FRF points of (1,1) and (1,13) where the blue is for the first measurement and pink for the second. 96
3.78 Overlay of the real and imaginary plots from the top row of points of the bottom face (1,1) - (1,9) with the chosen five most flexible modes. 96
3.79 Plot of peak picked values of Mode 1 at 209 Hz at each location of the bottom face normalized to (1,1) and scaled by -25.40. 98

3.80 FEA simulation of weldment at 210 Hz which shows a similar mode shape as found in impact testing for mode 1 where the amplitude is only shown in the Z-axis. 98
3.81 Plot of peak picked values of Mode 2 at 373 Hz at each location of the bottom face normalized to (1,1) and scaled by -25.40. 100
3.82 FEA simulation of weldment at 354 Hz which shows a similar mode shape as found in impact testing for mode 2 where the amplitude is only shown in the Z-axis. 100
3.83 Plot of peak picked values of Mode 3 at 377 Hz at each location of the bottom face normalized to (1,1) and scaled by -25.40. 102
3.84 FEA simulation of weldment at 373 Hz which shows a similar mode shape as found in impact testing for mode 3 where the amplitude is only shown in the Z-axis. 102
3.85 Plot of peak picked values of Mode 4 at 413 Hz at each location of the bottom face normalized to (1,1) and scaled by -25.40. 104
3.86 FEA simulation of weldment at 397 Hz which shows a similar mode shape as found in impact testing for mode 4 where the amplitude is only shown in the Z-axis. 104
3.87 Plot of peak picked values of Mode 5 at 545 Hz at each location of the bottom face normalized to (1,1) and scaled by -25.40. 106
3.88 FEA simulation of weldment at 520 Hz which shows a similar mode shape as found in impact testing for mode 5 where the amplitude is only shown in the Z-axis. 106
3.89 Real and imaginary FRF plots of (1,1) from the bottom face with the five identified modes of interest. 108
3.90 Real and imaginary FRF plots of mode 1 of (1,1) from the bottom face with a superimposed plot of the calculated real and imaginary plots. . 109
3.91 Real and imaginary FRF plots (1,1) from the bottom face with a superimposed plot of all the calculated real and imaginary plots summed. 110

3.92 Overlay of the real and imaginary plots from the top row of points of the front face (1,1) - (1,13) with the chosen five most flexible modes. . 112
3.93 Plot of peak picked values of Mode 1 at 209 Hz at each location of the front face normalized to (1,1) and scaled by -25.40. 114
3.94 FEA simulation of weldment at 210 Hz which shows a similar mode shape as found in impact testing for mode 1 where the amplitude is only shown in the X-axis. 114
3.95 Plot of peak picked values of Mode 2 at 375 Hz at each location of the front face normalized to (1,1) and scaled by -76.20. 116
3.96 FEA simulation of weldment at 354 Hz which shows a similar mode shape as found in impact testing for mode 2 where the amplitude is only shown in the Y-axis. 116
3.97 Plot of peak picked values of Mode 3 at 529 Hz at each location of the front face normalized to (1,1) and scaled by -76.20. 118
3.98 FEA simulation of weldment at 505 Hz which shows a similar mode shape as found in impact testing for mode 3 where the amplitude is only shown in the X-axis. 118
3.99 Plot of peak picked values of Mode 4 at 546 Hz at each location of the front face normalized to (1,1) and scaled by -76.20. 120
3.100FEA simulation of weldment at 519 Hz which shows a similar mode shape as found in impact testing for mode 4 where the amplitude is only shown in the X-axis. 120
3.101Plot of peak picked values of Mode 5 at 833 Hz at each location of the front face normalized to (1,1) and scaled by -76.20. 122
3.102FEA simulation of weldment at 800 Hz which shows a similar mode shape as found in impact testing for mode 5 where the amplitude is only shown in the X-axis. 122
3.103Real and imaginary FRF plots of (1,1) from the front face with the five identified modes of interest. 124

3.104Real and imaginary FRF plots of mode 1 of (1,1) from the front face with a superimposed plot of the calculated real and imaginary plots. . 124
3.105Real and imaginary FRF plots (1,1) from the front face with a superimposed plot of all the calculated real and imaginary plots summed.125

4.1 Rough exterior surface of WAAM print. 130
4.2 Front isometric view of the finalized WAAM design. 135
4.3 Back isometric view of the finalized WAAM design. 135
4.4 Front view of the finalized WAAM design. 136
4.5 Top view of the finalized WAAM design. 136
4.6 Back view of the finalized WAAM design. 137
4.7 Bottom view of the finalized WAAM design. 137
4.8 Left and right side views of the finalized WAAM design. 138
4.9 Top view of the separated and larger A36 steel build plates that are 25.40 mm thick. 140
4.10 Isometric view of the bottom of the build plates with the beveled edges.140
4.11 Isometric view of the final design with the new build plate. 141
4.12 Top view of the final design with the new build plate. 141
4.13 Centered configuration with red gravity vector arrow for WAAM cross beam. 143
4.14 Centered configuration with red gravity vector arrow with the remote mass attached via rigid connections for WAAM cross beam. 144
4.15 Simulation of WAAM cross beam in the centered configuration along with a remote X-cutting force in the -X direction. 144
4.16 Simulation of WAAM cross beam in the centered configuration along with a remote Y-cutting force in the -Y direction. 145
4.17 Simulation of WAAM cross beam in the centered configuration along with a remote Z-drilling force in the +Z direction. 145

4.18 Simulation of WAAM cross beam in the centered configuration along with torque about the Z-axis of the tool tip. 146
4.19 FEA resultant displacement of the WAAM cross beam in the rails centered configuration with gravity only. 146
4.20 FEA resultant displacement of the WAAM cross beam in the rails centered configuration with gravity and the remote mass. 147
4.21 FEA resultant displacement of the WAAM cross beam in the rails centered configuration with gravity, remote mass, and X-cutting force. 147
4.22 FEA resultant displacement of the WAAM cross beam in the rails centered configuration with gravity, remote mass, and Y-cutting force. 148
4.23 FEA resultant displacement of the WAAM cross beam in the rails centered configuration with gravity, remote mass, and Z-drilling force. 148
4.24 FEA resultant displacement of the WAAM cross beam in the rails centered configuration with gravity, remote mass, and torque force. . 149
4.25 FEA resultant displacement of the WAAM cross beam in the rails offset configuration with gravity only. 149
4.26 FEA resultant displacement of the WAAM cross beam in the rails offset configuration with gravity and the remote mass. 150
4.27 FEA resultant displacement of the WAAM cross beam in the rails offset configuration with gravity, remote mass, and X-cutting force. 150
4.28 FEA resultant displacement of the WAAM cross beam in the rails offset configuration with gravity, remote mass, and Y-cutting force. 151
4.29 FEA resultant displacement of the WAAM cross beam in the rails offset configuration with gravity, remote mass, and Z-drilling force. 151
4.30 FEA resultant displacement of the WAAM cross beam in the rails centered configuration with gravity, remote mass, and torque force . . 152

5.1 The five separate build plates placed on the print table of the MedUSA system. 157

5.2 Two end clamps highlighted in the red box held down one end of the printed part. 157
5.3 Isometric front view of the WAAM cross beam's initial layers. 158
5.4 Back view of the WAAM cross beam's initial layers and the step clamps can be seen around the outer perimeter of the print. 158
5.5 Corner view of the WAAM cross beam's initial layers. 159
5.6 Side view of WAAM cross beam initial layers with the front step clamps. 159
5.7 Isometric front view of the WAAM cross beam's print progress 2. . . 160
5.8 Side view of WAAM cross beam's print progress 2 160
5.9 Corner view of the WAAM cross beam's print progress 2 161
5.10 Front view of WAAM cross beam's print progress 2 161
5.11 Back view of WAAM cross beam's print progress 2 162
5.12 Top view of WAAM cross beam's side print progress 2 162
5.13 Isometric front view of the WAAM cross beam's print progress 3. . . 163
5.14 Front view of WAAM cross beam's print progress 3. 163
5.15 Isometric back view of the WAAM cross beam's print progress 3. . . . 164
5.16 Far back view of WAAM cross beam's print progress 3 with the MedUSA system. 164
5.17 Front top view of the WAAM cross beam's print progress 3. 165
5.18 Isometric view of the WAAM cross beam when stopped, on the build table. 165
5.19 Side view of the WAAM cross beam when stopped with the bowed build table. 167
5.20 Front view of the WAAM cross beam when stopped with a gap between the middle of a straight edge and the table. 167
5.21 Front view of WAAM cross beam at the end of the print. 171
5.22 Back isometric view of WAAM cross beam at the end of the print. . . 171
5.23 Back view of WAAM cross beam at the end of the print. 172
5.24 Top view of WAAM cross beam at the end of the print. 172

5.25 Additional back view of WAAM cross beam at the end of the print. . 173
5.26 Corner view of WAAM cross beam at the end of the print. 173
5.27 Front isometric of the new model of the WAAM cross beam when print stopped. 174
5.28 Back isometric of the new model of the WAAM cross beam when print stopped. 174
5.29 Bottom face of WAAM print with all of the impact points marked in red dots. 175
5.30 Front face of WAAM print with all of the impact points marked in red dots. 175
5.31 Bottom face of WAAM print with dimensions of impact points. . . . 176
5.32 Front face of WAAM print with dimensions of impact points. 177
5.33 Bottom face of physical WAAM print with all of the impact points marked in black points. 178
5.34 Front face of physical WAAM print with all of the impact points marked in black points. 178
5.35 Overhead crane lifting WAAM print to establish free-free tap testing conditions. 179
5.36 Overhead crane lifting WAAM print to establish free-free tap testing conditions close up. 180
5.37 Accelerometer location of direct FRF point on the bottom face of the WAAM print. 180
5.38 Accelerometer location of direct FRF point on the front face of the WAAM print. 181
5.39 Coordinate locations for the bottom face of the WAAM cross beam. . 183
5.40 Coordinate locations for the front face of the WAAM cross beam. . . 183
5.41 Reciprocity check of real and imaginary plots of the bottom face cross FRF points of (1,1) and (1,19) where the blue is for the first measurement and pink for the second. 184

5.42 Reciprocity check of real and imaginary plots of the front face cross FRF points of (1,2) and (1,12) where the blue is for the first measurement and pink for the second. 186
5.43 Overlay of the real and imaginary plots from the top row of points of the bottom face (1,1) - (1,19) with the chosen five most flexible modes. 186
5.44 Plot of peak picked values of Mode 1 at 184 Hz at each location of the bottom face normalized to (1,1) and scaled by -50.80. 189
5.45 FEA simulation of WAAM print at 164 Hz which shows a similar mode shape as found in impact testing for mode 1 where the amplitude is only shown in the Z-axis. 189
5.46 Plot of peak picked values of Mode 2 at 233 Hz at each location of the bottom face normalized to (1,1) and scaled by -25.40. 192
5.47 FEA simulation of WAAM print at 245 Hz which shows a similar mode shape as found in impact testing for mode 2 where the amplitude is only shown in the Z-axis. 192
5.48 Plot of peak picked values of Mode 3 at 291 Hz at each location of the bottom face normalized to (1,1) and scaled by 76.20. 195
5.49 FEA simulation of WAAM print at 293 Hz which shows a similar mode shape as found in impact testing for mode 3 where the amplitude is only shown in the Z-axis. 195
5.50 Plot of peak picked values of Mode 4 at 377 Hz at each location of the bottom face normalized to (1,1) and scaled by -50.80. 198
5.51 FEA simulation of WAAM print at 469 Hz which shows a similar mode shape as found in impact testing for mode 4 where the amplitude is only shown in the Z-axis. 198
5.52 Plot of peak picked values of Mode 5 at 687 Hz at each location of the bottom face normalized to (1,1) and scaled by -76.20. 201

5.53 FEA simulation of WAAM print at 704 Hz which shows a similar mode shape as found in impact testing for mode 5 where the amplitude is only shown in the Z-axis. 201
5.54 Real and imaginary FRF plots of (1,1) from the bottom face with the five identified modes of interest. 202
5.55 Real and imaginary FRF plots of mode 1 of (1,1) from the bottom face with a superimposed plot of the calculated real and imaginary plots. . 203
5.56 Real and imaginary FRF plots (1,1) from the bottom face with a superimposed plot of all the calculated real and imaginary plots summed. 205
5.57 Overlay of the real and imaginary plots from the top row of points of the front face (1,2) - (1,12) with the chosen five most flexible modes. . 206
5.58 Plot of peak picked values of Mode 1 at 483 Hz at each location of the front face normalized to (1,2) and scaled by 50.80. 208
5.59 FEA simulation of WAAM print at 481 Hz which shows a similar mode shape as found in impact testing for mode 1 where the amplitude is only shown in the X-axis. 208
5.60 Plot of peak picked values of Mode 2 at 486 Hz at each location of the front face normalized to (1,2) and scaled by 50.80. 210
5.61 FEA simulation of WAAM print at 483 Hz which shows a similar mode shape as found in impact testing for mode 2 where the amplitude is only shown in the X-axis. 210
5.62 Plot of peak picked values of Mode 3 at 566 Hz at each location of the front face normalized to (1,2) and scaled by -76.20. 212
5.63 FEA simulation of WAAM print at 625 Hz which shows a similar mode shape as found in impact testing for mode 3 where the amplitude is only shown in the X-axis. 212
5.64 Plot of peak picked values of Mode 4 at 610 Hz at each location of the front face normalized to (1,2) and scaled by -50.80. 214

5.65 FEA simulation of WAAM print at 666 Hz which shows a similar mode shape as found in impact testing for mode 4 where the amplitude is only shown in the X-axis. 214
5.66 Plot of peak picked values of Mode 5 at 674 Hz at each location of the front face normalized to (1,2) and scaled by 50.80. 216
5.67 FEA simulation of WAAM print at 677 Hz which shows a similar mode shape as found in impact testing for mode 5 where the amplitude is only shown in the X-axis. 216
5.68 Real and imaginary FRF plots of (1,2) from the front face with the five identified modes of interest. 217
5.69 Real and imaginary FRF plots of mode 1 and mode 2 of (1,2) from the front face with a superimposed plot of the calculated real and imaginary plots. 219
5.70 Real and imaginary FRF plots (1,2) from the front face with a superimposed plot of all the calculated real and imaginary plots summed. 220

Chapter 1

Introduction

This thesis describes the design of a machine tool cross beam using metal big area additive manufacturing (mBAAM). Oak Ridge National Laboratory (ORNL) has a three-axis machine tool that was built with a concrete base. A steel box tube weldment serves as the cross beam for the machine tool. For this project, mBAAM was selected to produce a new cross beam. The new design was required to serve the same purpose as the current weldment, but a new design strategy was then available using the unique mBAAM capabilities. It was desired to reduce mass in the new design to improve machine tool performance. The ORNL MedUSA system provided the wire arc additive manufacturing (WAAM) deposition capabilities for this project.

Before the new design, the weldment cross beam was characterized through digital modeling and finite element analysis (FEA). With an accurate digital model, the static deflection behavior of the weldment was able to be quantified. The deflection behavior served as a design input for the design of the WAAM cross beam. To validate the FEA model, modal analysis through impact testing was performed on a replica weldment. Dynamic mode shapes of the weldment were found and compared to the FEA-simulated mode shapes. Modal analysis validated the digital model.

The design of the WAAM cross beam was dependent on design constraints. Because the function of the final cross beam was to be part of a machine tool,

traditional machine tool building constraints needed to be considered in the design. Additionally, the design had to incorporate the capabilities and limitations of the MedUSA system. The MedUSA system uses three robotic arms to perform WAAM. Various concepts were generated and eliminated through FEA models and design reviews. A final design was selected that met the following criteria: 1) comparable deflection levels to the current weldment; 2) lower mass than the current weldment; and 3) could be printed using MedUSA.

The final design was printed on the MedUSA system. However, the part was stopped before completion. Multiple factors led to this stoppage, but thermal distortion was the main contributor. A digital model of the incomplete WAAM cross beam was analyzed using FEA. The mode shapes of the incomplete part were simulated and compared to measurements obtained by modal analysis. The results validated the digital model and demonstrated that digital models of mBAAM parts can be used as a design tool.

Chapter 2

Literature Review

This section provides the background knowledge and current state of technology pertaining to the design of a machine cross beam using mBAAM.

2.1 Machine tools

2.1.1 General machine tools

Machine tools are used to form or shape various materials [10]. To form or shape various materials, machine tools are typically power-driven and have played a significant role in the creation of the modern world since the Industrial Revolution[11]. Almost every item in everyday life is made with a machine tool. To cover all the various tasks, machine tools come in different configurations and sizes as seen in Figures 2.1 and 2.2. Modern machine tools are also automated to achieve more complex parts with higher efficiency. Machine tools rely on a controller that interprets geometric code (G-code) to execute machine tool motions. These machine tools are commonly referred to as computer numerically controlled (CNC) machines.

A subsection of CNC machine tools is milling machines. Milling machines are described as machines that rotate a cutting tool and move it relative to a workpiece to produce the desired geometry [12]. Milling machines are primarily composed of

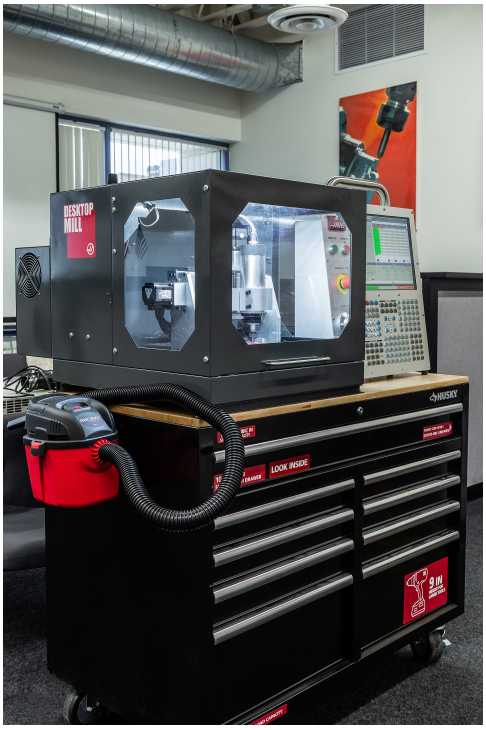

Figure 2.1: Haas desktop machine tool which is used for teaching and machine tool introduction [1].

Figure 2.2: Large machining center from K&M Machine Fabricating, Inc which is used for large-scale parts [2].

a base, table, spindle, and axes which provide linear or rotary motion. The base is the main body of the machine tool and it is the structure that supports the entire machine. A table provides support for the workpiece(s). The table can either be stationary or be able to be moved. The spindle is motor driven and rotates the cutting tool. Similar to the table, the spindle can either be stationary or moving. The motions of the machine tool are referred to as the axes of motion. The axes of motion provide combinations of three axes of translation and three axes of rotation. The translational axes are commonly referred to as the X-, Y-, and Z-axis which form a standard Cartesian coordinate system. The rotational axes are commonly referred to as the A-, B-, and C-axes which are rotations about the X-, Y-, and Z-axes, respectively. The relative motions of the components of a machine tool are made possible with guideways and bearings that are most commonly driven by motors and ballscrews. Due to the various applications of milling machines, many configurations are made possible by varying the base structure, type of spindle, style of table, and desired combination of axes of motion.

2.1.2 Concrete base machine

A concrete base milling machine was created by West *et al.* at Oak Ridge National Laboratory (ORNL) [13]. The concrete base machine was established to investigate the implementation of new additive technologies in combination with concrete to replace traditional castings. The mold for the concrete base was additively manufactured using 20% carbon fiber ABS polymer. A rebar cage was then inserted in the mold and the cavity was filled with concrete which was allowed to cure seen in Figure 2.3 [13]. Most machine tool bases are composed of cast iron which has desirable material properties such as a high damping ratio. Betters *et al.* and Sugishita *et al.* have shown that concrete is a suitable replacement to cast iron due to its material characteristics [14, 15]. The concrete base milling machine was composed of its base,

Figure 2.3: Printing of polymer mold with rebar and concrete [3].

a translating table that is the X-axis, a static weldment cross beam that has linear rails that provide motion in the Y-axis that sits on top of the concrete base, and a spindle column that translates up and down providing the Z-axis motion which translates along the weldment as shown in Figures 2.4, 2.5, and 2.6.

2.1.3 Machine tool design

Modern machine tools are tasked with making features that have tolerances that are less than a millimeter. To achieve the desired tolerances, machines must be designed to ensure the machine can achieve its performance targets. Slocum's *Precision Machine Design* provides guidance for the machine tool design process that focuses on deterministic design [16]. The deterministic design process quantifies the physical attributes and performance of the desired machine into an error budget. The error budget apportions the total allowable tolerance of the machine into its components. The components can then be chosen or designed to meet or have a tighter tolerance than originally assigned. Key aspects of the machine's motion can be traced back to the error budget to ensure that the machine performs at the intended level. With new technology such as better motors, controllers, and drives, machine tools have been able to improve over time and reduce tolerances while increasing production rates.

Along with new technologies, more advanced materials and manufacturing processes have enabled the expansion of design space for machine tools and their components. As previously discussed, materials other than metals have been implemented into machine tool bases. High speed machining typically involves rapid acceleration rates that are difficult to achieve with massive structures. Composites provide a good compromise between mass and stiffness. Suh *et al.* investigated the improvements of replacing structural components of a machine tool with composite sandwich structures and showed a reduction in mass while increasing the damping and no significant loss in stiffness [17]. Möhring summarized new composite machine tool components such as spindles made with carbon fiber reinforced polymers (CFRP)

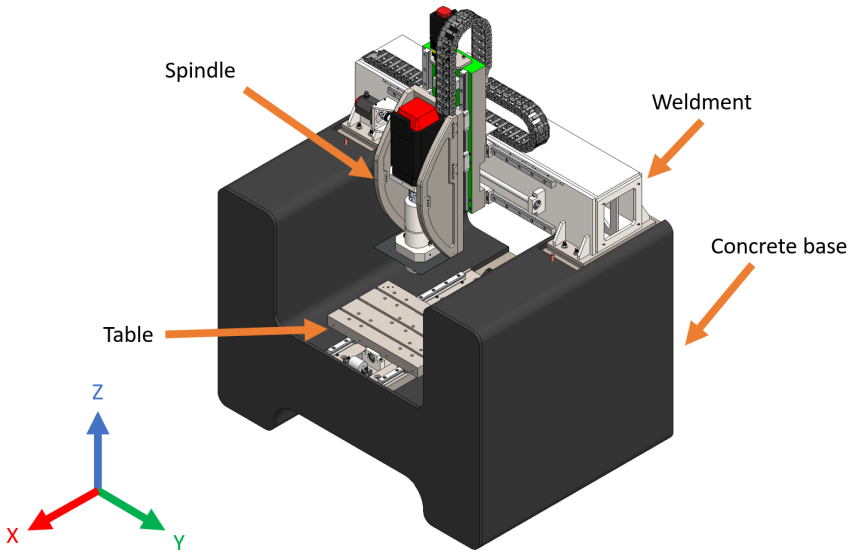

Figure 2.4: Concrete base machine tool components in the isometric orientation.

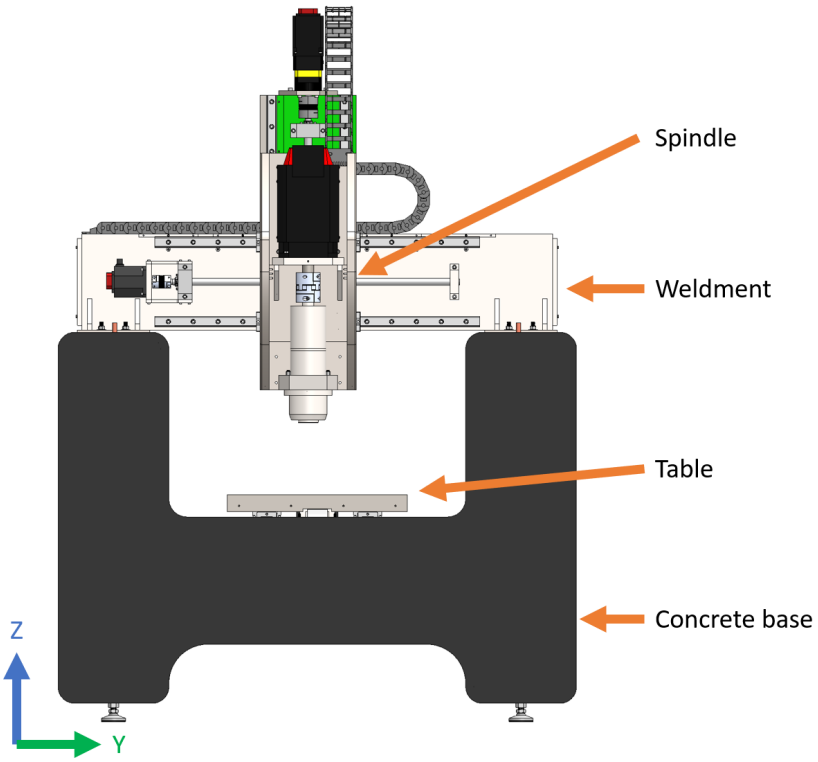

Figure 2.5: Concrete base machine tool components from the YZ-plane.

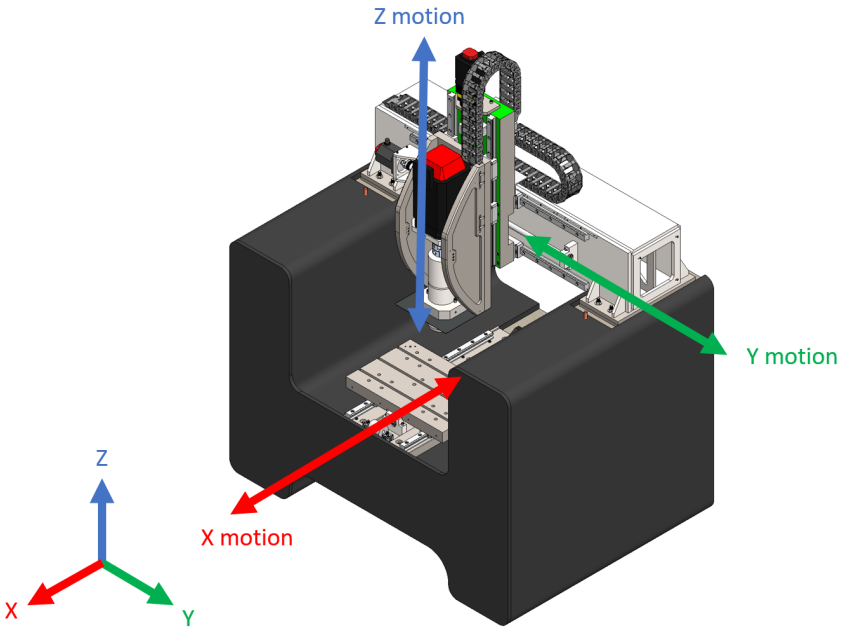

Figure 2.6: Concrete base machine tool axes of motion.

[18]. EEW Protec makes lightweight and fast CNC machine tools with carbon fiber as shown in Figure 2.7 while map dynamic inside implements carbon fiber spindle column seen in Figure 2.8 in their production machine tools. Lee *et al.* showed that hybrid structures, such as bonding glass fiber-reinforced epoxy composite plates onto an existing cast iron machine tool column, can improve the structure's overall damping [19].

2.2 Additive manufacturing

2.2.1 Additive manufacturing technologies

Additive manufacturing (AM) has become more prevalent in making parts that are acceptable for use, but geometry and surface finish challenges remain. Machining, or subtractive manufacturing, has many capabilities in making accurate parts, but also has its limitations. Combining AM and machining, or hybrid manufacturing [20], offers advantages over either separately.

There are many forms of AM. They all follow the principle that a design is sliced into finite layers that are joined together via various printing methods that form the final design [21]. AM is also commonly referred to as 3D printing where a 3-dimensional design in a digital environment is recreated in the physical space with a layer-wise approach. The process flow of AM involves several steps that transform a digital design into a physical part [21]. The process starts with a computer-aided design (CAD) model where a model of the part is formed. The CAD file is then converted to an STL file. According to the inventor of the STL file, Chuck Hull, STL is an acronym for stereolithography [22]. The STL file conversion transforms the original CAD file into a geometry that is approximated and formed by triangles. The STL file is then transferred to the desired machine that will perform the printing of the part. The part is then adjusted to fit the printer's capabilities, such as size, while the machine is also set up appropriately to perform the print. Once all the settings

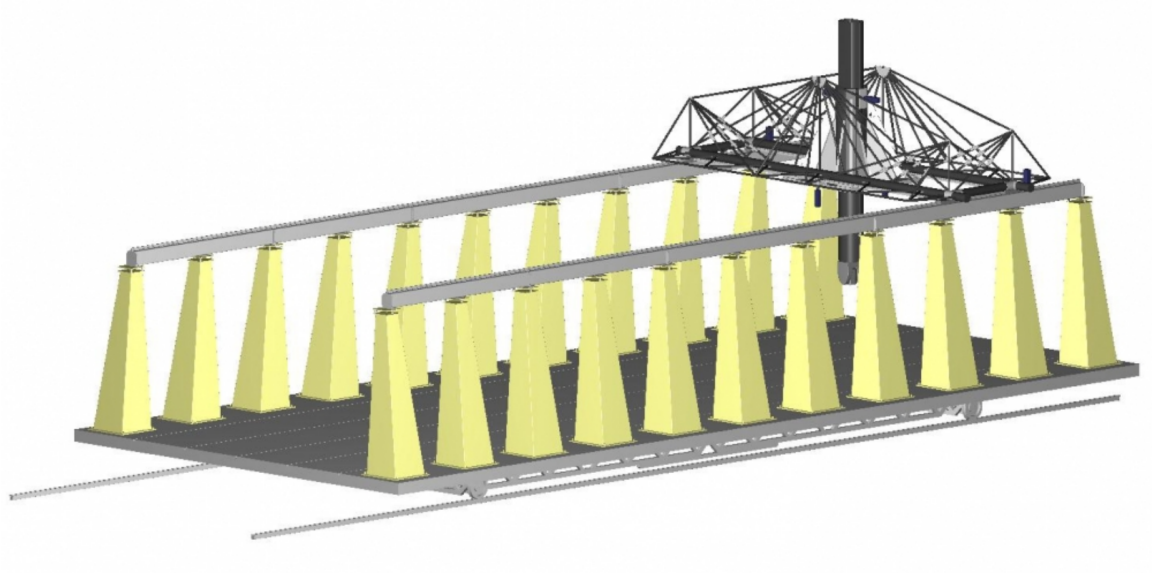

Figure 2.7: Lightweight and fast CNC machine by EEW Protec[4].

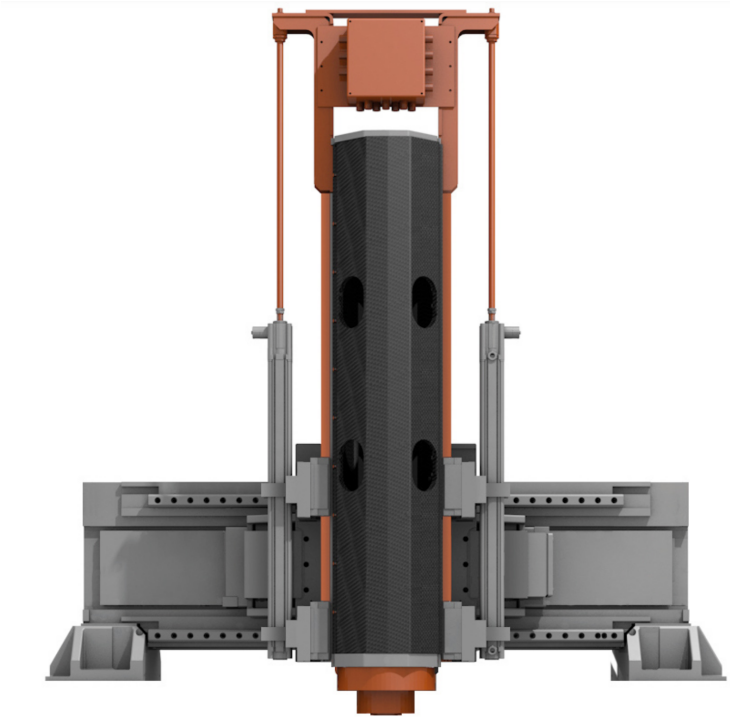

Figure 2.8: Carbon fiber column within CNC machines produced by map dynamic inside [5].

for the machine are configured, the machine can proceed with the build of the part. After the part is fully printed, the part is removed from the machine. Depending on the application and design of the part, post-processing such as support removal or machining can be done. At this point, the part is complete and it can be installed, assembled, or manipulated to perform its function [23].

There are many categories of AM because of the various materials and energy sources. The main forms of AM are binder jetting, directed energy deposition (DED), material extrusion, material jetting, powder bed fusion, sheet lamination, and vat polymerization [24]. The material that is used for printing is referred to as the feedstock. Feedstock can be plastic or metal in the form of a powder, filament, or liquid. To transform the material into the layers of the final part, various energy sources can be used depending on the AM process, including an electrical arc or laser [23]. Each AM process has its constraints and capabilities. It is essential to any AM part that the printing method and constraints are considered when designing the part in CAD.

2.2.2 mBAAM

The mBAAM process is a subset of big area additive manufacturing (BAAM) [25]. The purpose of BAAM was to increase the scale with which AM is typically associated and this is done through choosing the feasible technologies that can be scaled up along with higher deposition rates. mBAAM leverages wire arc additive manufacturing (WAAM) and laser wire additive manufacturing (LWAM) [25]. Both WAAM and LWAM are processes that have high metal deposition rates. The cross beam produced in this project was designed to be printed on an mBAAM system located at the ORNL Manufacturing and Demonstration Facility (MDF). WAAM was chosen as the material deposition method.

WAAM is a form of DED [26]. DED is characterized by melting the material as it is being deposited, typically in wire or powder form. Although other materials

can be printed using DED, the process is typically used for metals. The heat source on a DED system is focused at the site of the material that is being deposited. The melted material solidifies as the head moves away from the melted pool to form tracks of solidified material. These tracks form each layer of the final part and the layers are stacked to form the final geometry. The layers of metal are joined together via the melting and solidification of the feedstock (i.e., fusion).

Gas metal arc welding (GMAW) or metal inert gas (MIG) welding is a popular WAAM material deposition method [27]. The key MIG components are shown in Figure 2.9. The MIG process generates its heat source via an electrical arc that is formed between the machine-fed wire rod's contact tip, which is housed within the torch assembly, and the grounded base material [28]. The arc is established through a power supply with voltage and current that are adjusted for various materials. The feedstock, which is in wire form, is fed through rollers that push the material through the contact tube which conducts the current through the tip of the wire. An arc is formed between the tip and base material. The arc generates heat to melt the wire and base material. As the tip melts into the weld pool, the torch is moved to form beads that are solidified once the melted material is cooled outside of the arc zone. To form properly welded material properties, oxygen must be eliminated from the molten weld pool because it rapidly oxidizes the heated metal as well as leads to porosity issues of the weld [28]. To remove the oxygen, inert gas is blown out of the gas nozzle, which encases the contact tube, to the melt pool to eliminate oxygen. Depending on the material and welding parameters, different mixtures of inert gas or shielding gas can be used. Most inert gas mixtures are composed of argon, helium, carbon dioxide, hydrogen, or nitrogen [28]. Once the melted material solidifies, the previous base metal is fused with the new material.

The MIG process has a few welding parameters that can be adjusted to meet the needs of the weld [28]. The wire size of the material can affect the range of the current

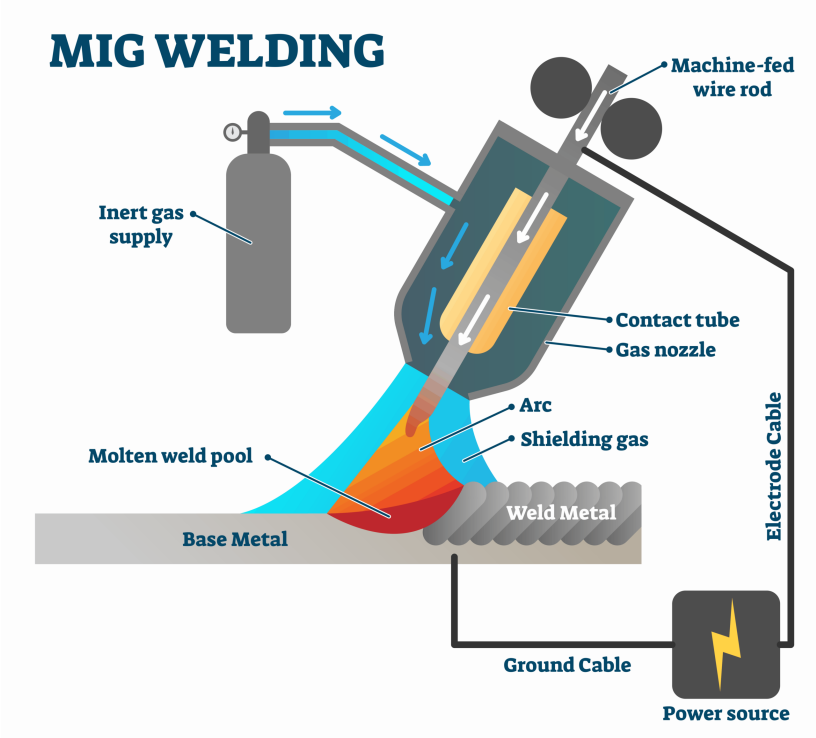

Figure 2.9: Components of the MIG process [6].

that can be selected. Current can be adjusted to increase or decrease the arc length. Depending on the welding current, the wire feed speed through the nozzle must be adjusted to match the welding parameters. The rate at which the torch is moved also affects the weld quality. The stability of the arc can be adjusted through the inductance of the welding machine. Wire stick-out length affects the current as well as the deposition rate of the system. As stated previously, there are many mixtures of shielding gas along with different gas flow rates. With the incorrect shielding gas and flow rate, the weld quality will not be satisfactory. Other factors, such as the angle at which the torch is positioned, as well as torch paths and strategies can change the properties and characteristics of a weld bead. However, the MIG process is a well-understood technology and automated MIG systems take advantage of historical welding parameters or through general testing.

The goal of mBAAM is to scale up existing metal AM technologies. For this project, WAAM through MIG was chosen because it offers a high deposition rate and can print the desired material at the desired scale. The MIG process alone is not considered WAAM. In addition to the welding aspect, a control system is leveraged to manipulate the bead and layer behaviors of the MIG process to form the beads, layers, and final shape [25]. WAAM has been scaled up due to its high deposition rates and its ability to have an easily expandable build volume.

The system at ORNL that was used in this project is MedUSA. It is an mBAAM system that was created by ORNL through a partnership with Lincoln Electric and Wolf Robotics. As seen in Figure 2.10, the MedUSA system is composed of three six-axis robotic arms as well as a circular build table located in the center of the three robot bases. Each of the arms, as seen in Figure 2.11, is fitted with a MIG torch as the end effector. Each robot has six degrees of freedom to weld material onto the center table [29]. The center table is capable of rotating and the three robots, through path planning and ORNL's control system software, can work on the same part simultaneously. The MIG torches on the end of the arm shown in Figure 2.12

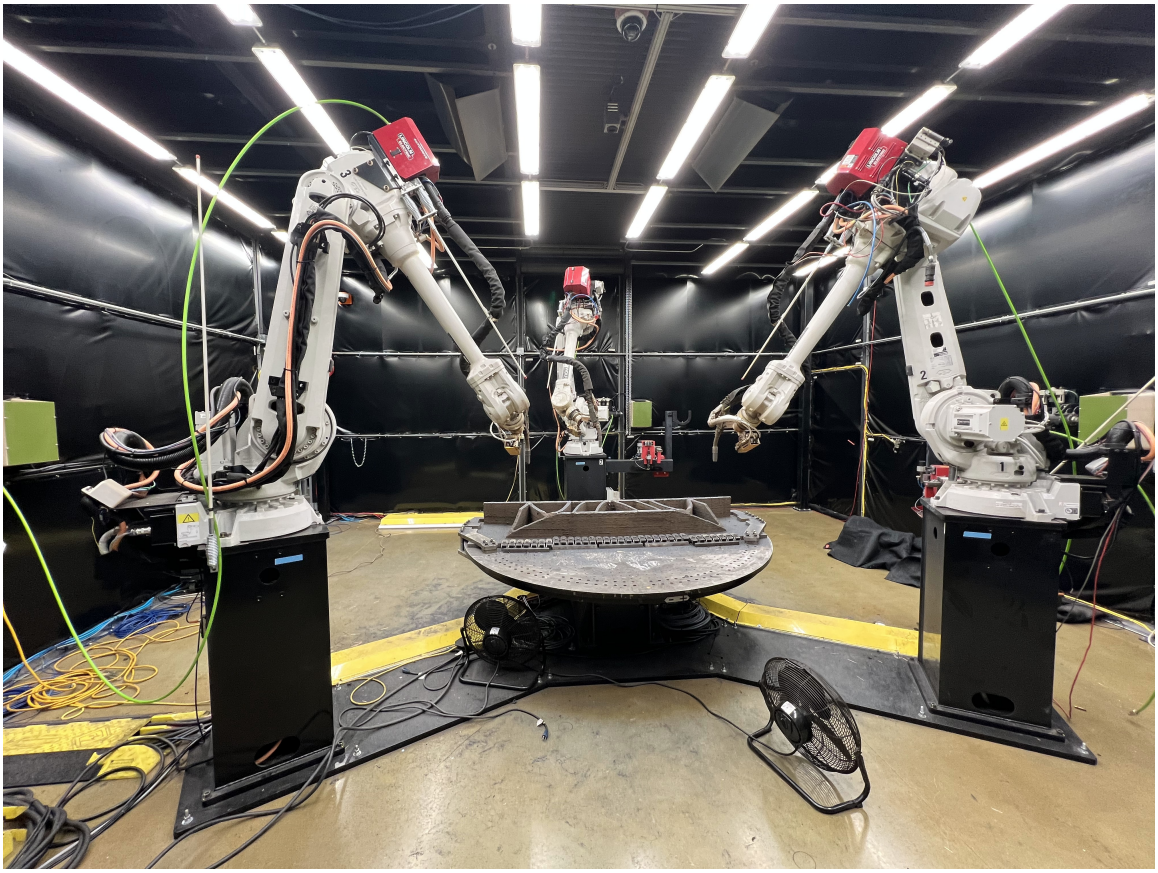

Figure 2.10: The MedUSA mBAAM system at ORNL consists of three six-axis robotic arms fitted with MIG torches along with the circular build table.

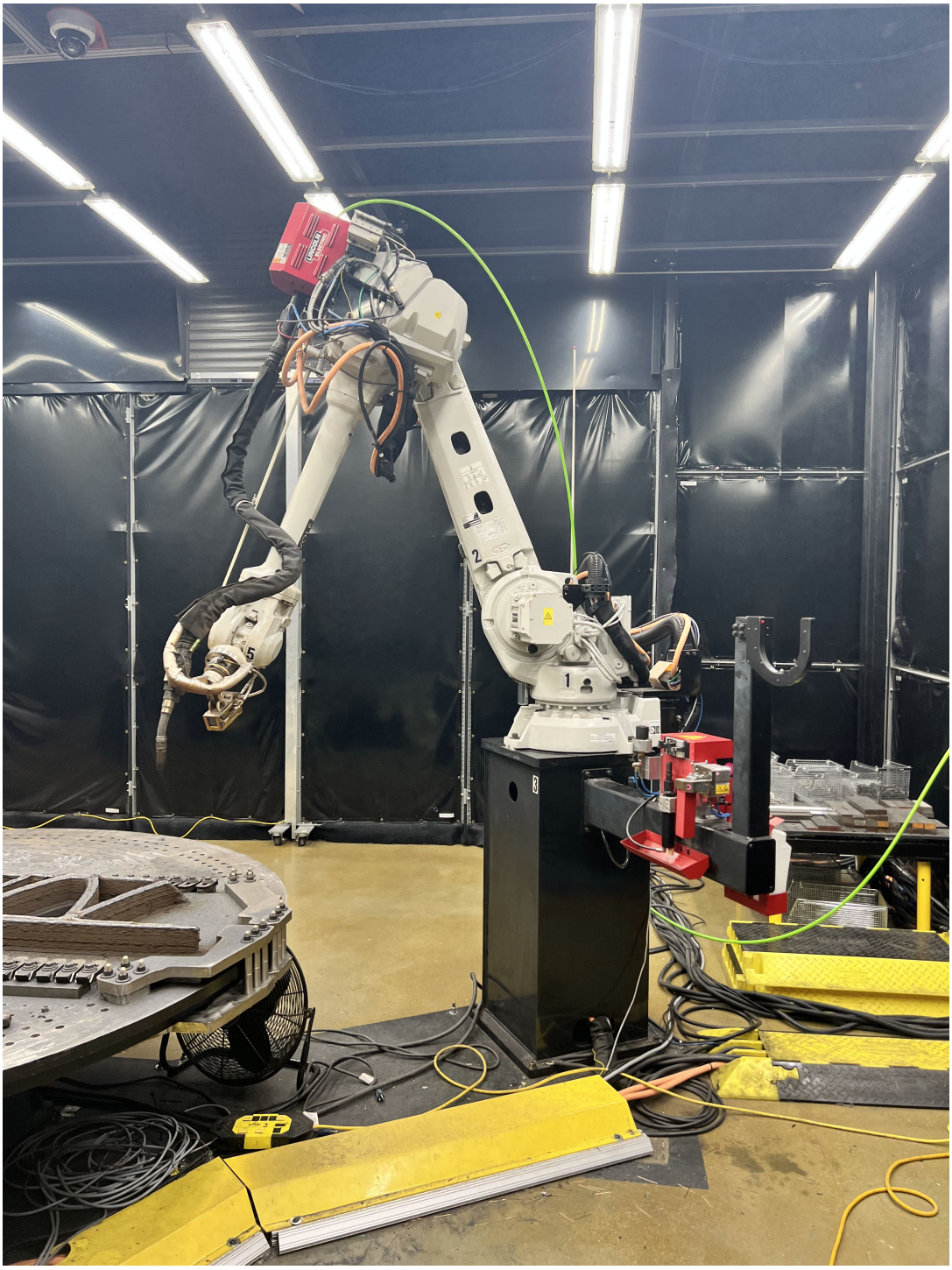

Figure 2.11: The MedUSA mBAAM print cell at ORNL consists of three six-axis robotic arms fitted with MIG torches along with the circular build table.

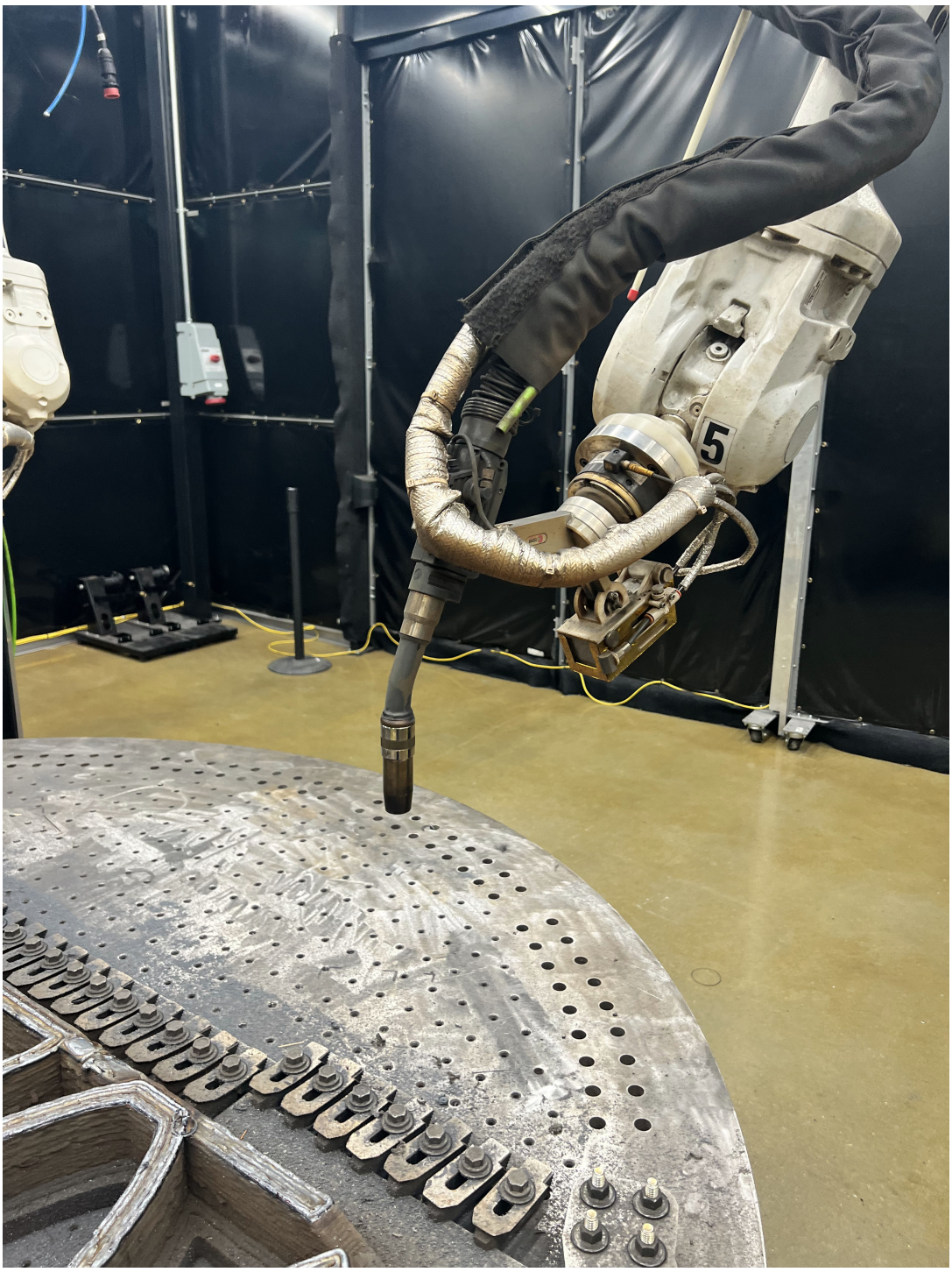

Figure 2.12: MIG torch at the end of one of the robotic arms from the MedUSA cell.

are from Lincoln Electric. The concept of the cell was to increase the deposition rate by increasing the number of print heads. With three print heads, MedUSA is capable of printing more than 23 kilograms of material per hour [30]. ORNL has been successful in printing large structures, such as the excavator arm shown in Figure 2.13, and has produced its own set of design guidelines for large-scale metal AM parts [7, 31]. The part for this project was the second-largest printed part that the ORNL WAAM team has attempted with MedUSA and was made possible from the lessons learned by previous large-scale prints.

2.3 Finite element analysis

An important tool used in engineering is implementing the finite element method (FEM) to model and predict design behaviors through finite element analysis (FEA). FEA is a powerful method to understand and approximate how physical systems behave and change due to external or internal factors [32]. The finite element method is a numerical method that is used to analyze differential equations that pertain to structural mechanics, solid mechanics, heat transfer, fluid dynamics, and other fields. FEA is largely dependent on computing power because simulations of complex parts are resource intensive. The process of FEA involves discretizing a geometry or problem into smaller elements. The smaller elements are referred to as finite elements because they can are individually analyzed to understand their interaction with their surrounding elements [32].

Instead of solving a large continuous system that has no specific solution or infinite elements, smaller finite elements can be assigned properties that are solvable through FEA software. Each finite element is assigned and solved through smaller element-level equations that characterize each element's interactions and its degrees of freedom (DOF) [32]. It is worth noting that FEA solvers implement linear or polynomial equations to each element and they connect to their surrounding elements to establish larger global equations. Since the equations are approximations of physical systems,

Figure 2.13: Excavator arm that was printed on the MedUSA system [7].

the overall result is an approximation of the overall behavior of the system. The approximation becomes more accurate with an increase in the number of elements. The trade-off with more elements is more computation time that can range from hours to days and even weeks depending on the system. Nonetheless, the simulation will converge to a result that can then be used to understand the system.

Depending on the solver implemented, inputs can have a large effect on the result. The element size and shape can be varied along with the physical attributes of the system. Physical attributes can include mass, density, damping ratio, and thermal conductivity, for example. [32]. Many methods exist to solve the various types of problems and can change the efficiency with which the answer converges. Boundary conditions for interacting parts and the physical environment are essential to the simulation since they enable the structure to behave as it does in the physical world. FEA can only be accurate if all the boundary conditions and physical properties are selected correctly. Whenever possible, it is best to have some form of testing to validate the simulated values because there can be a drastic change in the result if one variable is incorrectly implemented.

2.4 Modal analysis and impact testing

2.4.1 Modal analysis

Modal analysis is essential in identifying the dynamic behavior of complex structures. Before investigating the behavior of a structure, a single and two- degree freedom systems are summarized to establish the foundations on which modal analysis is based [33, 34]. For linear systems, the vibrational behavior is comprised of inertial forces, damping forces, and spring forces [35]. Linearity is assumed in this analysis.

Physical systems have mass and elasticity. Elasticity allows a body to change its shape without permanent deformation [8]. The combination of mass, stiffness, and damping results in one or more natural frequencies.

Three vibration types are exhibited by structures, including free vibration, forced vibration, and self-excited vibration. Free vibration occurs at one or more natural frequencies when a short-term excitation force, such as an impulse, is imposed on a physical system. The fact that all physical structures and systems have some form of damping results in decaying oscillation seen in Figure 2.14. Forced vibration occurs when an external force acts continuously on a system. When the forcing frequency, ω, is equal to the natural frequency, ω_n, resonance occurs. Resonance is typically avoided because it causes the system to vibrate at its largest amplitude which can cause damage as seen in Figure 2.15. Self-excited vibration requires a steady input force, but the system vibrates near one of its natural frequencies.

For a single degree of freedom spring-mass-damper system, equation 2.1 provides the time dependent equation of motion [8]. The system dynamics are described using the mass, m, damping coefficient, c, and spring constant, k. The variables x, $\dot{x}$, and $\ddot{x}$ represent the displacement, velocity, and acceleration, respectively. When there is no damping, Equation 2.1 simplifies to Equation 2.2. Without damping, the natural frequency is solved using Equation 2.3 where the result has units of rad/s. If the desired natural frequency is in Hertz (Hz), Equation 2.4 is applied.

$$m\ddot{x} + c\dot{x} + kx = 0 \tag{2.1}$$

$$m\ddot{x} + kx = 0 \tag{2.2}$$

$$\omega_n = \sqrt{\frac{k}{m}} \tag{2.3}$$

$$f_n = \frac{\omega_n}{2\pi} \tag{2.4}$$

In reality, all systems have some form of damping. Damping can be described as viscous, Coulomb, solid, or any combination of the three. Viscous damping is

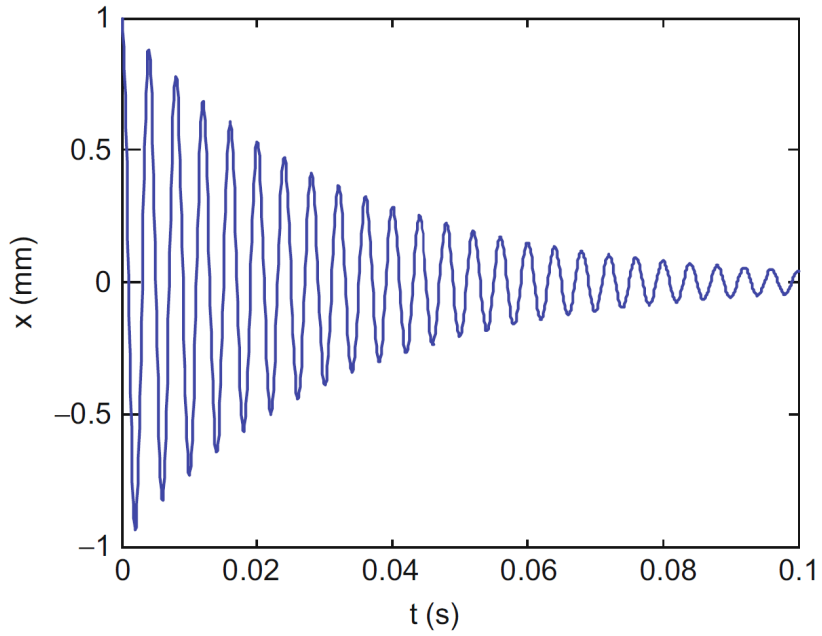

Figure 2.14: Example of a damped free vibration system in the time domain [8].

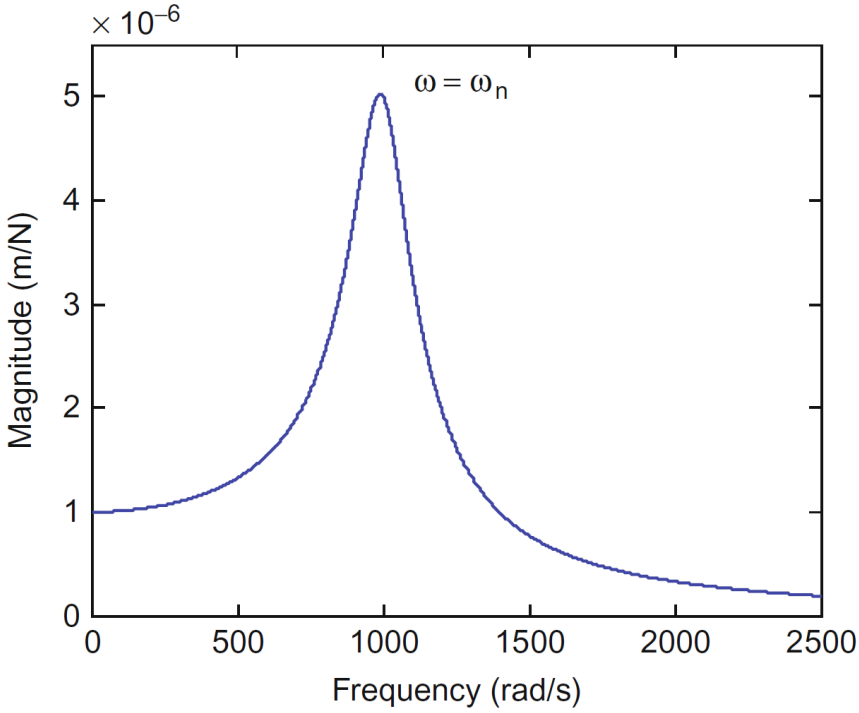

Figure 2.15: Example of forced vibration magnitude in the frequency domain [8].

represented by Equation 2.5 where the damping force, f, is equal to the damping coefficient multiplied by the velocity. Coulomb damping is also known as dry sliding friction. The behavior of this form of damping is in a piecewise function where the dissipative force opposes the velocity, $\dot{x}$, and is modeled as the product of the friction coefficient, μ, and normal force, N, as shown in Equation 2.6. Lastly, solid damping is due to the internal energy loss of a system. The focus of this section will be on viscous damping.

$$f = c\dot{x} \tag{2.5}$$

$$f = \begin{cases} -\mu N & \dot{x} > 0 \\ 0 & \dot{x} = 0 \\ \mu N & \dot{x} < 0 \end{cases} \tag{2.6}$$

For a single degree of freedom spring-mass-damper system with viscous damping, three vibratory behaviors can exist. The equations that dictate which behavior a system will exhibit are shown in Equation 2.7. Underdamped systems will exhibit vibratory motion. Critically damped and overdamped systems do not have vibratory motions and are not pertinent in the investigation of the structure for this project. For an underdamped system, Equations 2.8 and 2.9 show the relationship between the damping ratio, ζ, damped natural frequency, ω_d, and the (undamped) natural frequency from Equation 2.3. The vibratory motion of a system with viscous damping consists of a sinusoidal motion that decays exponentially. The exponential decay profile is known as the decaying exponential envelope and it encapsulates the vibratory motion of the system until it reaches zero.

$$\left(\frac{c}{2m}\right)^2 - \frac{k}{m} \begin{cases} < 0 & \textit{underdamped} \\ = 0 & \textit{critically damped} \\ > 0 & \textit{overdamped} \end{cases} \tag{2.7}$$

$$\zeta = \frac{c}{2\sqrt{km}} \tag{2.8}$$

$$\omega_d = \omega_n \sqrt{1 - \zeta^2} \tag{2.9}$$

Once a harmonic force is added to a spring-mass-damper system, the system undergoes forced vibration. The equation of motion for forced vibration is shown in Equation 2.10. The total solution includes the homogeneous and particular solutions. The homogeneous part of the solution is the transient component, while the particular solution is the steady-state behavior. Because the force is persistent as well as the assumption that the input force is sinusoidal, Equation 2.10 can be modified into Equation 2.11 with an assumed solution o of $x = Xe^{i\omega t}$. Both the velocity and acceleration can be written as $\dot{x} = i\omega Xe^{i\omega t}$ and $\ddot{x} = -\omega^2 Xe^{i\omega t}$. The force,$f$, can also be rewritten as $f = fe^{i\omega t}$.

$$m\ddot{x} + c\dot{x} + kx = f \tag{2.10}$$

$$(-\omega^2 m + i\omega c + k)Xe^{i\omega t} = fe^{i\omega t} \tag{2.11}$$

Equation 2.11 can be rewritten as a complex-valued frequency response function (FRF) as shown in Equation 2.12. Equation 2.12 can be separated into its magnitude and phase components or its real and imaginary parts. The magnitude and phase components are shown in Equations 2.13 and 2.14 respectively. The real and imaginary parts of the system are shown in Equations 2.15 and 2.16. The frequency ratio, r, is the ratio of the forcing frequency and the natural frequency of the system ($r = \frac{\omega}{\omega_n}$). The magnitude and frequency components of the FRF give insight into the motion of the system. The external force causes the system to undergo forced vibration and the magnitude is the size of the motion compared to the input force while the phase describes the time delay between the force peak and the displacement

peak. The real and imaginary components of the FRF are the cosine and sine components of the external sinusoidal force that show the relationship of the combined motion of the cosine and sine parts of the motion; these are also related to the magnitude and phase.

$$\frac{X}{F} = \frac{1}{-m\omega^2 + ic\omega + k} \tag{2.12}$$

$$\left|\frac{X}{F}\right| = \frac{1}{k}\sqrt{\frac{1}{\left(1 - \left(\frac{\omega}{\omega_n}\right)^2\right)^2 + \left(2\zeta\frac{\omega}{\omega_n}\right)^2}} \tag{2.13}$$

$$\Phi = tan^{-1}\left(\frac{Im\left(\frac{X}{F}\right)}{Re\left(\frac{X}{F}\right)}\right) = tan^{-1}\left(\frac{-2\zeta\frac{\omega}{\omega_n})}{1 - \left(\frac{\omega}{\omega_n}\right)^2}\right) \tag{2.14}$$

$$Re\left(\frac{X}{F}\right) = \frac{1}{k}\left(\frac{1 - r^2}{(1 - r^2)^2 + (2\zeta r)^2}\right) \tag{2.15}$$

$$Im\left(\frac{X}{F}\right) = \frac{1}{k}\left(\frac{-2\zeta r}{(1 - r^2)^2 + (2\zeta r)^2}\right) \tag{2.16}$$

Examples of magnitude and phase plots as well as the real and imaginary parts for a single degree of freedom system are shown in Figure 2.16 and 2.17. For the plots, when $r = 1$ the forcing frequency is equal to the system's natural frequency ($\omega = \omega_n$). The magnitude of the system at resonance can be calculated using Equation 2.17 which is a simplification of Equation 2.13. The maximum of the real part occurs at $r = \sqrt{1 - 2\zeta}$ and the minimum of the real part occurs at $r = \sqrt{1 + 2\zeta}$. If the difference between the maximum and the minimum of the real plot yields the peak value of the magnitude which is also the same equation as Equation 2.17. The minimum of the imaginary part also yields the magnitude value via $-\frac{1}{2k\zeta}$. It is also worth noting that the DC offset, the value at zero frequency, for both the magnitude and real plots yields the stiffness of the system via Equation 2.18.

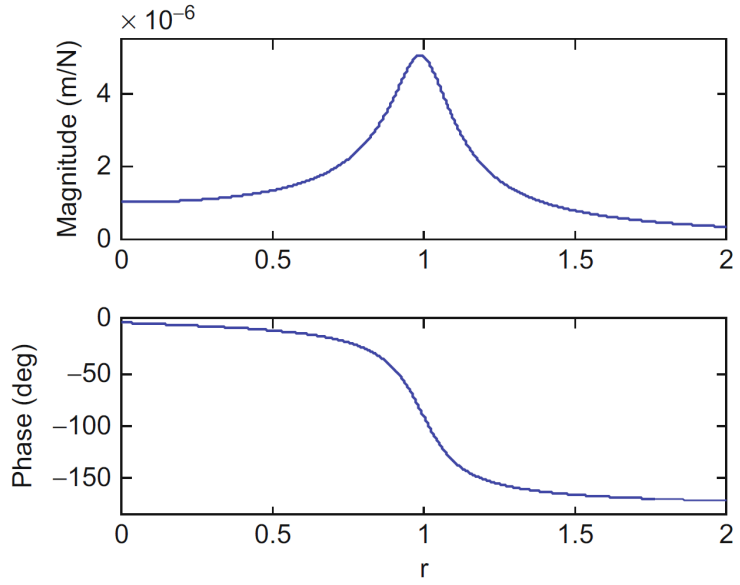

Figure 2.16: Example of a magnitude and phase plot for a single degree of freedom system [8].

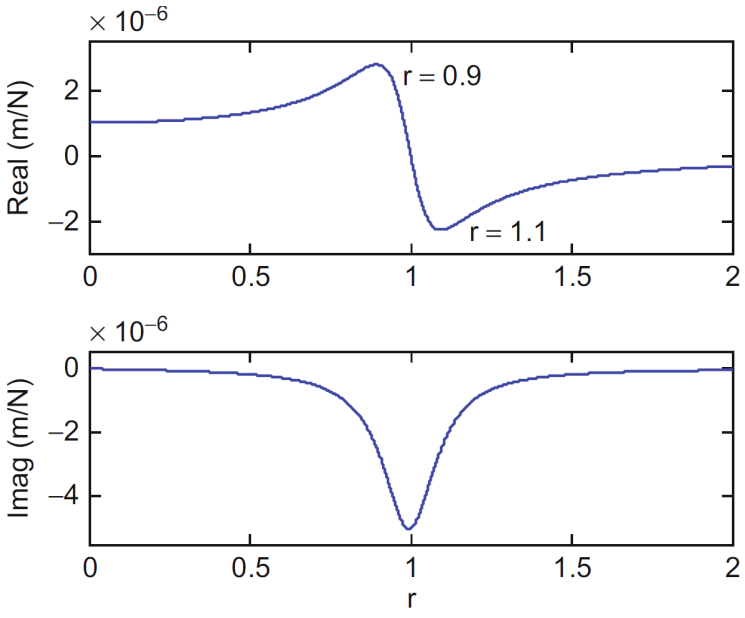

Figure 2.17: Example of a real and imaginary plot for a single degree of freedom [8].

$$\left|\frac{X}{F}\right| = \frac{1}{2k\zeta} \tag{2.17}$$

$$k = \frac{1}{\left|\frac{X}{F}\right|} \quad \left(\left|\frac{X}{F}\right| \; at \; r = 0\right) \tag{2.18}$$

Single degree of freedom forced vibration models can be extended to incorporate multiple degrees of freedom. The more degrees of freedom a system has the more natural frequencies (or eigenvalues) that exist. Multiple degree of freedom systems exhibit different vibration amplitudes at different spatial locations on the structure. These shapes that the structure take when vibrating at each natural frequency are referred to as mode shapes. These characteristic deformation patterns are the eigenvectors in a mathematical

context [8]. Mode shapes are representations of the system's relative shape and do not provide the size of the motion.

Expanding Equation 2.11 to incorporate multiple degrees of freedom requires implementing matrices to solve for the eigenvalues of the system. Substituting the single-degree system values with matrices, Equation 2.11 becomes 2.19. The matrices $[M]$, $[C]$, $[K]$, $\{X\}$, and $\{F\}$ describe the individual degrees of freedom as well as how they are connected. Solving the equations of motion using modal analysis gives the system FRFs. These are used to determine the mass, damping ratio, and stiffness for each vibration mode.

$$(-\omega^2[M] + i\omega[C] + [K])\{X\}e^{i\omega t} = \{F\}e^{i\omega t} \tag{2.19}$$

An experimental approach to quantifying and understanding a system's dynamic behavior is modal testing and modal fitting. Modal testing gives the FRFs at various points across a system. The real and imaginary components of the data can be analyzed through modal fitting. One method of modal fitting is the "peak picking" method. Peak picking extracts the modal values from the real and imaginary

FRFs using selected points. A mode's damping ratio is calculated using the natural frequency, ω_n, and the difference between the frequencies of the maximum, ω_{max}, and minimum, ω_{min}, peaks in the real FRF plot. Using these frequencies, the modal (represented by subscript q) damping ratio, ζ_q is determined using Equation 2.20. The (negative) peak value, A, of the imaginary plot at the natural frequency can be used to find the modal stiffness, k_q, with Equation 2.21. Also the modal mass, m_q is found with Equation 2.22 after solving for the natural and stiffness.

$$\zeta_q = \frac{\omega_{max} - \omega_{min}}{2\omega_n} \tag{2.20}$$

$$k_q = \frac{-1}{2\zeta_q A} \tag{2.21}$$

$$m_q = \frac{k_q}{\omega_n^2} \tag{2.22}$$

Peak picking works best when the mode shapes are distinct and not affected by the surrounding mode shapes. However, mode shapes that are overlapping can occur for complex systems. Peak picking can still be implemented but the calculated values may need to be adjusted. The goal of modal fitting is to construct a discrete mathematical model that replicates the measured FRF of the physical system with sufficient accuracy [8].

2.4.2 Impact testing

To measure the FRF of a system, there needs to be a source of force input that can output the amount of force that was transmitted, a transducer that will record the vibrational data of the system and a dynamic signal analyzer that converts the time domain force and vibration data to the frequency domain. It is important to ensure that both the force input can excite the system and the transducer can measure the system across the desired frequency range. The common types of forces that

can be imposed on structures are fixed frequency sine waves, random signals, and impulse [36]. The chosen input force for this project was the impulse method which uses an impact hammer shown in Figure 2.18. The impulse method excites multiple frequencies of a structure which can be analyzed and captured. Typical options for transducers include capacitance probes and laser vibrometers which are non-contact methods as well as low-mass accelerometers which are contact transducers [36]. The chosen transducer for this project was the low-mass accelerometer shown in Figure 2.19.

To obtain the mode shapes of large structures. multiple measurements of the system need to be captured. When multiple measurements of the same structure are taken, there are direct and cross measurements. Figure 2.20 shows that the direct measurement is the measured value that is co-located with the force input. The measured values where the input force and senor are not co-located with each other are considered cross measurements. Regardless of the geometry of the structure that is being measured, points of interest should be established and marked. There are two measurement styles with the hammer and accelerometer which are the roving hammer and roving accelerometer method. The roving hammer entails that the accelerometer stays at one point while the hammer impacts various select locations. The roving accelerometer method moves the accelerometer to the various select points while the hammer impacts the same point for all the measurements. The roving hammer method was implemented in this study.

The direct measurement for the roving hammer method is the data set where the hammer impacted the point immediately adjacent to the accelerometer. All the other measurements were cross-measurements. To experimentally identify mode shapes, the peak values from the imaginary plot can be used. The values of the imaginary peaks at the same natural frequency are extracted to construct the mode shape for the desired natural frequency. The peak values are normalized to unity at the direct measurement location. By plotting the normalized amplitudes to the corresponding

Figure 2.18: Large impact hammer used for impact testing with a nylon tip and extended mass.

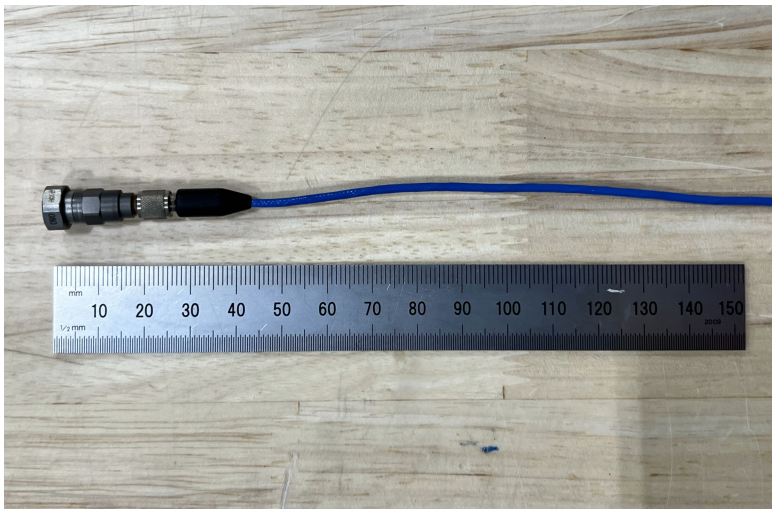

Figure 2.19: Large magnetic accelerometer that was used for impact testing.

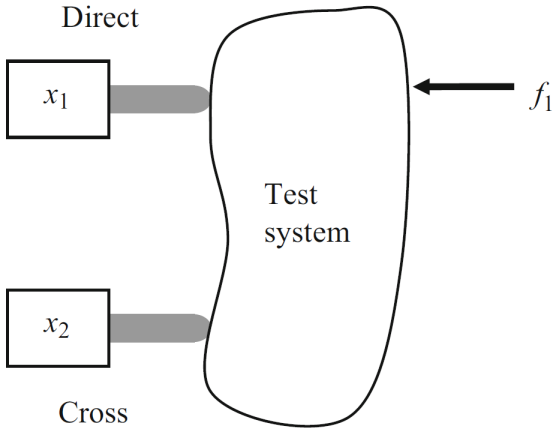

Figure 2.20: Representation of direct and cross FRF measurements on an example test system where f_1 is the input force and the x values represent different locations[9].

geometric locations, the overall mode shape of a large structure can be constructed and visualized.

Chapter 3

Weldment Cross Beam

3.1 Weldment design

3.1.1 Original design and purpose

The weldment cross beam was designed for the concrete base machine at ORNL. The concrete base machine tool was intended to demonstrate a replacement for large metal castings typically selected as machine tool bases [13]. The machine tool was designed as a three-axis machine. The three axes of the machine are shown in Figure 2.6. The cross beam is mounted on top of the concrete base and the spindle and Z-axis assembly are mounted onto the cross beam as shown in Figure 3.1.

The cross beam, shown in Figures 3.2 and 3.3, connects the base and the Z-axis assembly. The cross beam is mounted onto the concrete base through bolts to metal plates on each side of the machine tool as seen in Figure 3.4. The metal pads were leveled to ensure that the cross beam would sit flat on top of the machine tool base and be mounted securely. The front face of the cross beam is where the guide rails and motors for the Y-axis motion are mounted seen in Figures 3.5 and 3.6. The Z-axis assembly, which is attached to the spindle, is connected to the guideways through

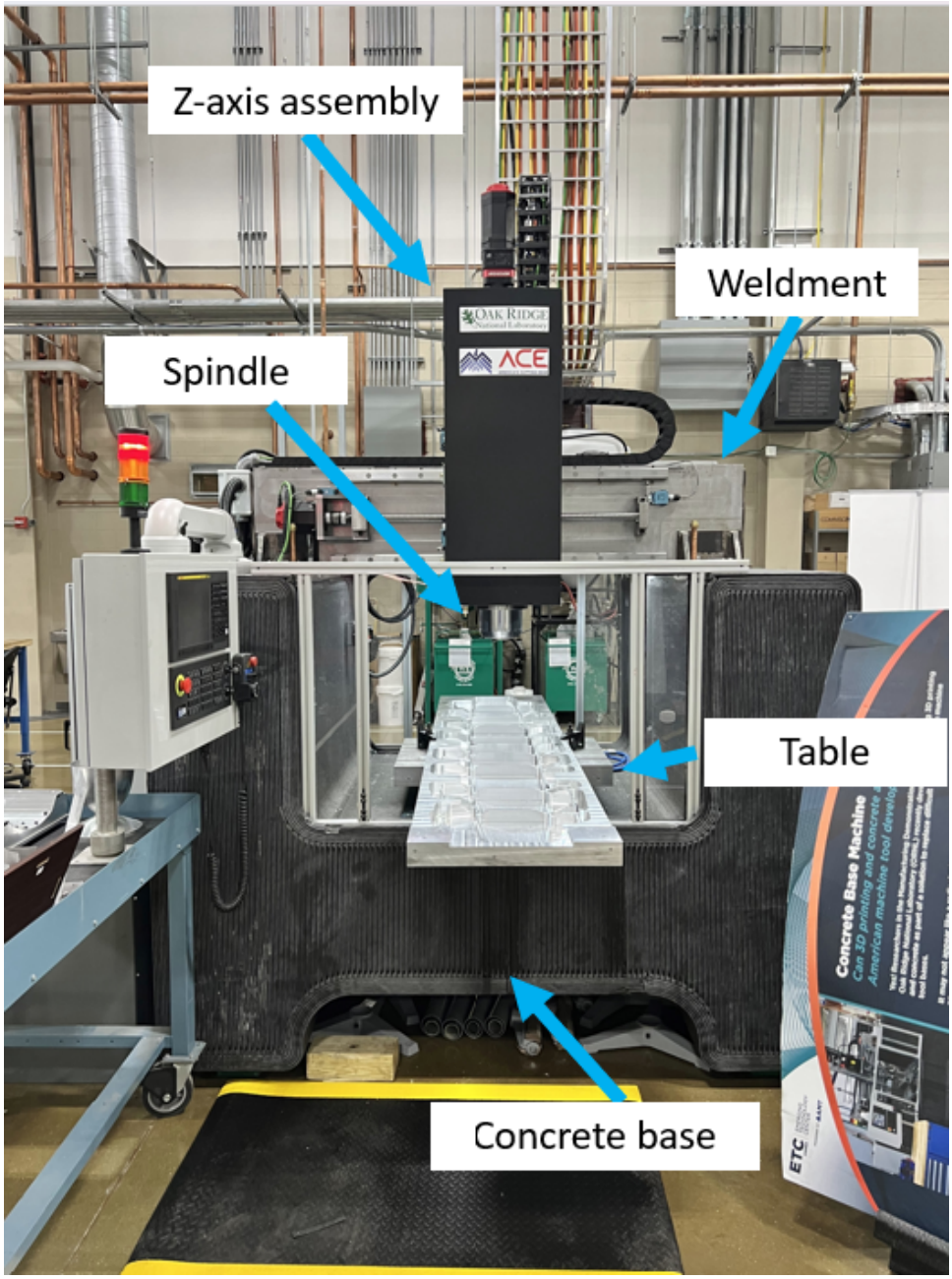

Figure 3.1: Concrete base machine tool with the cross beam supporting the Z-axis and spindle assembly on top of the concrete base.

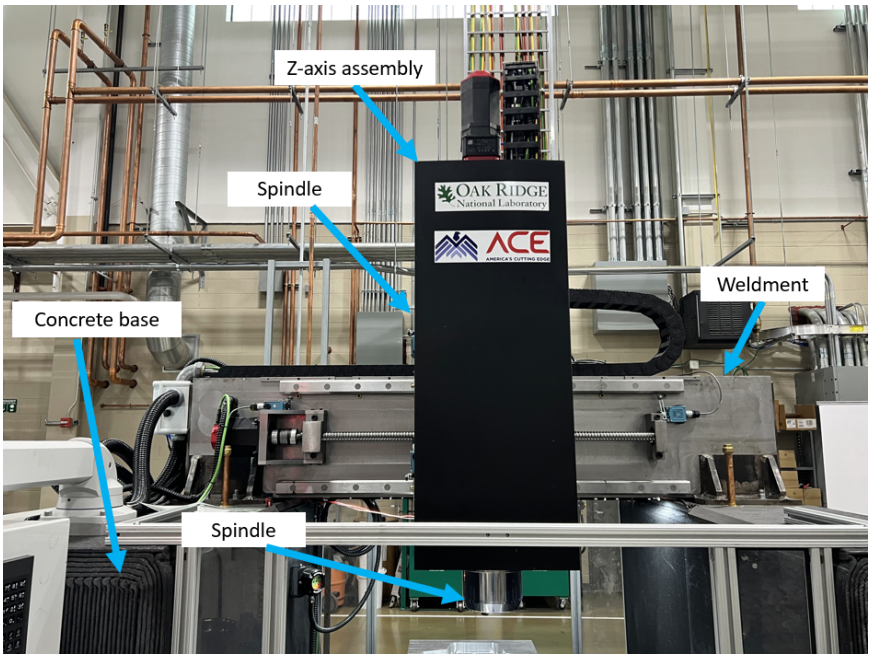

Figure 3.2: Front view of cross beam weldment on concrete base machine.

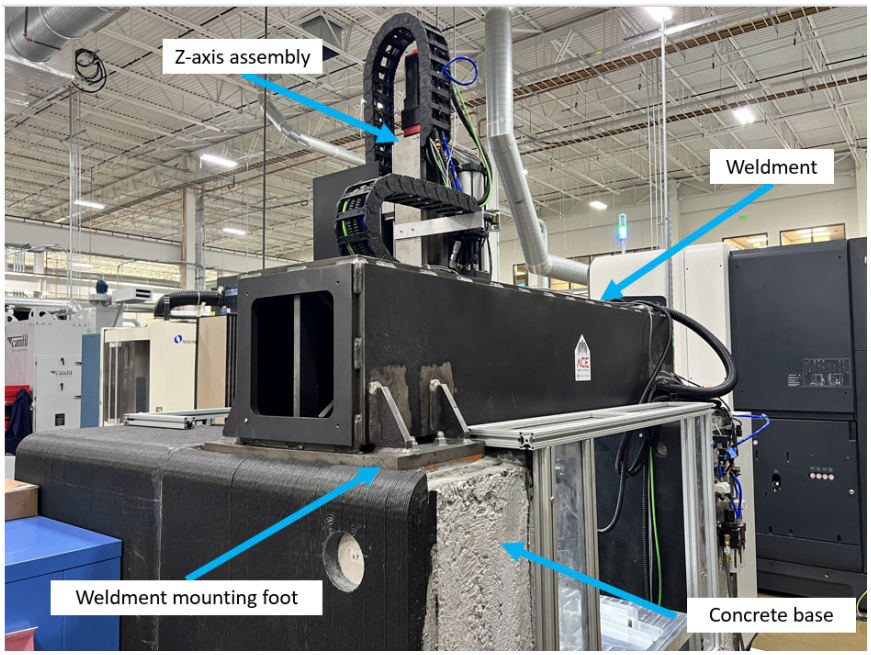

Figure 3.3: Back right corner view of the cross beam weldment on concrete base machine

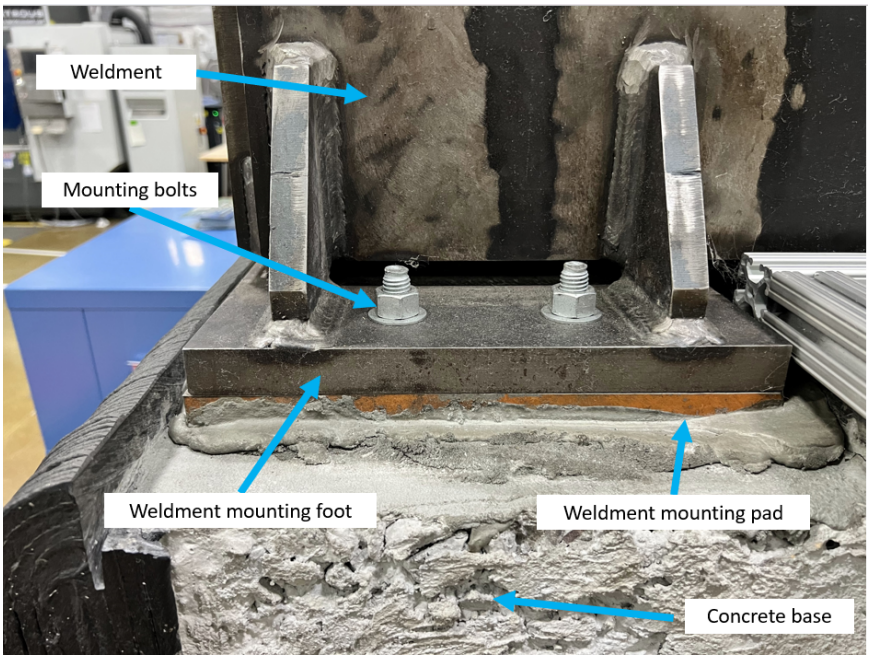

Figure 3.4: Connection of a foot of the cross beam to the concrete base.

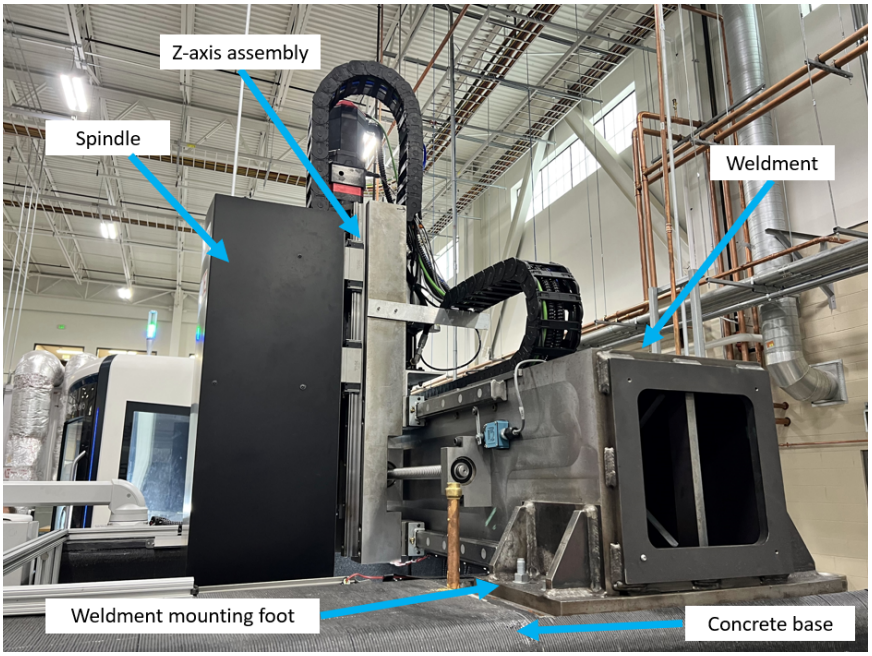

Figure 3.5: Right side view of guideways on the front face of the cross beam.

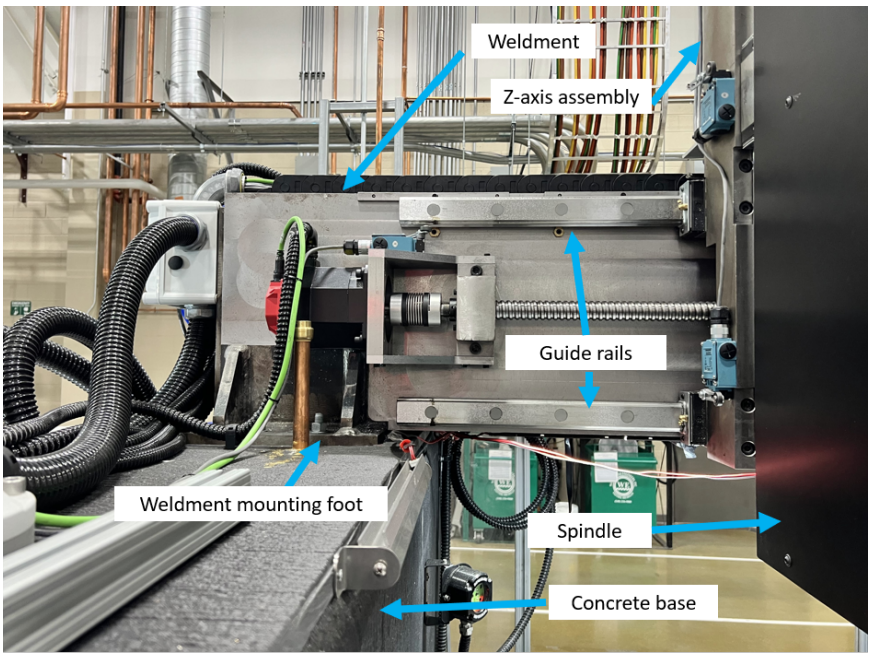

Figure 3.6: Left side view of guideways on the front face of the cross beam.

bearing pads. In addition to the purpose of supporting the spindle and Z-axis assembly, the cross beam was used for mounting wires and tubing for the machine shown in Figure 3.7.

The cross beam itself is an assembly of steel plates that were welded together. The weldment is comprised of one main rectangular box section that has an internal supporting rib and two footpads that support each end of the rectangular box. The Z-axis and spindle assembly can be referred to as the column assembly. The design began with an L-shaped weldment because the bottom and front plates of the current structure were necessary for mounting the column assembly as well as the mounting feet to the base. The top, back, and side plates were added to form a box tube geometry which has less mass compared to a solid block of steel. After static analysis, an internal rib was added to the inside of the beam to stiffen the structure since the mass of the column assembly is cantilevered from the front face of the cross beam. The details and dimensions of the structure are discussed in Section 3.1.2. One important design feature of the cross beam weldment is that the front face is the primary mounting surface for the guide rails as well as the motor assembly which drives the column assembly. The second most important mating surfaces are the two steel feet that mount to the concrete base. Aside from the importance of the mounting surfaces, the box structure was also primarily designed to support the column assembly.

3.1.2 Dimensions and features

The weldment cross beam is an assembly of multiple pieces of A36 steel as seen in Figure 3.8. The overall dimensions for the assembly are shown in Figures 3.9 through 3.13. The various components of the cross beam are identified and named in Figures 3.14 through 3.16. The components are welded together to create the final structure. Individual components for the assembly along with their dimensions and how the assembly was assembled are provided in Appendix A.

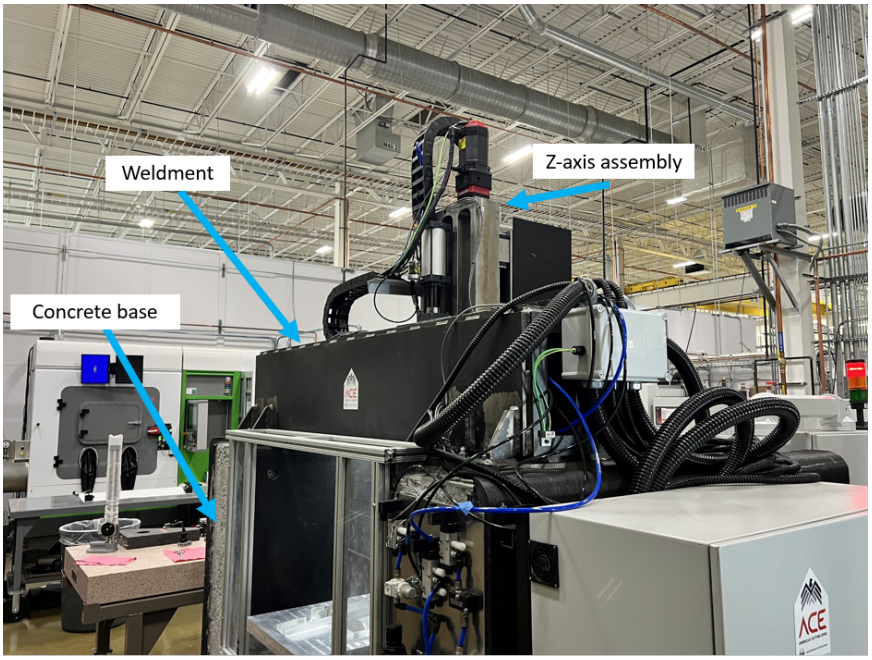

Figure 3.7: Back right corner view of cross beam weldment on the concrete base machine with cables.

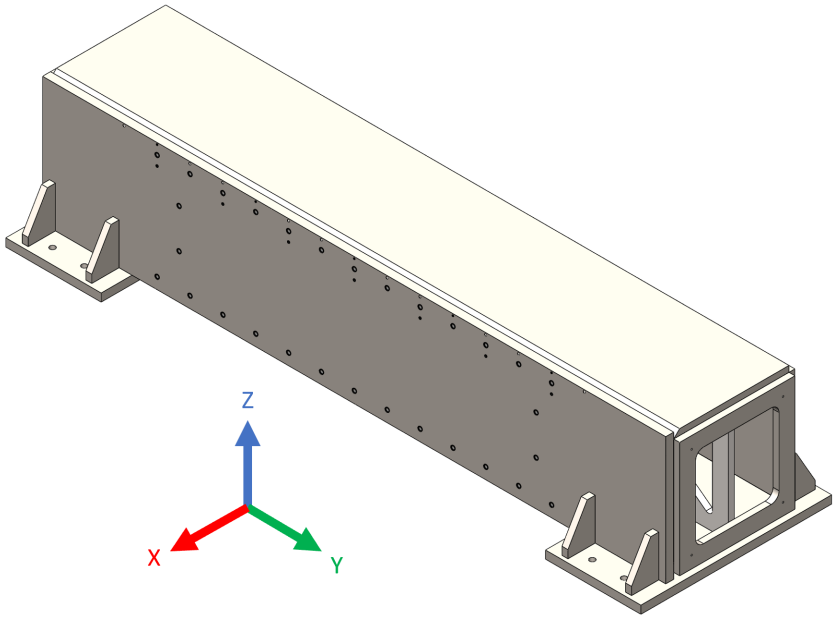

Figure 3.8: Isometric view of digital weldment cross beam.

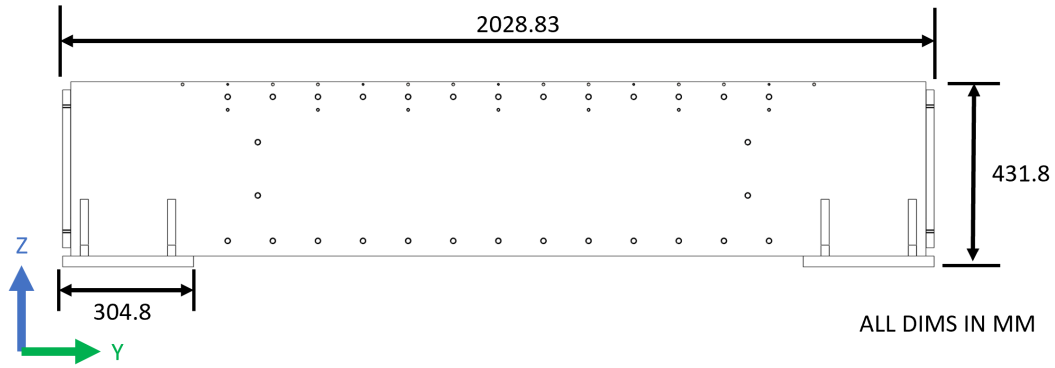

Figure 3.9: Front view of digital weldment cross beam with dimensions in millimeters.

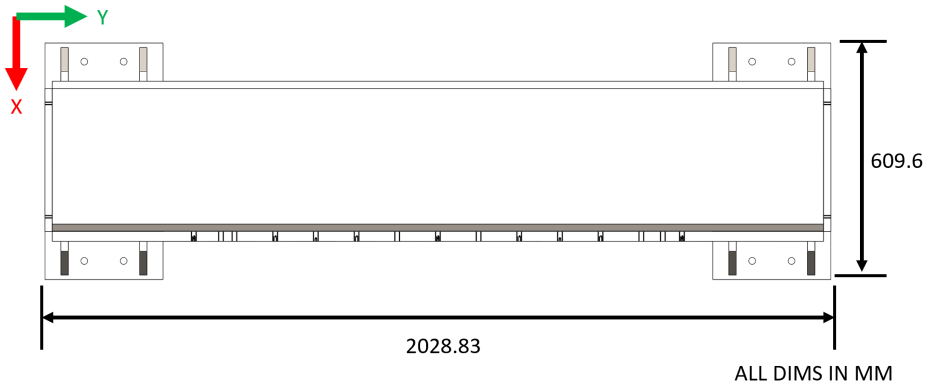

Figure 3.10: Top view of digital weldment cross beam with dimensions in millimeters.

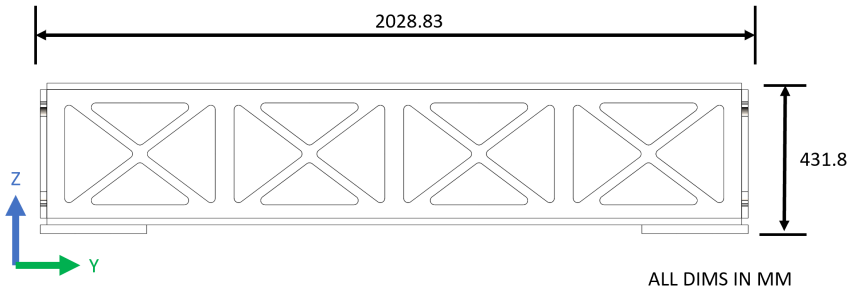

Figure 3.11: Front section view of digital weldment cross beam showing the center plate with dimensions in millimeters.

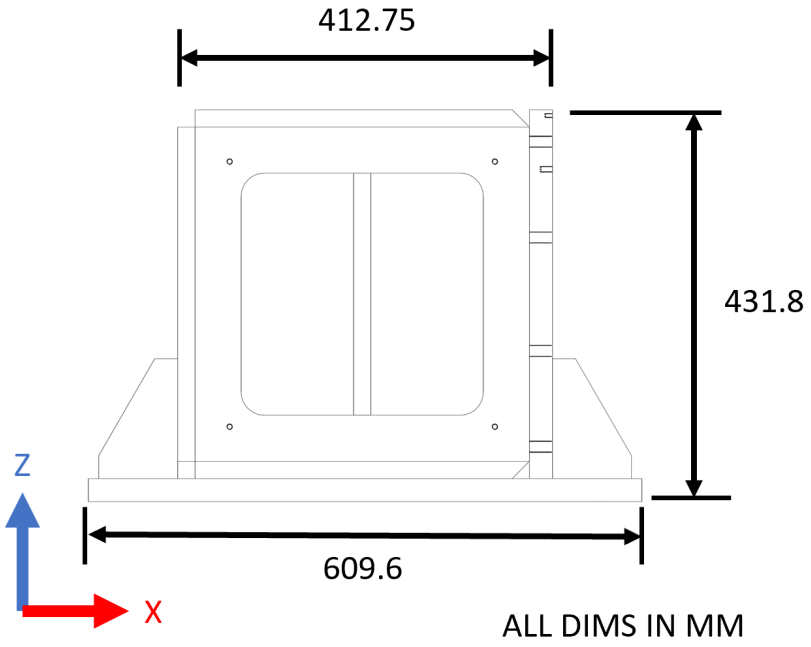

Figure 3.12: Side view of digital weldment cross beam with dimensions in millimeters.

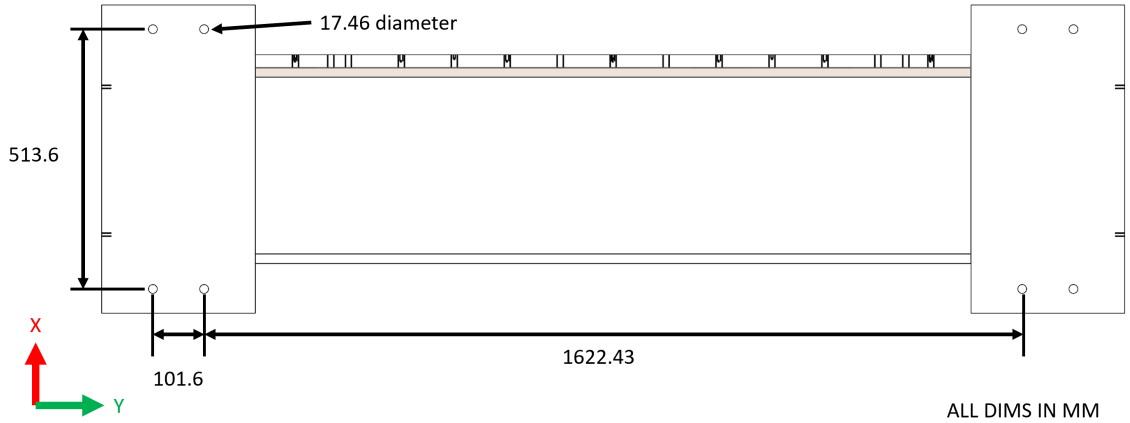

Figure 3.13: Bottom view of digital weldment cross beam with dimensions in millimeters showing mounting hole locations and dimensions.

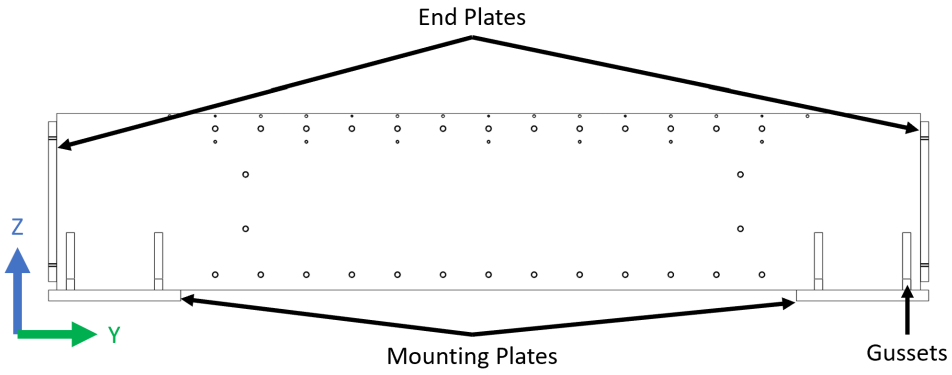

Figure 3.14: Front view with side and mounting plates with gussets identification.

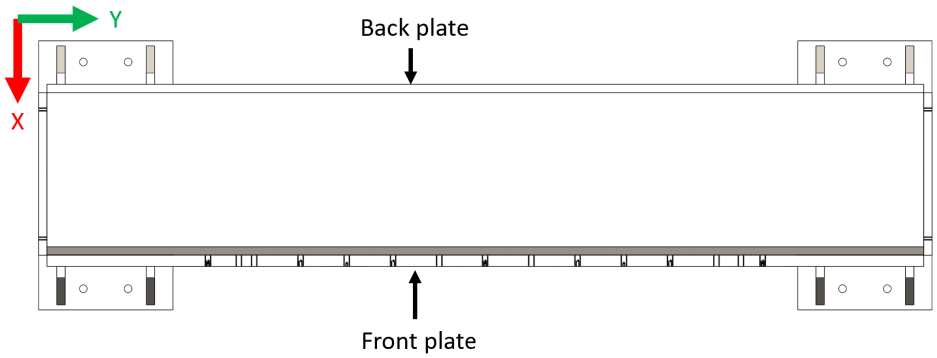

Figure 3.15: Top view with front and back plate identification.

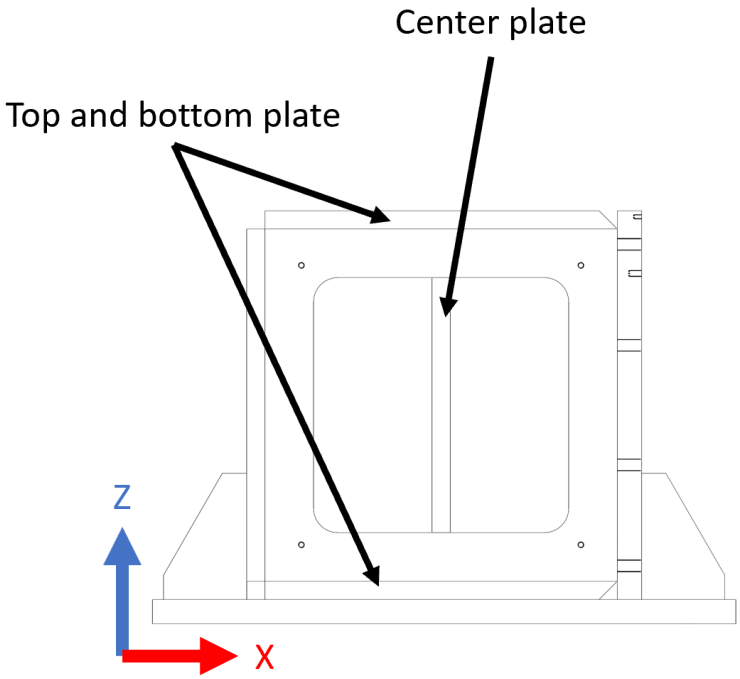

Figure 3.16: Side view with top, bottom, and center plate identification.

The cross beam weldment was outsourced for manufacturing; this weldment was identical to the original design for the concrete base machine tool, but was available for impact testing and comparison to the FEA predictions and mBAAM version. Because the plates needed to be welded, chamfers were added to the edges of select plates. The welding specifications are found in the assembly drawings in Appendix A. The mounting features of the cross beam weldment for the original design were removed because they were unnecessary for the subsequent impact testing (described in Section 3.2.3).

3.2 Weldment analysis

3.2.1 Digital modeling

The cross beam weldment modeling was completed using SolidWorks. Two models were used to investigate the weldment. Both models were simplified from the actual model by removing unnecessary mounting features for the guideways that would have been used for the column assembly. One model is referred to as the simplified model, while the other is referred to as the refined model. The simple model was generated to investigate the static behavior of the system. The refined model was used for the frequency analysis that yielded the mode shapes of the structure.

The simplified model shown in Figure 3.17 included minor modifications to the original plate dimensions to reduce computational complexity. Figures 3.18 and 3.19 show the modifications for the front, back, top, and bottom plates. These changes affected the method by which the joints of the box structure are formed shown in Figure 3.20. These modified joints simplify the model to ignore the effects of the welds. In doing so, the simplified model exhibits stiffer behaviors due to the increase in contact between the modeled surfaces. Each plate and component was assembled through surface mates. The plates were also assigned material properties of A36 steel.

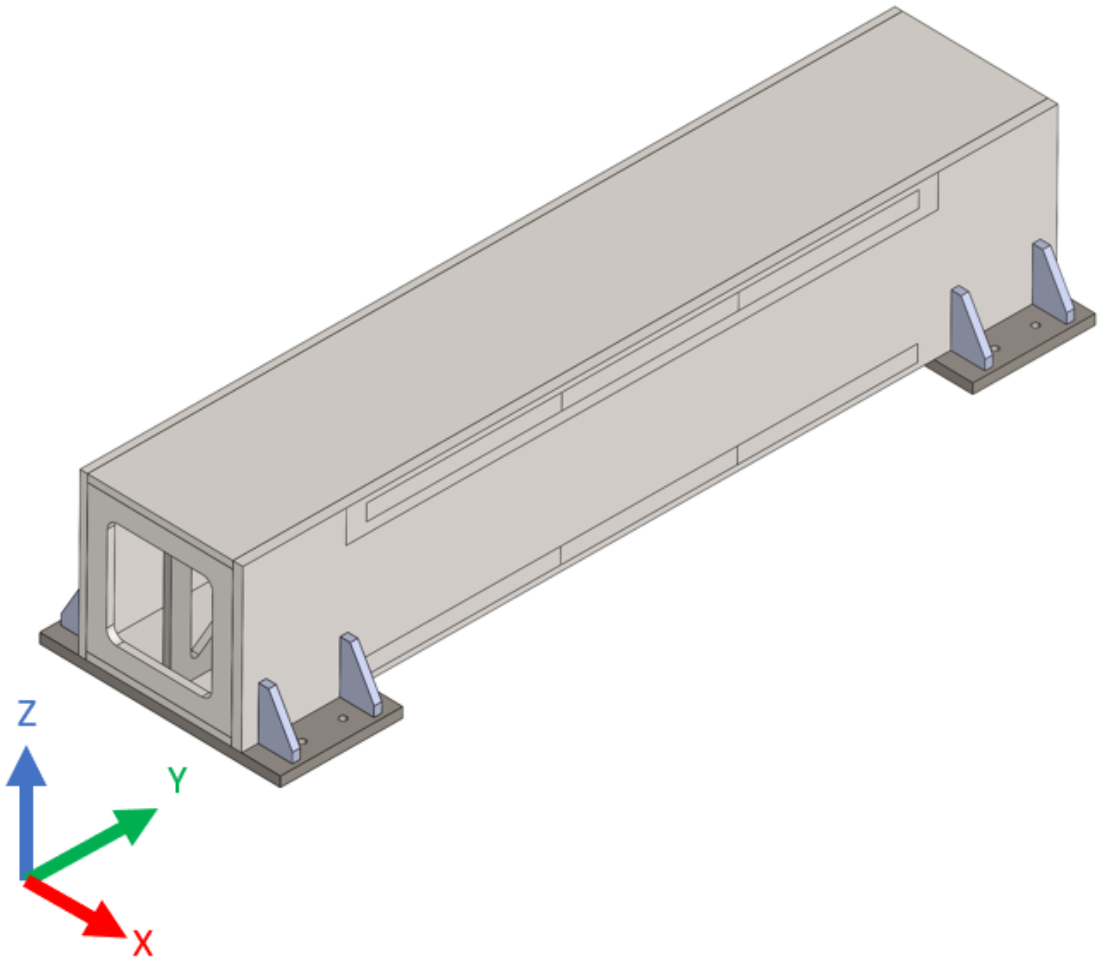

Figure 3.17: Isometric view of simplified cross beam weldment model.

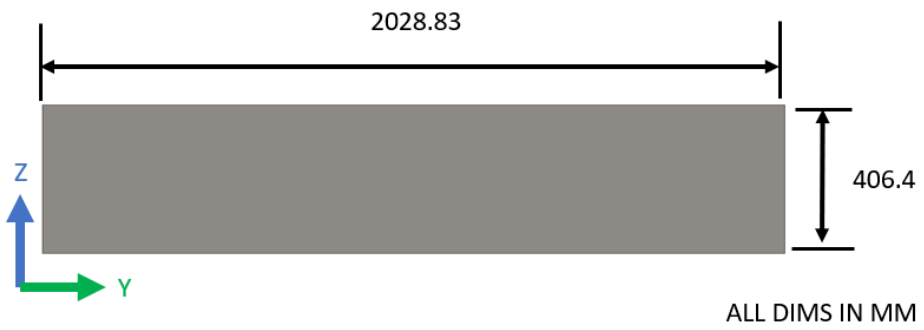

Figure 3.18: View of modified plate dimensions for the front and back plates while the respective thickness of the plates remained the same.

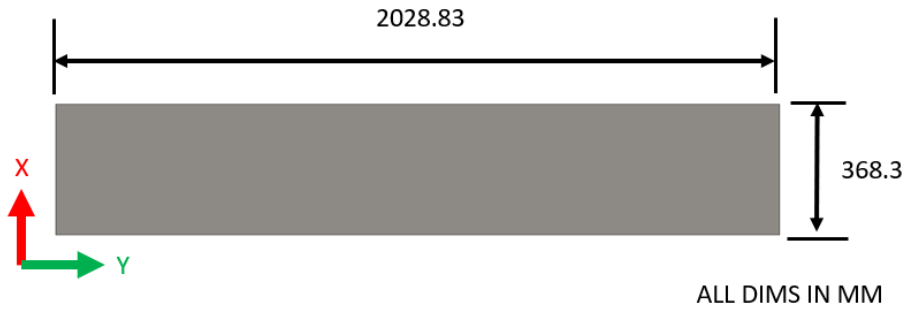

Figure 3.19: View of modified plate dimensions of the plate used for the top and bottom which are identical.

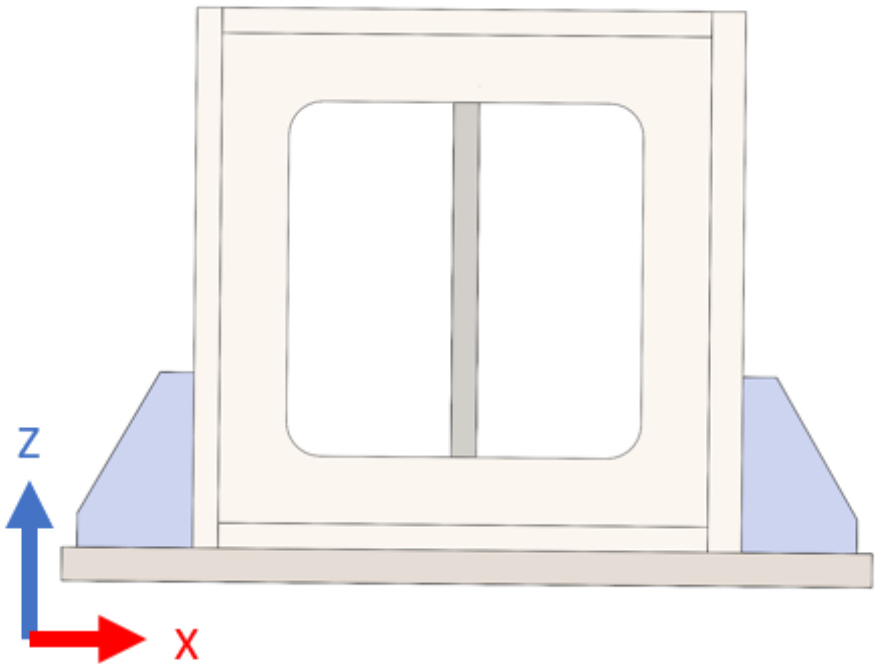

Figure 3.20: Side view of the overlap pattern used for the simplified model where both the top and bottom plates were butted against the front and back plates.

For the static simulations of the simplified weldment, it was important to model the load bearing areas on the front face of the weldment. The simulation was dependent on the model details and it was deemed necessary to model the area in which the column's load interacts with the guide rails. The two configurations shown in Figures 3.21 and 3.22 highlight the load bearing area of the column in red. The area was calculated through the span of the linear bearing pads that hold the column assembly for both the top and bottom rails. The reason for the two configurations was to investigate the structure's static deflection at its most extreme cases.

For the refined model, shown in Figures 3.23 and 3.24, the weld beads were modeled. The refined model was implemented to improve simulation accuracy.

The weld beads shown in Figure 3.23 were modeled by extruding triangular profiles that were attached to the appropriate bead patterns per the specification provided in the assembly of the weldment. Per the drawing requirements, the beads were to have 12.70 mm legs that were 50.8 mm long with a separation of 152.4 mm between each weld bead. Figure 3.25 shows the weld beads of the rectangular beam section and Figure 3.26 provides the bead geometry. The weld beads are approximate geometries because it is difficult to model material penetration, thermal defects, and bead surfaces.

3.2.2 Finite element simulation of weldment

Static analysis

To understand the behavior of the cross beam weldment when under load, static FEA was used to solve for the system deflection. Many parameters need to be input into the model including material type, boundary conditions, and loads. This section summarizes the inputs that were chosen for this model. As stated earlier, the software that was used for this analysis was SolidWorks.

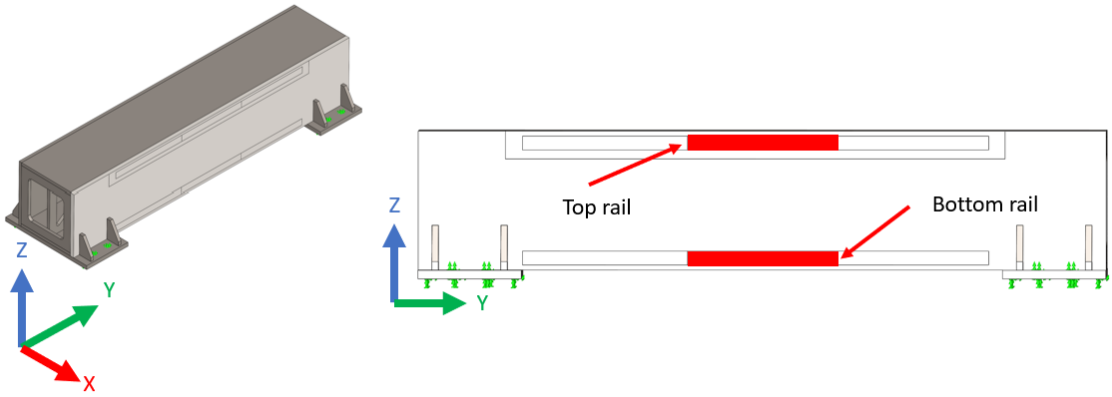

Figure 3.21: Location of the load bearing region on the rails in the column-centered configuration.

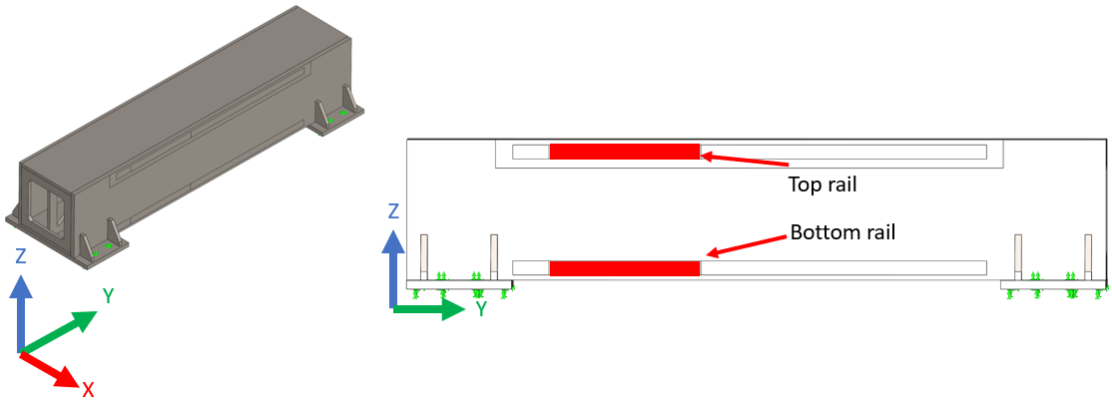

Figure 3.22: Location of the load bearing region on the rails in the column-offset configuration.

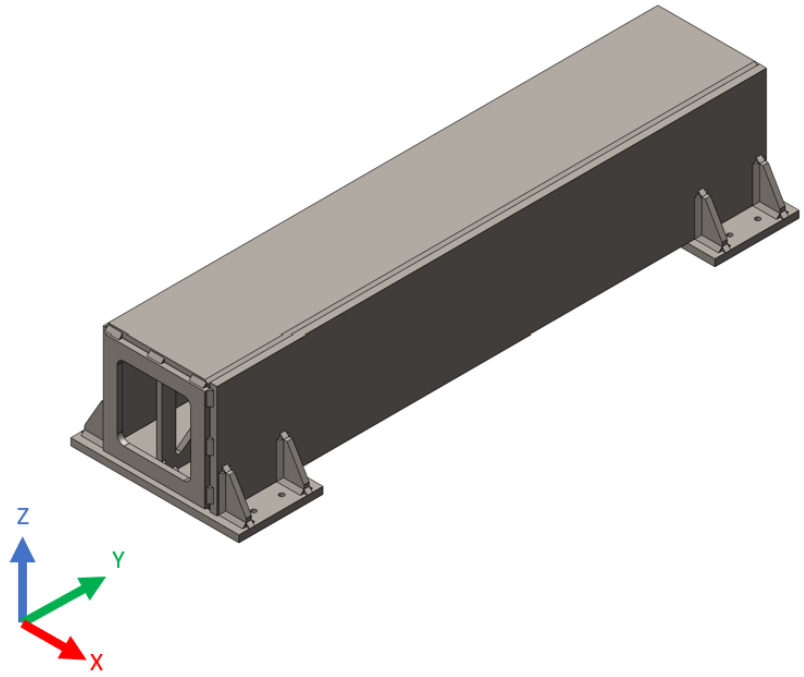

Figure 3.23: Front isometric view of refined model with weld beads.

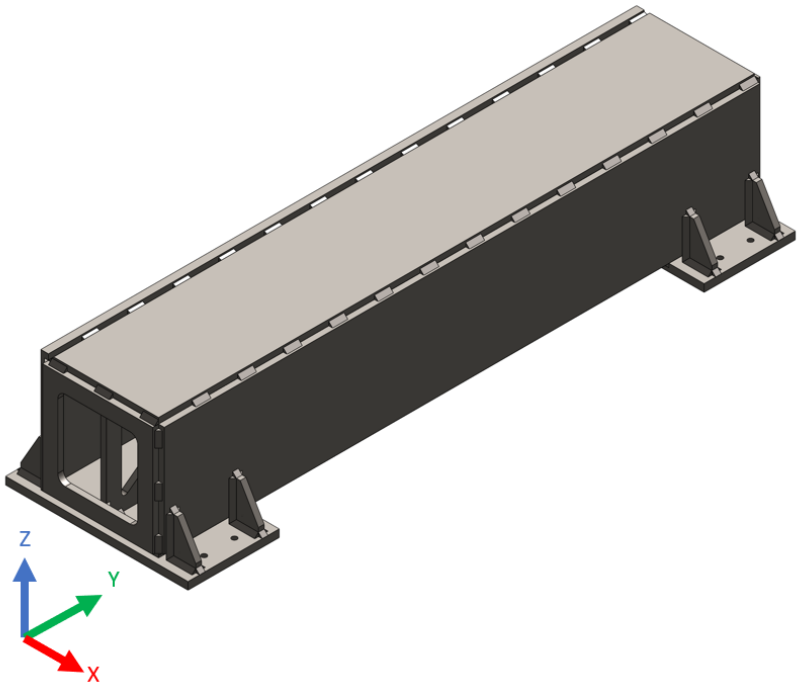

Figure 3.24: Back isometric view of refined model with weld beads.

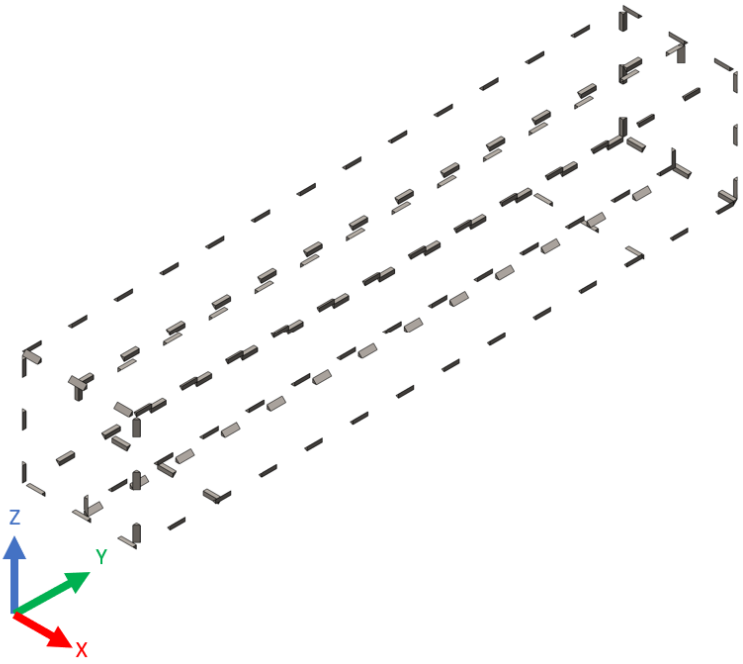

Figure 3.25: Isometric view of weld beads on and in the cross beam body.

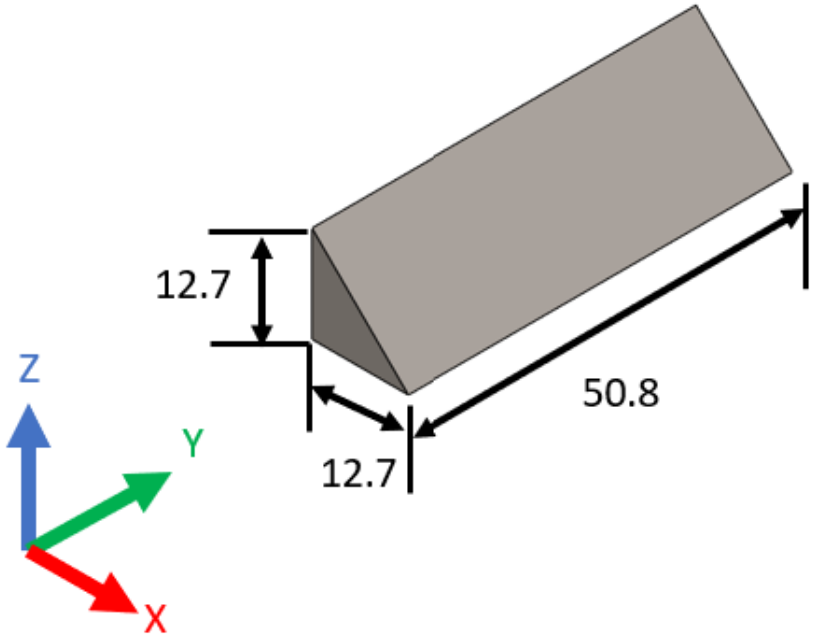

Figure 3.26: Isometric view and dimensions of a single weld bead from the refined model.

The simplified model was composed of machined A36 steel plates. The material characteristics for the simulation are listed in Table 3.1. This material was chosen for all components in the assembly.

For fixturing, the intent was to mimic how the cross beam would be mounted to the concrete machine shown in Figure 3.27. The concrete base had two metal pads where the cross beam foot pads were bolted. The metal pads were modeled identically to the mounting pads but without the bolt holes and all six sides of each plate were fixed, which are represented by the green arrows in Figure 3.28. Doing so constrained the plates from deformation and translations. In addition, the internal diameter of all eight mounting holes, seen in Figure 3.29, were constrained to be fixed to replicate the bolts' constraints of the weldment to the mounting plates.

To reduce the simulation complexity and preserve the external forces that were imposed on the weldment, remote loads were calculated and various combinations were chosen to be simulated. The column assembly was attached to the cross beam. This assembly was replaced with a remote mass. The additional forces that the cross beam experienced are the machining forces at the tip of the machine tool spindle. The cutting forces were solved through milling force equations. Lastly, gravity was imposed on the system to understand the deflections due to the remote mass as well as the cross beam's deflections from gravity. The value implemented by SolidWorks is $9.81 \frac{m}{s^2}$.

The column structure that is attached to the cross beam was composed of two sub-assemblies shown in Figure 3.30. The assemblies were the Z-axis motion components along with the spindle assembly. The mass of the Z-axis assembly was estimated to be 306.71 kilograms and the spindle assembly was estimated to be 387.69 kilograms. After summing both values and multiplying by a safety factor of 1.5, the final remote mass value used for the remote mass was 1042 kilograms. In addition to the mass, the center of mass of the column assembly was calculated to identify the placement of the remote mass relative to the cross beam.

Table 3.1: Material properties for A36 steel

Property	**Value**	**Unit**
Elastic modulus	2.00×10^{11}	$\frac{N}{m^2}$
Poisson's ratio	0.26	-
Shear modulus	7.93×10^{10}	$\frac{N}{m^2}$
Mass density	7.85×10^{3}	$\frac{kg}{m^3}$
Tensile strength	4.00×10^{8}	$\frac{N}{m^2}$
Yield Strength	2.50×10^{8}	$\frac{N}{m^2}$

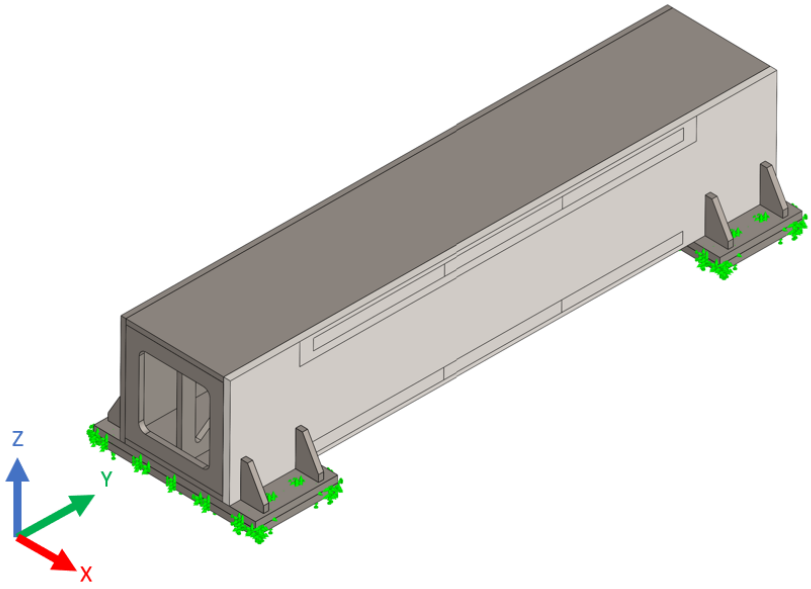

Figure 3.27: Isometric view of simplified weldment with fixed metal pads.

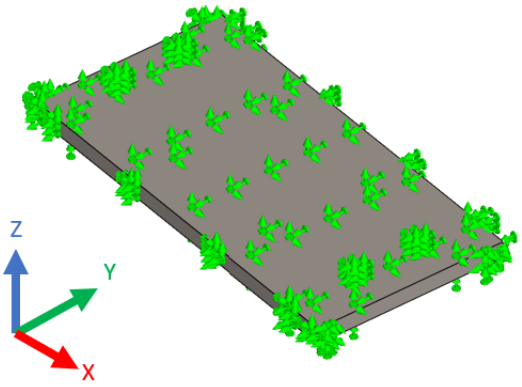

Figure 3.28: Isometric view of one of the two fixed metal pads simulating the mounting location of the concrete base machine (the green arrows represent the fixed condition).

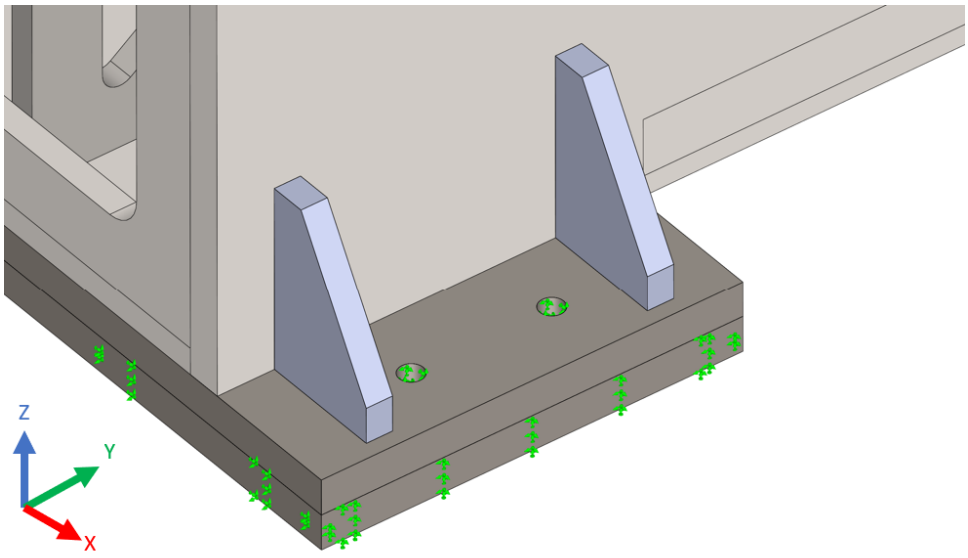

Figure 3.29: Zoomed in view of the bolt-hole fixed constraint (the green arrows represent the fixed condition).

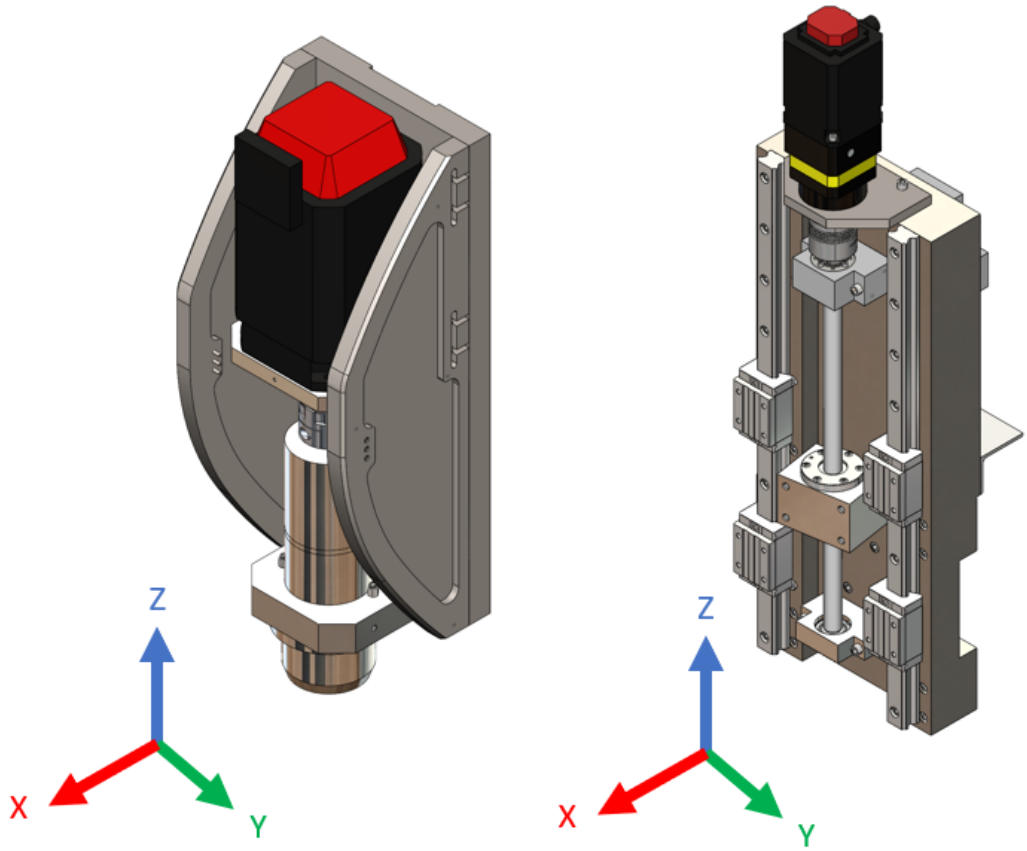

Figure 3.30: Spindle assembly (left) and Z-axis assembly (right) of the concrete base machine

To simulate the cutting forces that the milling machine would experience, cutting parameters needed to be prescribed. The concrete base machine was intended to cut aerospace parts which lead to three milling conditions. The conditions were milling aluminum with both ten-percent and one-hundred-percent (full-slot) radial engagement and milling titanium with ten-percent radial engagement. The ten-percent radial engagement in both the aluminum and titanium were to simulate finishing passes on machined parts. The full-slot cut in aluminum was to replicate a roughing pass that would remove a significant amount of material from a part. The aluminum cutting endmill was selected to have a diameter,D, of 19.05 millimeters that have two cutting flutes,$\#t$. The titanium cutting endmill was selected to have the same diameter but with six flutes instead of two. All milling cuts were assumed to be for climb (down) milling.

To simulate the cutting forces that the milling machine would experience, cutting parameters needed to be prescribed. The concrete base machine was intended to cut aerospace parts which lead to three milling conditions. The conditions were milling aluminum with both 10% and 100% (full slot) radial engagement and milling titanium with 10% radial engagement. The 10% radial engagement in both the aluminum and titanium was to simulate finishing passes on machined parts. The full slot cut in aluminum was to replicate a roughing pass that would remove a significant amount of material from a part. The aluminum cutting endmill was selected to have a diameter, D, of 19.05 millimeters (radius, r, of 9.525 mm) with two cutting flutes, $\#t$. The titanium cutting endmill was selected to have the same diameter, but with six flutes instead of two. All milling cuts were assumed to be in the climb (down) milling direction.

Figures 3.31, 3.32, and 3.33 are representations of the simulated cuts. Using Equations 3.1 through 3.4, and the values for each cut listed in Table 3.2, the cutting force and torque for each cut were calculated [37]. The results of the calculation are

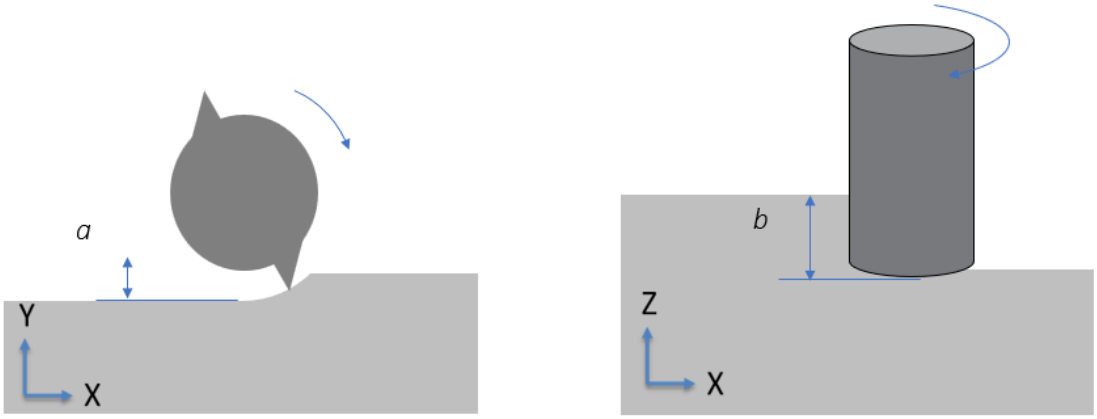

Figure 3.31: Top and side view of a two-flute endmill cutting aluminum for a finishing pass.

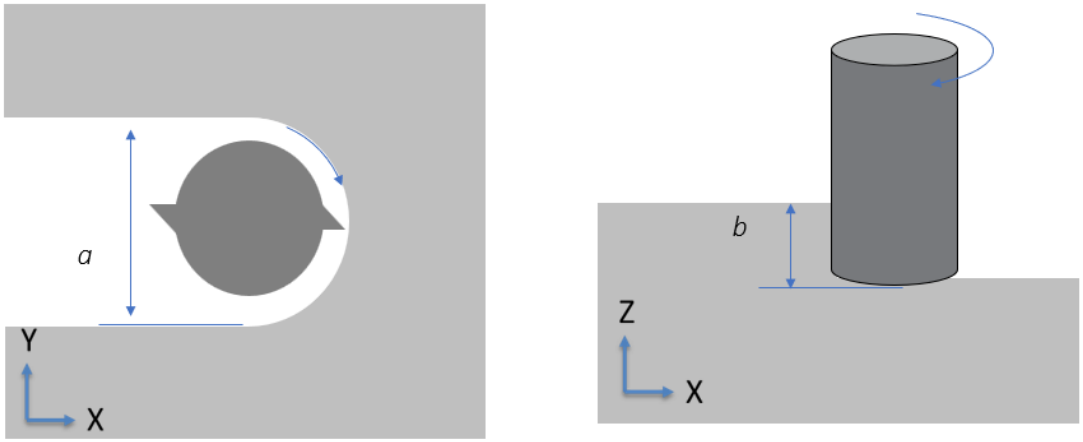

Figure 3.32: Top and side view of a two-flute endmill cutting aluminum for a roughing pass.

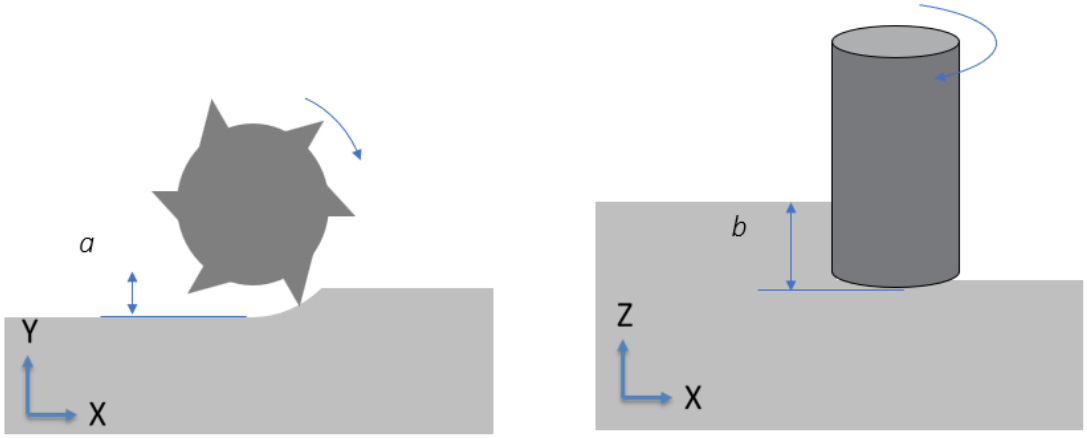

Figure 3.33: Top and side view of a six-flute endmill cutting titanium for a finishing pass.

Table 3.2: Cutting parameter inputs for calculations

Parameter	**Variable**	**Aluminum finishing**	**Aluminum slotting**	**Titanium finishing**
Diameter	D	19.05 mm	19.05 mm	19.05 mm
Axial depth of cut	b	25.40 mm	25.40 mm	25.40 mm
Number of teeth	$\#t$	2	2	6
Tangential cutting force coefficient	k_t	$850\frac{N}{mm^2}$ [38]	$850\frac{N}{mm^2}$ [38]	$3000\frac{N}{mm^2}$ [38]
Feed per tooth	f_t	0.178 $\frac{mm}{tooth}$	0.127 $\frac{mm}{tooth}$	0.089 $\frac{mm}{tooth}$

shown in Table 3.3 where the maximum cutting force is 4000 N and the maximum cutting torque is 39 N-m. Both values were for the titanium finishing cut.

$$F_t = k_t \times h \times b \tag{3.1}$$

$$h = f_t sin(\phi) \tag{3.2}$$

$$\phi = 180 - cos^{-1}\left(\frac{r-a}{r}\right) \ (deg) \tag{3.3}$$

$$T = F_t\left(\frac{D}{2}\right) \tag{3.4}$$

Another common function of milling machines is to drill holes. Drilling materials generate axial load on the spindle and the drilling force needs to be considered for the machine's deflections. However, various parameters can change the drilling force. For the static simulations, an axial force of 2000 N was chosen to simulate a drilling force that the spindle would experience.

The external forces imposed on the system were forces in the X-direction, Y-direction, Z-direction, torque, and gravity. Each of the forces affects the structure. To quantify and understand the deformation of the weldment, twelve simulation configurations were chosen to represent the extreme deflections of the cross beam. Two categories for the simulations are the centered and offset rail mount locations. The central location, shown in Figure 3.34, was chosen to simulate the behavior of the cross when it is supporting the entire column assembly in the center of the cross beam. Because the weldment is modeled as a simply supported beam on each end, the center should exhibit the deflections with the largest magnitude. The offset location, shown in Figure 3.35, was chosen to mimic the behavior of the column assembly at the end of its travel. Because the column assembly for this machine traverses along

Table 3.3: Cutting parameter results after using Equations 3.1 through 3.4

Parameter	**Variable**	**Aluminum finishing**	**Aluminum slotting**	**Titanium finishing**
Radius	r	9.53 mm	9.53 mm	9.53 mm
Radial depth of cut	a	1.91 mm	19.05 mm	1.91 mm
Maximum force angle	ϕ	143°	90°	143°
Chip thickness	h	0.107 mm	0.127 mm	0.054 mm
Tangential cutting force	F_t	2310 N	2742 N	4081 N
Torque	T	22.0 Nm	26.1 Nm	38.8 Nm

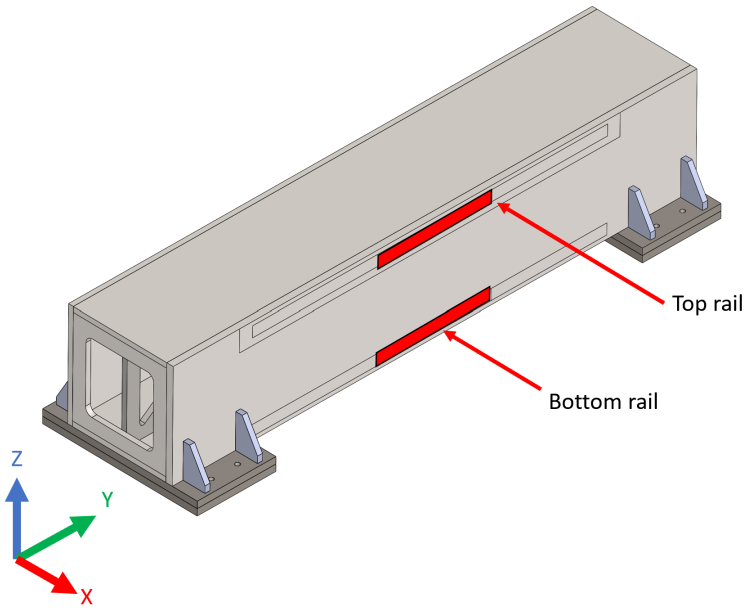

Figure 3.34: Top and bottom rails highlighted in red for the centered configuration.

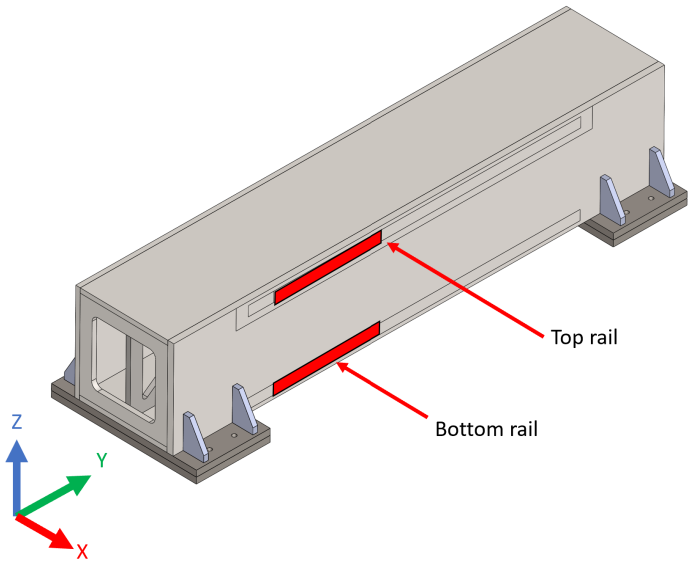

Figure 3.35: Top and bottom rails highlighted in red for the offset configuration.

the weldment, there are an infinite number of positions that could be simulated. The center and offset positions represent two extreme cases of deflection that the weldment would experience.

Each force applied to the system contributes to the deflection of the cross beam in the X-, Y-, and Z-directions. The force contributions are separated into contributions due to gravity, the remote mass, X-axis force, Y-axis force, Z-axis force, and torque. Force due to gravity was imposed on all the simulations and it was oriented to match the physical weldment with the force along the -Z-axis as shown in Figure 3.36. The remote mass was attached to both rail attachment areas through rigid connections. The remote mass center of gravity was calculated and was located 250 mm away from the front of the weldment in the + X direction and 203 mm from the bottom edge of the weldment front face in the +Z direction as seen in Figure 3.37. The cutting, drilling, and torque forces were imposed at the remote tool tip location. The tool tip was calculated to be 429 mm away in the +X direction from the center of the rail attachments with an additional 639 mm in the -Z direction. This tool tip location was also attached to the top and bottom rail attachment points through rigid connections as seen in 3.38.

Another input for the simulation is the method in which the components in the assembly interact with each other. For the simplified model simulation, there were two connection types. For all the components in the weldment model, a bonded-meshed independent connection was implemented [39]. The other local interaction connection type was a contact interaction between the bottom surfaces of the mounting pad with the metal pads on the machine base as shown in Figure 3.39. The contact connection allowed the mounting pad to deform appropriately because each foot was only secured by four fasteners.

Lastly, the FEA analysis needed to be broken down into a mesh that was able to generate accurate results. The parameters that were able to be selected for the mesh are the type of meshed used, maximum element size, minimum element size, the

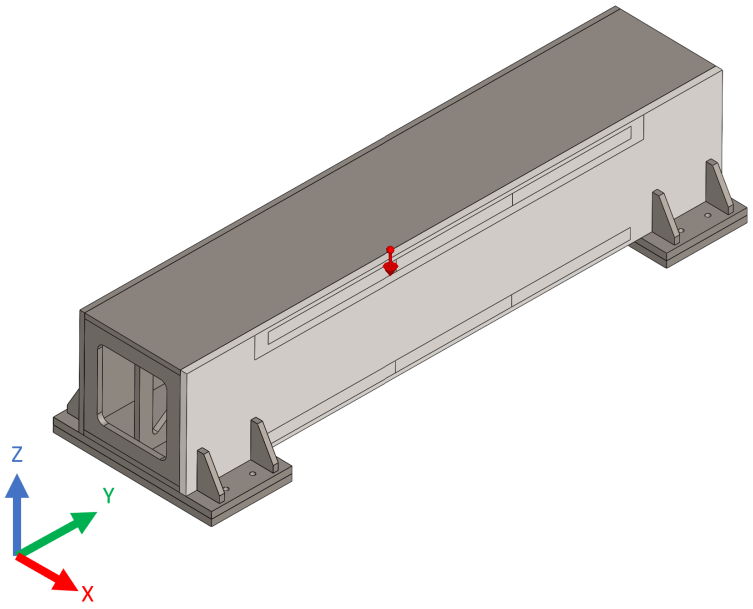

Figure 3.36: Centered configuration with red gravity vector arrow.

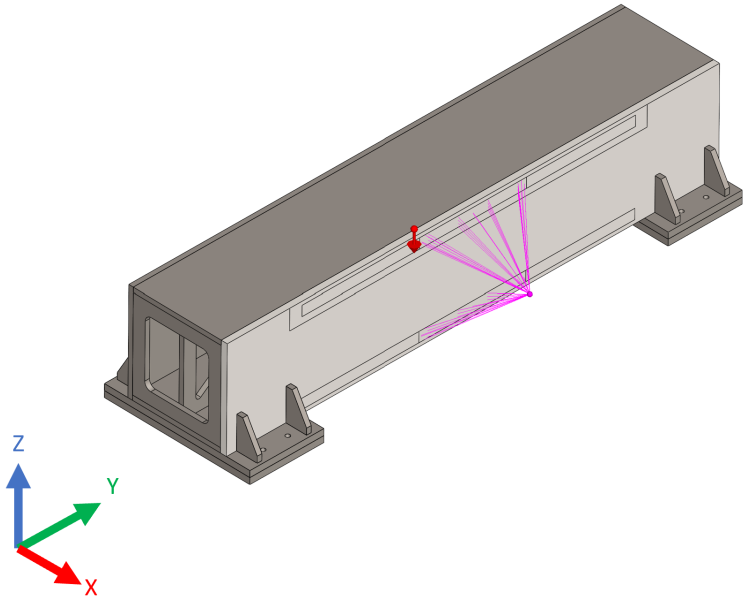

Figure 3.37: Centered configuration with red gravity vector arrow with the remote mass attached via rigid connections.

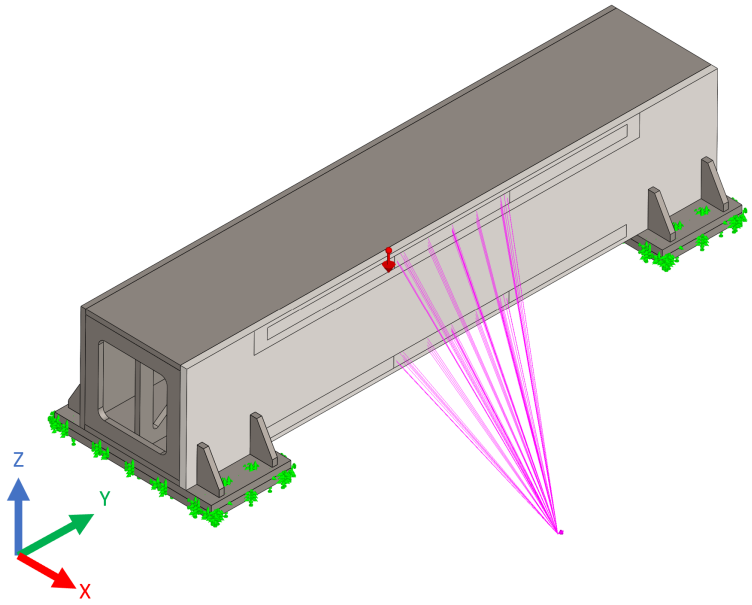

Figure 3.38: Centered continuation with red gravity vector arrow with the too tip attached via rigid connections.

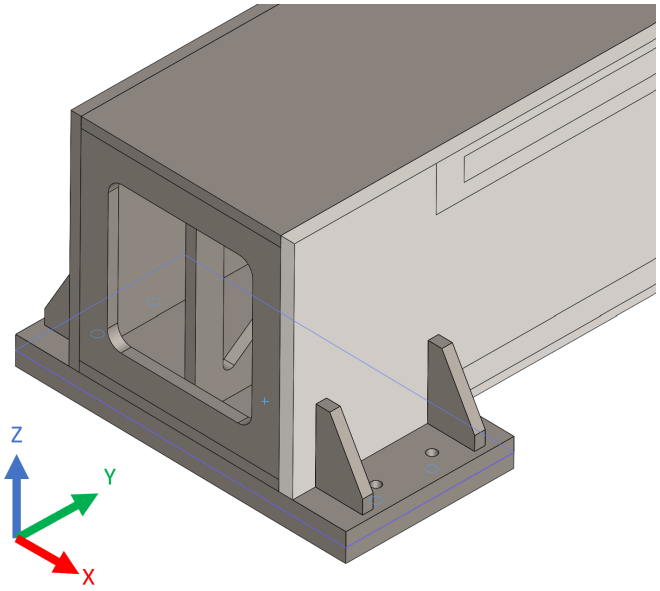

Figure 3.39: The purple outline highlights the contact interaction between the bottom of the mounting feet and the top of the fixed metal plates.

minimum amount of points around a circle, the element size growth ratio, and the number of Jacobian Points. For all the simulations, blended curvature-based mesh with a minimum of eight points around a circle, an element size ratio of 1.4, and 16 Jacobian points. The maximum and minimum element sizes were adjusted to achieve convergence of the model. An initial maximum element size of 240 mm and a minimum element size of 12 mm was chosen. Once the simulation was complete, the maximum deflection value in the X-direction of the top rail was recorded. The maximum and minimum values were then halved to a maximum element size of 120 and a minimum element size of 6 mm. The maximum deflection value of the top rail was recorded and compared to the previous maximum deflection value. Convergence was achieved when the new value had a less than or equal to a 5% change. The final mesh size that met the criteria was a maximum element size of 60 mm and a minimum size of 3 mm as shown in Figure 3.40 and 3.41. This mesh was implemented for all static simulations.

To quantify the cross beam behavior, maximum deflections of the top and bottom rails in each axis direction were recorded to serve as a baseline. For the separation of force contributions, values needed to be extracted from simulations with multiple inputs. To start the simulations, the weldment was simulated with only a gravitational load as shown in Figure 3.36. Maximum deflections in the X-axis, Y-axis, and Z-axis of the top rail and the bottom rail were recorded. Next, the remote mass was added to the cross beam with the gravitational load as shown in Figure 3.37. The maximum deflections in the X-axis, Y-axis, and Z- axis of the top rail and the bottom rail were recorded once again. To separate the contribution of the deflection of the weldment due to the remote mass, the first simulations' maximum deflections were subtracted from the second simulations' deflections. The result was the deflection due to the remote mass.

For the other forces, a similar subtraction method was implemented. For the cutting and torque forces, the simulations had gravity and the remote mass in addition

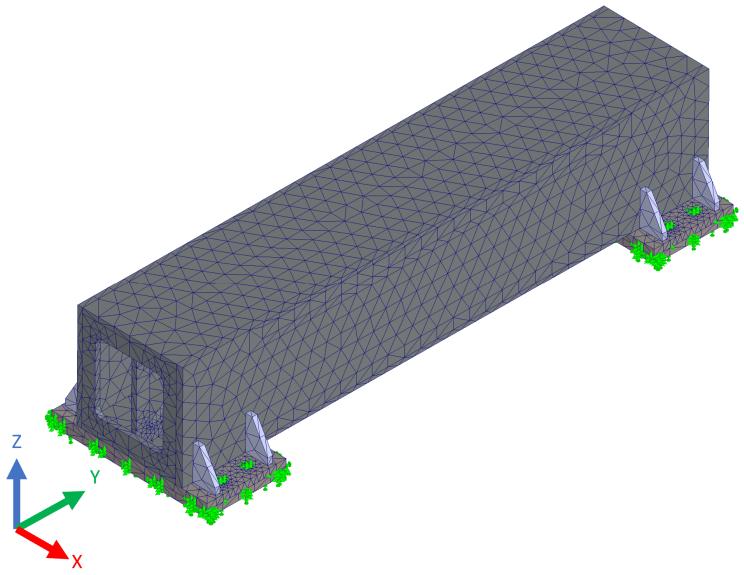

Figure 3.40: Isometric view of the front of the weldment with its final mesh.

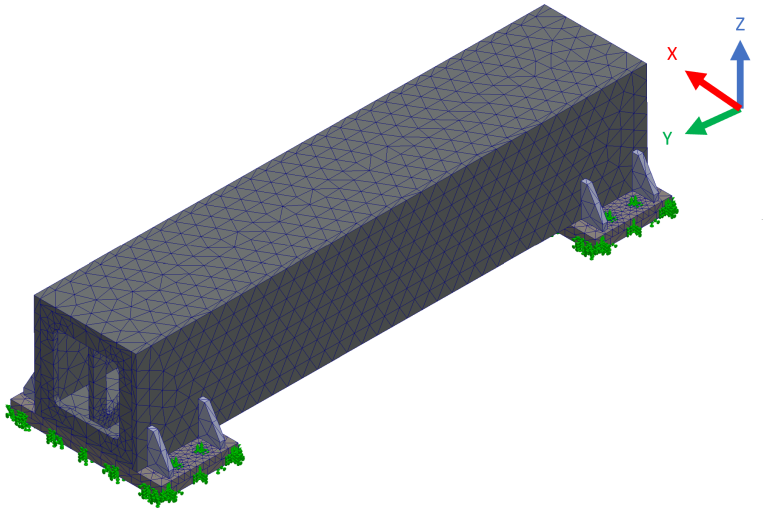

Figure 3.41: Isometric view of the back of the weldment with its final mesh.

to the individual force components as seen in Figure 3.42. The X-force simulation had the force vector at the tool tip acting in the -X direction shown in Figure 3.43. The Y-force simulation had the force vector at the tool tip acting in the -Y direction shown in Figure 3.44. The Z-force simulation had the force vector at the tool tip acting in the +Z direction shown in Figure 3.45. The torque simulation had the torque applied to the tool tip along the Z-axis as shown in Figure 3.46. Both the X- and Y-axis forces were 4,000 N each. The Z-axis force was 2000 N. The torque was 39 N-m. These configurations were also repeated for the offset configuration.

With all of the configuration variables, there were a total of twelve simulations completed to quantify the deformation behavior of the weldment. Figures 3.47 through 3.58 showcase the resultant deformation of the weldment. From these simulations, the max deflections of the top and bottom rails were extracted. The extracted values were broken down into the principle directions along the X-, Y-, or, Z-axis.

With all configuration variables, 12 simulations were completed to quantify the deformation. Figures 3.47 through 3.58 showcase the resultant weldment deformation. From these simulations, the max deflections of the top and bottom rails were extracted. The extracted values were separated into the principal directions along the X-, Y-, or, Z-axis.

The results of the deflection calculations are provided in Table 3.4. The two main configurations were the column locations at the center versus at the end of the travel. The contributions of each force are isolated and rounded to the nearest micrometer. Also, both the top and bottom rail maximum values were recorded because they give insight into the column's behavior as a beam and how it moves such as nodding of the column.

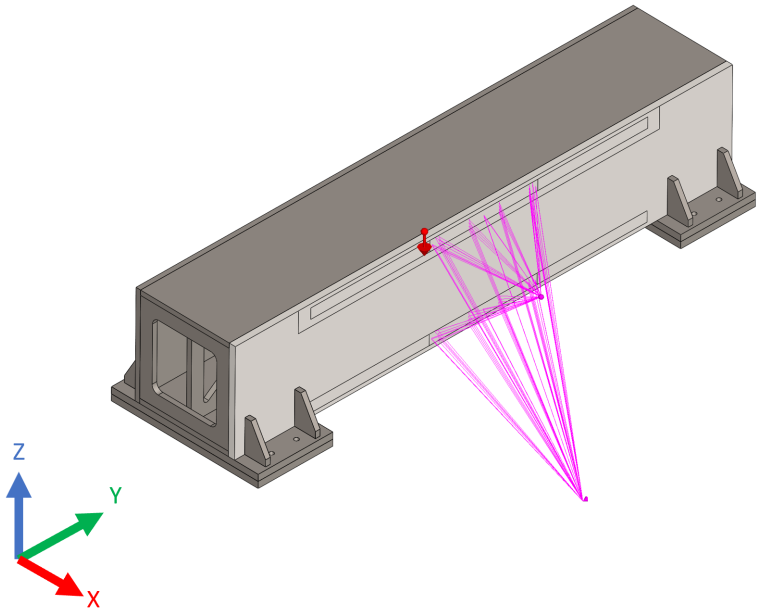

Figure 3.42: Weldment simulation with gravity, remote mass, and the remote tool tip point.

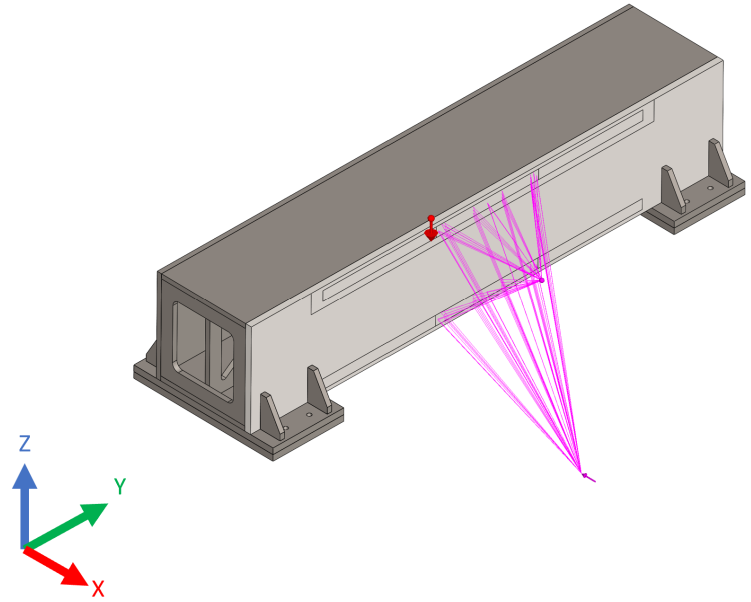

Figure 3.43: Simulation of weldment in the centered configuration along with a remote X-cutting force in the -X direction.

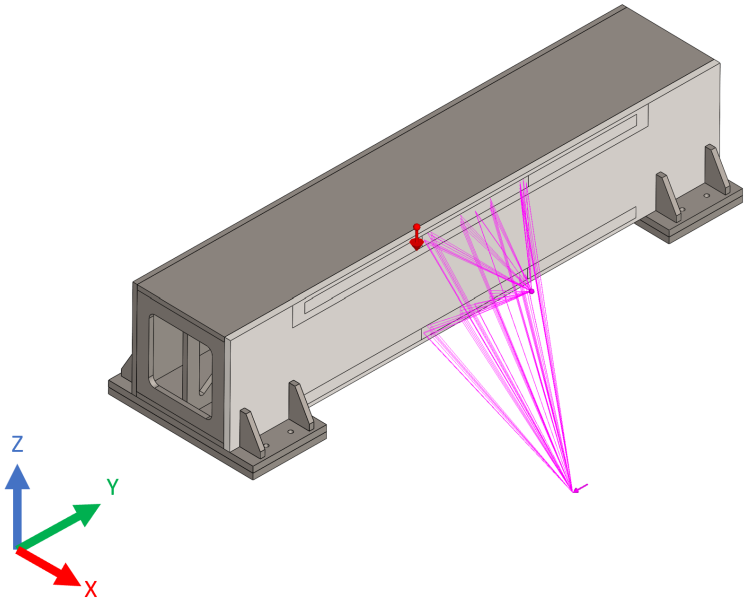

Figure 3.44: Simulation of weldment in the centered configuration along with a remote Y-cutting force in the -Y direction.

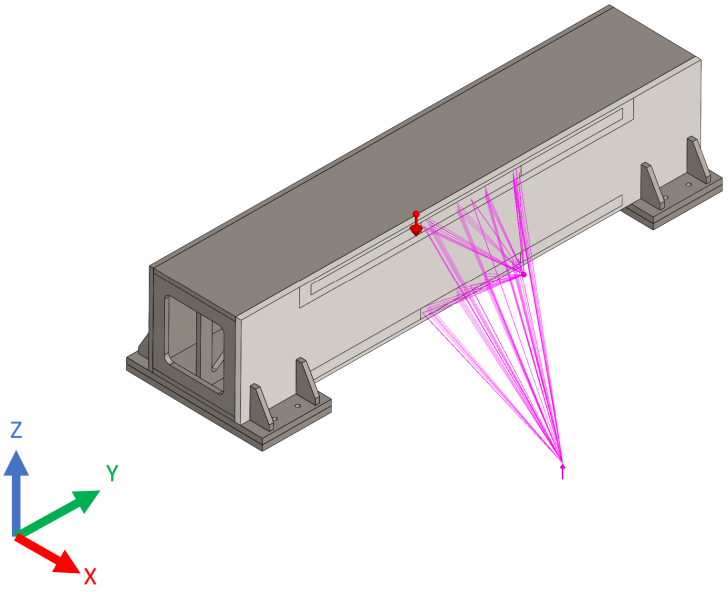

Figure 3.45: Simulation of weldment in the centered configuration along with a remote Z-drilling force in the +Z direction.

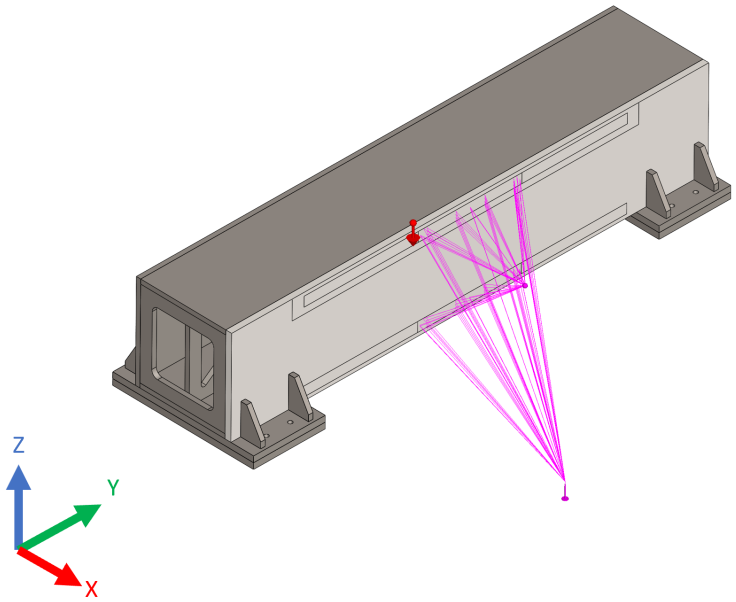

Figure 3.46: Simulation of weldment in the centered configuration along with torque about the Z-axis of the tool tip.

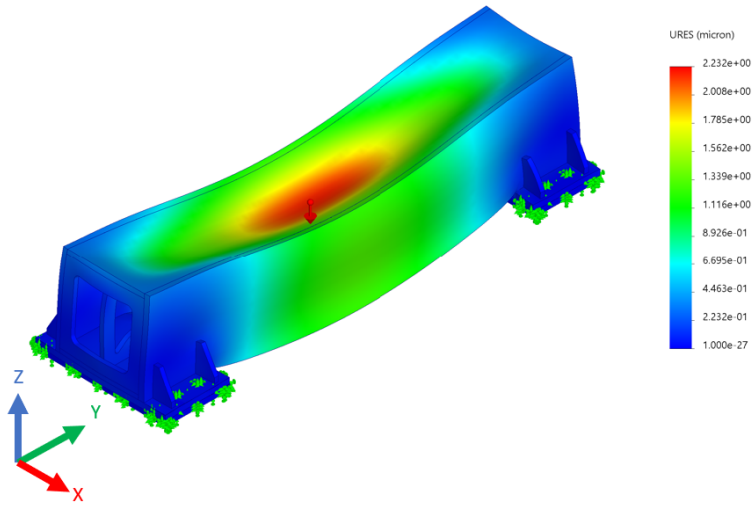

Figure 3.47: FEA resultant displacement of the weldment in the rails centered configuration with gravity only.

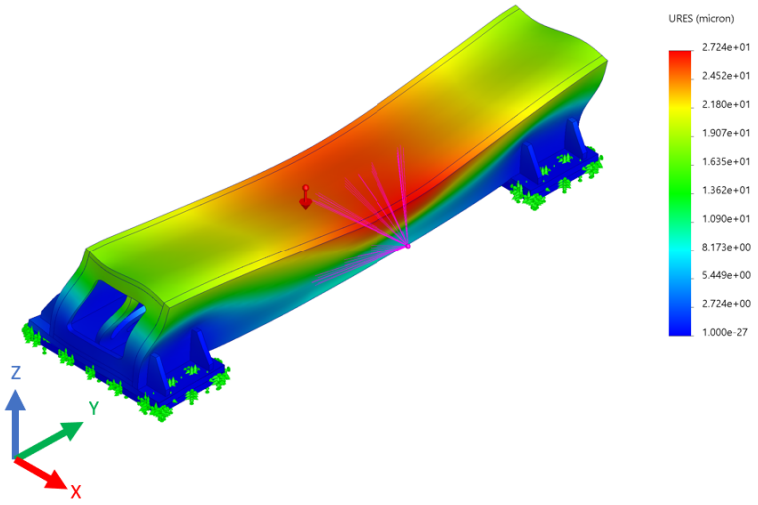

Figure 3.48: FEA resultant displacement of the weldment in the rails centered configuration with gravity and the remote mass.

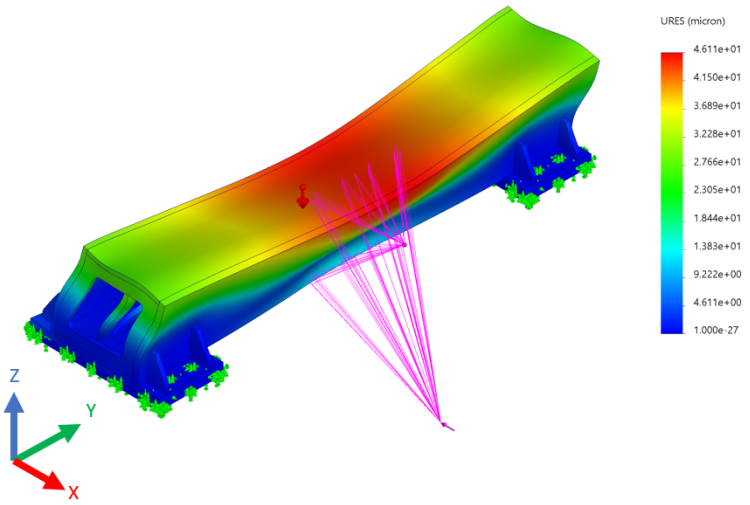

Figure 3.49: FEA resultant displacement of the weldment in the rails centered configuration with gravity, remote mass, and X-cutting force.

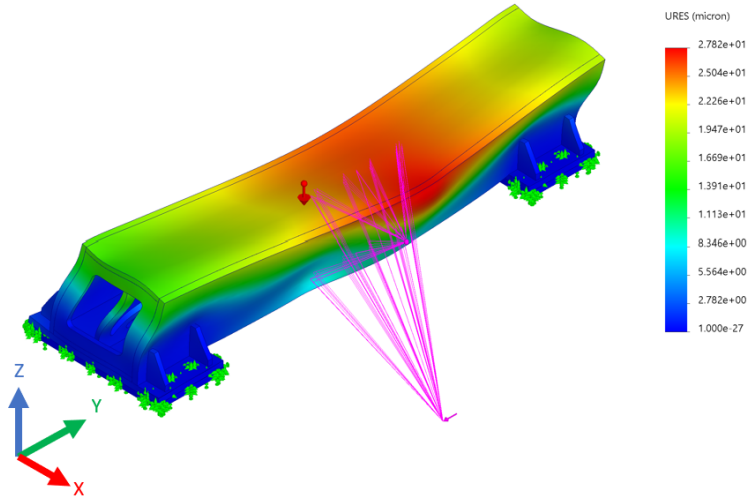

Figure 3.50: FEA resultant displacement of the weldment in the rails centered configuration with gravity, remote mass, and Y-cutting force.

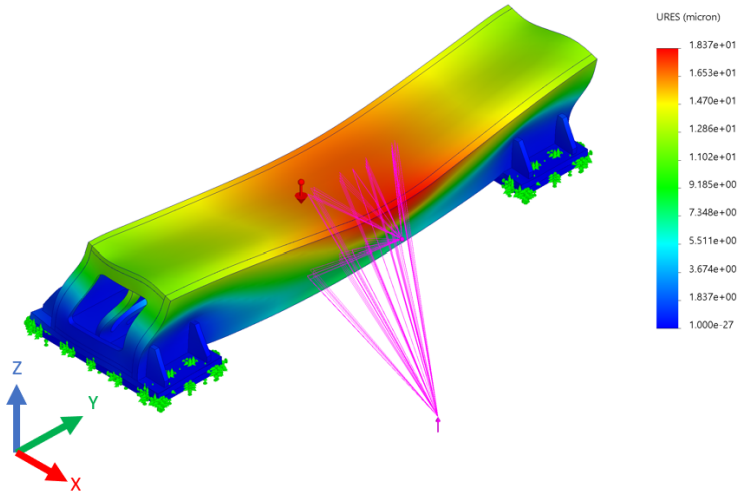

Figure 3.51: FEA resultant displacement of the weldment in the rails centered configuration with gravity, remote mass, and Z-drilling force.

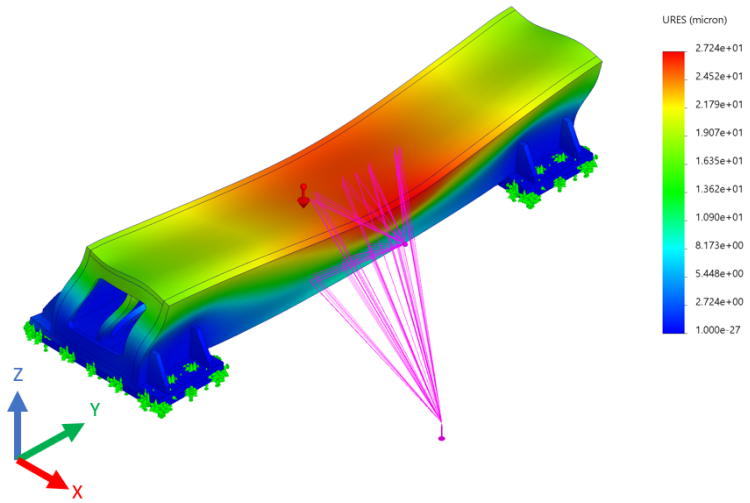

Figure 3.52: FEA resultant displacement of the weldment in the rails centered configuration with gravity, remote mass, and torque force.

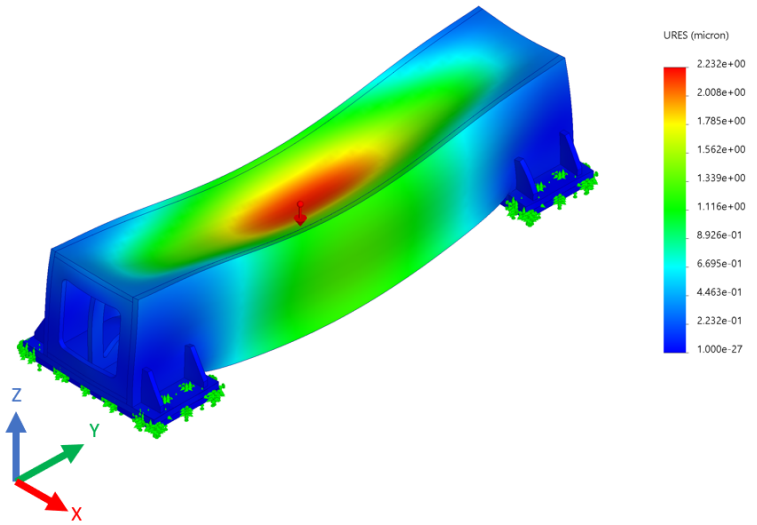

Figure 3.53: FEA resultant displacement of the weldment in the rails offset configuration with gravity only.

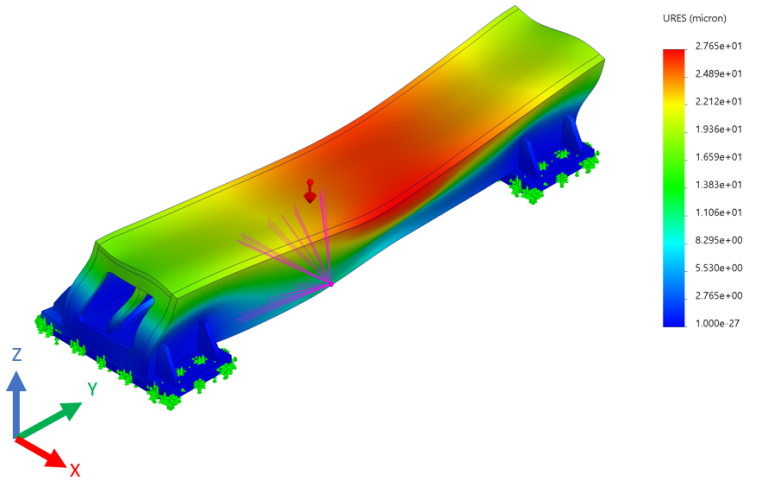

Figure 3.54: FEA resultant displacement of the weldment in the rails offset configuration with gravity and the remote mass.

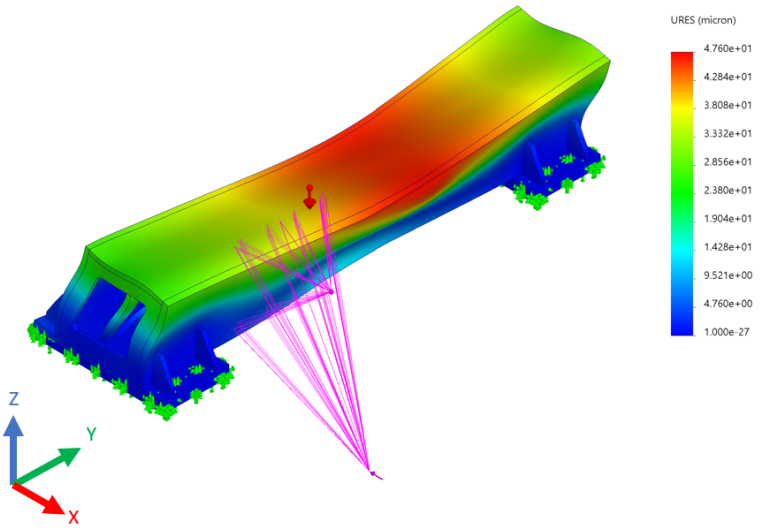

Figure 3.55: FEA resultant displacement of the weldment in the rails offset configuration with gravity, remote mass, and X-cutting force.

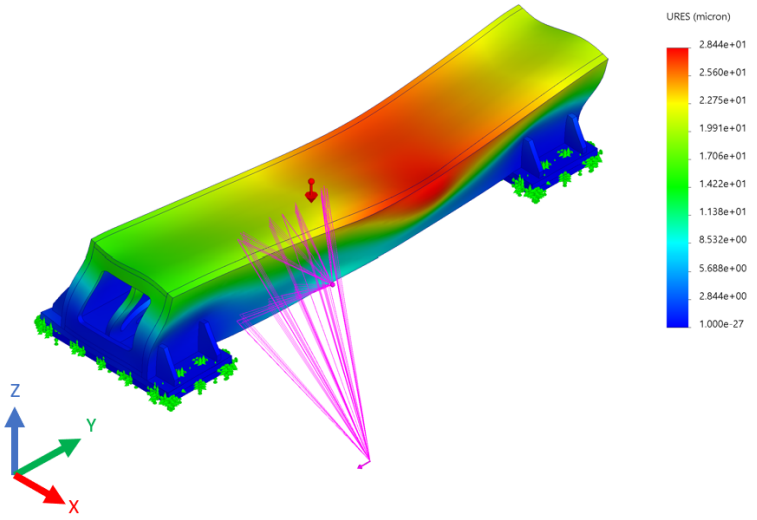

Figure 3.56: FEA resultant displacement of the weldment in the rails offset configuration with gravity, remote mass, and Y-cutting force.

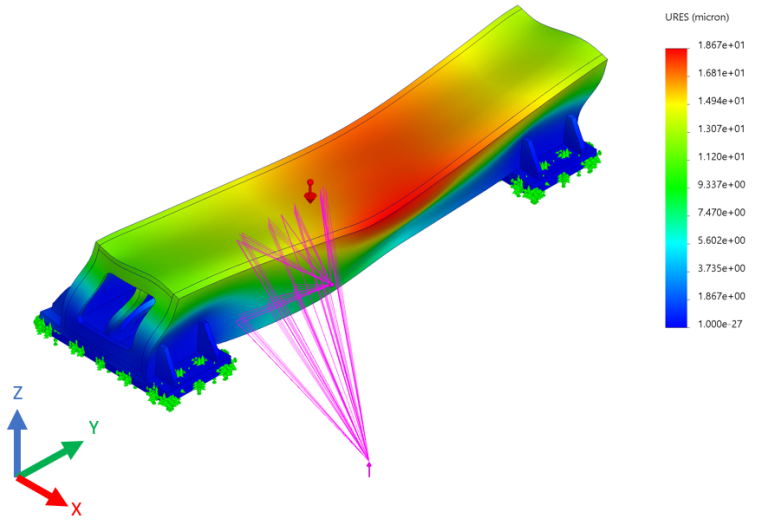

Figure 3.57: FEA resultant displacement of the weldment in the rails offset configuration with gravity, remote mass, and Z-cutting force.

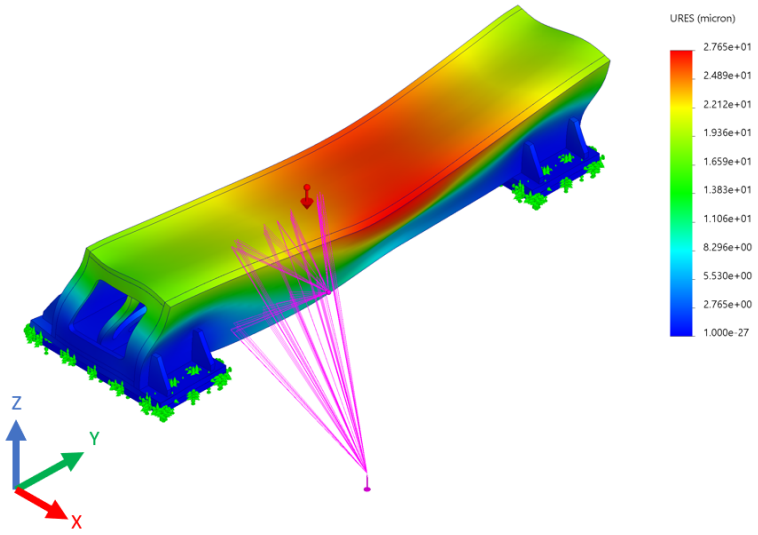

Figure 3.58: FEA resultant displacement of the weldment in the rails offset configuration with gravity, remote mass, and torque force.

Table 3.4: Break down of deflections due to various forces in various configurations for the simplified weldment

Rail location	Axis	Gravity contribution [µm]		Remote mass contribution [µm]		X-force contribution [µm]		Y-force contribution [µm]		Z-force contribution [µm]		Torque contribution [µm]	
		Top	Bottom	Top	Bottom	Top	Bottom	Top	Bottom	Top	Bottom	Top	Bottom
Centered	X	0	0	25	-1	20	-6	1	3	-9	1	0	0
	Y	0	0	-1	0	0	0	0	-2	0	0	0	0
	Z	-1	-1	-8	-7	2	3	0	-1	1	1	0	0
Offset	X	0	0	26	0	21	-5	1	1	-9	0	0	0
	Y	0	0	-2	1	-1	0	0	-1	0	0	0	0
	Z	-1	-1	-9	-8	2	3	1	1	1	1	0	0

Modal analysis

The structure's dynamic behavior was also predicted using FEA. The frequency simulation from SolidWorks was implemented to find the natural frequencies and mode shapes of the structure, where the refined model shown in Figure 3.23 was used for the simulation. Because the welded beads did not entirely seal the edges of the box structure along with its mounting feet, the individual welds needed to be modeled to provide accurate results.

One major difference between static and frequency analysis is that the refined weldment was simulated using free-free boundary conditions, while the simplified weldment was supported on two fixed plates. To enable confidence in the experimental boundary conditions, free-free conditions were selected because the cross beam could be supported using thin flexible straps to reasonably approximate the simulated free-free ideal.

The material was assigned to be A36 steel in the refined simulation. The plates were modeled per the drawings in Appendix A in addition to the proper assembly and weld bead locations. There were no connections between the plates of the model and they were assigned free contact behaviors. Instead, all the weld bead contact faces were assigned to bonded conditions to simulate the actual weld. As a result, the refined structure was only held together through the bonded weld beads which is identical to the physical structure.

Free-free simulation reduces the complexity of the simulation. No fixtures were implemented. In addition, no external loads were imposed. A similar mesh convergence method was implemented to ensure that the results were accurate. With the same initial start mesh size as the simplified model, a mesh element size of 240 mm maximum and 12 mm minimum was chosen for the initial mesh. This was then refined by finding the convergence of the natural frequency of the first dynamic mode. A less than 5% convergence difference was achieved with a maximum element size of

15 mm and a minimum element size of 0.75 mm. The remaining parameters were the same as the static simulation.

Due to the structure's mass and size, the dynamic modes occur at relatively low frequencies. The frequency analysis was set to find the modes of the refined weldment from 0 to 5,000 Hz. A total of 39 mode shapes were identified in this frequency range, where the first six mode shapes were rigid body modes (i.e., rigid motion of the structure without deformation). The six rigid body modes constitute the motions of the structure in its six free-free degrees of freedom.

The first dynamic mode is shown in Figures 3.59 and 3.60. It occurred at a frequency of 210 Hz. To enable visual interpretation, the figure's deformation shape is exaggerated. weldment. The other mode shapes are not provided below for the analysis in the next section provided insight into the modes of interest.

3.2.3 Impact (tap) testing of weldment

Impact (tap) testing was used to measure the mode shapes. This testing was completed using the MetalMAX hardware kit and TXF software from Manufacturing Laboratories Inc. (MLI) [40]. The items that were used from the kit were the large modal hammer (PCB Piezotronics model 086D05), large magnetic single-axis accelerometer (PCB Piezotronics model 352C68), and data acquisition (DAQ) unit (Data Translation model DT9837B). The large modal hammer seen in Figure 3.61 has a force sensor at the tip along with a nylon impact tip. Due to the large weldment mass, an additional mass was added to the end of the hammer to increase the force input level for the hammer and provide adequate excitation. The large magnetic single-axis accelerometer, as seen in Figure 3.62, was chosen because it provided the required frequency bandwidth. In addition, only the motion in one axis of the structure was analyzed from each series of testing. Lastly, the DAQ shown in Figure 3.63 was used to sample and record the force and vibration signals. The TXF software was used to convert the time domain signals to the frequency domain and calculate

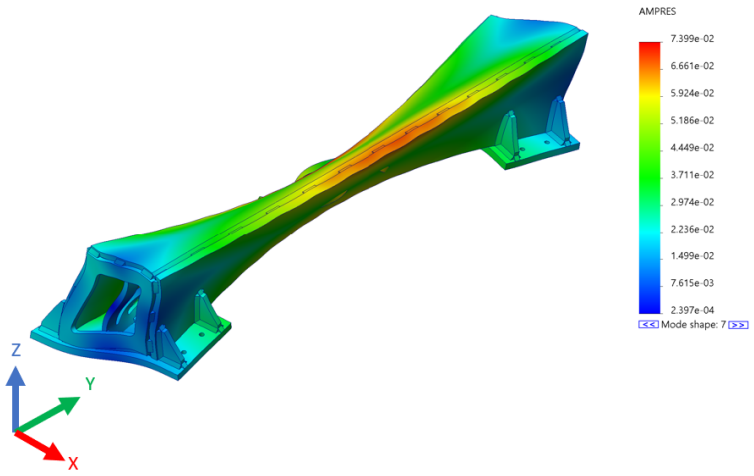

Figure 3.59: Isometric front view of FEA simulation of the first mode shape of the refined weldment.

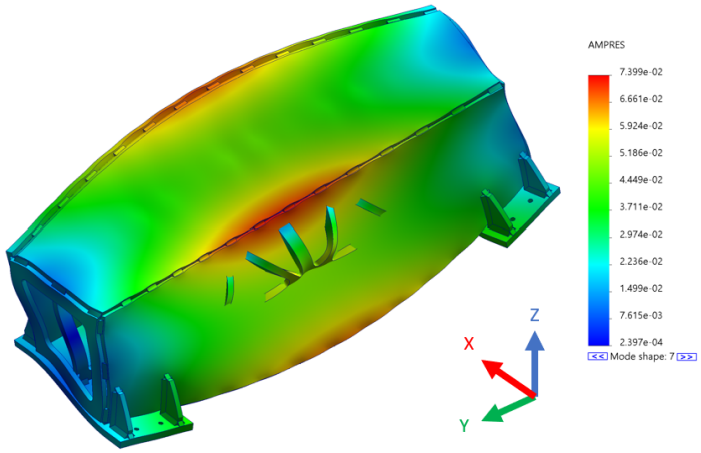

Figure 3.60: Isometric back view of FEA simulation of the first mode shape of the refined weldment.

Figure 3.61: Modal hammer used for impact testing with a nylon tip and extended mass.

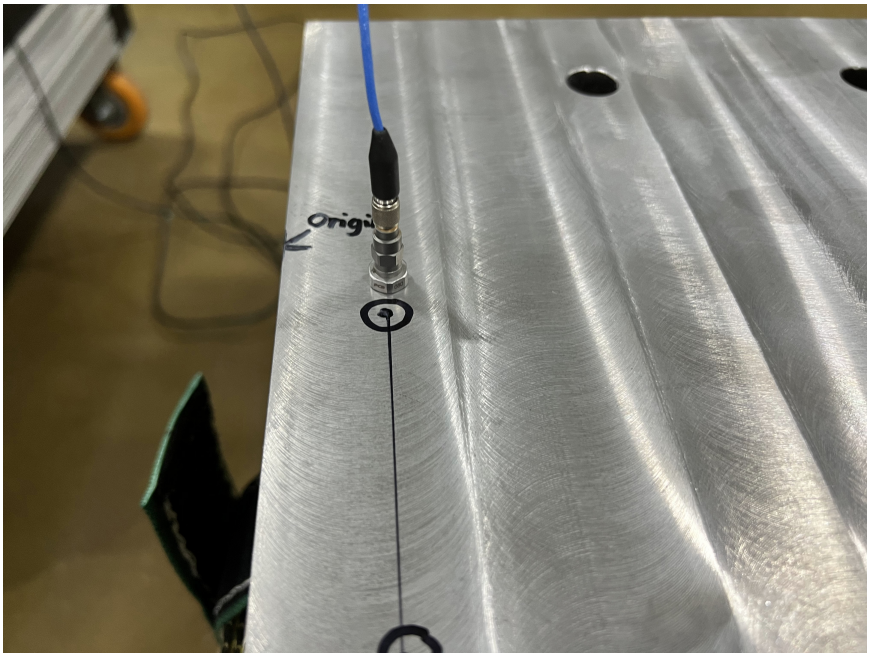

Figure 3.62: Magnetic accelerometer used for impact testing.

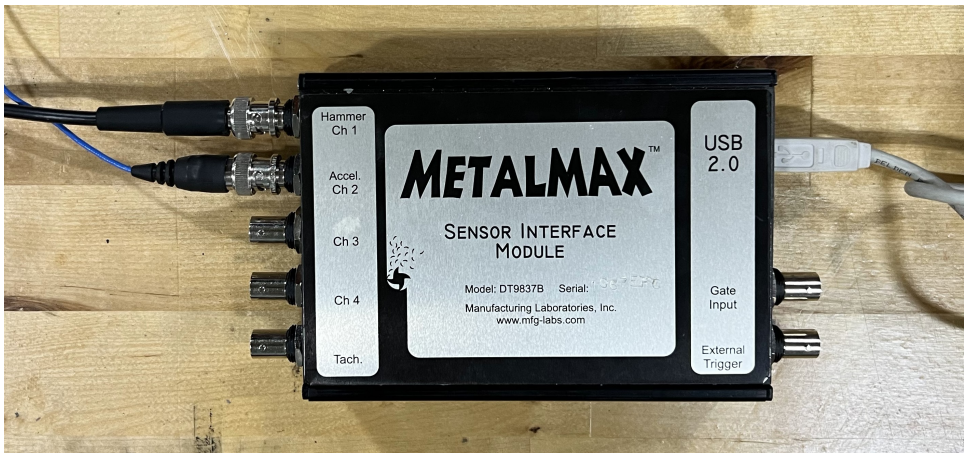

Figure 3.63: MetalMAX data acquisition unit that was used to connect the modal hammer, accelerometer, and computer.

the FRF for each measurement location.

The two sides of the weldment that were chosen were the front and bottom sides of the structure. The front and bottom surfaces interact with other components of the entire system and provide a good representation of the motion of two perpendicular faces of the weldment. In addition, the two faces chosen provide insight into the motion that would most significantly affect the machine tool's column assembly.

From the FEA modal analysis, the bottom and front face mode shapes were used to select the density and grid layout of the measurement points on each surface. The force locations for the bottom and front faces are shown in Figures 3.64 and 3.65. The dimensions of the grid layout for the bottom and front faces are shown in Figures 3.66 and 3.67. The locations were then marked on the weldment as shown in Figures 3.68 and 3.69.

The weldment was suspended using an overhead crane as seen in Figures 3.70 and 3.71. The weldment was suspended upside down using rigging straps. This support simulated free-free boundary conditions.

For the measurements, a roving hammer approach was implemented. The accelerometer was mounted at the first testing point and the direct FRF was collected as shown in Figure 3.72 for the bottom face and Figure 3.73 for the front face. The accelerometer for the bottom face remained at the X-location of -25.40 mm and Y-location of 25.40 mm. The accelerometer for the front face remained at the Z-location of 381.00 mm and Y-location of 25.40 mm. Both accelerometer locations are designated as the direct FRF location while the other points are the cross FRF locations. Each location was hit eight times to reduce noise in the measured FRFs. This was repeated for all points in Figures 3.64 and 3.65. The FRF coherence was checked to ensure that the force energy input was received by the accelerometer.

The data from the tap testing was processed and saved through TXF. The TXF data was later converted to real and imaginary parts of the complex-valued FRF and plotted versus frequency. The data were processed as described in the next section to seek out mode shapes of interest.

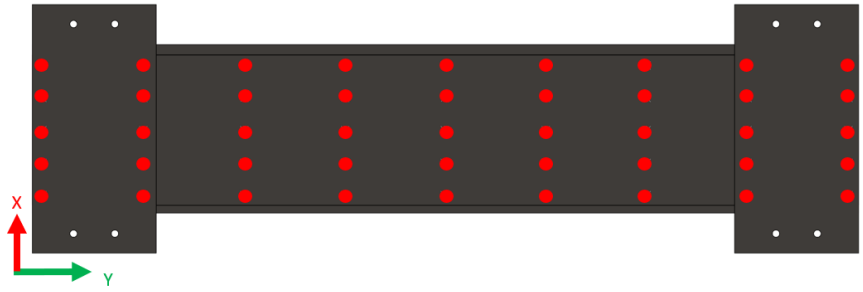

Figure 3.64: Bottom face of weldment with all of the impact points marked in red dots.

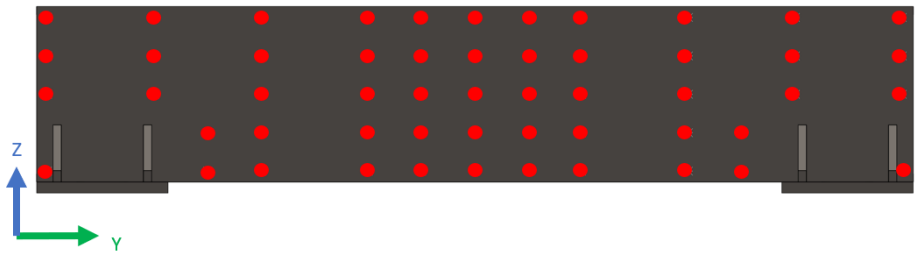

Figure 3.65: Front face of weldment with all of the impact points marked in red dots.

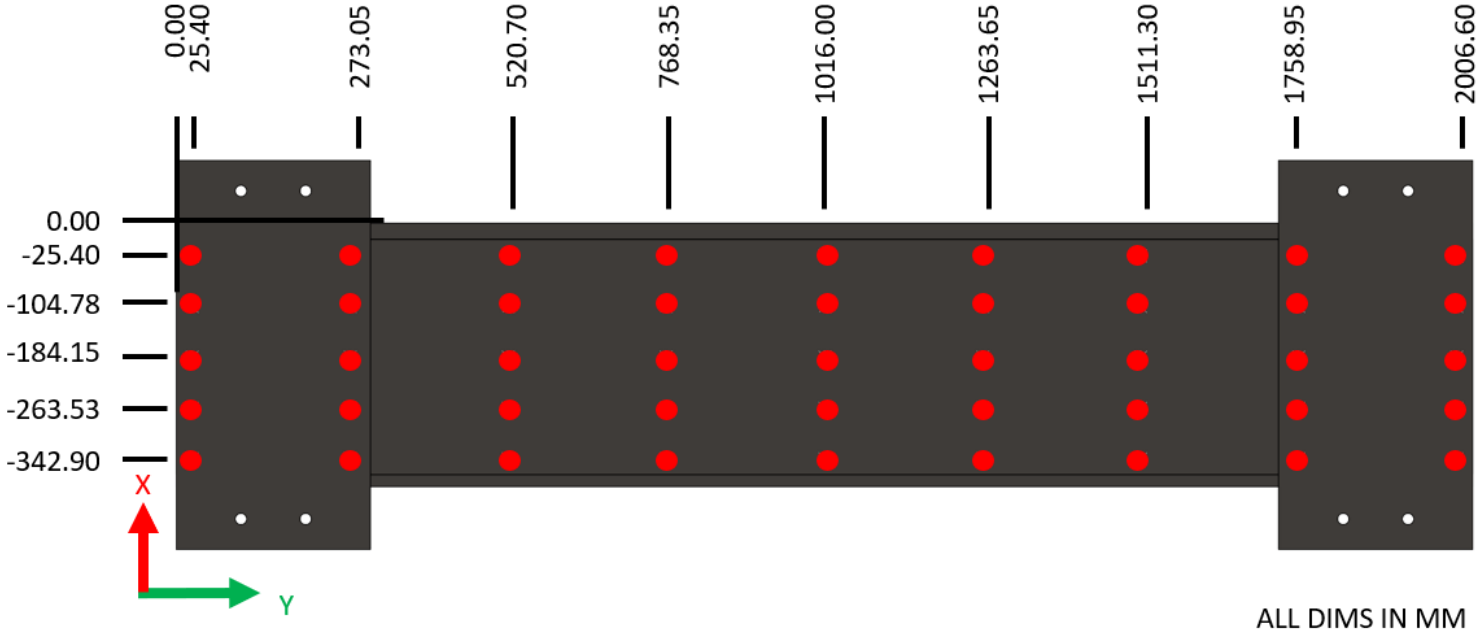

Figure 3.66: Bottom face of weldment with dimensions of impact points.

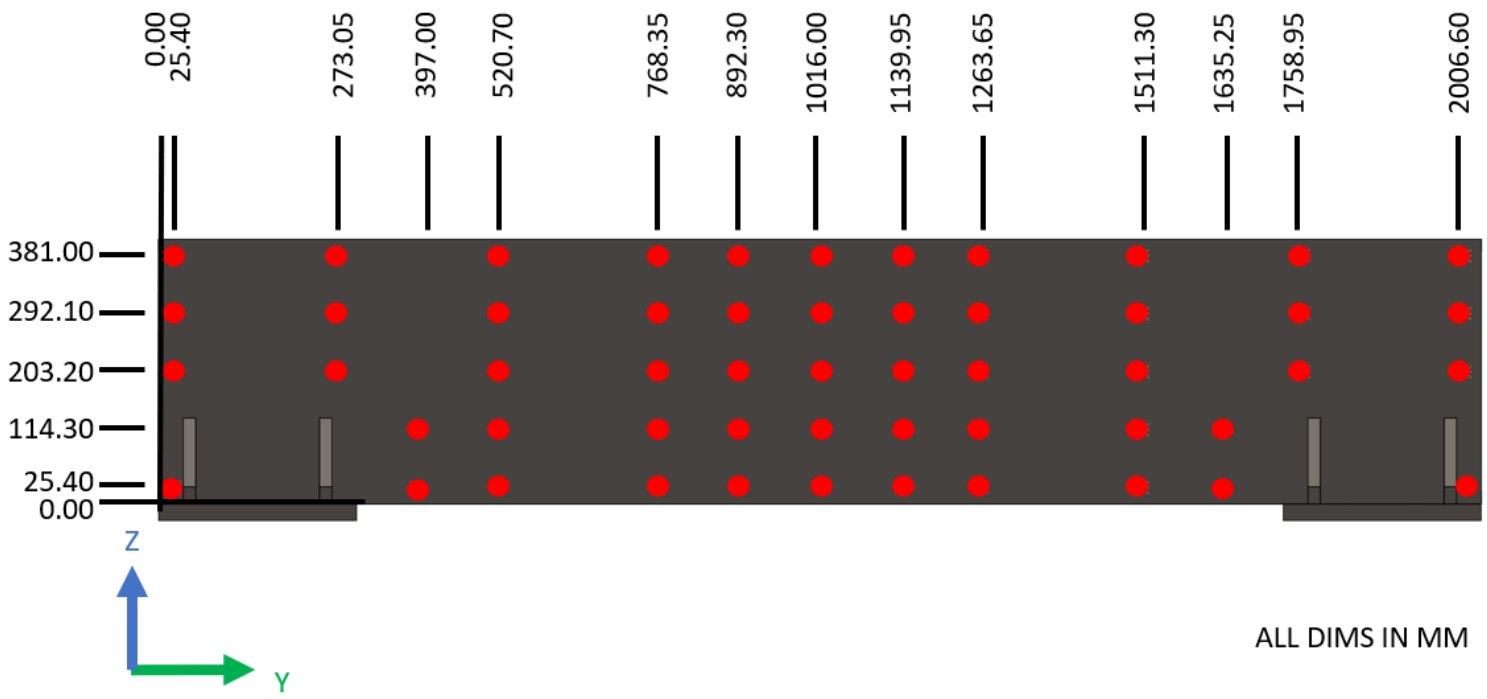

Figure 3.67: Front face of weldment with dimensions of impact points.

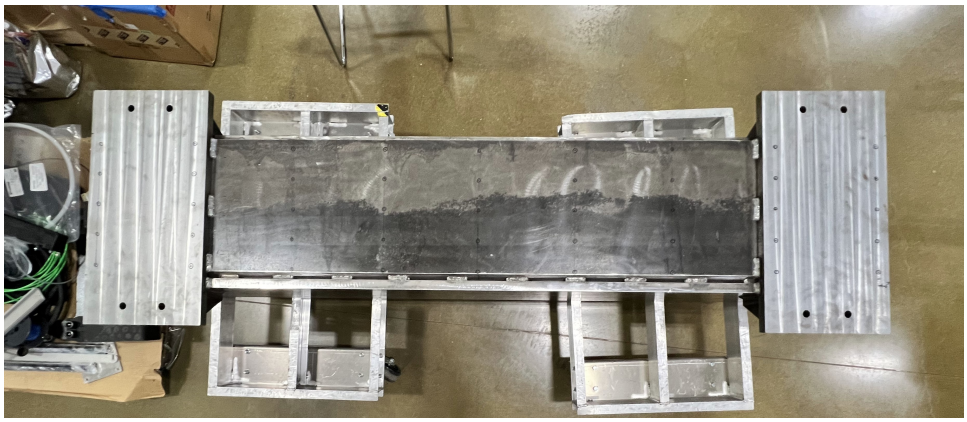

Figure 3.68: Bottom face of physical weldment with all of the impact points marked in black points.

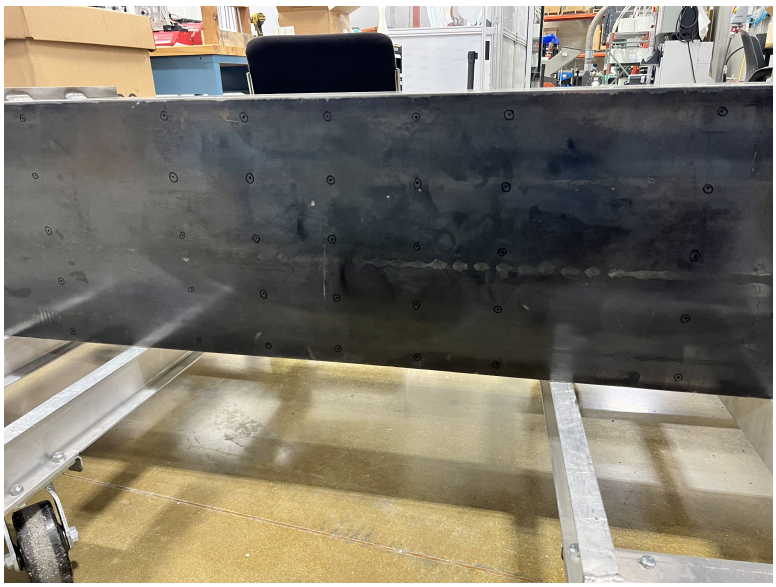

Figure 3.69: Front face of physical weldment with all of the impact points marked in black points.

Figure 3.70: Overhead crane lifting weldment to establish free-free tap testing conditions.

Figure 3.71: Overhead crane lifting weldment to establish free-free tap testing conditions close up.

Figure 3.72: Accelerometer location of direct FRF point on the bottom face of the weldment.

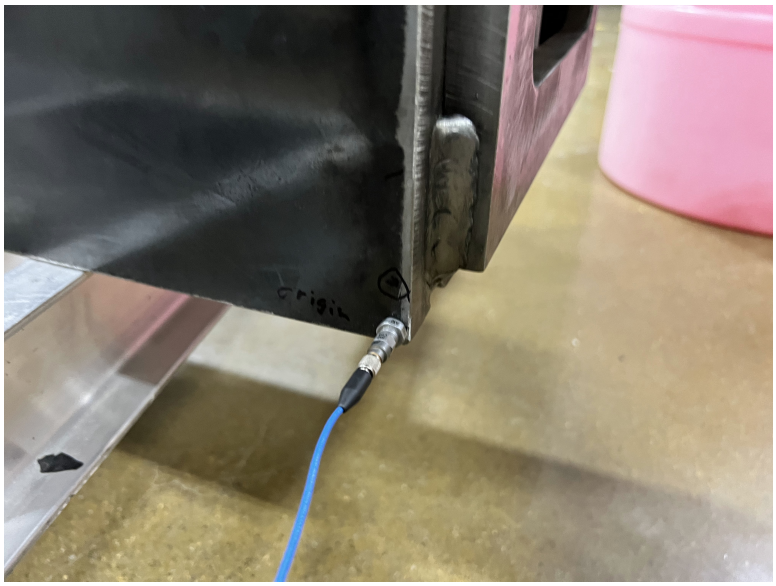

Figure 3.73: Accelerometer location of direct FRF point on the front face of the weldment.

3.2.4 Comparison of finite element simulation and impact testing

To compare the FEA simulation results with the impacting testing data, mode shapes were extracted from the impact data. Five modes with the largest amplitude from both the bottom and front face of the structure were selected for comparison. A large amplitude indicates lower dynamic stiffness and more importance for the machine tool's dynamic performance. Machine tool components are typically designed to be as stiff as possible. Considering the five least stiff modes on each face provides a baseline for the structure's dynamic behavior. In addition, the accuracy of the simulated mode shapes was verified using the experimental mode shapes.

To reference the individual points selected for impact testing, a grid coordinate system was assigned. The row and column values for the bottom face are shown in Figure 3.74, and the row and column values for the front face are shown in 3.75. The referred point locations will be in terms of a row value and column value. For example, point (2,1) will be associated with the point location that is in row 2 column 1. Note that both (1,1) locations are direct FRF locations.

To ensure that the weldment's impact data was accurate as well as repeatable, the concept of reciprocity was implemented to confirm that the measurement hardware and analysis were performing as expected. For the first measurement of the bottom face, the accelerometer was placed at (1,1) while the impact was performed at point (1,9). The second measurement for the bottom face was the opposite; the accelerometer was placed at (1,9) and the impact was performed at (1,1). The overlay of the real and imaginary plots of both FRFs for the bottom face is shown in Figure 3.76. For the first measurement of the front face, the accelerometer was placed at (1,1) while the impact was performed at (1,13). For the second measurement of the front face, the accelerometer was placed at (1,13) and the impact was performed at (1,1). The overlay of the real and imaginary plots of both FRFs for the front face is

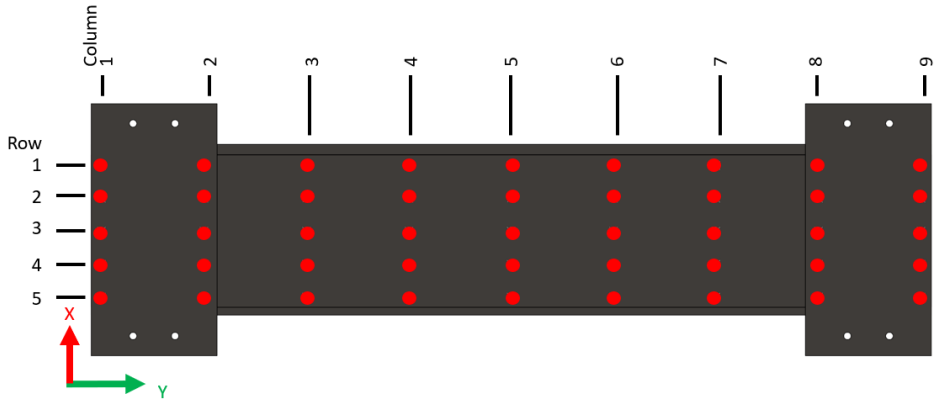

Figure 3.74: Coordinate locations for the bottom face of the weldment.

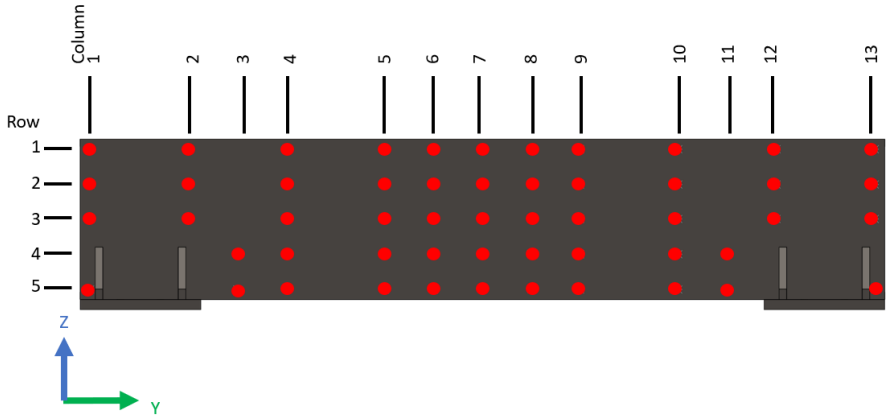

Figure 3.75: Coordinate locations for the front face of the weldment.

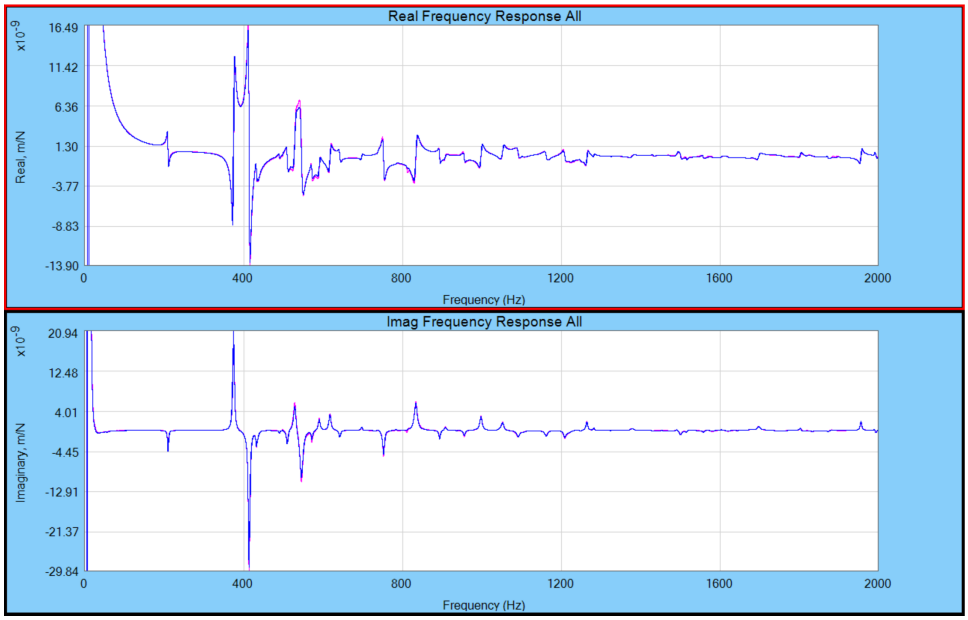

Figure 3.76: Reciprocity check of real and imaginary plots of the bottom face cross FRF points of (1,1) and (1,9) where the blue is for the first measurement and pink for the second.

shown in Figure 3.77. The result from both plots is that the structure shows good reciprocity and that the measurements were repeatable.

Bottom face

To find the five modes with the largest amplitudes for the bottom face, the real and imaginary FRFs of the top row of points in Figure 3.64 were plotted together in TXF. By observing the amplitudes of the imaginary plot, the most flexible modes were chosen as shown in Figure 3.78. The mode shape frequencies for the bottom face that were compared were 209, 373, 377, 413, and 545 Hz. These values were extracted through peak-picking and finding the corresponding frequencies.

With the selected natural frequencies, the corresponding magnitudes for each impact location can be extracted. The magnitudes are the corresponding maximum or minimum values at the selected frequency. Once extracted, all the magnitude values are normalized to the direct FRFs magnitude at the desired frequency. The normalized amplitudes were then mapped to corresponding geometric coordinates shown in Figure 3.66 to generate a surface that visualizes the mode shape.

The following tables and figures are the results of peak picking for the five most flexible mode shapes for the bottom face. Table 3.5 contains the normalized points from peak picking for mode 1 which was peak picked at 209 Hz. Figures 3.79 and 3.80 are the plotted points from Table 3.5 onto a surface in MATLAB and the deformed weldment in the FEA simulation. The motion and deformation of the mode shapes were compared and matched visually. The same sequence of tables and images for the other four modes are presented in Tables 3.6 through 3.9 and Figures 3.81 through 3.88.

As seen in Figures 3.79 through 3.88, there is a good match in the peak picking mode shapes and the FEA simulated mode shapes. Only one mode shape, mode shape 3, has an actual difference in the mode shape of the peak picking result and simulation result. Mode 2 and 3, as seen in Figure 3.78, are dynamic modes that are

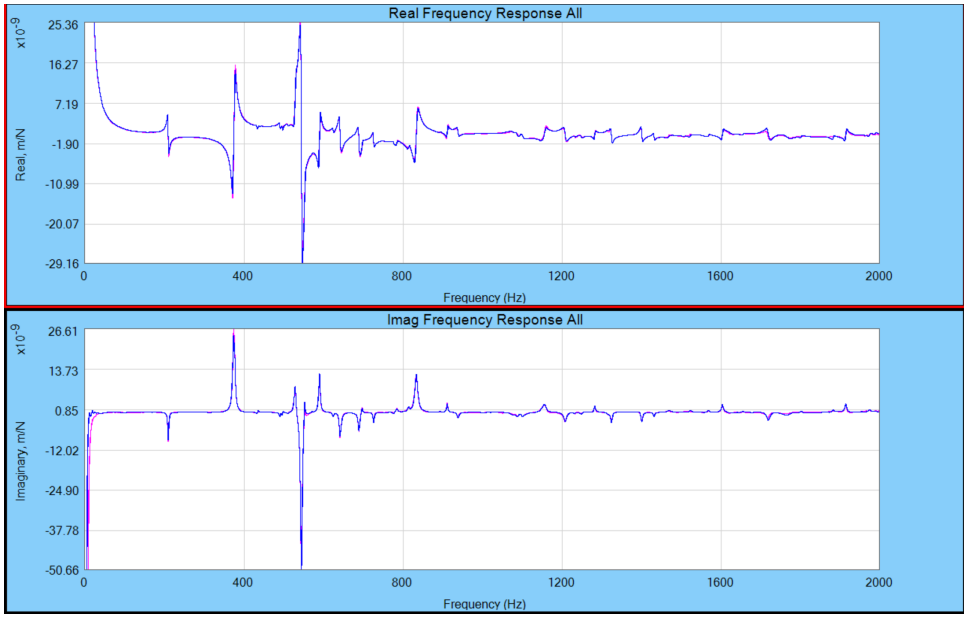

Figure 3.77: Reciprocity check of real and imaginary plots of the front face cross FRF points of (1,1) and (1,13) where the blue is for the first measurement and pink for the second.

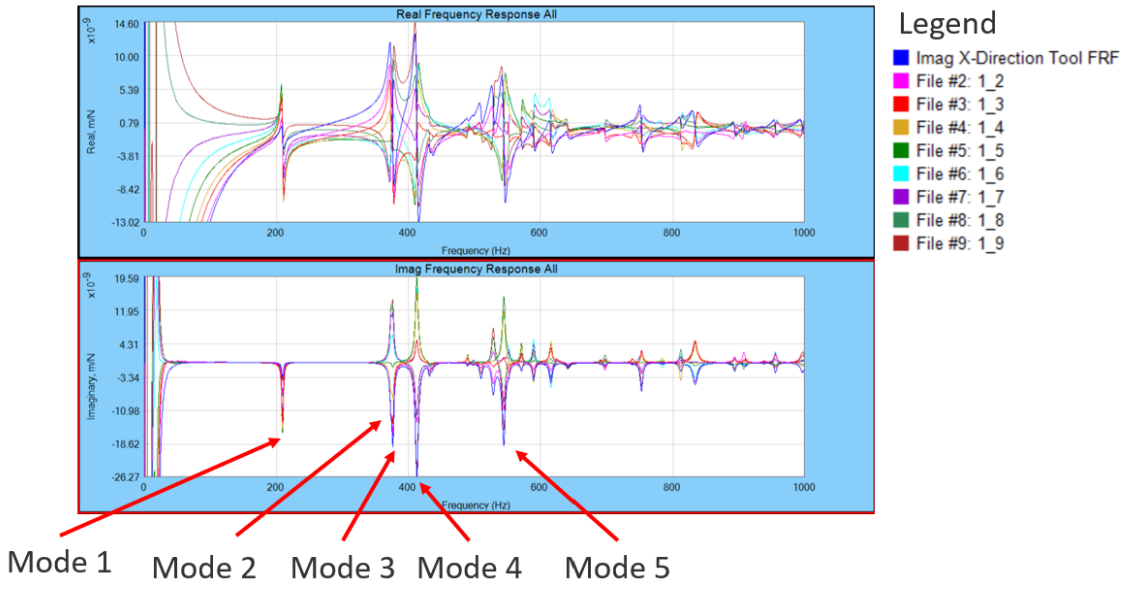

Figure 3.78: Overlay of the real and imaginary plots from the top row of points of the bottom face (1,1) - (1,9) with the chosen five most flexible modes.

Table 3.5: Peak picked values of Mode 1 at 209 Hz at each location of the bottom face normalized to (1,1) and scaled by -25.40

Row \ Column	1	2	3	4	5	6	7	8	9
1	-25.40	-57.32	-107.25	-119.22	-126.12	-120.23	-97.47	-60.04	-31.41
2	-14.41	-26.60	-43.49	-63.30	-65.66	-67.72	-53.39	-30.86	-12.73
3	4.87	8.24	8.56	1.64	2.75	-0.06	0.22	4.61	7.59
4	27.79	51.81	64.77	77.62	78.06	78.13	57.83	47.78	29.59
5	48.02	90.66	122.47	146.47	157.62	148.67	128.95	83.28	49.29

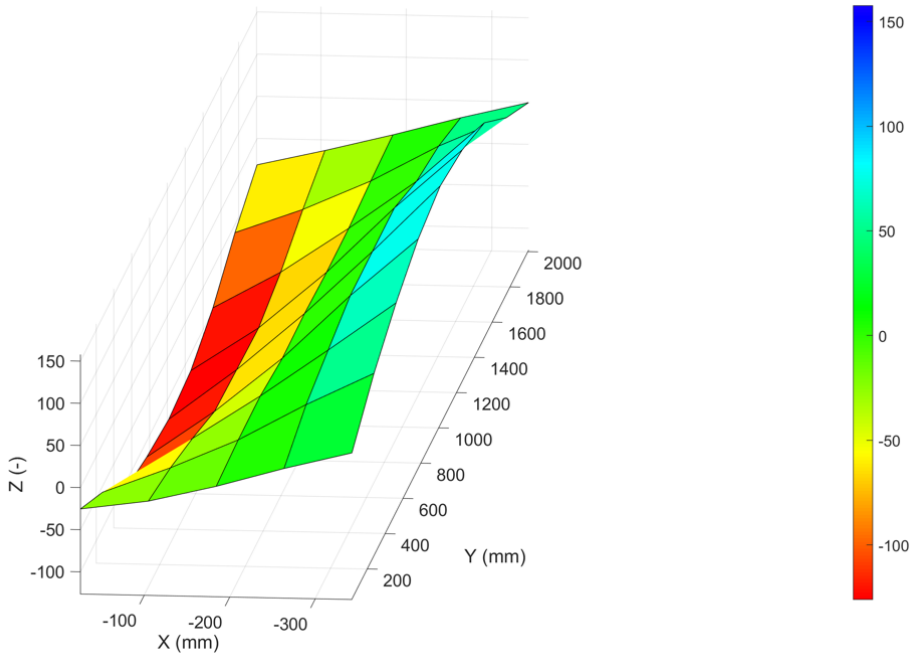

Figure 3.79: Plot of peak picked values of Mode 1 at 209 Hz at each location of the bottom face normalized to (1,1) and scaled by -25.40.

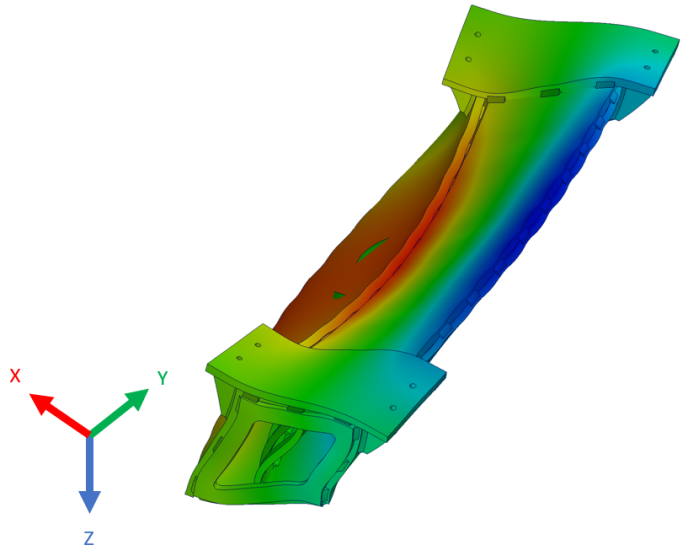

Figure 3.80: FEA simulation of weldment at 210 Hz which shows a similar mode shape as found in impact testing for mode 1 where the amplitude is only shown in the Z-axis.

Table 3.6: Peak picked values of Mode 2 at 373 Hz at each location of the bottom face normalized to (1,1) and scaled by -25.40

Row \ Column	1	2	3	4	5	6	7	8	9
1	-25.40	-24.68	-24.70	-13.45	-0.51	11.36	21.39	24.50	25.80
2	-14.71	-11.97	-9.99	-5.88	0.34	6.77	11.09	14.38	12.70
3	0.67	1.09	2.09	1.27	1.66	0.82	0.79	-0.92	-4.65
4	16.89	16.12	13.31	8.11	1.25	-7.04	-11.72	-17.26	-22.65
5	30.09	29.17	24.75	14.36	-0.33	-14.95	-26.85	-30.22	-35.59

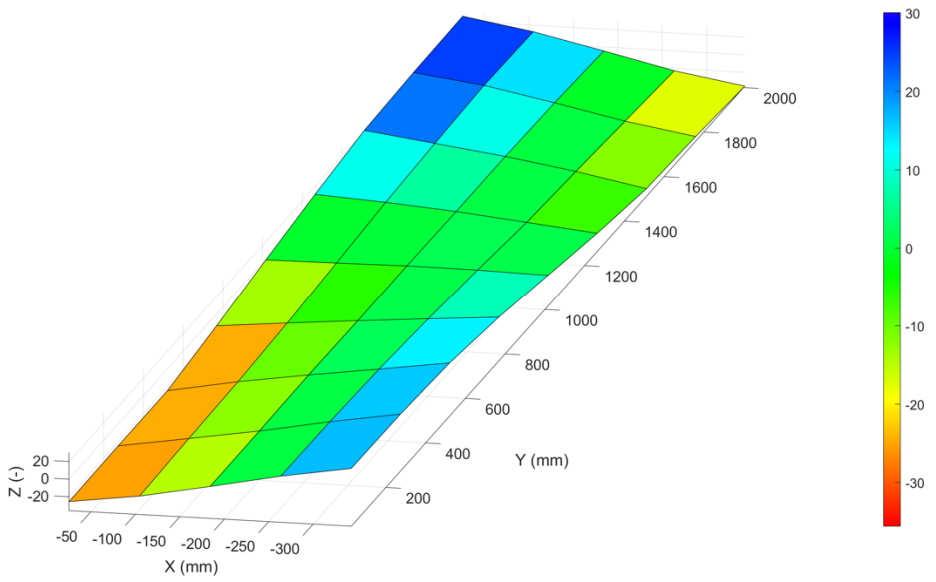

Figure 3.81: Plot of peak picked values of Mode 2 at 373 Hz at each location of the bottom face normalized to (1,1) and scaled by -25.40.

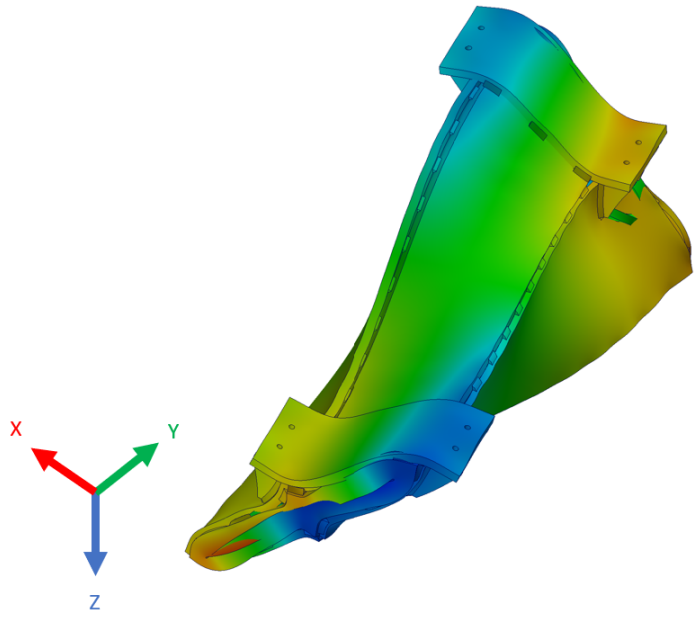

Figure 3.82: FEA simulation of weldment at 354 Hz which shows a similar mode shape as found in impact testing for mode 2 where the amplitude is only shown in the Z-axis.

Table 3.7: Peak picked values of Mode 3 at 377 Hz at each location of the bottom face normalized to (1,1) and scaled by -25.40

Row \ Column	1	2	3	4	5	6	7	8	9
1	-25.40	-19.89	-15.86	-9.54	-0.85	8.45	14.26	16.68	18.21
2	-13.44	-9.07	-7.18	-4.54	-0.18	6.52	8.48	9.14	7.99
3	1.46	2.24	2.85	3.03	0.89	0.98	0.08	-0.28	-1.98
4	15.79	13.37	12.60	10.02	2.99	-3.49	-7.47	-10.20	-14.30
5	30.40	24.11	19.53	13.06	3.63	-7.36	-15.19	-20.22	-24.88

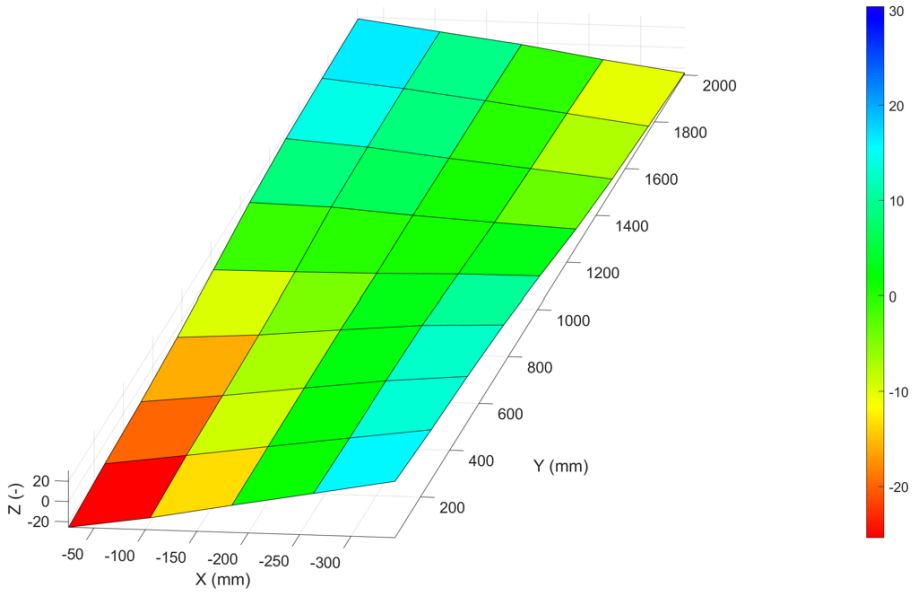

Figure 3.83: Plot of peak picked values of Mode 3 at 377 Hz at each location of the bottom face normalized to (1,1) and scaled by -25.40.

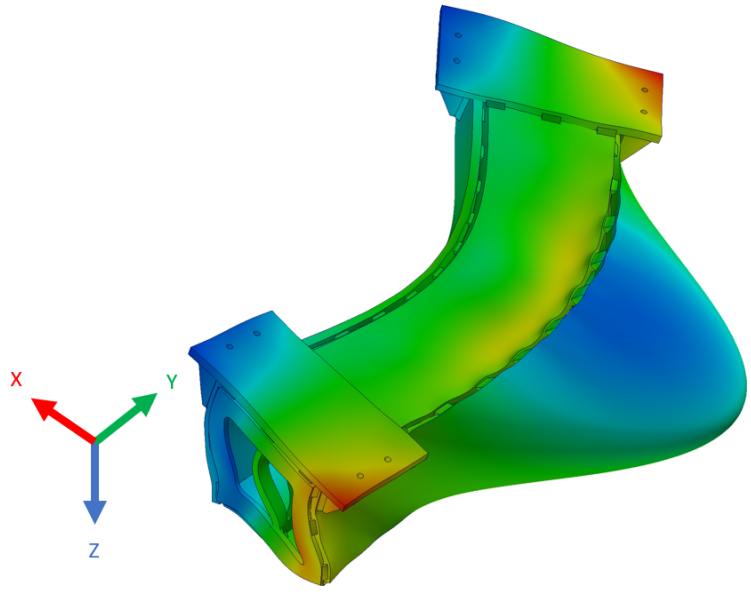

Figure 3.84: FEA simulation of weldment at 373 Hz which shows a similar mode shape as found in impact testing for mode 3 where the amplitude is only shown in the Z-axis.

Table 3.8: Peak picked values of Mode 4 at 413 Hz at each location of the bottom face normalized to (1,1) and scaled by -25.40

Row \ Column	1	2	3	4	5	6	7	8	9
1	-25.40	-13.16	4.82	15.43	18.95	16.53	4.97	-11.51	-24.46
2	-26.36	-11.99	14.00	34.08	37.34	33.75	15.25	-11.76	-26.65
3	-25.45	-10.61	19.70	43.17	46.31	42.14	18.77	-11.80	-26.69
4	-26.06	-10.88	15.89	37.40	41.67	36.57	16.38	-12.53	-27.84
5	-26.34	-11.87	6.85	20.52	24.39	20.02	5.93	-14.02	-28.67

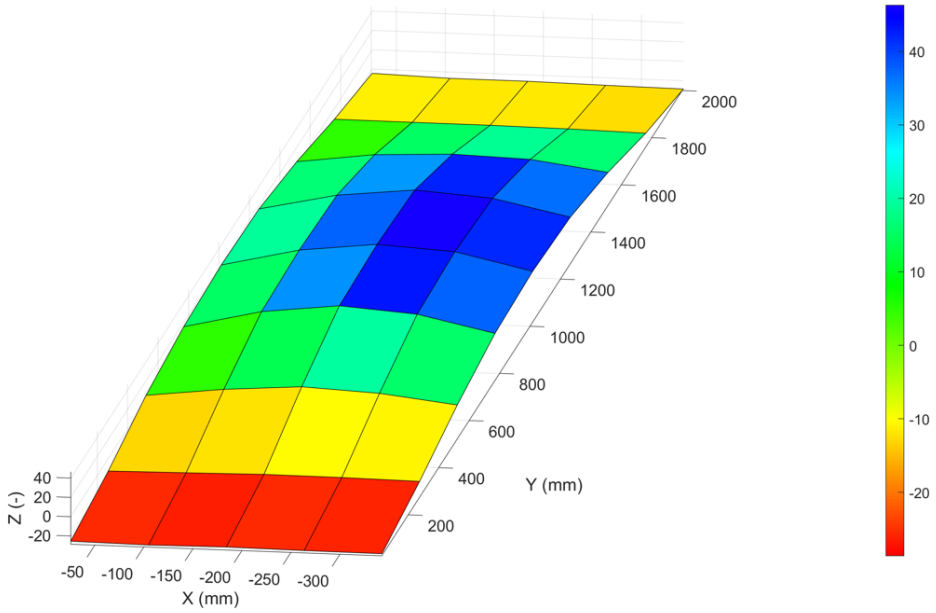

Figure 3.85: Plot of peak picked values of Mode 4 at 413 Hz at each location of the bottom face normalized to (1,1) and scaled by -25.40.

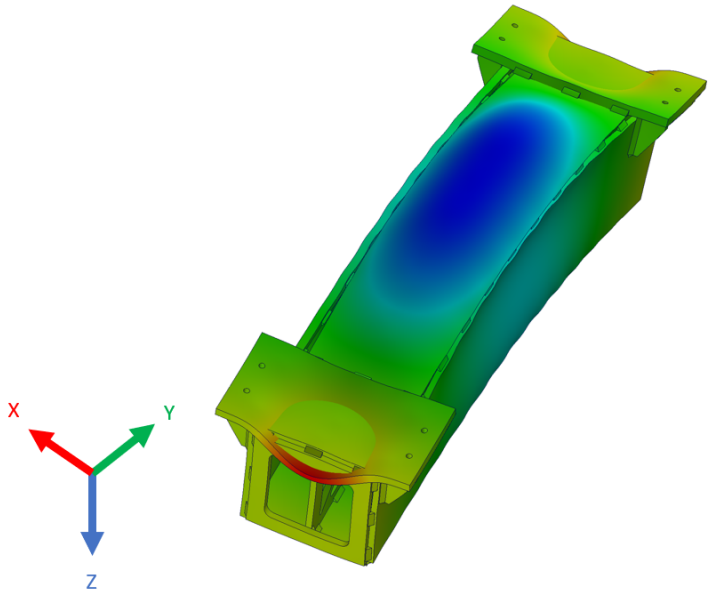

Figure 3.86: FEA simulation of weldment at 397 Hz which shows a similar mode shape as found in impact testing for mode 4 where the amplitude is only shown in the Z-axis.

Table 3.9: Peak picked values of Mode 5 at 545 Hz at each location of the bottom face normalized to (1,1) and scaled by -25.40

Row \ Column	1	2	3	4	5	6	7	8	9
1	-25.40	-14.47	1.60	15.85	20.16	14.87	1.33	-12.02	-20.58
2	-15.97	-10.44	-0.70	11.14	11.54	8.92	-2.21	-11.75	-12.60
3	-1.11	-3.60	-0.99	3.55	-0.70	0.70	-3.32	-5.73	0.04
4	13.74	4.72	-0.38	-3.66	-8.34	-6.14	-3.17	2.23	14.72
5	26.76	12.68	-0.11	-8.90	-13.21	-10.32	-2.48	10.51	26.18

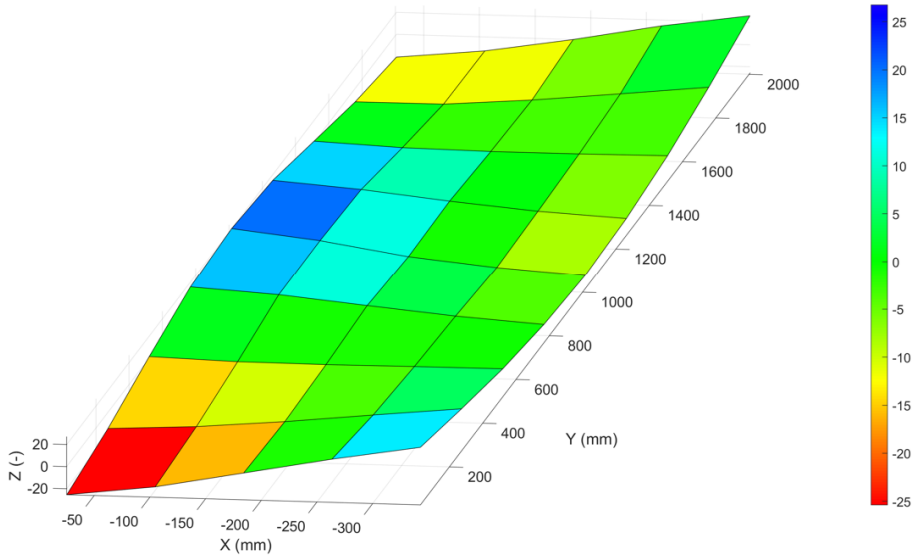

Figure 3.87: Plot of peak picked values of Mode 5 at 545 Hz at each location of the bottom face normalized to (1,1) and scaled by -25.40.

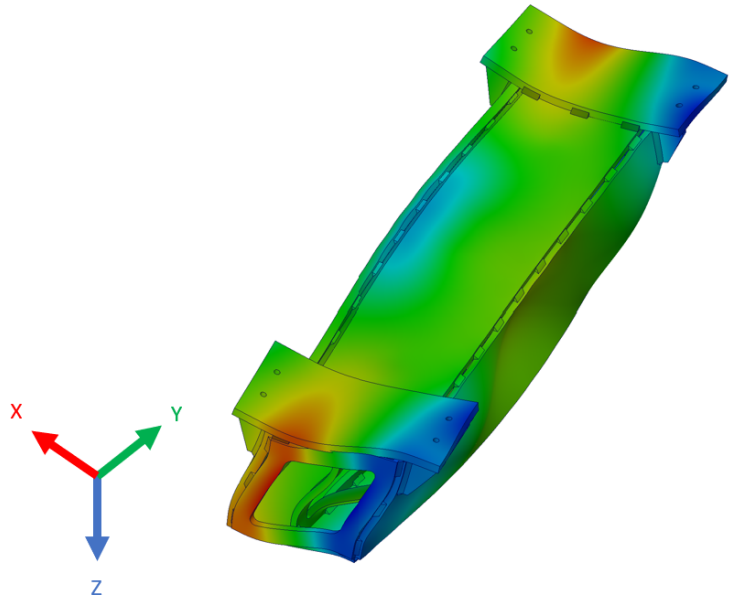

Figure 3.88: FEA simulation of weldment at 520 Hz which shows a similar mode shape as found in impact testing for mode 5 where the amplitude is only shown in the Z-axis.

not clearly separated. The peak picked frequencies for modes 2 and 3 were 373 Hz and 377 Hz, respectively. The result is that both peak-picked modes show the same motion while the FEA simulation was able to clearly define the two mode shapes. However, the other four mode shapes show good visual agreement, and thus the peak picked and simulated mode shape frequencies are shown in Table 3.10. The percent difference is calculated using Equation 3.5. The result is that the peak-picking method resulted in a less than 5% difference from the FEA simulated results. This validates that the FEA model is accurate enough and that it can be trusted.

$$Percent\ difference = \frac{FEA - peak\ picking}{FEA} \times 100 \tag{3.5}$$

Peak-picking of the mode shapes was also used to find the damping ratio and stiffness values of the five mode shapes of the bottom face of the weldment. The real and imaginary plot of (1,1) shown in Figure 3.89 highlights the same five dynamic modes of interest. Using Equations 3.6 and 3.7, the modal damping ratio and modal stiffness of each peak were able to be calculated. The calculated values were then re-plotted as real and imaginary plots that were superimposed on top of the measured data as demonstrated in Figure 3.90 which is of mode 1. The resulting calculated damping ratios and stiffness values for mode shapes of the bottom face are shown in Table 3.11. The superposition of the calculated real and imaginary plots are shown in Figure 3.91.

$$\zeta_q = \frac{\omega_3 - \omega_2}{2\omega_n} \tag{3.6}$$

$$k_q = \frac{-1}{2A\zeta_q} \tag{3.7}$$

Table 3.10: Dynamic mode frequencies from peak-picking and FEA of modes 1-5 for the bottom face in addition to the percent difference

Mode shape	Peak-picking [Hz]	FEA [Hz]	Percent difference [%]
1	209	210	0.5
2	373	354	-5.4
3	377	373	-1.1
4	413	397	-4.0
5	545	520	-4.8

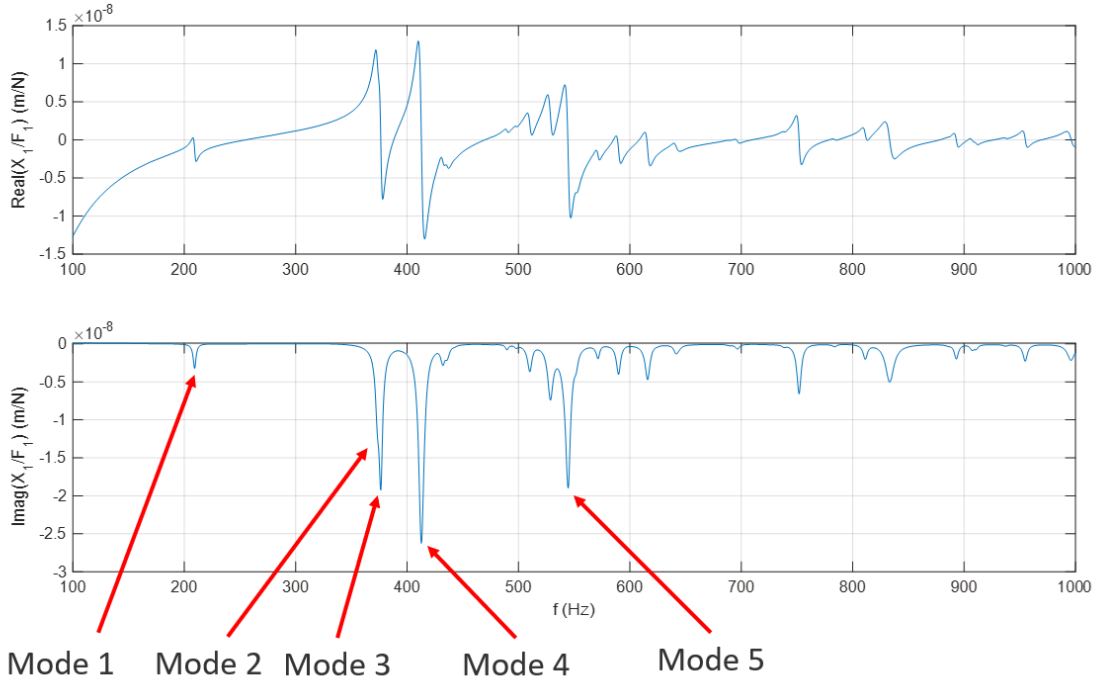

Figure 3.89: Real and imaginary FRF plots of (1,1) from the bottom face with the five identified modes of interest.

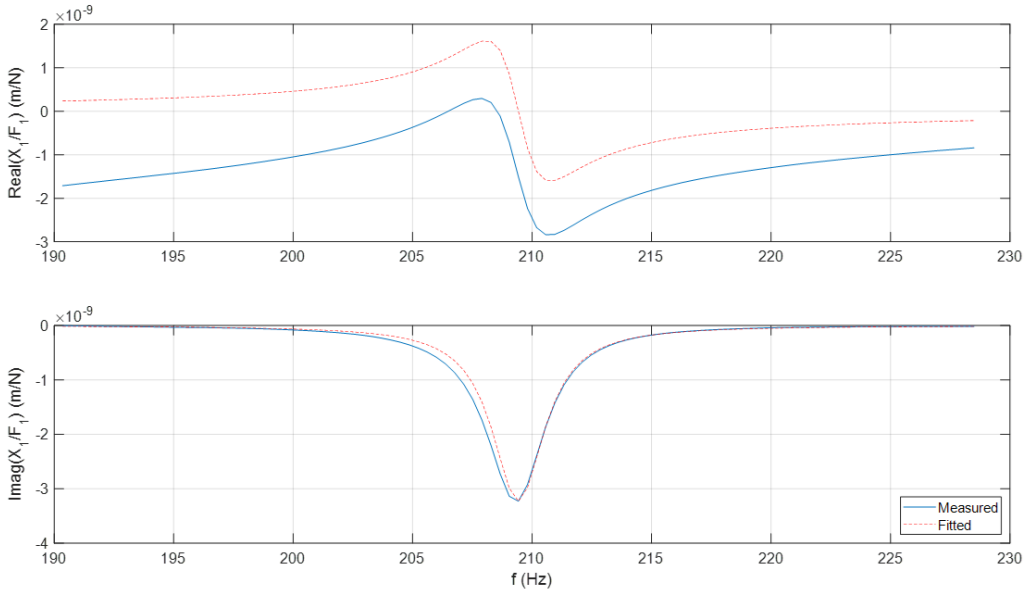

Figure 3.90: Real and imaginary FRF plots of mode 1 of (1,1) from the bottom face with a superimposed plot of the calculated real and imaginary plots.

Table 3.11: Calculated damping ratio and stiffness values from the five modes of the bottom face through peak-picking

Mode	Peak-picking frequency [Hz]	Damping ratio [-]	Stiffness [N/m]
1	209	0.006	2.43×10^{10}
2	373	0.004	2.40×10^{10}
3	377	0.006	4.50×10^{9}
4	413	0.007	2.75×10^{9}
5	545	0.005	5.30×10^{9}

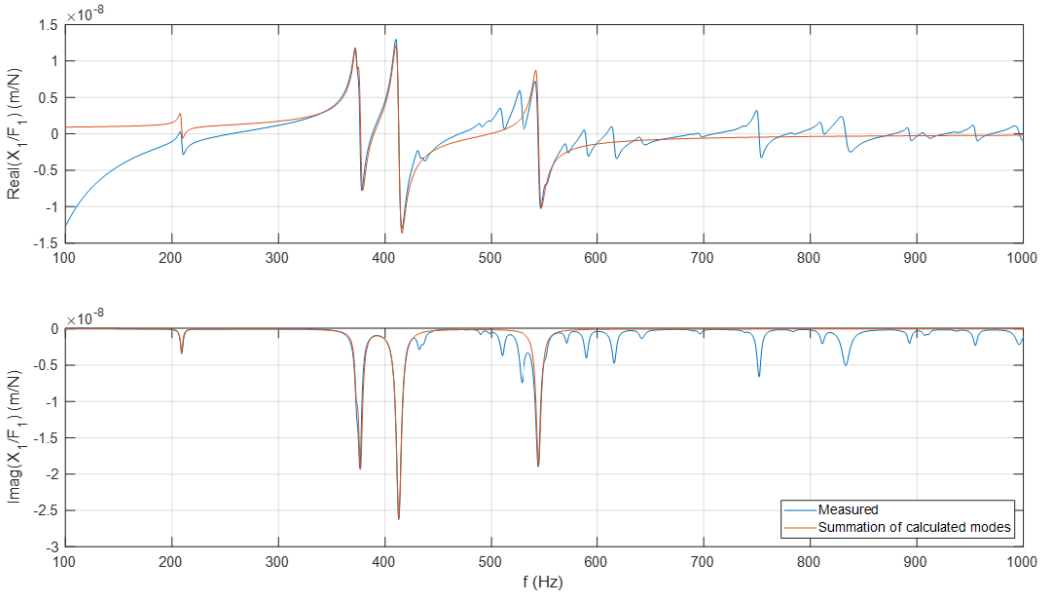

Figure 3.91: Real and imaginary FRF plots (1,1) from the bottom face with a superimposed plot of all the calculated real and imaginary plots summed.

Front face

To find the five modes with the largest amplitudes for the front face, the real and imaginary FRF plots of the top row of points in Figure 3.65 were plotted together in TXF. By looking at the amplitudes of the imaginary plot, the most flexible modes were chosen as shown in Figure 3.92. The mode shape frequencies for the bottom face that were compared were 209, 375, 529, 546, and 833 Hz. These values were extracted through peak-picking and finding the corresponding frequencies.

The approach for finding the mode shapes for the front surface is the same as finding the mode shapes of the bottom face. The same sequence of tables and figures is shown in the same order shown for the front face. Tables 3.12 through 3.16 show the plotted points of the peak-picked values. Figures 3.93 through 3.102 showcase the plotted mode shapes of the front face in MATLAB as well as the FEA simulated mode shapes. The result is that the mode shapes that were from the tap testing match that of the FEA simulations. This again validates the FEA model that has been used for the frequency simulations. Table 3.17 provides the frequencies of the peak picking and simulated mode shape frequencies. The percent difference in the table was calculated with Equation 3.5. The result was that the largest percent difference was 6%.

Peak-picking of the mode shapes was also used to find the damping ratio and stiffness values of the five mode shapes of the front face of the weldment. The real and imaginary plot of (1,1) shown in Figure 3.103 highlights the same five dynamic modes of interest. Using Equations 3.6 and 3.7, the modal damping ratio and modal stiffness of each peak were able to be calculated. The calculated values were then re-plotted as real and imaginary plots that were superimposed on top of the measured data as demonstrated in Figure 3.104 which is of mode 1. The resulting calculated damping ratios and stiffness values for mode shapes of the front face are shown in Table 3.18. The superposition of the calculated real and imaginary plots are shown in Figure 3.105.

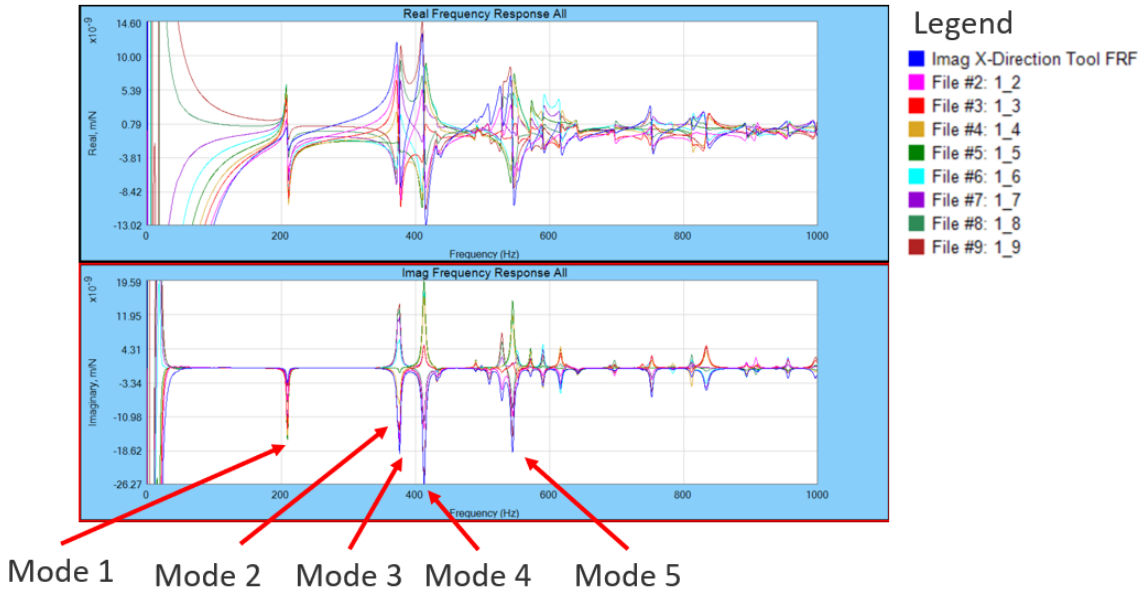

Figure 3.92: Overlay of the real and imaginary plots from the top row of points of the front face (1,1) - (1,13) with the chosen five most flexible modes.

Table 3.12: Peak picked values of Mode 1 at 209 Hz at each location of the front face normalized to (1,1) and scaled by -25.40

Row \ Column	1	2	3	4	5	6	7	8	9	10	11	12	13
1	-25.40	-46.31	-59.07	-71.25	-85.18	-87.76	-84.66	-87.81	-83.20	-66.98	-55.72	-45.12	-24.15
2	-14.42	-19.85	-26.52	-37.14	-50.01	-52.33	-51.10	-49.08	-47.70	-67.41	-51.27	-18.58	-15.00
3	1.62	7.82	4.48	-2.23	-7.32	-8.80	-5.23	-7.87	-5.80	-0.86	6.87	10.07	-1.06
4	14.16	36.71	31.27	28.20	34.23	36.80	36.71	37.89	34.80	31.17	29.94	40.81	11.18
5	14.65	66.83	47.82	53.79	65.78	67.75	71.99	70.62	69.44	56.69	50.53	73.66	15.19

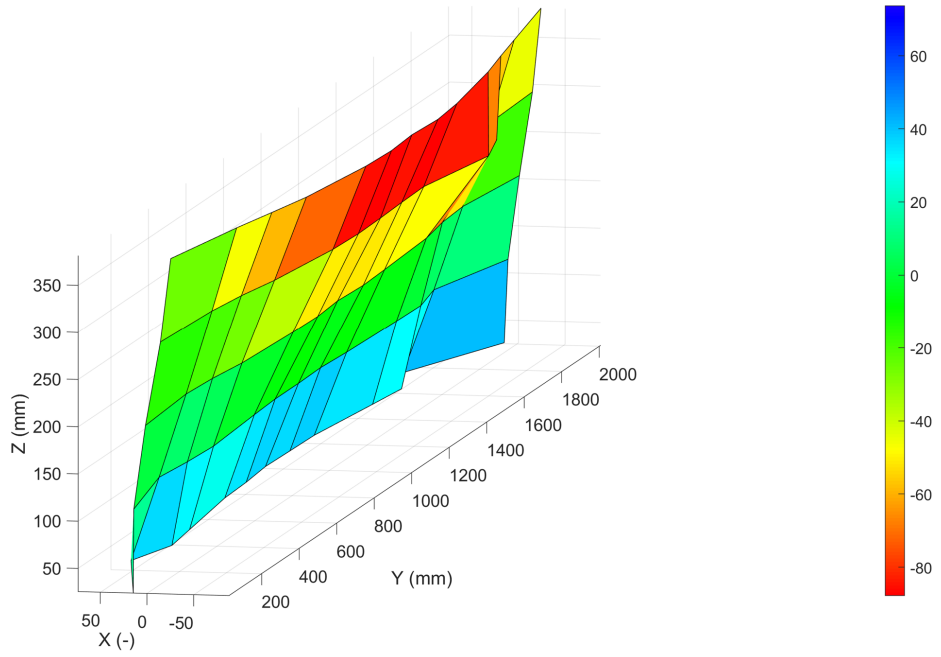

Figure 3.93: Plot of peak picked values of Mode 1 at 209 Hz at each location of the front face normalized to (1,1) and scaled by -25.40.

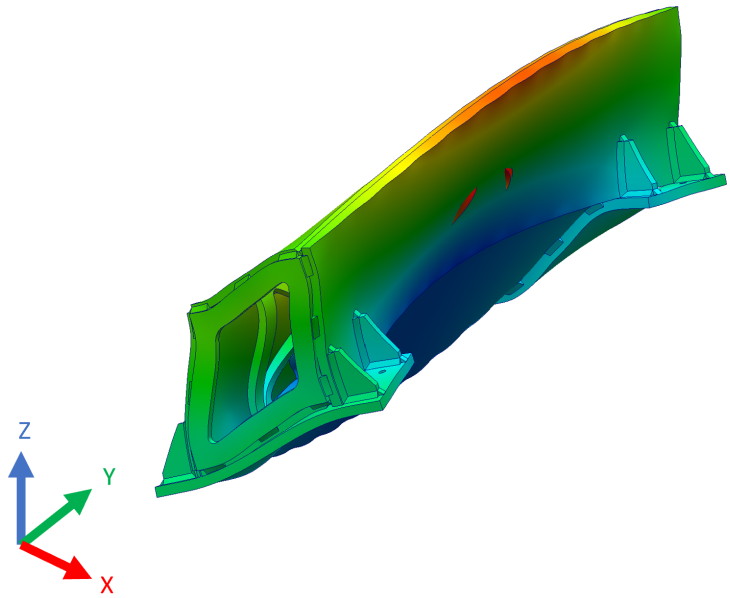

Figure 3.94: FEA simulation of weldment at 210 Hz which shows a similar mode shape as found in impact testing for mode 1 where the amplitude is only shown in the X-axis.

Table 3.13: Peak picked values of Mode 2 at 375 Hz at each location of the front face normalized to (1,1) and scaled by -76.20

Row \ Column	1	2	3	4	5	6	7	8	9	10	11	12	13
1	-76.20	-59.48	-54.49	-42.68	-17.17	-3.34	10.46	19.64	28.60	37.90	39.78	37.01	35.63
2	-58.50	-39.13	-33.53	-23.29	-0.97	9.98	20.42	26.85	29.58	38.27	24.80	5.95	13.39
3	-28.44	-14.54	-11.08	-3.64	13.42	20.97	26.56	27.46	23.87	4.31	-15.78	-26.62	-22.17
4	-2.54	14.28	11.10	13.37	24.13	26.34	25.48	20.06	12.09	-13.24	-28.55	-60.70	-52.51
5	2.70	47.32	23.43	26.81	28.39	25.11	19.49	10.16	-1.49	-25.39	-39.04	-96.29	-59.05

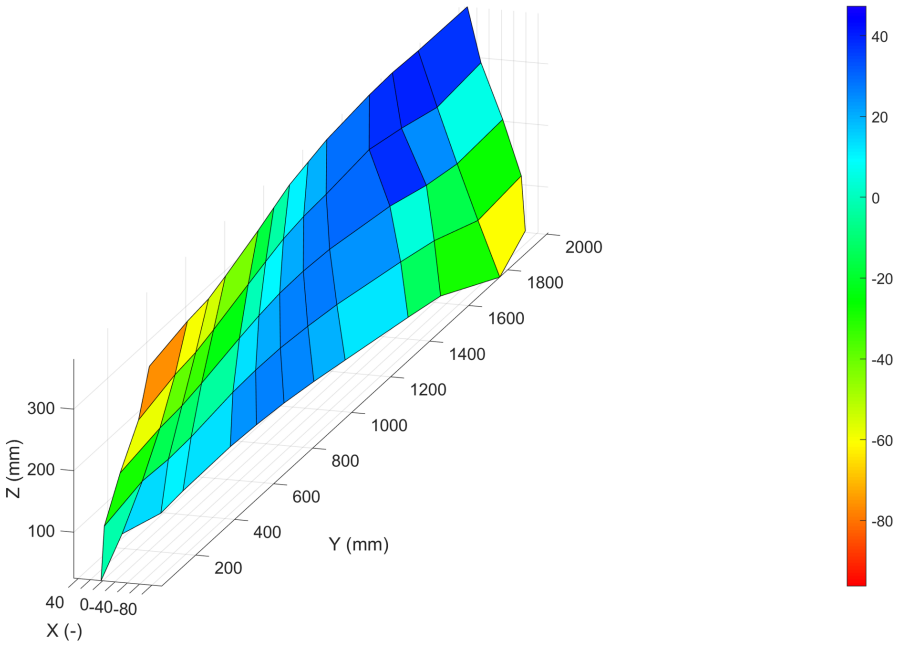

Figure 3.95: Plot of peak picked values of Mode 2 at 375 Hz at each location of the front face normalized to (1,1) and scaled by -76.20.

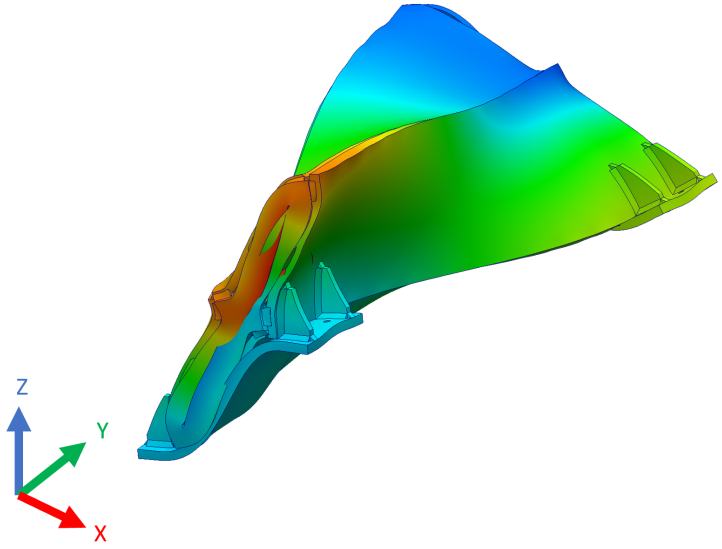

Figure 3.96: FEA simulation of weldment at 354 Hz which shows a similar mode shape as found in impact testing for mode 2 where the amplitude is only shown in the Y-axis.

Table 3.14: Peak picked values of Mode 3 at 529 Hz at each location of the front face normalized to (1,1) and scaled by -76.20

Row \ Column	1	2	3	4	5	6	7	8	9	10	11	12	13
1	-76.20	-83.74	-81.61	-64.20	-34.94	-17.28	6.83	23.42	39.90	61.46	68.39	62.24	51.81
2	-56.35	-114.77	-145.14	-136.47	-90.53	-42.42	17.21	72.98	111.19	60.00	66.26	91.98	32.77
3	-18.90	-100.56	-147.78	-150.43	-108.87	-51.85	22.15	84.01	130.00	150.04	132.76	84.39	15.69
4	27.19	-41.10	-60.89	-88.71	-67.81	-33.88	10.10	48.08	78.76	85.62	65.80	39.46	-14.07
5	72.94	63.62	37.60	23.33	4.36	0.22	-1.64	-3.81	-10.51	-23.86	-31.40	-42.81	-71.16

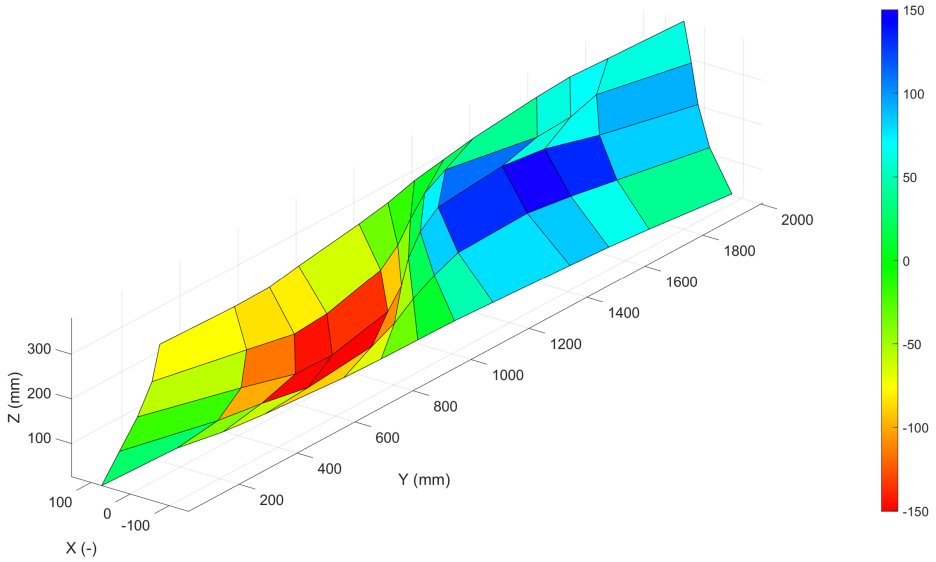

Figure 3.97: Plot of peak picked values of Mode 3 at 529 Hz at each location of the front face normalized to (1,1) and scaled by -76.20.

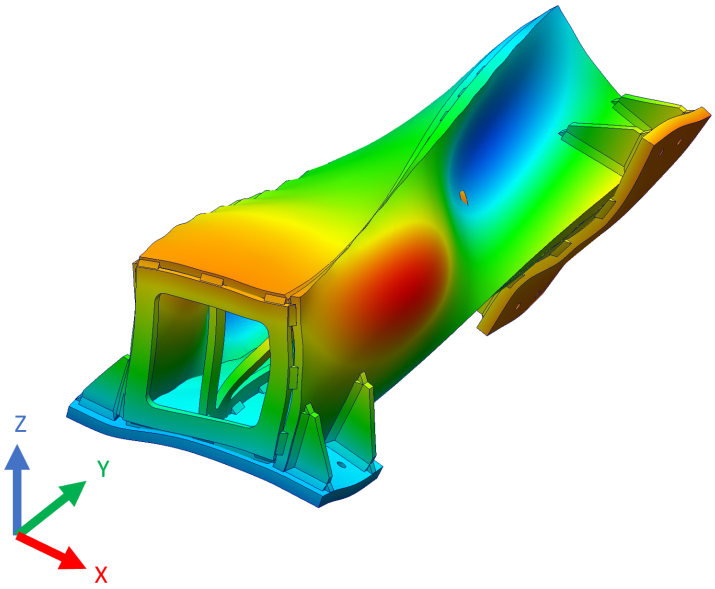

Figure 3.98: FEA simulation of weldment at 505 Hz which shows a similar mode shape as found in impact testing for mode 3 where the amplitude is only shown in the X-axis.

Table 3.15: Peak picked values of Mode 4 at 546 Hz at each location of the front face normalized to (1,1) and scaled by -76.20

Row \ Column	1	2	3	4	5	6	7	8	9	10	11	12	13
1	-76.20	-43.69	-28.55	-9.90	19.47	28.98	31.55	24.68	14.98	-15.67	-35.10	-48.05	-73.30
2	-55.90	-30.73	-17.12	10.57	56.68	68.80	70.55	58.91	38.78	-15.76	-40.18	-42.83	-58.76
3	-17.88	-13.76	-6.45	20.37	65.05	77.88	76.08	64.95	42.22	-8.25	-28.99	-25.39	-25.24
4	16.20	7.22	3.11	13.71	39.29	44.49	43.79	31.19	19.93	-6.40	-10.99	4.26	8.60
5	24.67	32.21	0.72	-3.29	-10.08	-11.81	-16.63	-16.75	-16.19	-6.13	1.03	46.12	24.13

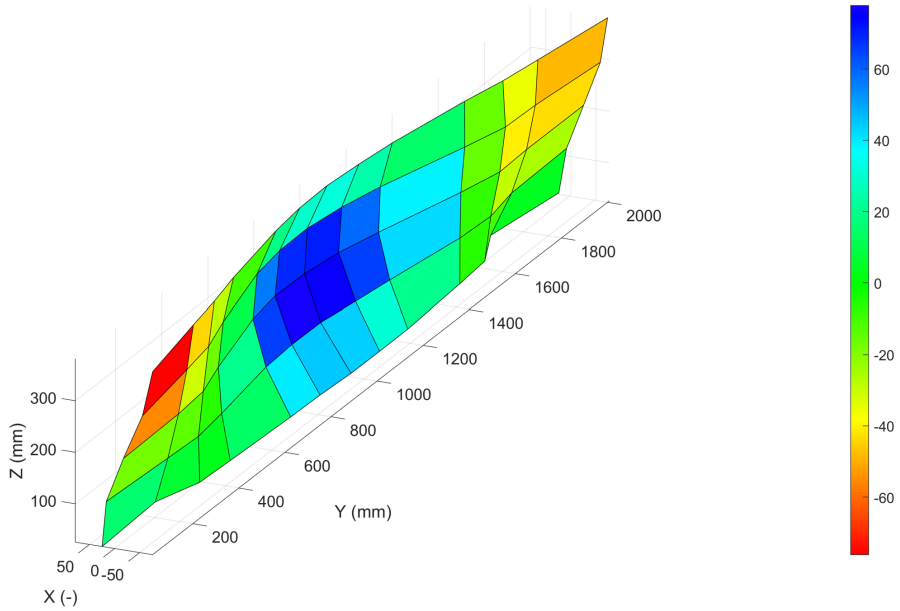

Figure 3.99: Plot of peak picked values of Mode 4 at 546 Hz at each location of the front face normalized to (1,1) and scaled by -76.20.

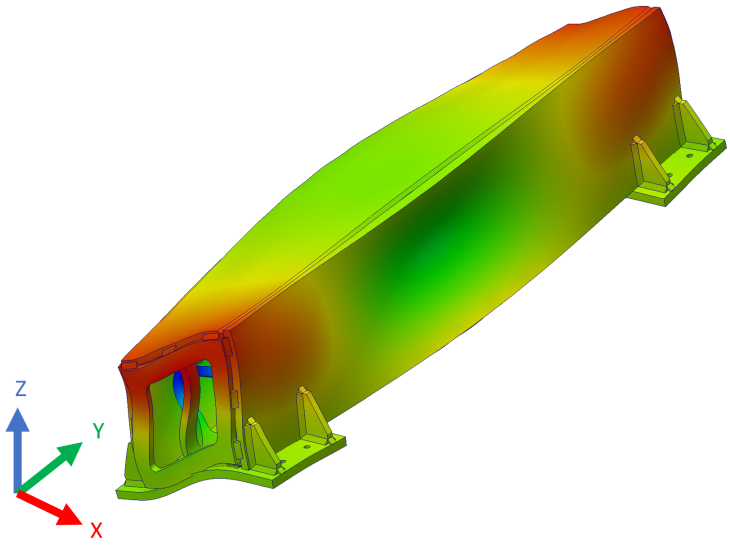

Figure 3.100: FEA simulation of weldment at 519 Hz which shows a similar mode shape as found in impact testing for mode 4 where the amplitude is only shown in the X-axis.

Table 3.16: Peak picked values of Mode 5 at 833 Hz at each location of the front face normalized to (1,1) and scaled by -76.20

Row \ Column	1	2	3	4	5	6	7	8	9	10	11	12	13
1	-76.20	-13.34	16.63	28.55	31.46	17.64	-2.11	-19.18	-32.07	-25.51	-8.57	23.39	80.74
2	-41.04	3.22	22.23	32.74	41.44	26.75	1.41	-25.51	-45.33	-25.49	-9.39	8.38	52.19
3	15.68	12.25	11.28	17.96	29.66	22.43	3.01	-18.50	-31.97	-21.24	-10.74	-5.37	-1.73
4	59.23	13.73	-14.44	-14.59	-5.01	0.70	4.20	6.27	6.30	13.43	10.74	-17.86	-47.54
5	54.87	7.67	-39.97	-50.70	-42.12	-21.38	2.20	28.36	48.64	51.76	36.98	-29.09	-51.80

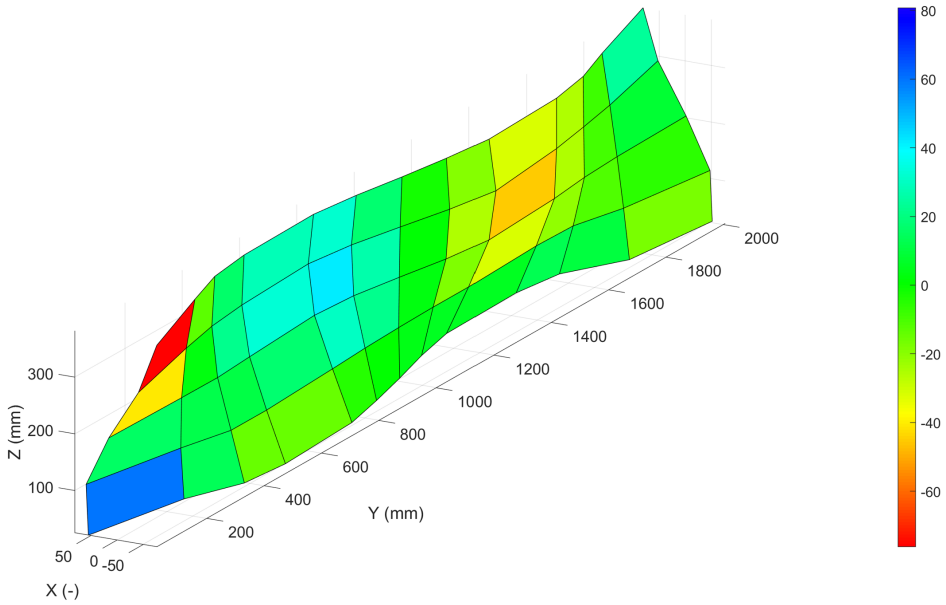

Figure 3.101: Plot of peak picked values of Mode 5 at 833 Hz at each location of the front face normalized to (1,1) and scaled by -76.20.

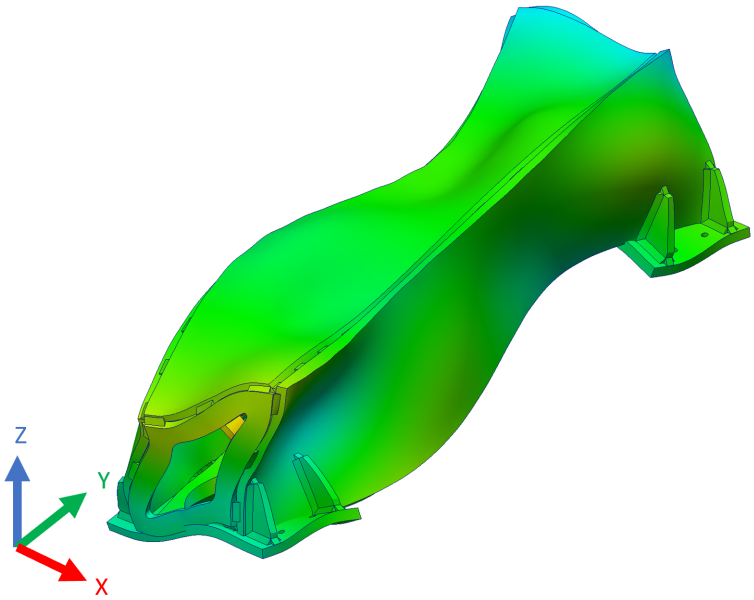

Figure 3.102: FEA simulation of weldment at 800 Hz which shows a similar mode shape as found in impact testing for mode 5 where the amplitude is only shown in the X-axis.

Table 3.17: Dynamic mode frequencies from peak-picking and FEA of modes 1-5 for the front face in addition to the percent difference

Mode shape	Peak-picking [Hz]	FEA [Hz]	Percent difference [%]
1	209	210	0.5
2	375	354	-5.9
3	529	505	-4.8
4	546	519	-5.2
5	833	800	-4.1

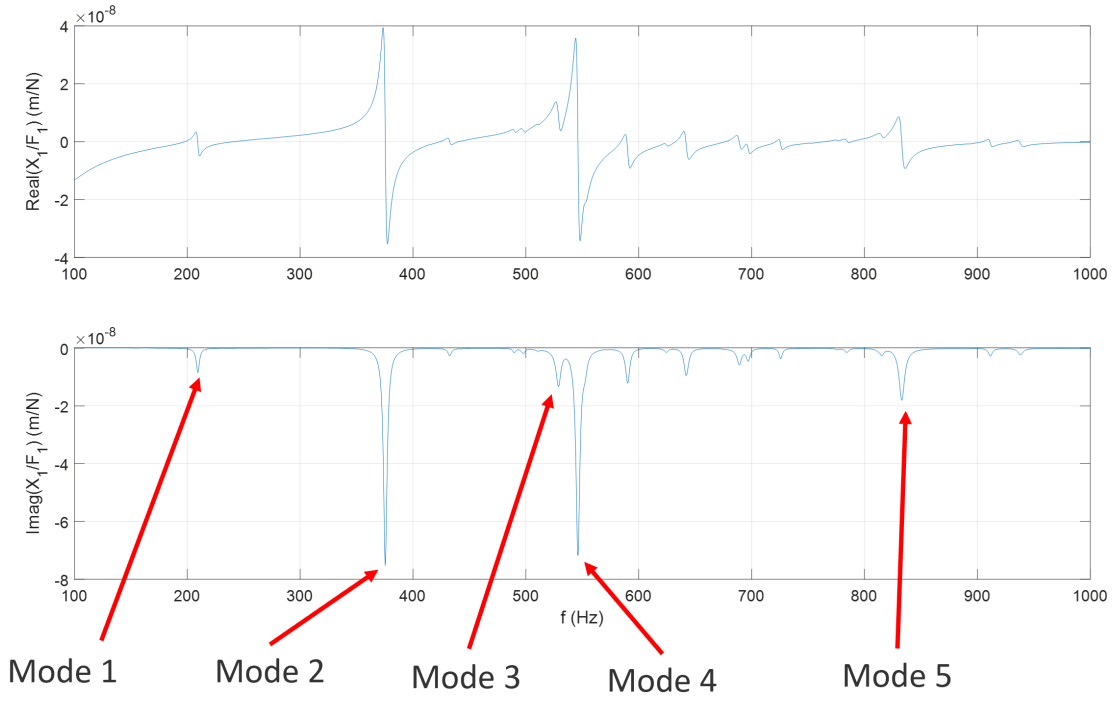

Figure 3.103: Real and imaginary FRF plots of (1,1) from the front face with the five identified modes of interest.

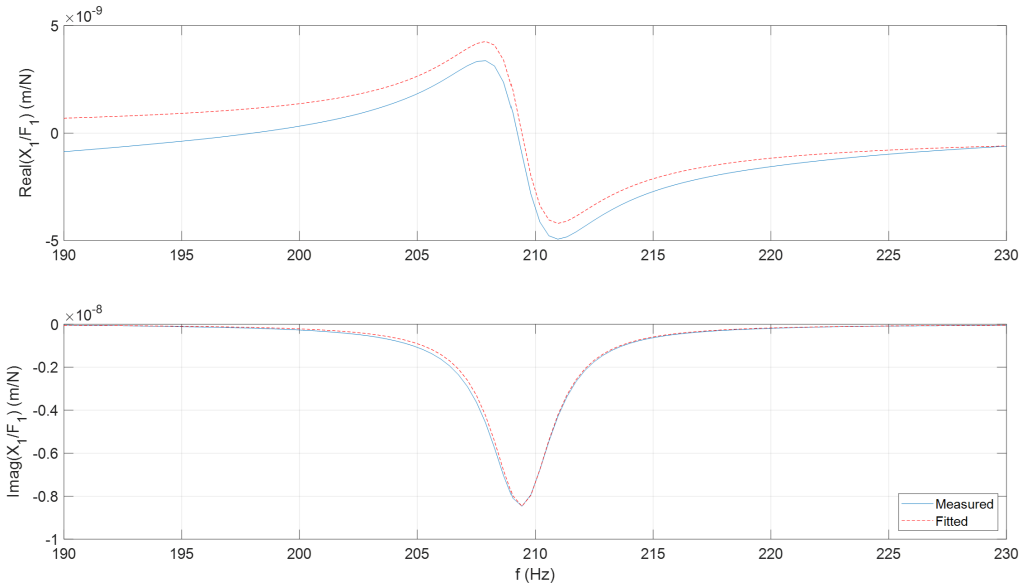

Figure 3.104: Real and imaginary FRF plots of mode 1 of (1,1) from the front face with a superimposed plot of the calculated real and imaginary plots.

Table 3.18: Calculated damping ratio and stiffness values from the five modes of the front face through peak-picking

Mode	Peak-picking frequency [Hz]	Damping ratio [-]	Stiffness [N/m]
1	209	0.007	8.10×10^9
2	375	0.005	1.31×10^9
3	529	0.005	8.35×10^9
4	546	0.004	1.75×10^9
5	833	0.003	9.20×10^9

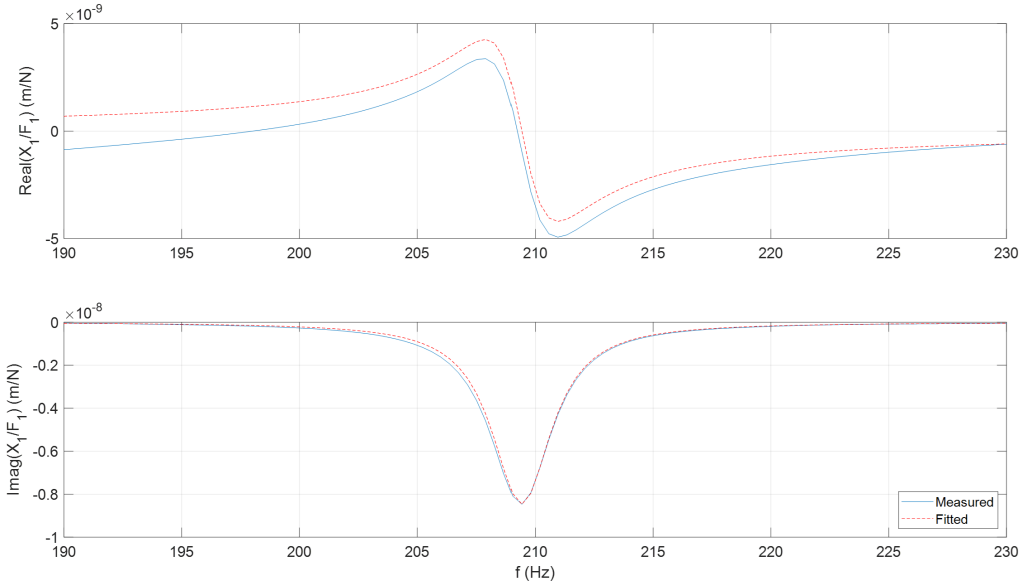

Figure 3.105: Real and imaginary FRF plots (1,1) from the front face with a superimposed plot of all the calculated real and imaginary plots summed.

Chapter 4

Design of mBAAM cross beam

4.1 Machine tool design constraints

Machine tools are designed to make components that meet specifications. As assemblies and parts become more complex, more stringent requirements are necessary for machine tools to achieve. Factors that affect precision and accuracy are commonly referred to as machine tool errors. The main sources of machine tool errors are geometric, thermal, dynamic, and static errors. To design an accurate machine tool, all the errors of the system must be taken into account [16].

Geometric errors are component-specific errors. Each component of the machine tool has its associated geometric errors such as flatness or straightness. The geometric errors cannot be eliminated, but can be reduced. Geometric tolerances can be reduced by sourcing more precise components or implementing smaller tolerances on components. Limitations such as part availability, cost, or feasibility make geometric errors impossible to eliminate. In addition, the tolerances of the components stack up and contribute to the error in the machine tool motion.

Thermal errors are errors due to the thermal expansion of the machine tool and its components. Thermal errors are prevalent due to the environment, machine tool operation, and various other sources. One significant aspect of thermal errors

is that the errors are not constant and vary with time. During a machine tool's operation, the machine tool will experience varying temperature gradients that affect all the components of the machine tool. In response to the temperature fields, the components expand or contract. Due to the difficulty in controlling and predicting the thermal errors of a machine tool, it is typically the largest source of error that affects the final part accuracy [41].

Dynamic errors are due to the motion of the machine tool. Every component of the machine tool has its mass, stiffness, and damping. The vibratory behavior of all the components results in machine tool errors. The vibratory motion can be due to external forces such as the motion of the ground that the machine is resting on or an internal force such as force from a cutting tool. A better understanding of the dynamics of machine tools has enabled dynamic errors to be reduced such as stability lobes have enabled machined components to be made more efficiently and accurately [42]. The characteristics that improve the dynamic errors of the system are a reduction in mass and an increase in stiffness.

Static errors are due to the deformation or motions of the system under various internal and external forces. When under load, components can move and deform. The loads and motions of the machine tool are difficult to quantify because many factors can affect the motion and loads that the machine experiences. External forces can vary from gravity to cutting forces. The stiffness of the machine tool is also difficult to quantify due to the various configurations that exist for multi-axis machines. In addition, the static errors can be compounded due to the dynamic errors of the system.

To redesign a machine tool component, the four error sources need to be considered. The geometric errors of the component can be reduced and quantified by the manufacturing processes. For design, the critical surfaces need to be identified for the part to function and interact with other components. The thermal errors for the cross beam are neglected for this study because the entire machine tool must be considered to predict the cross beam contributions. However, the dynamic and

static deflections of the cross beam can be used as metrics to compare one design to another. The significant attributes of the cross beam that affect both the static and dynamic performance are mass and stiffness. For this project, the goal is to reduce the mass without sacrificing stiffness or increase the stiffness without increasing the mass.

4.2 mBAAM design constraints

4.2.1 MedUSA welding system

The ORNL MedUSA system was used to print the cross beam. The MedUSA system was created for mBAAM and was designed to print WAAM parts. The intent of the redesign of the weldment cross beam was to improve the static and dynamic behavior of the structure while also making it compatible with the WAAM process and the MedUSA system.

Since its establishment, the MedUSA system was created to experiment with mBAAM. The redesign of the weldment was an experiment on the feasibility of making a WAAM part to match or exceed the performance of a traditional weldment and learn more about the capabilities of the MedUSA system. MedUSA has previously been used to create one-off and intricate parts that challenge the system's capabilities. The limitations and capabilities of MedUSA are constantly evolving and the design of the WAAM structure was with the guidance of the team of experts at ORNL that operate and experiment with the system.

4.2.2 Capabilities and limitations

The capabilities and limitations of the MedUSA system dictated the design parameters for the WAAM cross beam. Some capabilities and limitations are unique to the MedUSA system while others concern WAAM components in general. The design

parameters for the WAAM cross beam are concepts that can be applied to other structures.

The WAAM process is dependent on the metal wire feedstock. The weldment consisted of A36 steel and the feedstock and a readily available material was Lincoln Electrics' SuperArc® LA-100. The material is designed to be used on 690 MPa tensile base materials which are similar to A36 steel [43]. The WAAM team at ORNL has also had experience with the LA-100 and has achieved good prints with the material. As a result, the WAAM part was designed with LA-100.

A critical part of the structure is the build plate. The build plate is where the WAAM material is deposited. Without the build plate, the part would not be able to be removed from the build table. In addition, the build plate has to be either removed or modified post-printing. The removal of the build plate can be a difficult task due to the size of the desired part. Modifications to the build plate post-printing are typical due to the need for the extra base material to be secured to the build plate. For the MedUSA system, the team has used various fasteners and clamps to secure the build plate to the build table. As a result, the build plate must be considered when designing a mBAAM structure.

The material that is deposited is in the form of long weld beads. It was recommended that the minimum thickness for walls be 9 mm. This accounts for the single bead wall thickness of 6 mm to 8 mm and the overlap between the beads for the material to bond together. It was also advised to not have any single-beaded walls because the geometric stability was not favorable in single-wall prints. The sides of any WAAM print exhibit the layers and rough surface finish as shown in Figure 4.1. As a result, the 9 mm wall thickness is the core material that can be assumed to be solid material where an additional 1.5 mm on each surface is expected to be rough. The rough surfaces from WAAM prints cannot be used as functional surfaces unless machined.

Because the WAAM print is a layer-wise process, there are restrictions on how the layers can be welded on top of one another. The MedUSA system was unable to

Figure 4.1: Rough exterior surface of WAAM print.

accurately print overhangs that were more than 25° from normal. Typical layer-wise AM processes resolve overhang issues using support material that can be removed. Supports that are made through the WAAM process are difficult to remove and are typically avoided. Reducing the need for supports also reduces the amount of printed material, time for printing the supports, and post-processing the supports. Layer-wise AM also exhibits anisotropic material properties for the final part. The printed material layers have better material properties in each layer while the axis that has the layers built along shows a reduction in the bonding strength of the material. The axis is which the most loads that the print will experience should be the axis for the layers to be printed on.

Large prints are time intensive and some considerations of how the geometry would affect the print time. The finished WAAM part should have relative dimensions that are close to the weldment. The printing process favors long continuous beads. Starting and stopping the beads add time to the print. The MIG process also creates slag and debris while printing. Slag and debris build-up results in the need to change out the MIG torches' contact tip and gas nozzle which also adds time and is exacerbated by starting and stopping the weld bead.

Thermal distortion is prevalent in WAAM prints. The distortion is the result of internal stresses that reside in WAAM prints due to the temperature gradient and carious cooling rates of the material as its being manufactured. It is difficult to predict how a structure will deform for there are many variables that can affect the stability of the printed part.

4.3 Iterative design process

The engineering design process for the WAAM cross beam was iterative. Many designs were conceptualized and analyzed. With each iteration, the design was refined to meet the desired goal of the structure. The WAAM cross beam was designed to replace

the weldment cross beam with the intent of reducing the mass of the structure while retaining the weldment's stiffness.

Critical surfaces and clearance profiles needed to be preserved between the weldment and WAAM structure. For the WAAM print to mate with the concrete base as well as the column assembly, the mounting feet and rail locations needed to be preserved. For the mounting feet, shown in Figure 3.28, the plate sizes, hole sizes, and plate locations were preserved. The front face of the WAAM cross beam was designed to have the same guide rail locations and clearance profile as the weldment shown in Figures 3.34 and 3.35. Preserving both the mounting feet and front face mounting profiles allows for a standardized method of comparing the various designs to the weldment's deflection when under load which was discussed in Section 3.2.2.

Many concepts for the WAAM print were developed. While preserving the mounting profiles, various cross-sections and mass reduction patterns were implemented. To avoid overhangs, the concepts were all two-dimensional patterns that were extruded to generate wall features for the WAAM cross beam. The concepts also shared the intent to function as an AM part without adding features that were not made through the WAAM processes such as welding additional plates to the structure to improve stiffness. Concepts that had more mass than the weldment's 702 kg were also excluded.

FEA models of the various designs were used to compare designs to each other. Because there are infinite possibilities for the WAAM cross beam, using the deflection behaviors of the various designs under the same loading conditions serves as a tool for comparison. Comparing each design's deflections to the weldment deflections shown in Table 3.4 can validate whether or not a new design is better or worse. This method was the main comparative tool used to eliminate concepts from the finalized design. Quantitatively, the rubric for an improved design is similar to deflections under the various configurations as well as a mass.

The design process was also dependent on feedback from the WAAM team at ORNL. It was essential to the design process to have frequent and clear

communication of the design changes with the WAAM team. The WAAM team contributed to the design by communicating the feasibility of different print features as well as better print strategies based on previous print data. Integrating the manufacturing team's input into the design from the beginning of the design process reduced the need for major modifications.

A few of the important design factors are listed and summarized as follows:

- There is a list of materials that are compatible with the MedUSA cell; LA100 from Lincoln Electric was selected
- Material properties can differ from the wire properties and can be position dependent due to the WAAM process heating and cooling profiles
- The print bead width can vary from 6 mm to 8 mm
- The print must be made on a build plate (or several build plates) which must be later removed
- The WAAM process has shown better results for continuous bead prints than short, segmented print paths
- Overlapping joints should be avoided and, if necessary, there should be only one overlap
- The design must be able to be sliced using the in-house slicing software, which generates the robot tool paths
- The printed surface will be wavy (up to 1.5 mm surface height variation) and the cross-sectional area that is used for calculating mechanical properties must account for the surface variations
- The WAAM process is not suitable for printing large flat surfaces or walls due to thermal deformations and print time cost

- Overhangs should generally be avoided, but 20°-25° angles from vertical are possible
- If there is a surface that needs to be finished (by machining, for example), there should be at least 3 mm of additional material
- Features should be at least two beads thick and there should be bead overlap
- Making the design with the least amount of printed material will reduce the print time and cost dramatically

4.4 Finalized design

After reviewing the FEA simulation results for the various designs, a final design was reached. The final WAAM design features and dimensions are shown in Figures 4.2 through 4.8. The overall dimensions of the final design are 2028.8 mm by 609.6 mm by 601.4 mm.

A feature of the final design is the implementation of arches into the front and back faces of the WAAM cross beam as seen in Figures 4.4 and 4.6. The arch that was implemented was a catenary arch. Catenary arches have been implemented in many structures such as buildings or bridges. Catenary arches are formed through the hyperbolic cosine function shown in Equation 4.1 where a defines the position of the apex of the curve [44]. This geometry was chosen because it improved the stiffness of the design in the X-Z plane.

$$y(x) = a\ cosh\frac{x}{a} \tag{4.1}$$

As seen in Figure 4.4, curved walls connect the front and back walls. The internal walls act as supporting walls and provide stiffness to the WAAM part as well as minimize the mass. The curved walls also serve as smaller arches that mimic a sinusoidal wave. The sinusoidal wave allows the print paths to be continuous while

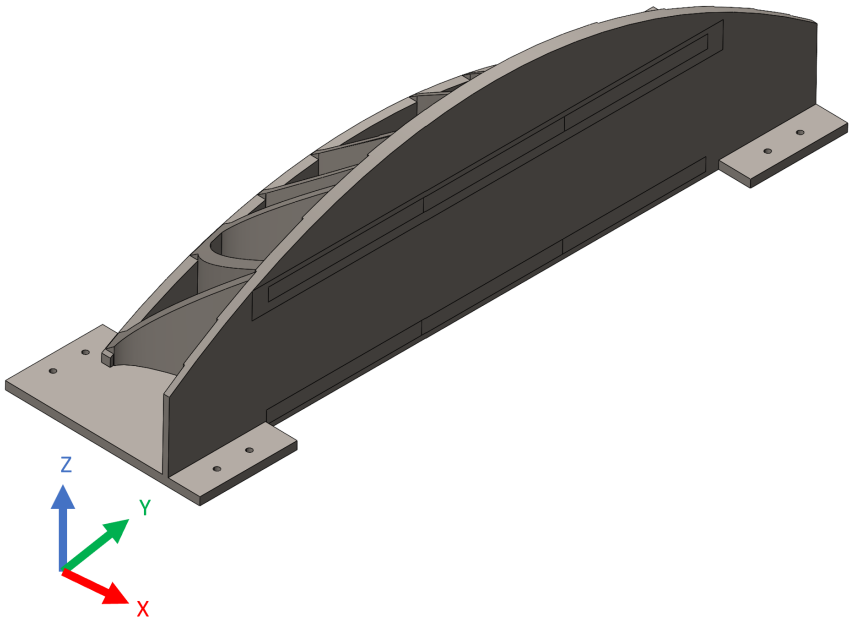

Figure 4.2: Front isometric view of the finalized WAAM design.

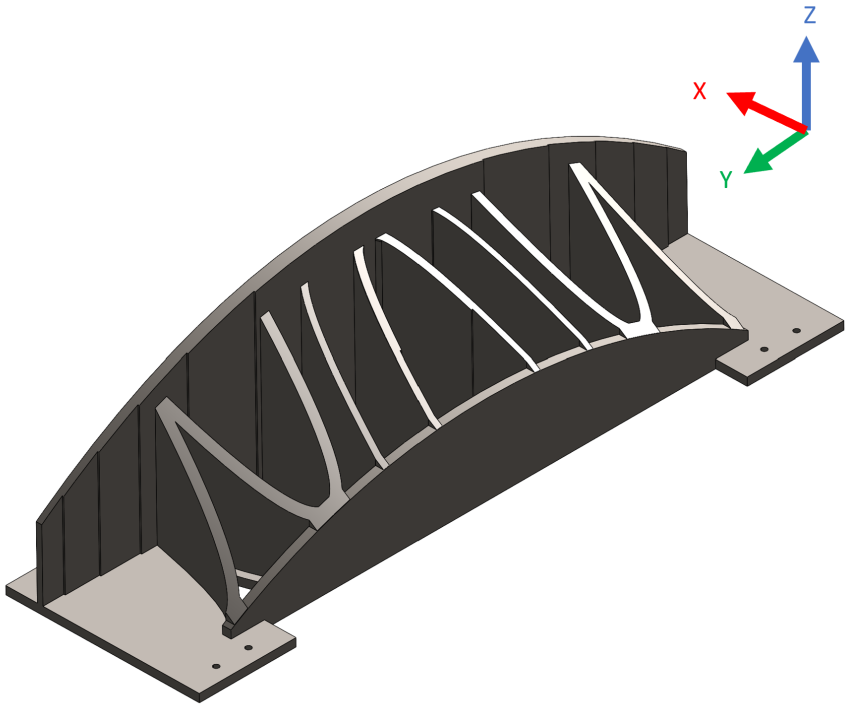

Figure 4.3: Back isometric view of the finalized WAAM design.

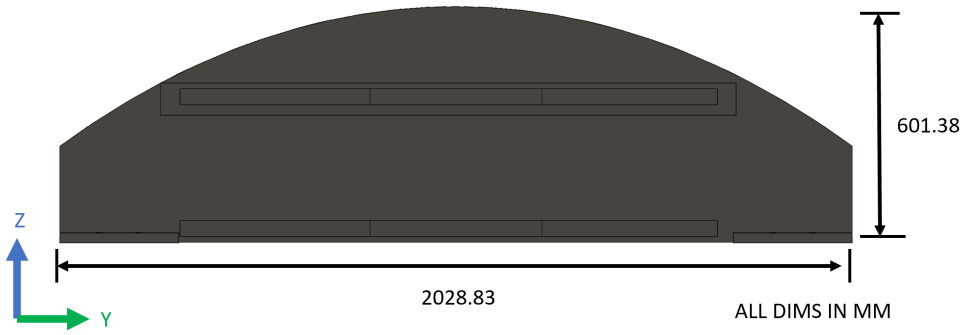

Figure 4.4: Front view of the finalized WAAM design.

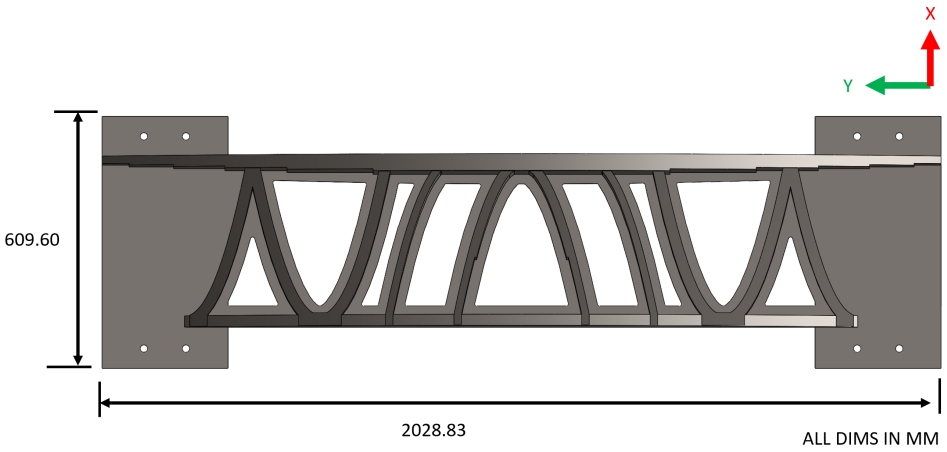

Figure 4.5: Top view of the finalized WAAM design.

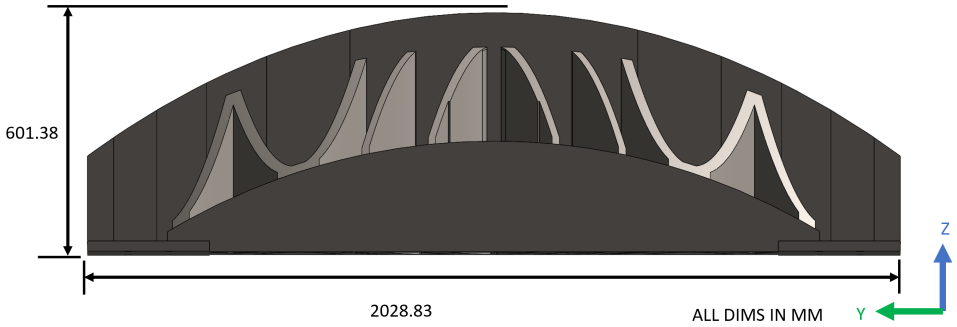

Figure 4.6: Back view of the finalized WAAM design.

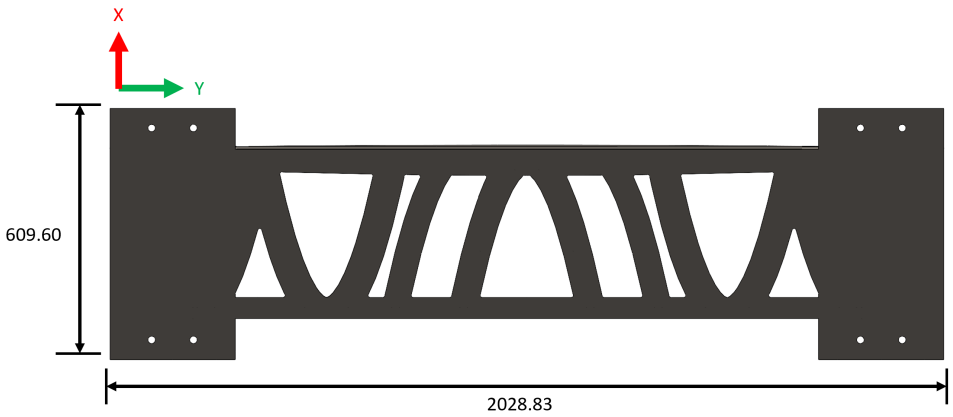

Figure 4.7: Bottom view of the finalized WAAM design.

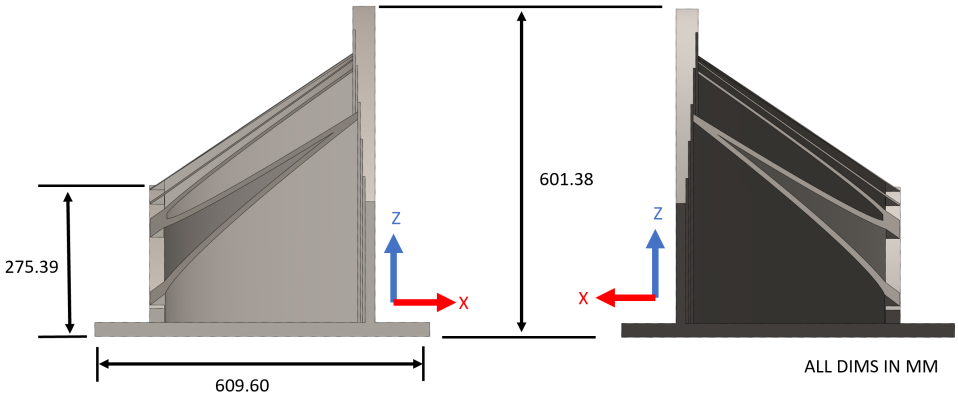

Figure 4.8: Left and right side views of the finalized WAAM design.

also providing stiffness to the structure. The curves also reduce the number of overlapping points or intersections compared to a honeycomb infill.

As seen from the sides, in Figure 4.8, the supporting walls are slanted from the front wall to the back. The front wall is also thicker in the middle and tapers as it reaches the sides of the part as seen in Figure 4.5. Both features were implemented to add mass to the areas of the WAAM cross beam that experienced some of the largest deflections to improve its stiffness while also reducing the mass by removing unnecessary material where there is no benefit to the structure's stiffness.

The base plate of the final design shown in Figure 4.7 was designed to be the build plate. However, the build plate had to be modified to be able to be secured to the build table of the MedUSA cell. The build plate was broken into five sections of 25.40 mm thick A36 steel plates that were beveled as seen in Figures 4.9 and 4.10. By splitting up the base plate into five smaller pieces, the build plate was more accessible and more cost-effective to be sourced. In addition, the separation of the build plate had the potential of allowing the individual plates to deform individually while being printed on to reduce the deformation of the entire WAAM print. The larger base plate seen in Figures 4.11 and 4.12 provided a clamping border around the base which will later need to be removed and welded together to stitch the separate plates into one. The clamping border was added to constrain and hold down the part during the print.

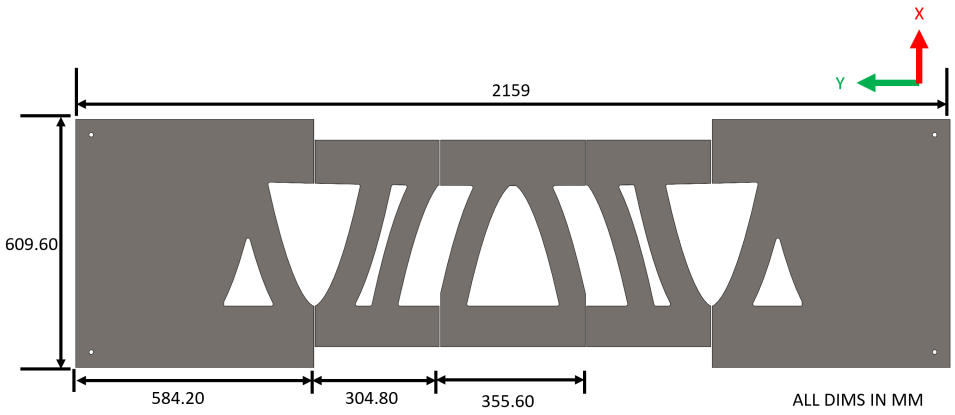

Figure 4.9: Top view of the separated and larger A36 steel build plates that are 25.40 mm thick.

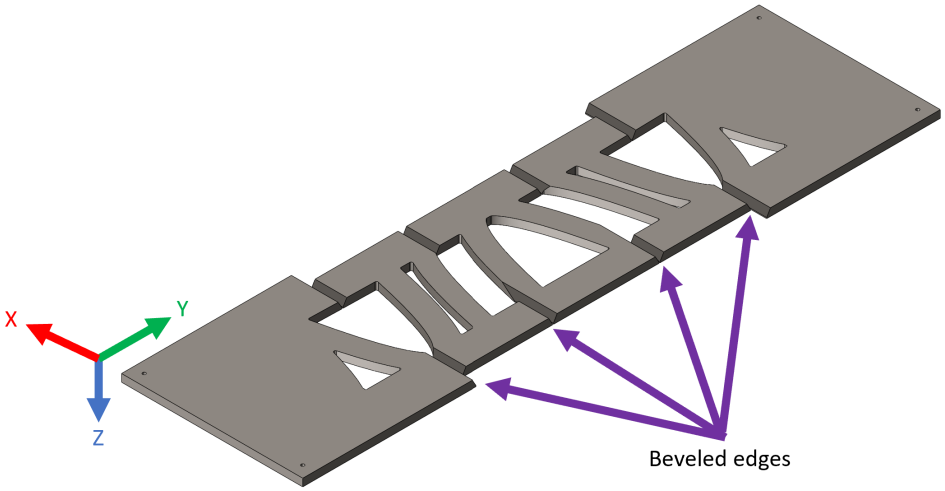

Figure 4.10: Isometric view of the bottom of the build plates with the beveled edges.

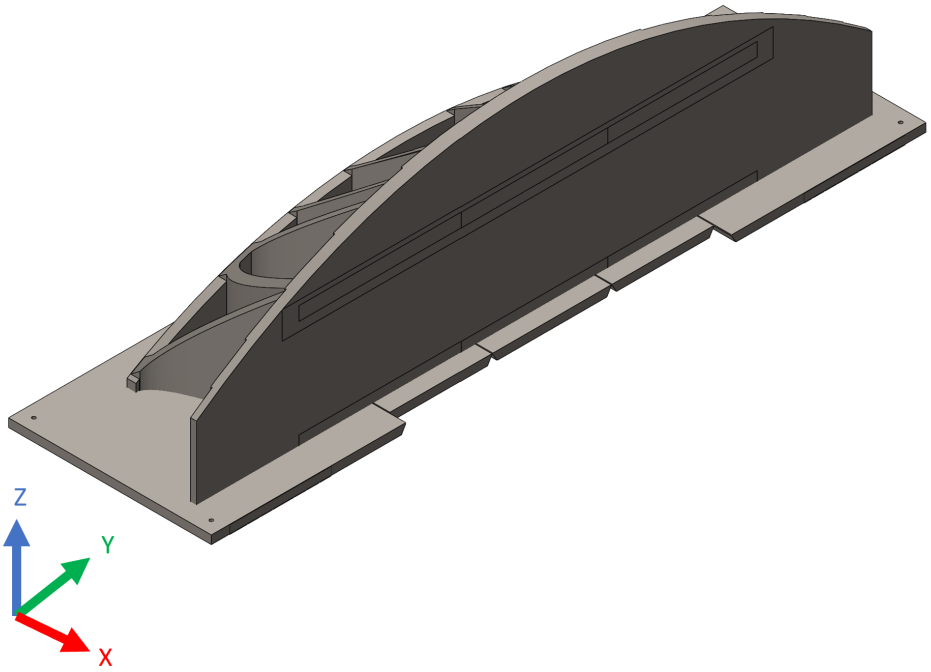

Figure 4.11: Isometric view of the final design with the new build plate.

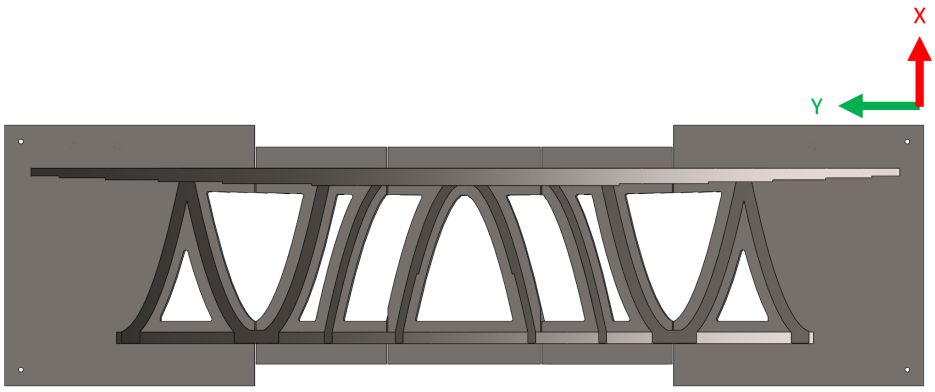

Figure 4.12: Top view of the final design with the new build plate.

4.5 Comparison of weldment and mBAAM cross beam

Both the static deflections and mass of the finalized WAAM cross beam were compared to the weldment's deflections and mass. The finalized design was modeled and analyzed with the same methods outlined in Section 3.2.2. Table 4.1 provides the material property values used for LA-100. Figures 4.13 through 4.18 are the centered configurations of the forces applied to the final design. The same configurations were applied to the offset rail locations. The same 12 simulations that were done to the WAAM cross beam were completed to quantify the deformation of the final design. Figures 4.19 through 4.30 showcase the resultant WAAM deformation. From these simulations, the max deflections of the top and bottom rails were extracted. The extracted values were separated into the principal directions along the X-, Y-, or, Z-axis.

The results of the deflection calculations are provided in Table 4.2. The two main configurations were the column locations at the center versus at the end of the travel. The contributions of each force are isolated and rounded to the nearest micrometer. Also, both the top and bottom rail maximum values were recorded because they give insight into the column's behavior as a beam and how it moves such as nodding of the column.

Table 4.3 shows the difference in magnitude between Tables 4.2 and 3.4. Subtracting the magnitude of the maximum deflections of the weldment from the WAAM cross beam results is the deflection difference between the two designs. A negative value result indicates that the WAAM structure deflected less than the weldment which is an improvement. A positive value result indicates that the WAAM structure deflected more than the weldment which is not an improvement. It was decided differences that were -1 μm through 1 μm were deemed acceptable for the performance of the final design. For Table 4.3, a color code was generated where

Table 4.1: Material properties for LA-100 steel

Property	**Value**	**Unit**
Elastic modulus	1.90×10^{11}	$\frac{N}{m^2}$
Poisson's ratio	0.29	-
Mass density	7.80×10^{3}	$\frac{kg}{m^3}$
Tensile strength	7.90×10^{8}	$\frac{N}{m^2}$
Yield Strength	7.50×10^{8}	$\frac{N}{m^2}$

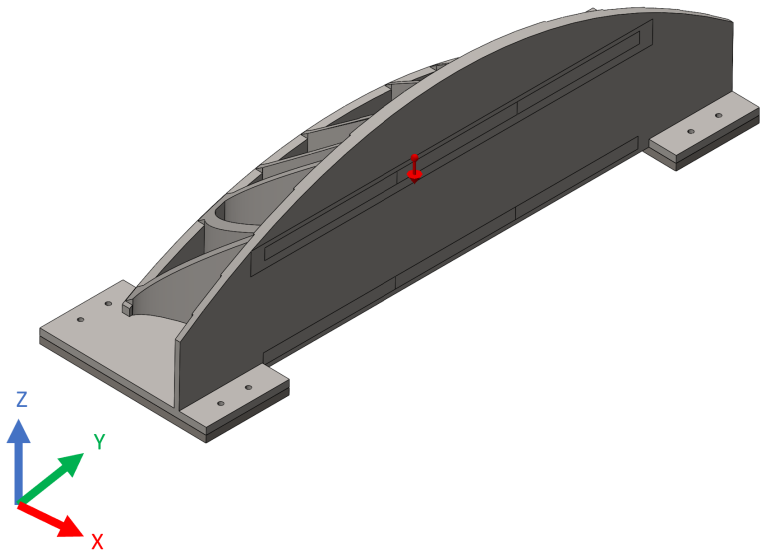

Figure 4.13: Centered configuration with red gravity vector arrow for WAAM cross beam.

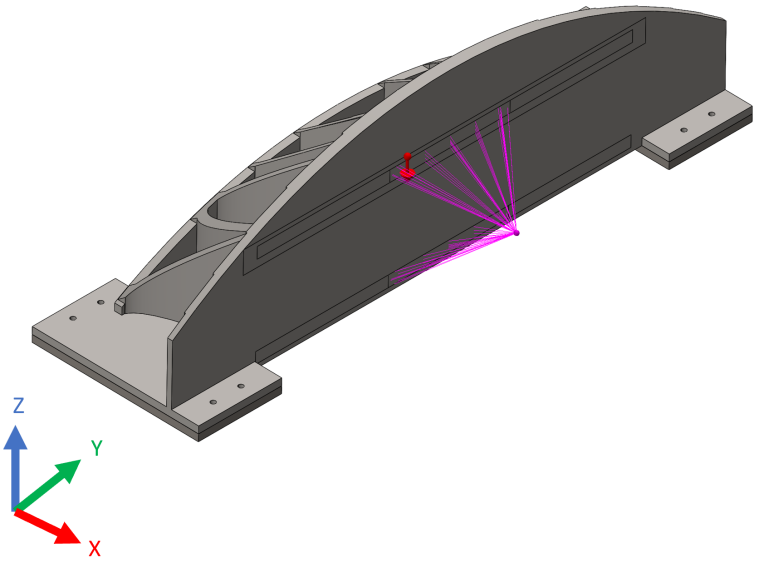

Figure 4.14: Centered configuration with red gravity vector arrow with the remote mass attached via rigid connections for WAAM cross beam.

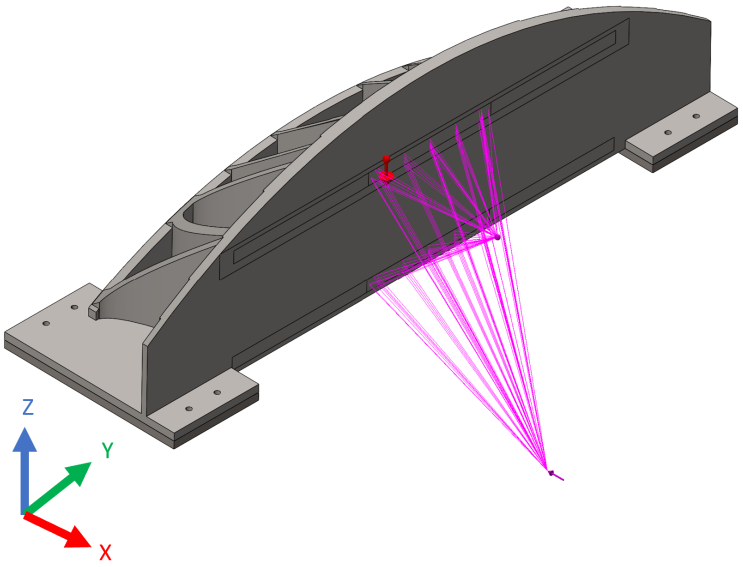

Figure 4.15: Simulation of WAAM cross beam in the centered configuration along with a remote X-cutting force in the -X direction.

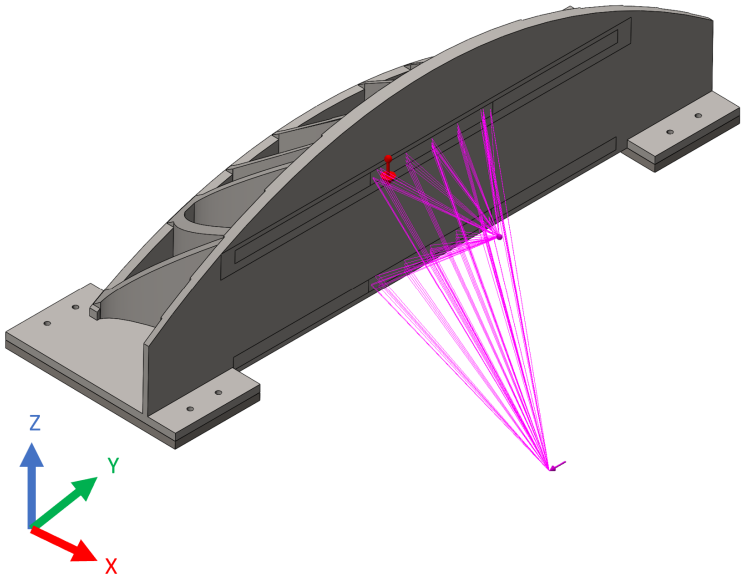

Figure 4.16: Simulation of WAAM cross beam in the centered configuration along with a remote Y-cutting force in the -Y direction.

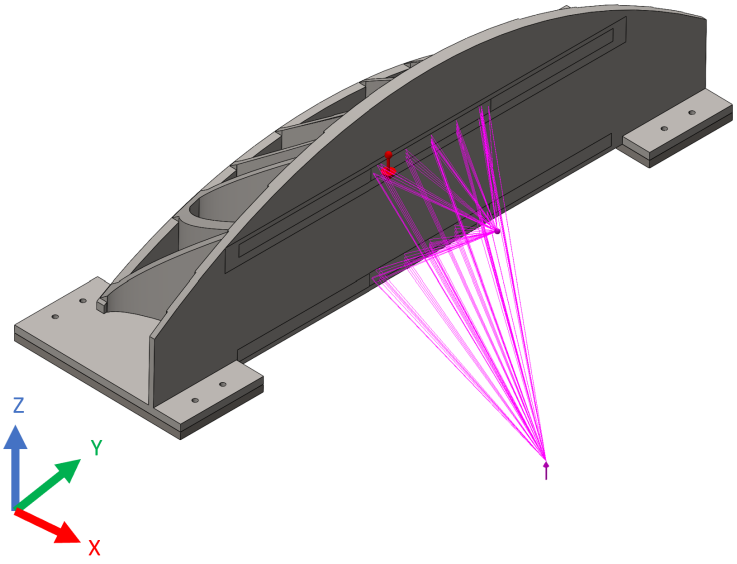

Figure 4.17: Simulation of WAAM cross beam in the centered configuration along with a remote Z-drilling force in the +Z direction.

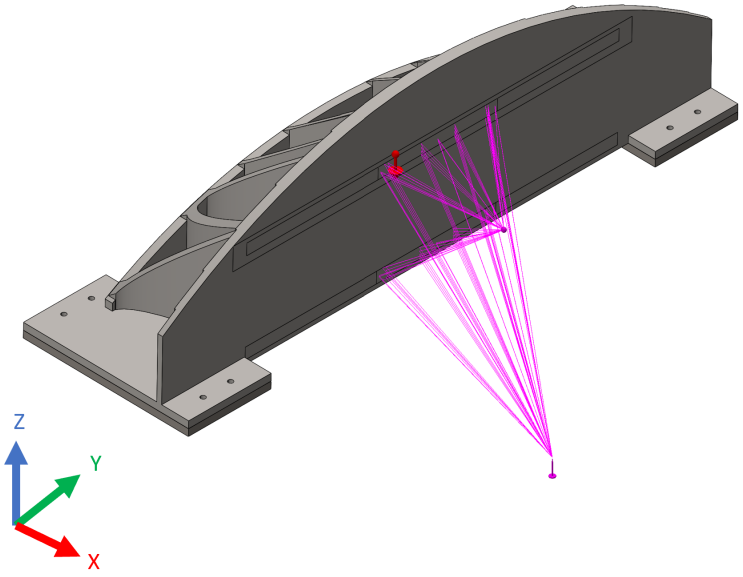

Figure 4.18: Simulation of WAAM cross beam in the centered configuration along with torque about the Z-axis of the tool tip.

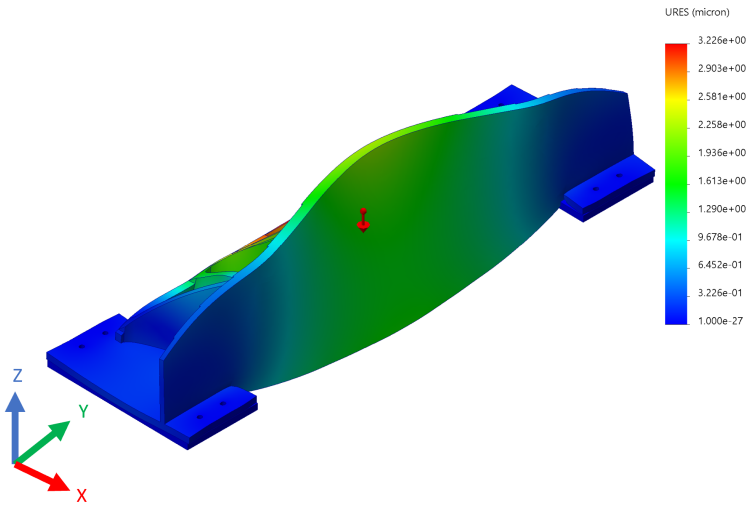

Figure 4.19: FEA resultant displacement of the WAAM cross beam in the rails centered configuration with gravity only.

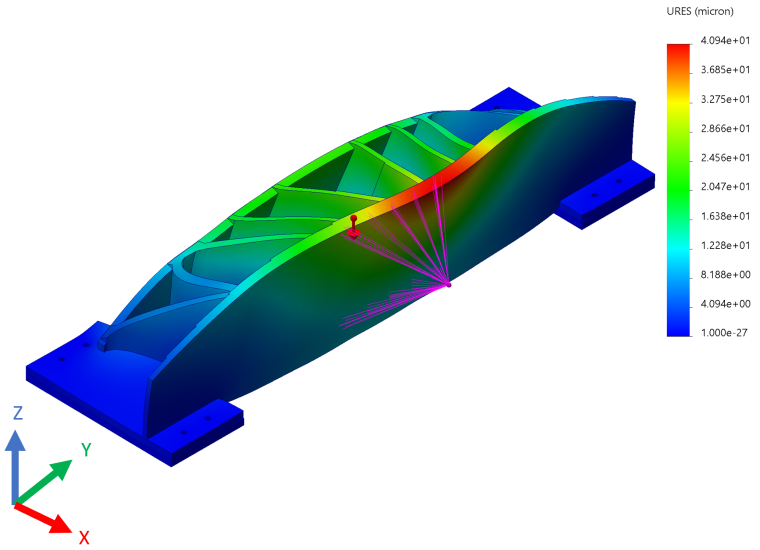

Figure 4.20: FEA resultant displacement of the WAAM cross beam in the rails centered configuration with gravity and the remote mass.

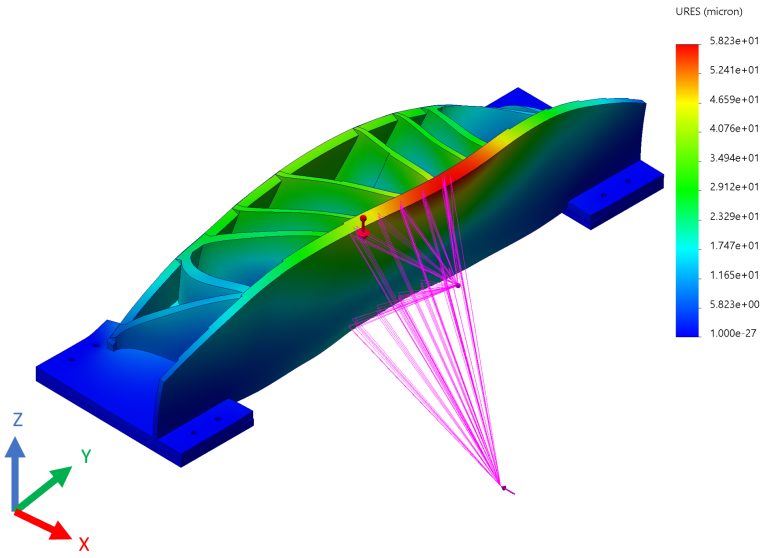

Figure 4.21: FEA resultant displacement of the WAAM cross beam in the rails centered configuration with gravity, remote mass, and X-cutting force.

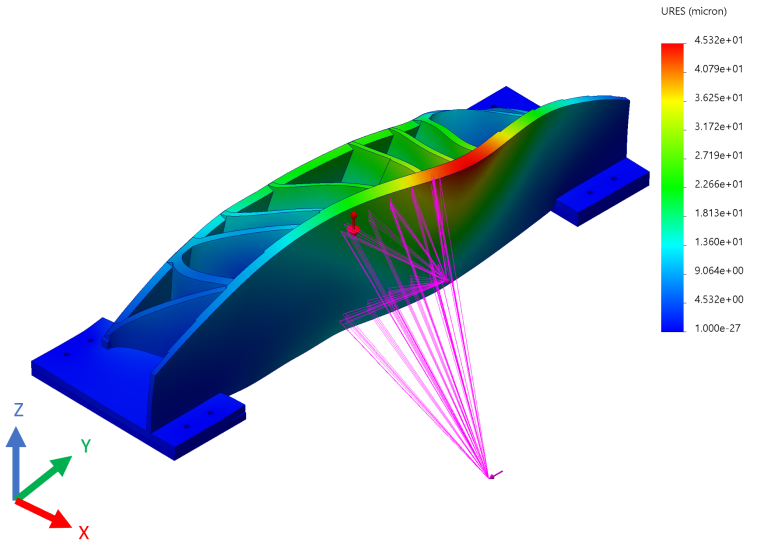

Figure 4.22: FEA resultant displacement of the WAAM cross beam in the rails centered configuration with gravity, remote mass, and Y-cutting force.

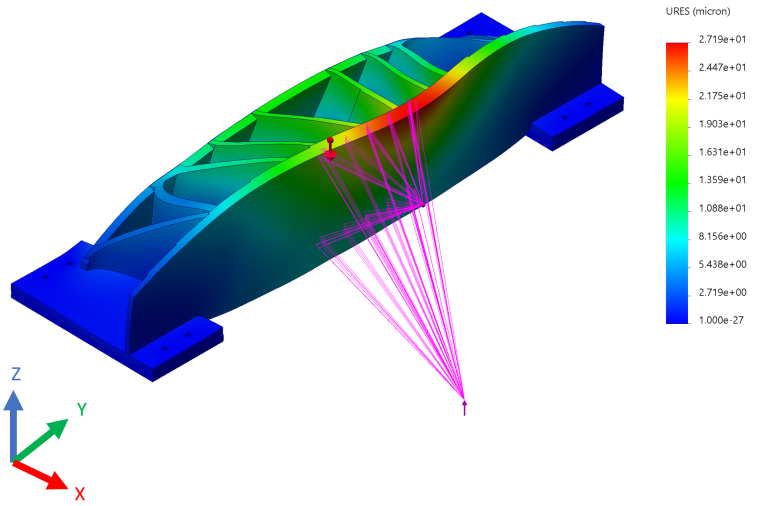

Figure 4.23: FEA resultant displacement of the WAAM cross beam in the rails centered configuration with gravity, remote mass, and Z-drilling force.

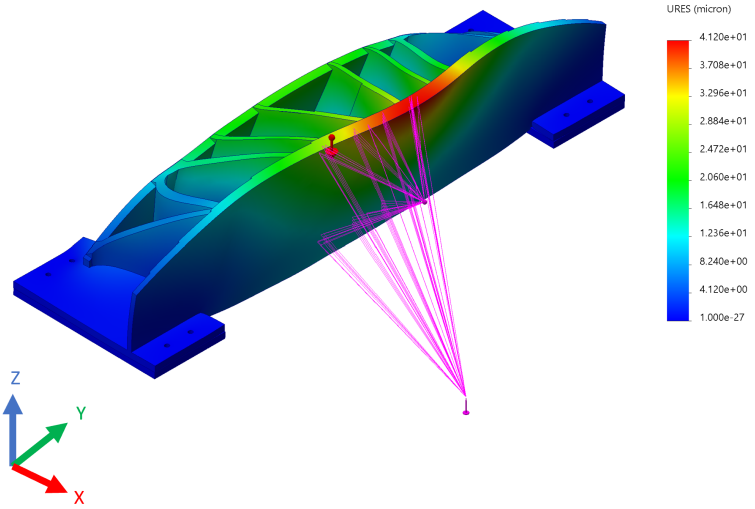

Figure 4.24: FEA resultant displacement of the WAAM cross beam in the rails centered configuration with gravity, remote mass, and torque force.

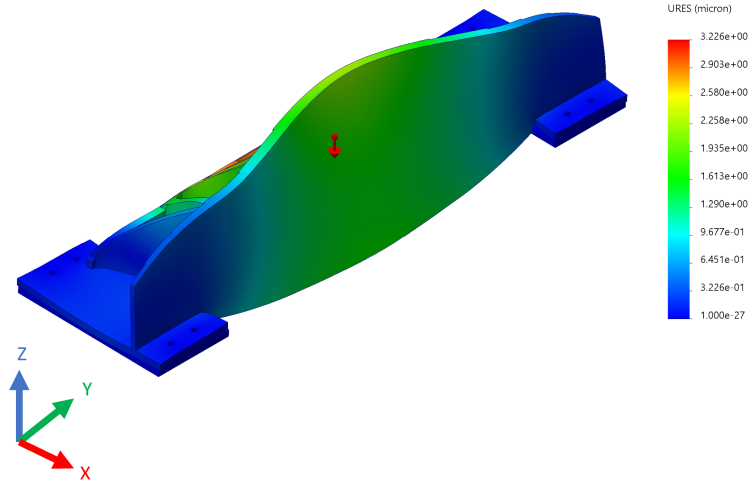

Figure 4.25: FEA resultant displacement of the WAAM cross beam in the rails offset configuration with gravity only.

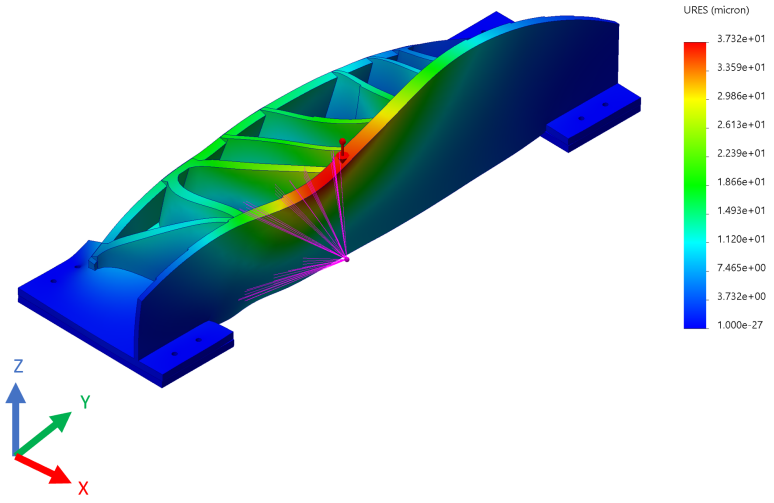

Figure 4.26: FEA resultant displacement of the WAAM cross beam in the rails offset configuration with gravity and the remote mass.

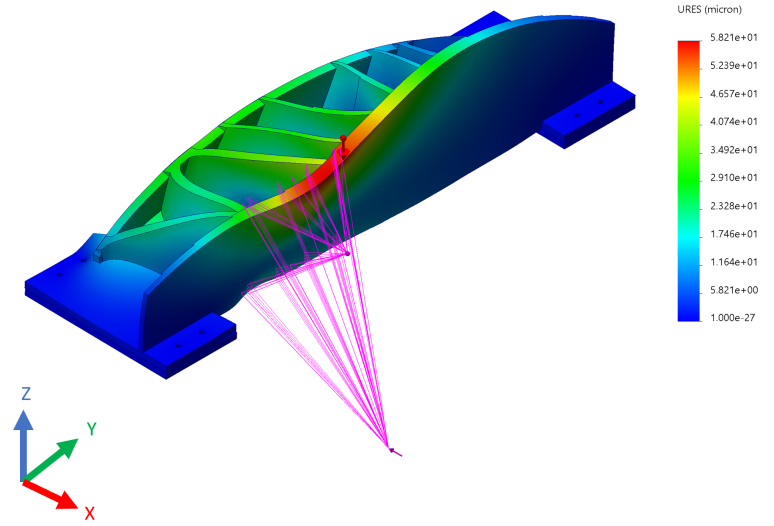

Figure 4.27: FEA resultant displacement of the WAAM cross beam in the rails offset configuration with gravity, remote mass, and X-cutting force.

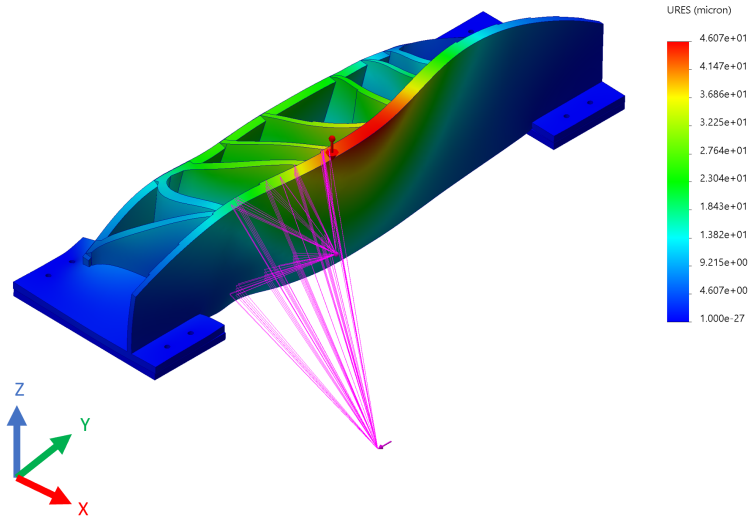

Figure 4.28: FEA resultant displacement of the WAAM cross beam in the rails offset configuration with gravity, remote mass, and Y-cutting force.

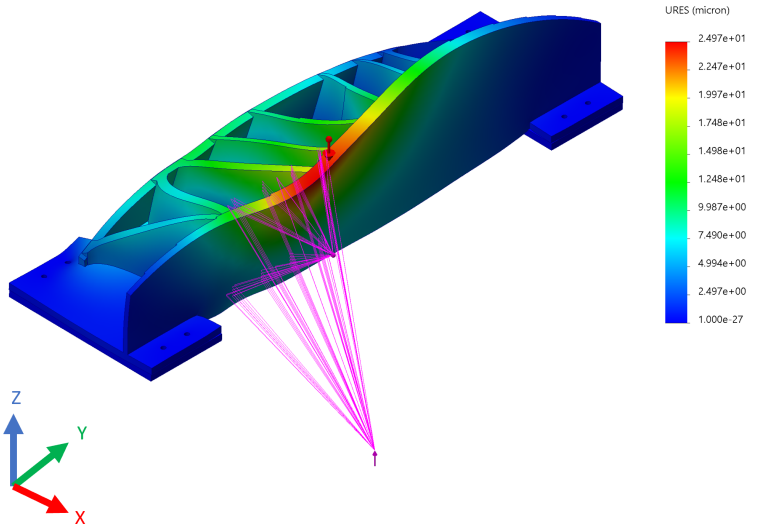

Figure 4.29: FEA resultant displacement of the WAAM cross beam in the rails offset configuration with gravity, remote mass, and Z-drilling force.

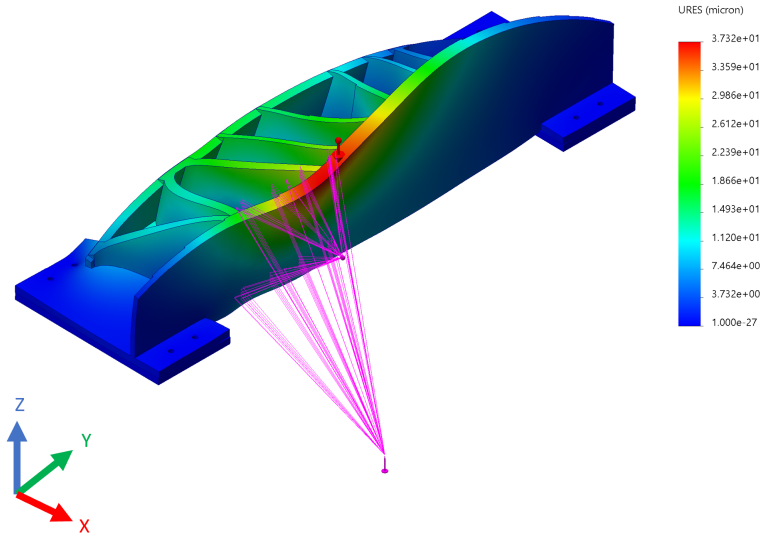

Figure 4.30: FEA resultant displacement of the WAAM cross beam in the rails centered configuration with gravity, remote mass, and torque force

Table 4.2: Summary of deflections due to various forces in various configurations for the WAAM cross beam

Rail location	Axis	Gravity contribution [µm]		Remote mass contribution [µm]		X-force contribution [µm]		Y-force contribution [µm]		Z-force contribution [µm]		Torque contribution [µm]	
		Top	Bottom	Top	Bottom	Top	Bottom	Top	Bottom	Top	Bottom	Top	Bottom
Centered	X	-1	0	24	0	7	-7	1	3	-8	0	0	0
	Y	0	0	0	-1	0	1	-1	-2	0	0	0	0
	Z	-1	-1	-9	-9	-2	-3	0	0	2	2	0	0
Offset	X	0	0	25	0	13	-2	3	7	-8	0	0	0
	Y	0	0	0	0	0	0	-1	-3	0	0	0	0
	Z	-1	-1	-8	-8	-2	-2	-1	-1	2	2	0	0

Table 4.3: Difference in the magnitude of deflection values of the WAAM cross beam and the weldment where green is acceptable, blue is an improvement, and red is not an improvement

Rail location	Axis	Gravity contribution [µm]		Remote mass contribution [µm]		X-force contribution [µm]		Y-force contribution [µm]		Z-force contribution [µm]		Torque contribution [µm]	
		Top	Bottom	Top	Bottom	Top	Bottom	Top	Bottom	Top	Bottom	Top	Bottom
Centered	X	1	0	-1	-1	-13	2	0	0	-1	0	0	0
	Y	0	0	0	0	0	0	1	0	0	0	0	0
	Z	0	0	2	2	0	0	0	-1	1	1	0	0
Offset	X	0	0	-1	0	-8	-3	2	5	-1	0	0	0
	Y	0	0	-1	0	0	0	1	1	0	0	0	0
	Z	0	0	-1	0	1	0	0	0	1	1	0	0

green indicated that the values had 1 μm deviation from the original design, red indicated that the difference was more than 1 μm, and blue indicated that the difference was less than -1 μm.

Of the total 72 deflection values, 64 configuration deflections showed an equal to or less than 1 μm deflection difference (green), three configuration deflections showed an improvement (blue), and five configuration deflections showed an increase in deflection (red). The overall deflection profile difference was deemed to be acceptable for the overall reduction in mass for the WAAM cross beam.

The original weldment had a mass of 702 kg and the final design had a mass of 673 kg. The mass difference is 29 kg. The WAAM design had a 4.13% mass reduction compared to the weldment. Thus, a similar deflection profile was able to be achieved with the reduction of mass while also being able to be additively manufactured. As a result, the reduction in mass and the similar deflection profile led to the decision of the final WAAM design.

Chapter 5

Fabrication

5.1 mBAAM printing results

The WAAM cross beam's printing started on April 4th, 2023 at the MDF. Due to the size of the WAAM cross beam, the print needed to take multiple days to complete. Instead of a continuous non-stop print, the team decided to run two print shifts each day for the print. The first shift was from 6:00 AM to 1:00 PM and the second shift was from 1:00 PM to 8:00 PM. The final WAAM cross beam model was given to the WAAM team to slice and generate tool paths for the print. Once the model was corrected and a finished path plan was generated for each layer, the print began.

Before printing, the build plates were machined and placed on the build table as shown in Figure 5.1. The WAAM team implemented a clamping strategy of placing steel step clamps around the perimeter of the part to hold down the print. Because the print was the longest print that was attempted on MedUSA, the WAAM team developed end clamps made from 25.40 mm thick A36 steel. Four end clamps were used to secure the four corners of the print as seen in Figure 5.2.

With the secured build plate, the three robotic arms began printing the WAAM cross beam. Figures 5.3 through 5.18 showcase the progression of the print. The initial layers of the print were the slowest printed layers. The slower print speed for

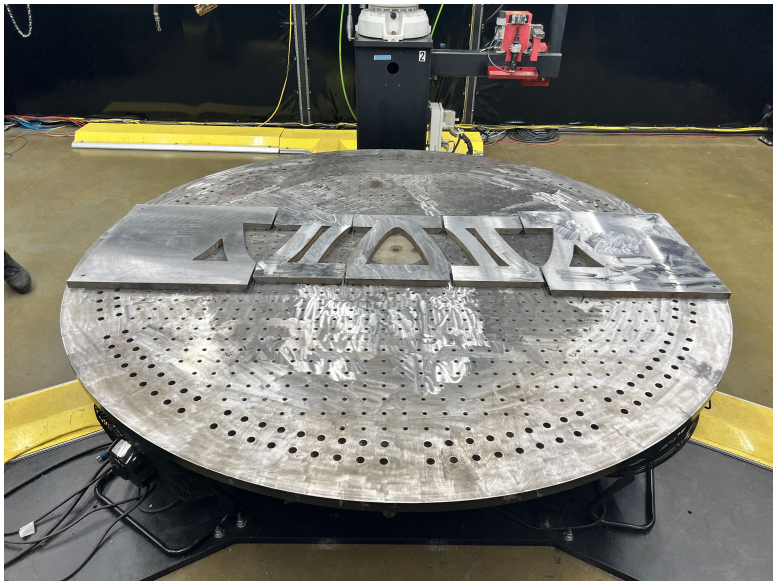

Figure 5.1: The five separate build plates placed on the print table of the MedUSA system.

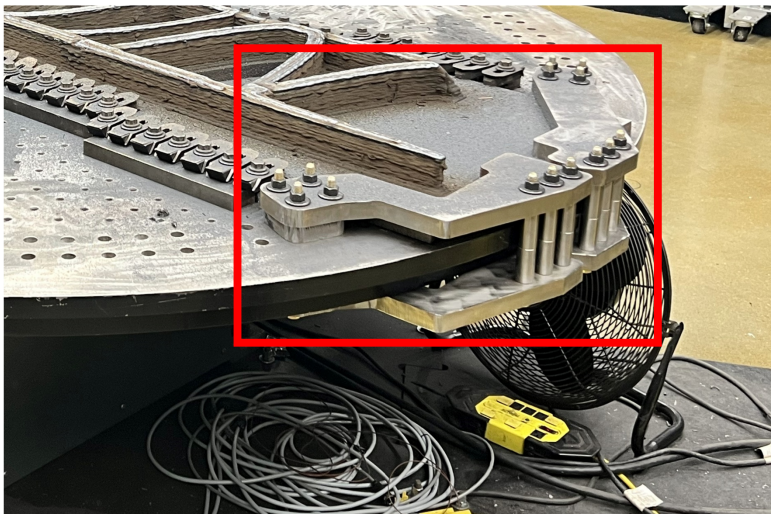

Figure 5.2: Two end clamps highlighted in the red box held down one end of the printed part.

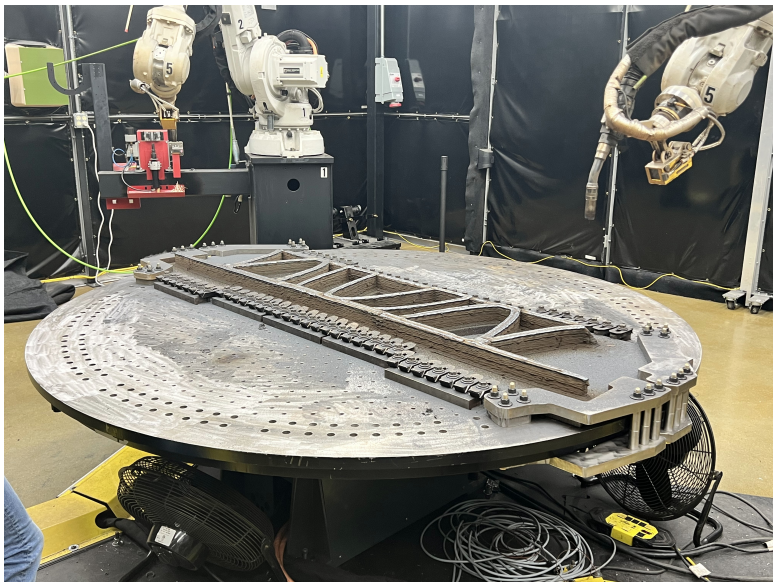

Figure 5.3: Isometric front view of the WAAM cross beam's initial layers.

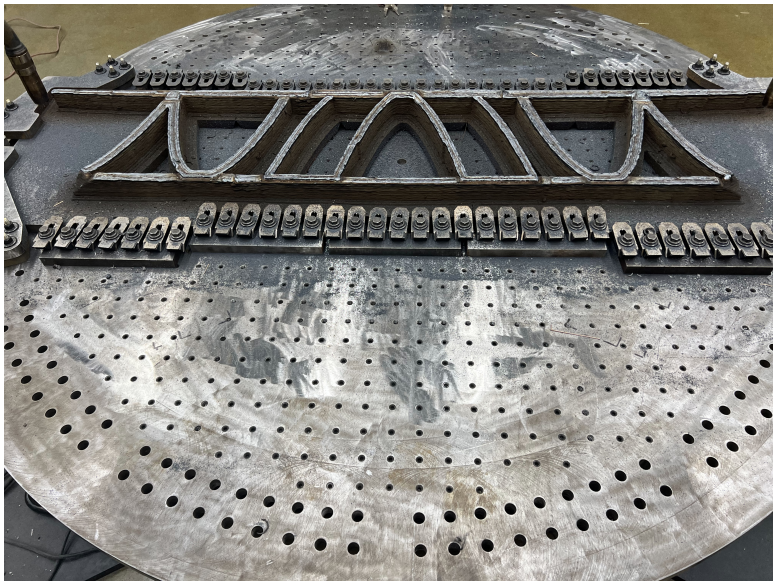

Figure 5.4: Back view of the WAAM cross beam's initial layers and the step clamps can be seen around the outer perimeter of the print.

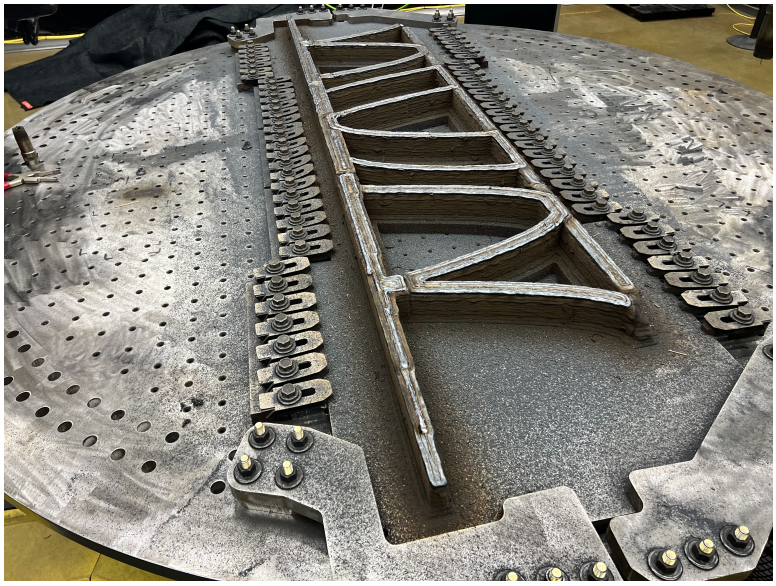

Figure 5.5: Corner view of the WAAM cross beam's initial layers.

Figure 5.6: Side view of WAAM cross beam initial layers with the front step clamps.

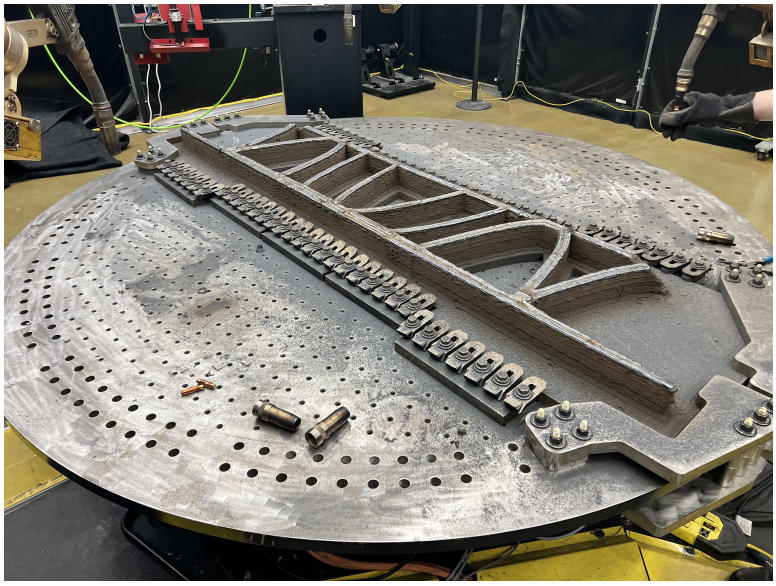

Figure 5.7: Isometric front view of the WAAM cross beam's print progress 2.

Figure 5.8: Side view of WAAM cross beam's print progress 2

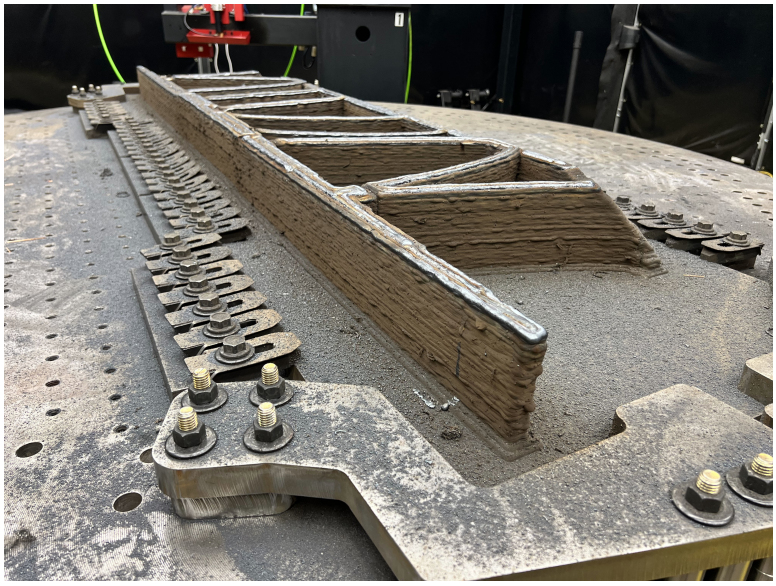

Figure 5.9: Corner view of the WAAM cross beam's print progress 2

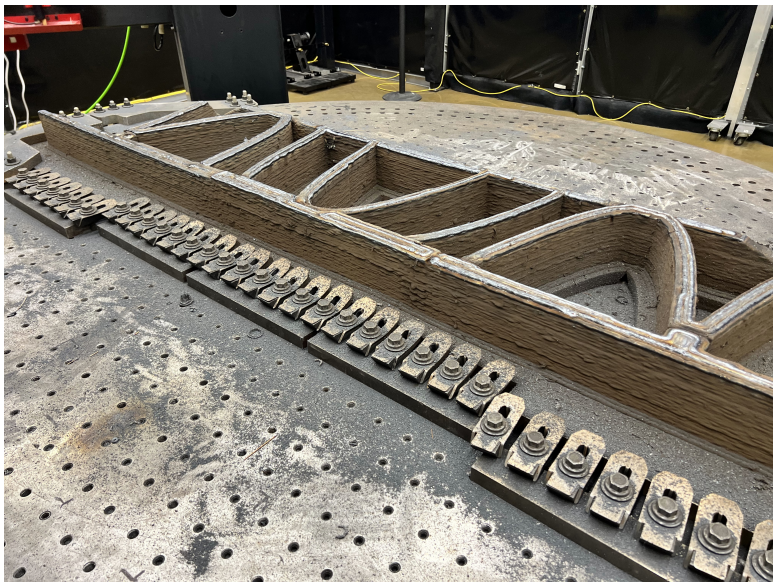

Figure 5.10: Front view of WAAM cross beam's print progress 2

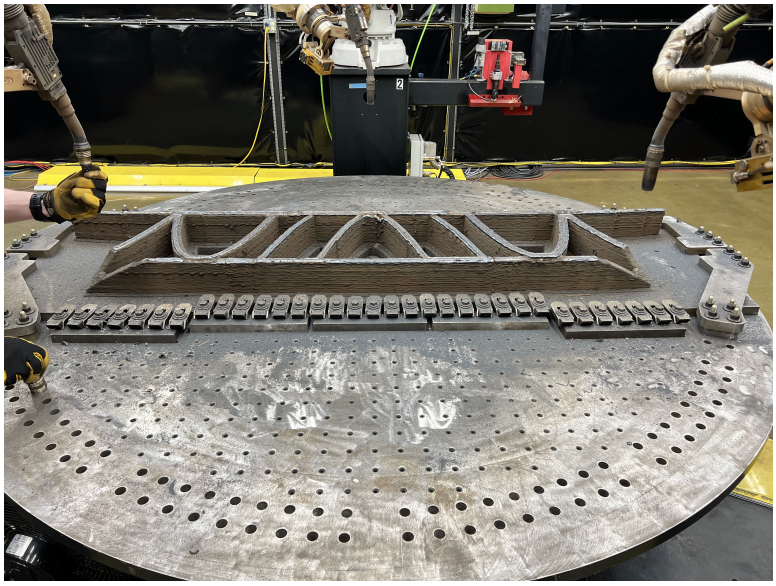

Figure 5.11: Back view of WAAM cross beam's print progress 2

Figure 5.12: Top view of WAAM cross beam's side print progress 2

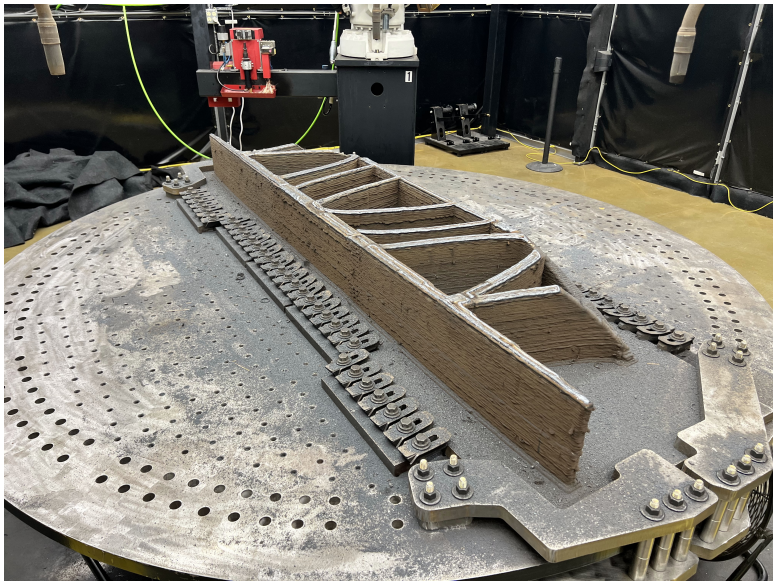

Figure 5.13: Isometric front view of the WAAM cross beam's print progress 3.

Figure 5.14: Front view of WAAM cross beam's print progress 3.

Figure 5.15: Isometric back view of the WAAM cross beam's print progress 3.

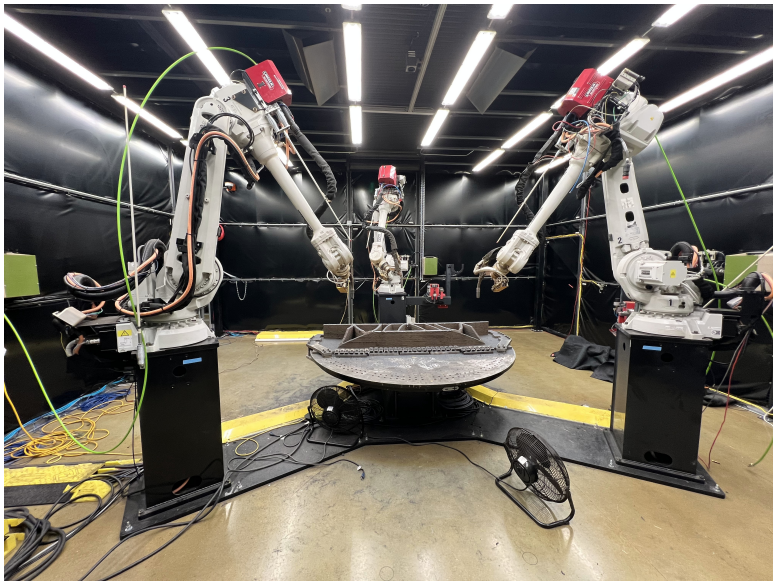

Figure 5.16: Far back view of WAAM cross beam's print progress 3 with the MedUSA system.

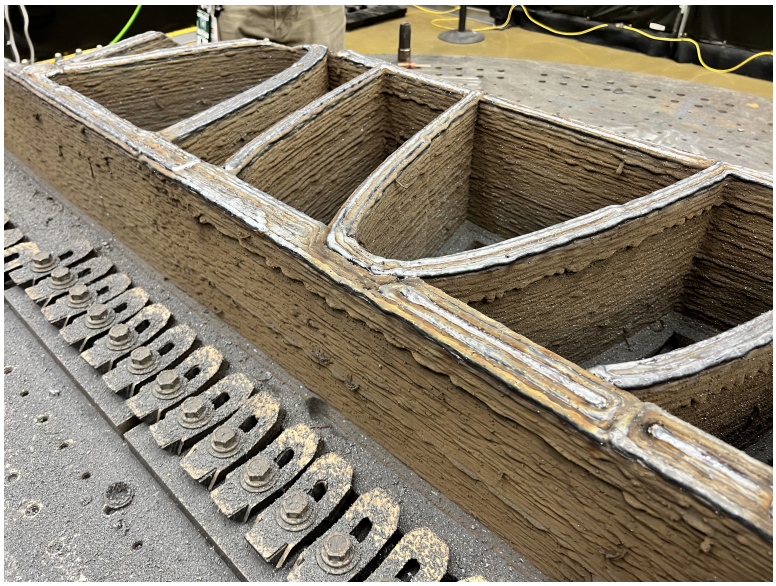

Figure 5.17: Front top view of the WAAM cross beam's print progress 3.

Figure 5.18: Isometric view of the WAAM cross beam when stopped, on the build table.

the initial layers was to ensure heat and material generation into the build plate. As the print progressed, the layer time was reduced because of the tapered design of the WAAM cross beam.

After six days of printing, the print was stopped. The printed structure initially broke all of the step clamps throughout the print. However, the end clamps were more robust than the step clamps and did not break. This led to the distortion of the part affecting the steel build table of the MedUSA system. As the part curved its ends upwards, the build table was bowed as well as seen in Figures 5.19 and 5.20. The distortion of the edges was approximated to be greater than 25 mm. Due to safety concerns, the project was stopped at the state shown in Figure 5.18. The part was later removed from the build table.

The WAAM cross beam print ended with no plans of continuing or restarting. The completed portion of the WAAM print had 245 completed layers and reached a height of 330 mm. The printed part was short by 271 mm. Approximately 406 kg of metal was deposited for the printed part. The remainder of the part was estimated to be about 122 kg. Using mass as an estimate, the part was 77% complete.

5.2 Residual stress and fixturing issues

The print was stopped due to significant deformation of the part which also deformed the build table. Once the print was stopped, the WAAM print was reviewed to understand what may have caused the print to deform as well as what should be done for future mBAAM parts. The major factors that contributed to the deformation of the WAAM cross beam were split into factors from the design, build plates, fixturing, print strategy, and thermal behavior as well as a few miscellaneous factors.

The design of the cross beam structure could have contributed to the distortion of the part. Two main concerns were the aspect ratio of the part and the material choice. The cross beam's length-to-width ratio was about 1:3. This shape led to a long narrow print that could have magnified the bowing distortion in the long axis.

Figure 5.19: Side view of the WAAM cross beam when stopped with the bowed build table.

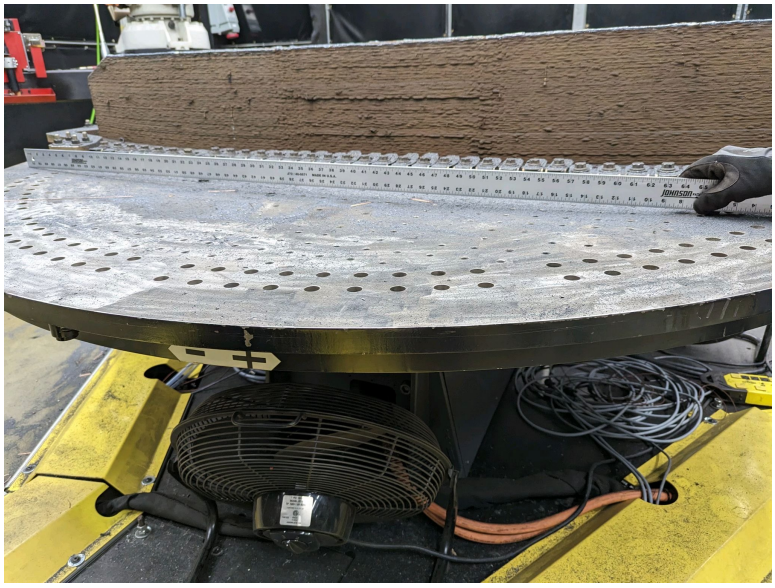

Figure 5.20: Front view of the WAAM cross beam when stopped with a gap between the middle of a straight edge and the table.

The material choice for this print was LA 100 which is a proprietary wire that is from Lincoln Electric. The material had a strong tensile strength, and this leads to more distortion compared to weaker steels. It has been observed that the distortion is significant enough that previous prints have ripped off their build plates. For this print, the material did not rip off the build plate due to the addition of a raft to the base. The raft consisted of initial layers that were larger than the print's dimensions which aided in the bonding of the structure to its base.

The build plates for this print were segmented to allow the plates to have some room for distortion and expansion to alleviate the overall distortion of the part. This was the first time a segmented build plate was implemented for a mBAAM print at ORNL. In addition, the interfaces between the plates were beveled. The beveled edges were for post-welding the underside of the cross beam. It is unsure whether the segmentation and beveled edges played a significant role in the distortion of the part or not. Because of the scale of the part along with the amount of total distortion, it is hard to isolate the contribution of the build plate design to the final part distortion.

It was understood going into the print that the part was too large for the existing table. To hold down the part, customized steel clamps were added to the exterior ends of the structure to accommodate the large structure. In addition to the large edge clamps, several smaller clamps were added along the edges of the part. The reasons for the numerous clamps were to ensure the flatness of the build plates, provide good electrical and thermal contact with the table, and allow for the welded material to yield internally due to the internal stress. Both the large steel end clamps and the build table were the main reasons for the stop print. The table was deemed to be plastically deformed along with the edge bolts being loaded close to yielding as seen in Figure 5.19. One of the biggest unknown factors for the print deformation is whether the part should be over-constrained to allow for the internal stresses to potentially yield via traditional welding knowledge experience, or just allow the part to deform on its own and compensate for the distortion as the part is built. The part may have

deformed without damaging the build table if dynamic clamps were implemented. Dynamic clamping entailed a fixturing method that can change the amount of force or deflection it has due to the change in the part geometry.

To alleviate the distortion and plastic deformation of the build table, a more robust table could have been implemented. However, a larger build table does not eliminate the internal stresses of the part due to the WAAM process. Thus, a more robust table can expand the capabilities of the MedUSA system, but it does not resolve the underlying issue of the part distortion.

Additively manufactured parts require the shape of the part to be sliced which then leads to a print path. There are multitudes of methods of printing each layer and the method that was made for this print was made for the three robotic welders. Multiple print heads allow for more material deposition and a higher thermal input compared to fewer print heads. However. The long-axis print beads may have contributed to more stress along the long axis which could have led to more distortion. Long-axis beads may have resulted in an overall lower temperature in the weld zone compared to shorter paths. It is worth noting that the implementation of the three robots was successful and it enabled the print to be printed significantly faster compared to a single print head strategy. With a single print head, the part would have had a larger thermal gradient and less heat input from the single torch.

WAAM print distortions are mostly attributed to the thermal behavior of the part. Due to the size and geometry of the part, the overall print base and material were at a relatively low temperature. The temperature gradient along with the start and stop of the print negatively affected the part's internal stresses and induced significant distortion. Ideally, the part should have been kept at a high temperature to allow for internal stress relief. A heated base plate or environment could have helped the print.

There are always other factors that affect the print. The major outside factor for this print was that it had to stop printing overnight. This allowed for the part to cool in addition to multiple thermal cycles which is not advantageous for metal prints. If

the part was to be printed again, it should be kept at an elevated temperature as well as printed continuously. Large unique geometry can be difficult to print via WAAM. Many factors can affect the final part and the WAAM cross beam showed significant distortion. Because there is still a large interest in mBAAM, the problems that affected the WAAM cross beam will need to be resolved to expand the capabilities of mBAAM.

5.3 Impact testing

Although the print was incomplete, Modal tap testing was used to measure the mode shapes of the printed WAAM cross beam. The final print as shown in Figures 5.21 through 5.26, was removed from the build table and impact tested with the same equipment and methodology for the weldment. The WAAM cross beam's bottom face and front face were impacted to retrieve the structural modes of the print. A new FEA model shown in Figures 5.27 and 5.28 was used to simulate the mode shapes of the printed structure.

From the FEA modal analysis, the bottom and front face mode shapes were used to select the density and grid layout of the measurement points on each surface. The force locations for the bottom and front faces are shown in Figures 5.29 and 5.30. The dimensions of the grid layout for the bottom and front faces are shown in Figures 5.31 and 5.32. The locations were then marked on the weldment as shown in Figures 5.33 and 5.34.

The weldment was suspended using an overhead crane as seen in Figures 5.35 and 5.36. The weldment was suspended upside down using rigging straps and swivel eye bolts. This support simulated free-free boundary conditions.

For the measurements, a roving hammer approach was implemented. The accelerometer was mounted at the first testing point and the direct FRF was collected as shown in Figure 5.37 for the bottom face and Figure 5.38 for the front face. The

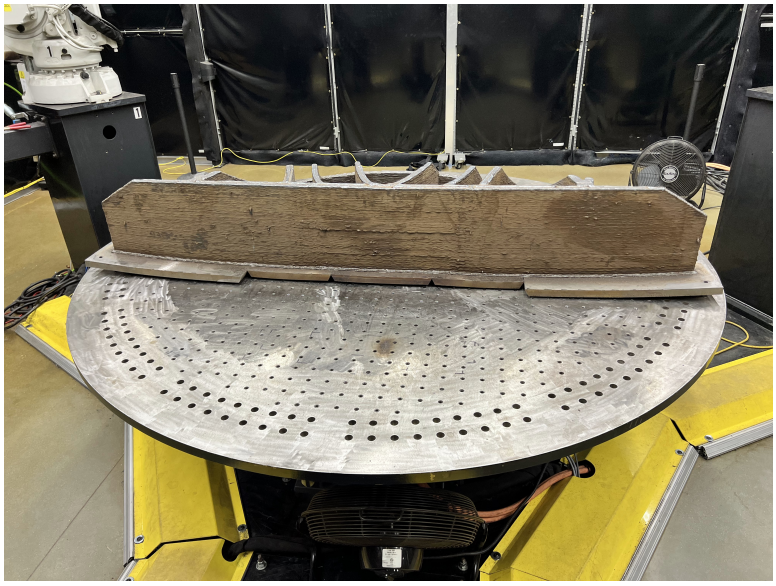

Figure 5.21: Front view of WAAM cross beam at the end of the print.

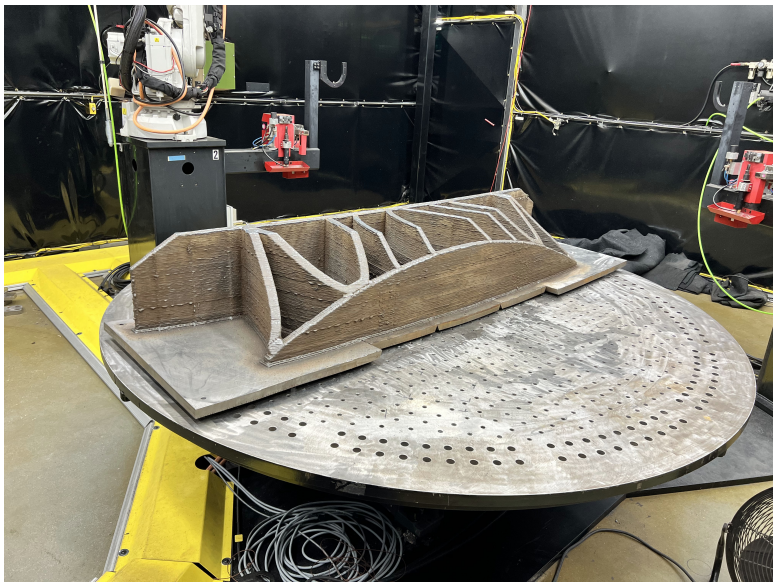

Figure 5.22: Back isometric view of WAAM cross beam at the end of the print.

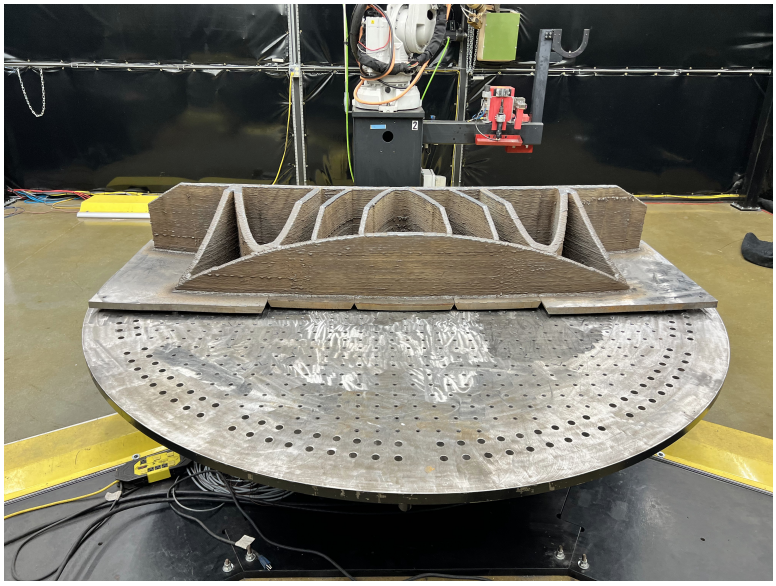

Figure 5.23: Back view of WAAM cross beam at the end of the print.

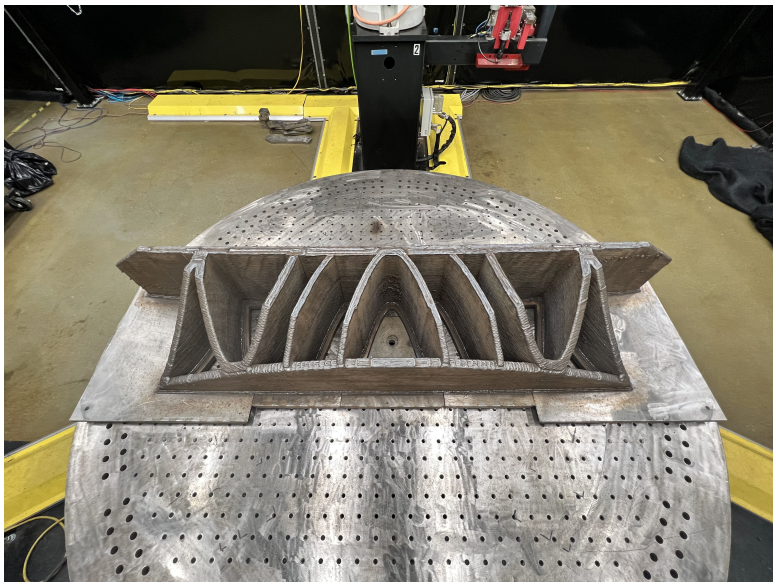

Figure 5.24: Top view of WAAM cross beam at the end of the print.

Figure 5.25: Additional back view of WAAM cross beam at the end of the print.

Figure 5.26: Corner view of WAAM cross beam at the end of the print.

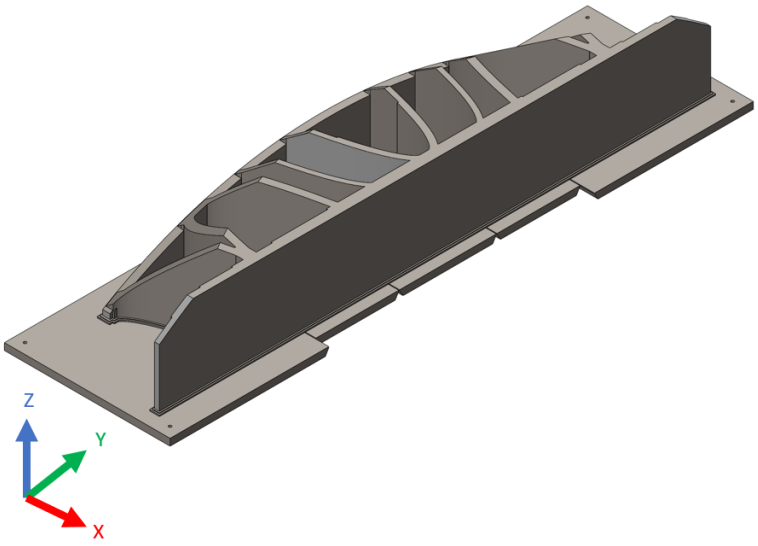

Figure 5.27: Front isometric of the new model of the WAAM cross beam when print stopped.

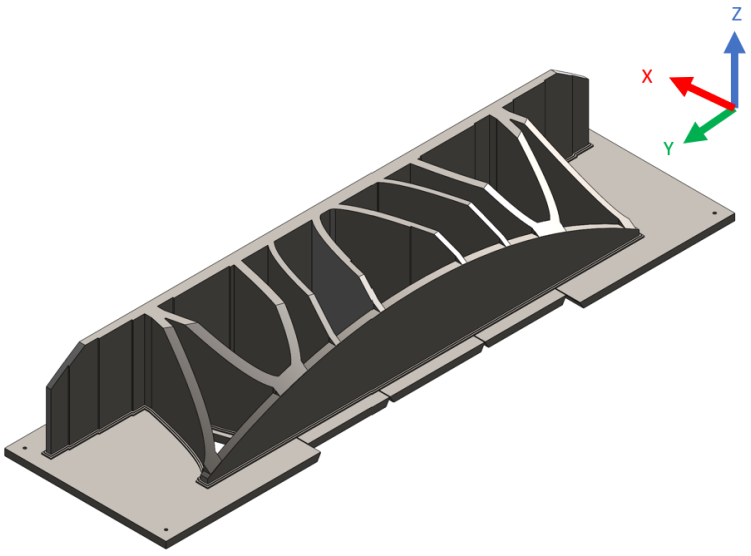

Figure 5.28: Back isometric of the new model of the WAAM cross beam when print stopped.

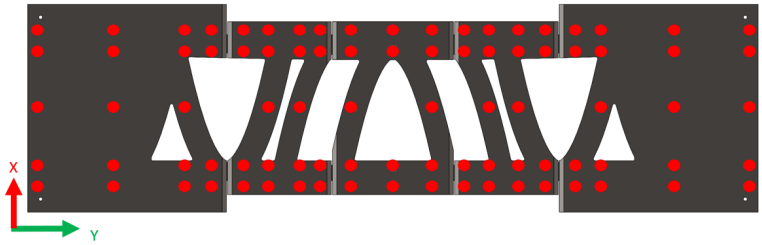

Figure 5.29: Bottom face of WAAM print with all of the impact points marked in red dots.

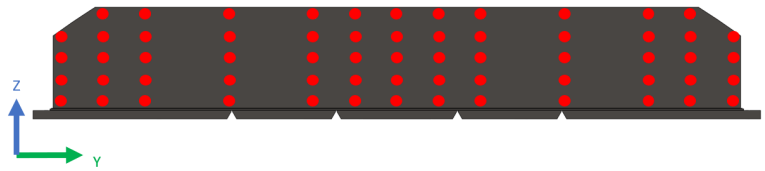

Figure 5.30: Front face of WAAM print with all of the impact points marked in red dots.

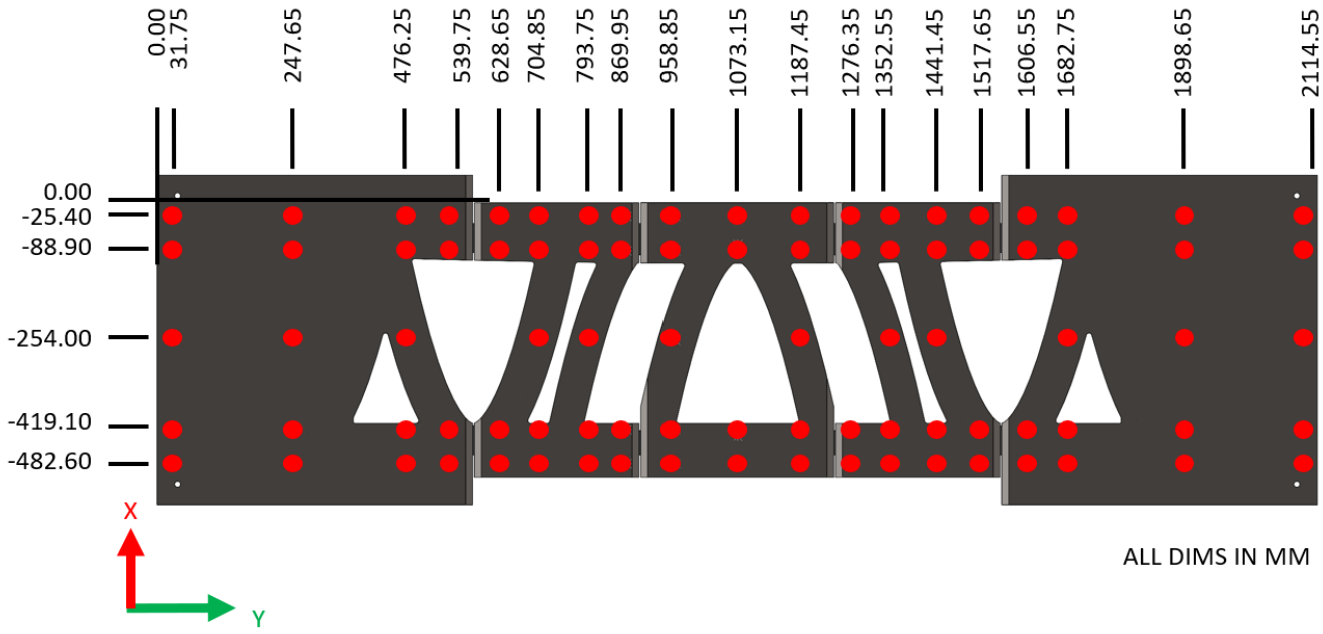

Figure 5.31: Bottom face of WAAM print with dimensions of impact points.

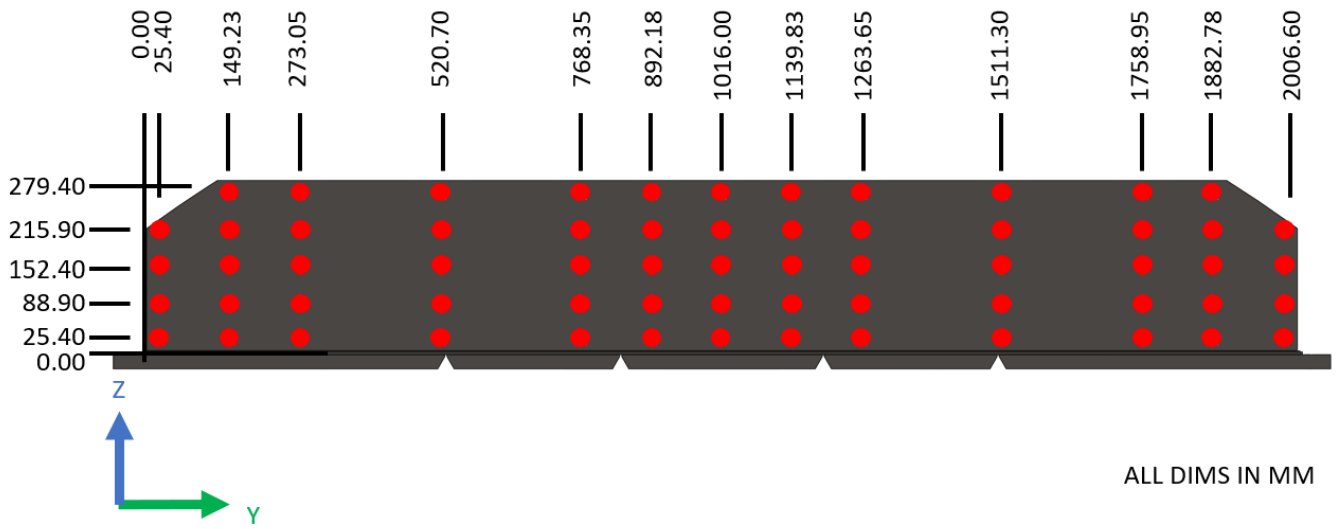

Figure 5.32: Front face of WAAM print with dimensions of impact points.

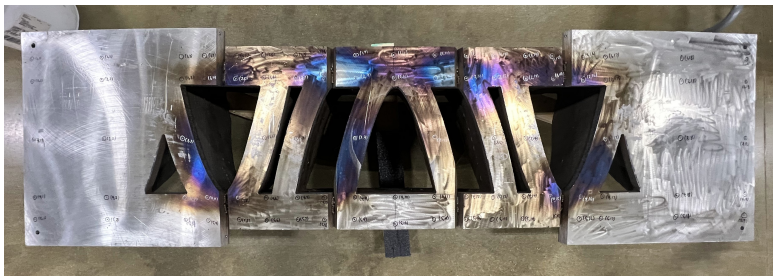

Figure 5.33: Bottom face of physical WAAM print with all of the impact points marked in black points.

Figure 5.34: Front face of physical WAAM print with all of the impact points marked in black points.

Figure 5.35: Overhead crane lifting WAAM print to establish free-free tap testing conditions.

Figure 5.36: Overhead crane lifting WAAM print to establish free-free tap testing conditions close up.

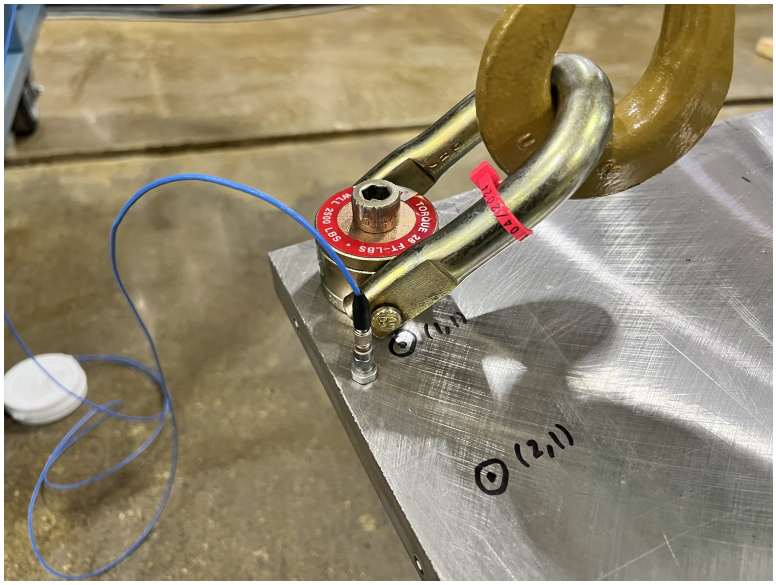

Figure 5.37: Accelerometer location of direct FRF point on the bottom face of the WAAM print.

Figure 5.38: Accelerometer location of direct FRF point on the front face of the WAAM print.

accelerometer for the bottom face remained at the X-location of -25.40 mm and Y-location of 31.75 mm. The accelerometer for the front face remained at the Z-location of 279.40 mm and Y-location of 25.40 mm. Both accelerometer locations are designated as the direct FRF location while the other points are the cross FRF locations. Each location was hit eight times to reduce noise in the measured FRFs. This was repeated for all points in Figures 5.29 and 5.30. The FRF coherence was checked to ensure that the force energy input was received by the accelerometer. The data from the tap testing was processed and saved through TXF. The TXF data was later converted to real and imaginary parts of the complex-valued FRF and plotted versus frequency. The data were processed as described in the next section to seek out mode shapes of interest.

To reference the individual points selected for impact testing, a grid coordinate system for the WAAM cross beam was assigned. The row and column values for the bottom face are shown in Figure 5.39, and the row and column values for the front face are shown in 5.40. The referred point locations will be in terms of a row value and column value. For example, point (2,1) will be associated with the point location that is in row 2 column 1. Note that both (1,1) locations are direct FRF locations.

To ensure that the weldment's impact data was accurate as well as repeatable, the concept of reciprocity was implemented to confirm that the measurement hardware and analysis were performing as expected. For the first measurement of the bottom face, the accelerometer was placed at (1,1) while the impact was performed at point (1,19). The second measurement for the bottom face was the opposite; the accelerometer was placed at (1,19) and the impact was performed at (1,1). The overlay of the real and imaginary plots of both FRFs for the bottom face is shown in Figure 5.41. For the first measurement of the front face, the accelerometer was placed at (1,2) while the impact was performed at (1,12). For the second measurement of the front face, the accelerometer was placed at (1,12) and the impact was performed at (1,2). The overlay of the real and imaginary plots of both FRFs for the front face

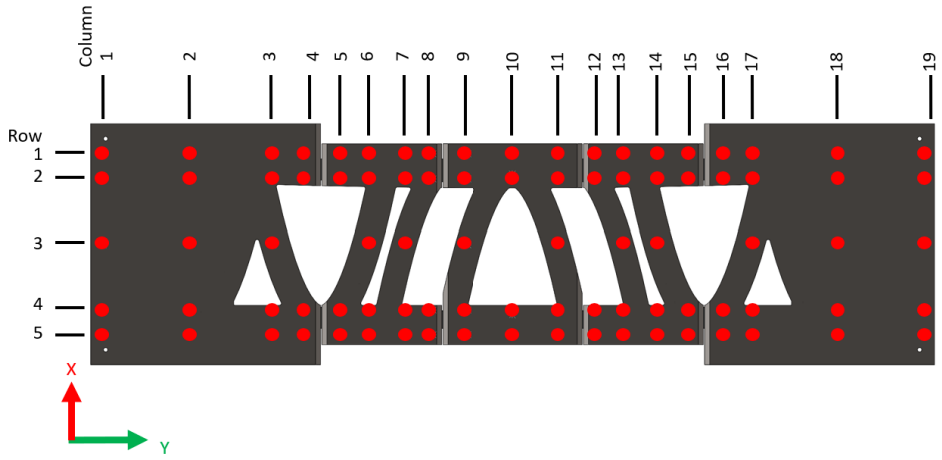

Figure 5.39: Coordinate locations for the bottom face of the WAAM cross beam.

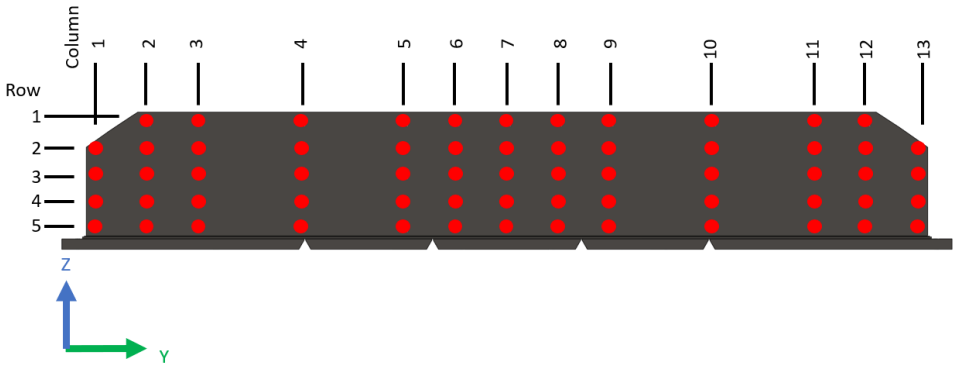

Figure 5.40: Coordinate locations for the front face of the WAAM cross beam.

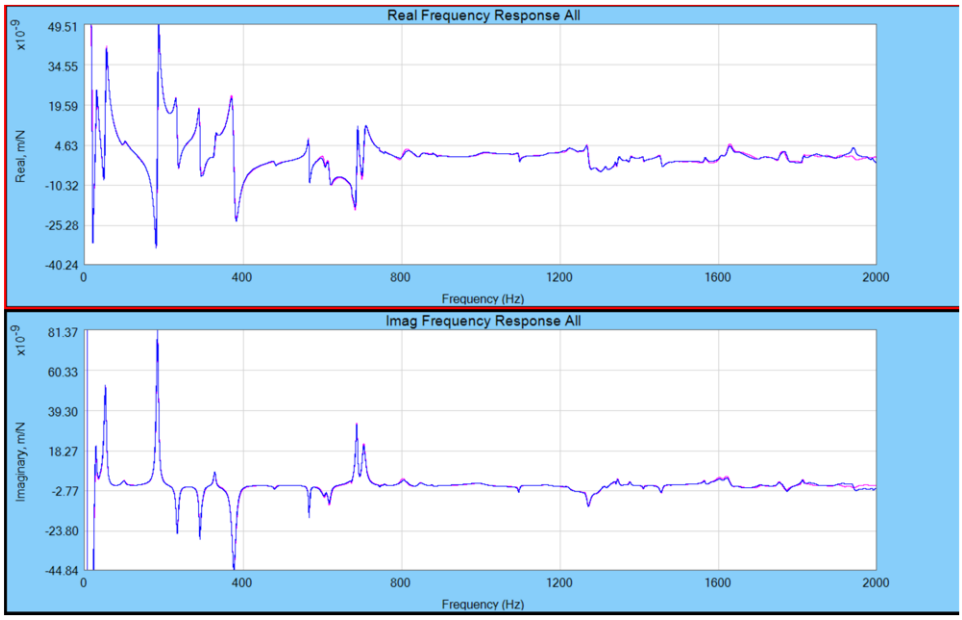

Figure 5.41: Reciprocity check of real and imaginary plots of the bottom face cross FRF points of (1,1) and (1,19) where the blue is for the first measurement and pink for the second.

is shown in Figure 5.42. The result from both plots is that the structure shows good reciprocity and that the measurements were repeatable.

5.3.1 Bottom face

To find the five modes with the largest amplitudes for the bottom face, the real and imaginary FRF plots of the top row of points in Figure 5.29 were plotted together in TXF. By looking at the amplitudes of the imaginary plot, the most flexible modes were chosen as shown in Figure 5.43. The mode shape frequencies for the bottom face that were compared were 184, 233, 291, 377, and 687 Hz. These values were extracted through peak-picking and finding the corresponding frequencies.

The approach for finding the mode shapes for the bottom surface of the WAAM cross beam is the same as finding the mode shapes of the bottom surface for the weldment. The same sequence of tables and figures is shown in the same order shown for the bottom face of the weldment. Tables 5.1 through 5.10 show the plotted points of the peak-picked values. Figures 5.44 through 5.53 showcase the plotted mode shapes of the bottom face in MATLAB as well as the FEA simulated mode shapes. The result is that the mode shapes that were from the tap testing match that of the FEA simulations. This again validates the FEA model that has been used for the frequency simulations. Table 5.11 provides the frequencies of the peak picking and simulated mode shape frequencies. The percent difference in the table was calculated with Equation 3.5. The result was that the largest percent difference was 20

Peak-picking of the mode shapes was also used to find the damping ratio and stiffness values of the five mode shapes of the bottom face of the WAAM cross beam. The real and imaginary plot of (1,1) shown in Figure 5.54 highlights the same five dynamic modes of interest. Using Equations 3.6 and 3.7, the modal damping ratio and modal stiffness of each peak were able to be calculated. The calculated values were then re-plotted as real and imaginary plots that were superimposed on top of the measured data as demonstrated in Figure 5.55 which is of mode 1. The resulting

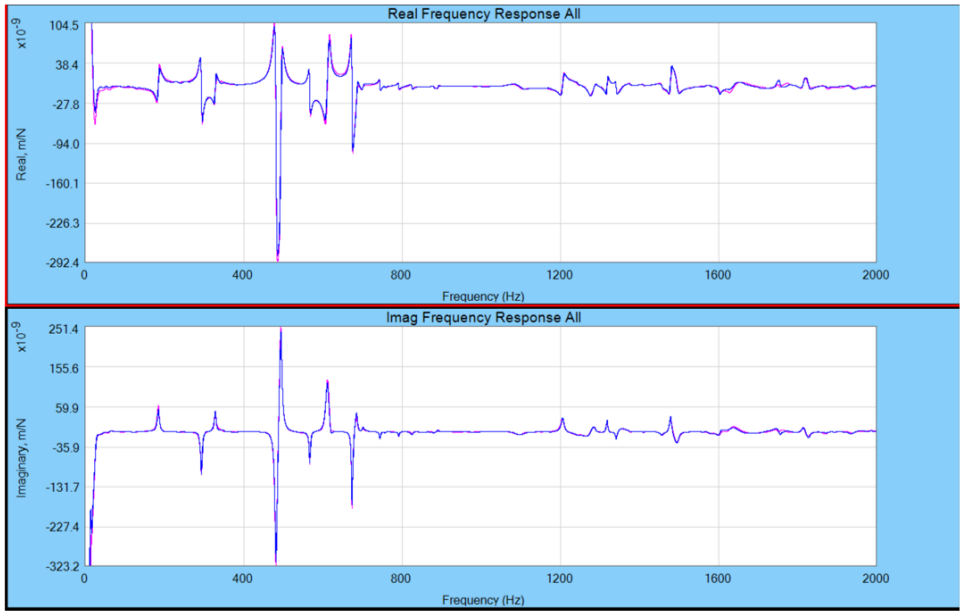

Figure 5.42: Reciprocity check of real and imaginary plots of the front face cross FRF points of (1,2) and (1,12) where the blue is for the first measurement and pink for the second.

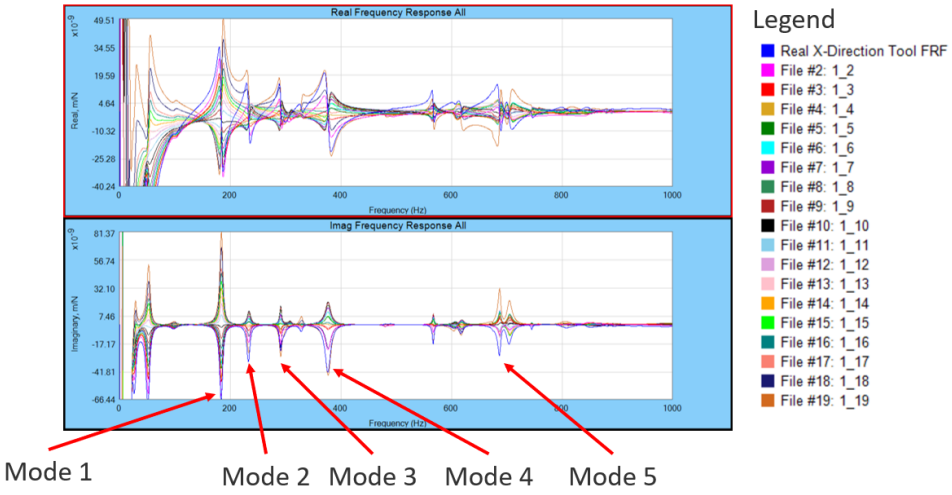

Figure 5.43: Overlay of the real and imaginary plots from the top row of points of the bottom face (1,1) - (1,19) with the chosen five most flexible modes.

Table 5.1: Peak picked values for columns 1 - 10 of Mode 1 at 184 Hz at each location of the bottom face normalized to (1,1) and scaled by -50.80

Row \ Column	1	2	3	4	5	6	7	8	9	10
1	-50.80	-48.39	-38.61	-35.98	-29.48	-26.24	-21.60	-16.09	-9.34	-1.82
2	-37.61	-34.50	-24.13	-23.05	-18.32	-16.34	-12.27	-9.04	-5.62	-1.57
3	25.90	10.14	6.83	7.17	8.21	8.44	6.94	4.76	1.83	-2.02
4	95.64	51.52	42.21	37.74	34.10	27.62	19.51	13.06	1.65	-2.58
5	123.08	68.87	56.45	53.47	41.70	34.37	24.48	16.76	7.94	-2.64

Table 5.2: Peak picked values for columns 11 - 19 of Mode 1 at 184 Hz at each location of the bottom face normalized to (1,1) and scaled by -50.80

Row \ Column	11	12	13	14	15	16	17	18	19
1	6.79	14.20	19.28	24.85	29.52	35.06	38.20	52.44	62.97
2	0.51	6.17	10.22	14.79	17.69	20.82	23.91	34.50	43.31
3	-5.62	-7.93	-9.73	-11.58	-11.92	-10.72	-8.53	-7.31	-14.70
4	-10.78	-18.01	-24.41	-31.89	-37.80	-42.28	-44.28	-51.14	-73.45
5	-12.70	-21.97	-29.79	-38.65	-45.60	-57.65	-59.82	-69.05	-93.43

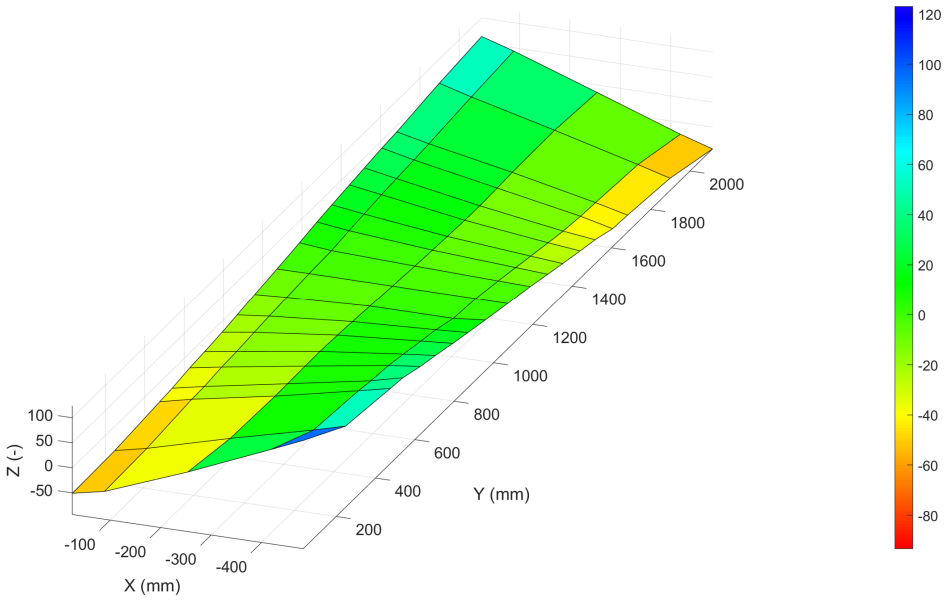

Figure 5.44: Plot of peak picked values of Mode 1 at 184 Hz at each location of the bottom face normalized to (1,1) and scaled by -50.80.

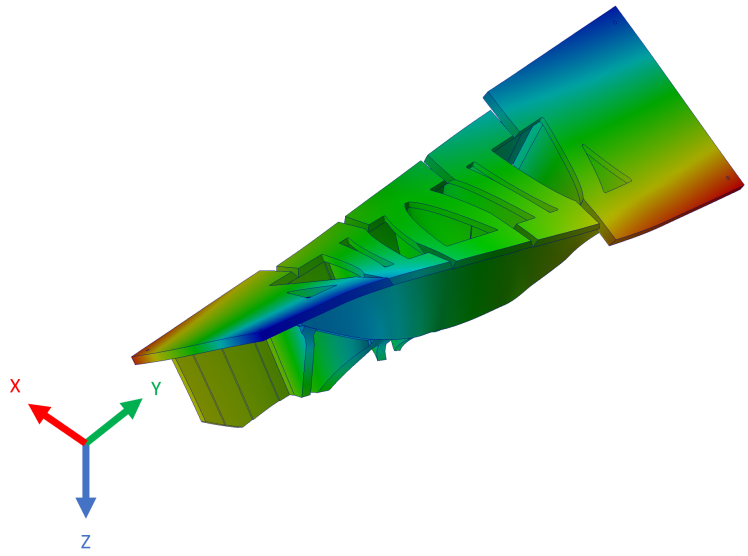

Figure 5.45: FEA simulation of WAAM print at 164 Hz which shows a similar mode shape as found in impact testing for mode 1 where the amplitude is only shown in the Z-axis.

Table 5.3: Peak picked values for columns 1 - 10 of Mode 2 at 233 Hz at each location of the bottom face normalized to (1,1) and scaled by -25.40

Row \ Column	1	2	3	4	5	6	7	8	9	10
1	-25.40	-12.75	-4.12	-1.59	1.95	4.02	5.99	7.80	8.58	9.43
2	-32.72	-14.95	-2.50	-0.33	3.47	5.54	7.91	9.47	10.34	10.93
3	-71.60	-19.49	1.68	9.15	10.49	10.88	13.55	15.19	15.52	15.30
4	-106.03	-16.31	6.26	9.39	13.83	16.35	18.30	19.80	15.45	19.66
5	-125.43	-16.98	8.33	11.74	15.79	18.40	19.99	21.46	21.74	21.75

Table 5.4: Peak picked values for columns 11 - 19 of Mode 2 at 233 Hz at each location of the bottom face normalized to (1,1) and scaled by -25.40

Row \ Column	11	12	13	14	15	16	17	18	19
1	9.33	8.84	7.77	6.25	4.34	2.22	-0.35	-8.23	-20.29
2	0.53	9.97	8.09	6.38	4.47	1.29	-0.85	-12.02	-29.85
3	14.56	13.15	10.84	8.31	8.19	6.90	-0.88	-22.18	-70.77
4	18.35	16.77	14.13	11.01	7.48	2.86	-1.01	-23.75	-106.79
5	19.71	18.17	15.63	12.17	8.45	3.15	-0.70	-25.65	-124.25

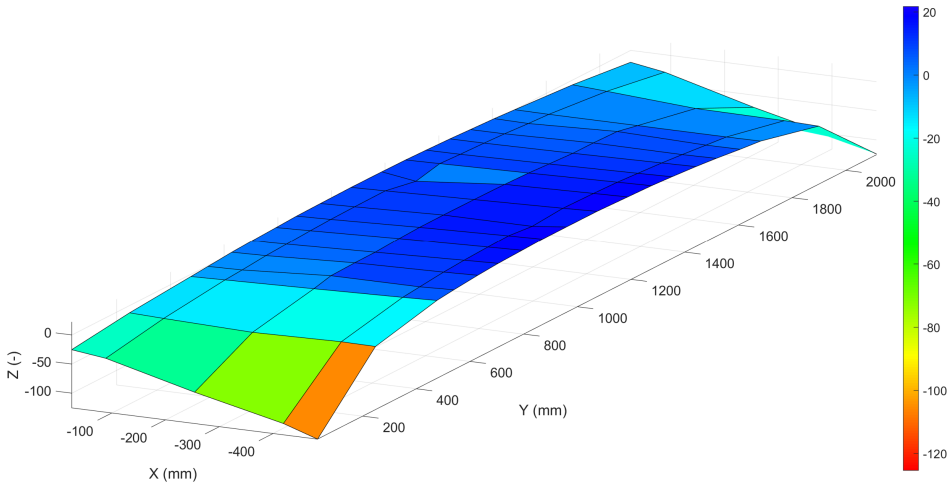

Figure 5.46: Plot of peak picked values of Mode 2 at 233 Hz at each location of the bottom face normalized to (1,1) and scaled by -25.40.

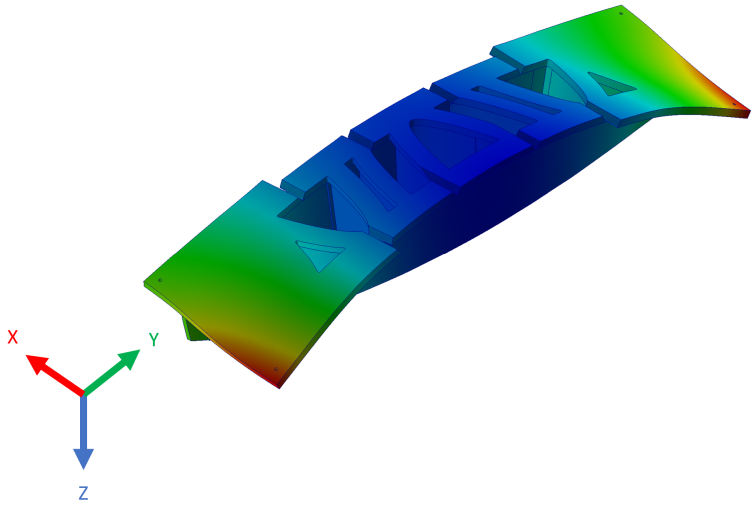

Figure 5.47: FEA simulation of WAAM print at 245 Hz which shows a similar mode shape as found in impact testing for mode 2 where the amplitude is only shown in the Z-axis.

Table 5.5: Peak picked values for columns 1 - 10 of Mode 3 at 291 Hz at each location of the bottom face normalized to (1,1) and scaled by 76.20

Row \ Column	1	2	3	4	5	6	7	8	9	10
1	76.20	57.35	25.28	14.05	-4.64	-17.12	-29.67	-42.98	-49.01	-53.52
2	59.71	42.56	20.87	8.93	-4.76	-16.40	-26.66	-36.77	-44.19	-47.42
3	-2.38	20.62	10.41	0.79	-4.40	-8.79	-14.68	-19.65	-22.14	-21.88
4	-66.42	-0.05	2.40	-0.40	4.40	6.58	7.13	12.17	-18.19	3.14
5	-94.95	-11.76	-2.89	1.46	7.40	12.20	15.41	16.01	15.93	20.62

Table 5.6: Peak picked values for columns 11 - 19 of Mode 3 at 291 Hz at each location of the bottom face normalized to (1,1) and scaled by 76.20

Row \ Column	11	12	13	14	15	16	17	18	19
1	-47.71	-39.84	-28.61	-14.53	-1.67	13.78	26.80	66.20	93.08
2	-47.15	-40.23	-28.48	-17.54	-6.96	7.97	19.23	54.49	78.36
3	-21.57	-23.38	-24.42	-22.78	-22.62	-18.79	-3.24	24.66	35.79
4	2.43	-2.14	-9.58	-16.37	-21.01	-24.72	-24.41	-9.17	0.63
5	9.04	6.62	-2.35	-11.81	-20.85	-29.99	-34.85	-18.18	-7.59

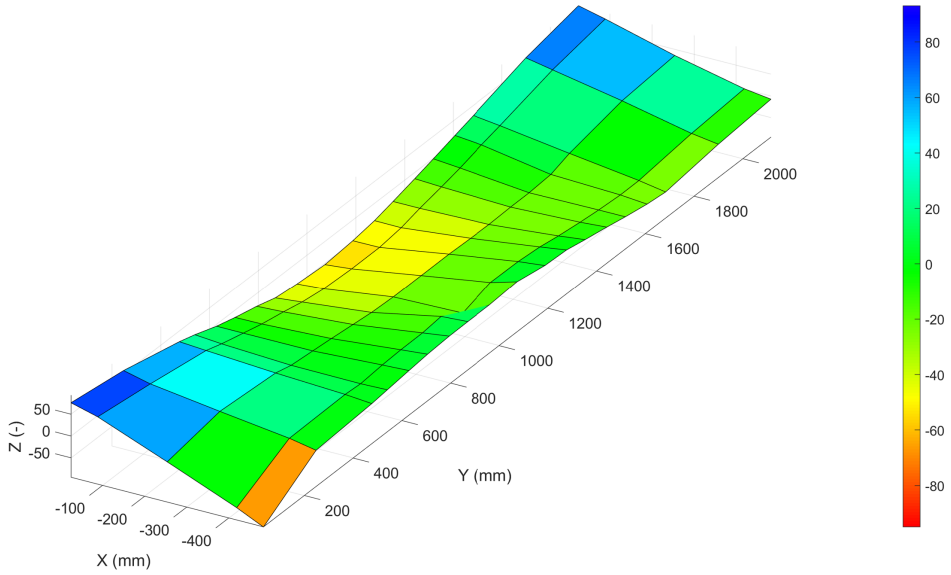

Figure 5.48: Plot of peak picked values of Mode 3 at 291 Hz at each location of the bottom face normalized to (1,1) and scaled by 76.20.

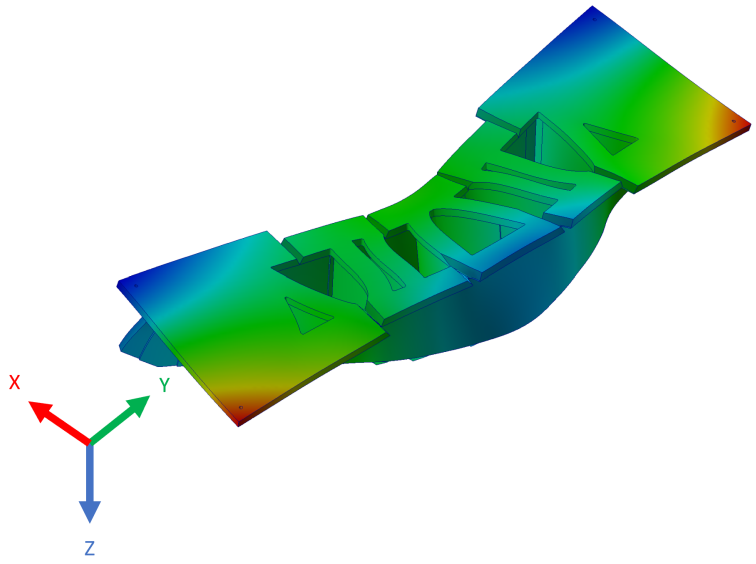

Figure 5.49: FEA simulation of WAAM print at 293 Hz which shows a similar mode shape as found in impact testing for mode 3 where the amplitude is only shown in the Z-axis.

Table 5.7: Peak picked values for columns 1 - 10 of Mode 4 at 377 Hz at each location of the bottom face normalized to (1,1) and scaled by -50.80

Row \ Column	1	2	3	4	5	6	7	8	9	10
1	-50.80	-26.99	-5.08	0.28	8.56	13.52	18.02	20.76	23.30	24.17
2	-45.00	-27.25	-6.47	-1.31	6.52	11.19	15.75	19.31	20.73	21.58
3	-12.00	-26.83	-11.00	0.01	3.85	6.46	11.40	14.32	15.52	16.51
4	51.77	-25.48	-14.84	-10.42	-3.30	1.44	5.86	9.33	16.76	10.48
5	83.90	-23.20	-17.48	-11.86	-5.55	-0.73	3.78	6.56	7.64	8.74

Table 5.8: Peak picked values for columns 11 - 19 of Mode 4 at 377 Hz at each location of the bottom face normalized to (1,1) and scaled by -50.80

Row \ Column	11	12	13	14	15	16	17	18	19
1	23.59	21.43	18.08	13.71	8.98	2.21	-3.44	-25.35	-54.24
2	20.58	19.25	15.80	10.74	6.87	-0.03	-5.27	-24.40	-40.40
3	16.59	14.72	10.61	5.39	3.01	-0.48	-11.31	-24.46	10.20
4	10.30	8.06	4.41	-0.24	-5.08	-11.86	-16.62	-25.19	77.05
5	7.50	6.22	2.42	-2.34	-7.47	-14.26	-19.90	-22.76	115.45

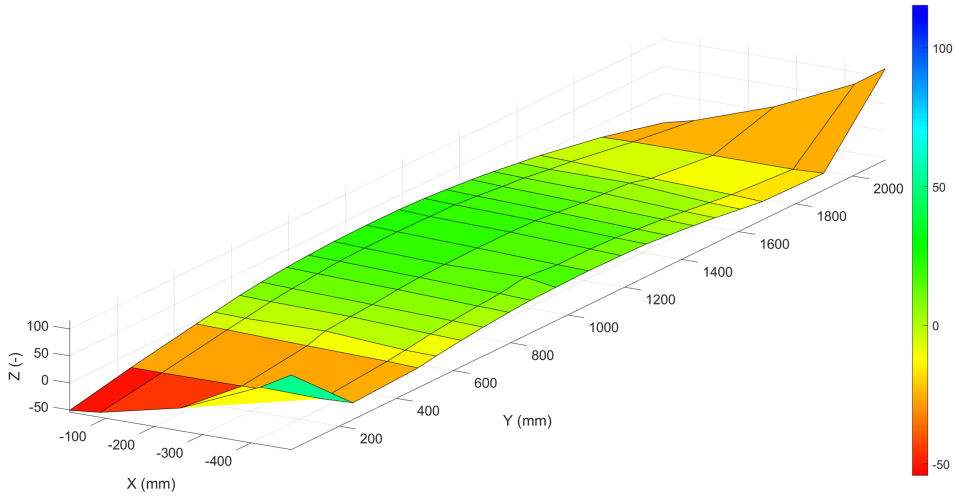

Figure 5.50: Plot of peak picked values of Mode 4 at 377 Hz at each location of the bottom face normalized to (1,1) and scaled by -50.80.

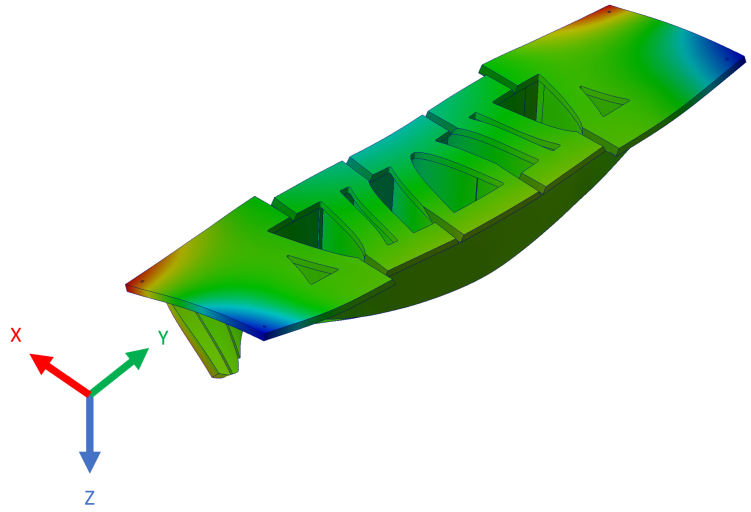

Figure 5.51: FEA simulation of WAAM print at 469 Hz which shows a similar mode shape as found in impact testing for mode 4 where the amplitude is only shown in the Z-axis.

Table 5.9: Peak picked values for columns 1 - 10 of Mode 5 at 687 Hz at each location of the bottom face normalized to (1,1) and scaled by -76.20

Row \ Column	1	2	3	4	5	6	7	8	9	10
1	-76.20	-25.02	15.94	26.34	30.92	35.39	37.04	34.59	21.83	4.21
2	-48.63	-20.80	12.63	22.40	28.91	34.18	32.90	32.79	20.31	1.81
3	39.29	-0.93	9.99	18.01	18.38	18.73	22.51	20.17	12.09	1.84
4	30.72	-3.18	5.06	7.99	4.14	2.97	1.16	-3.14	10.64	-1.51
5	8.55	-10.36	2.51	-1.56	0.93	-3.90	-5.92	-3.90	-4.13	-3.16

Table 5.10: Peak picked values for columns 11 - 19 of Mode 5 at 687 Hz at each location of the bottom face normalized to (1,1) and scaled by -76.20

Row \ Column	11	12	13	14	15	16	17	18	19
1	-15.54	-31.64	-35.02	-34.81	-32.25	-28.49	-19.37	21.05	94.17
2	-15.98	-28.13	-29.59	-32.77	-28.53	-21.46	-13.90	16.08	44.56
3	-8.55	-17.09	-20.55	-18.44	-18.77	-18.39	-10.62	1.56	-23.50
4	0.08	0.86	-2.27	-4.29	-4.86	-6.67	-4.07	9.79	-19.17
5	-0.45	1.73	3.73	2.90	-1.31	3.02	0.15	16.94	-11.23

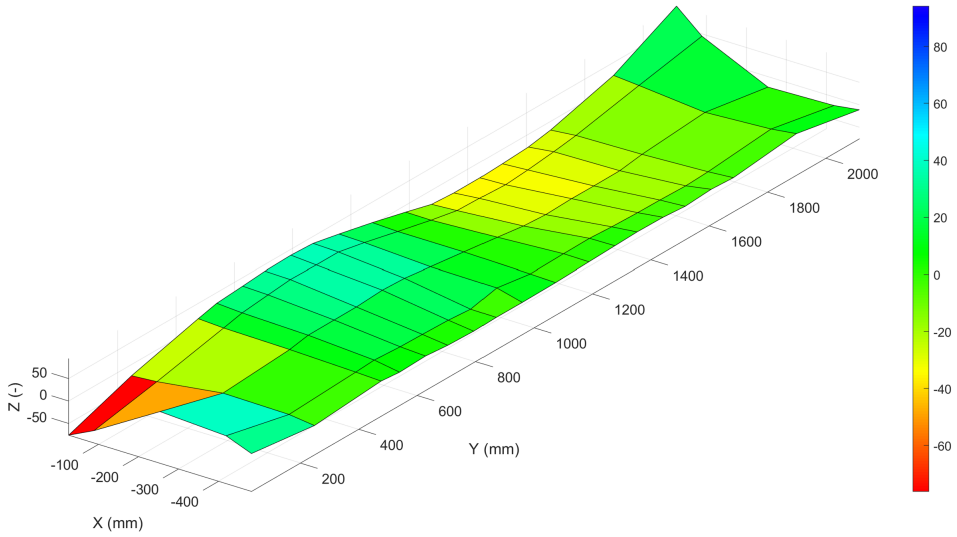

Figure 5.52: Plot of peak picked values of Mode 5 at 687 Hz at each location of the bottom face normalized to (1,1) and scaled by -76.20.

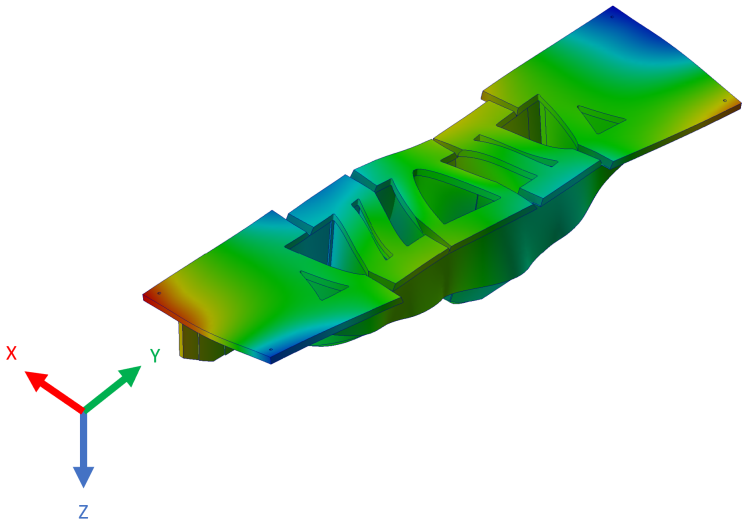

Figure 5.53: FEA simulation of WAAM print at 704 Hz which shows a similar mode shape as found in impact testing for mode 5 where the amplitude is only shown in the Z-axis.

Table 5.11: Dynamic mode frequencies from peak-picking and FEA of modes 1-5 for the bottom face of the WAAM print in addition to the percent difference

Mode shape	Peak-picking [Hz]	FEA [Hz]	Percent difference [%]
1	184	164	-12.2
2	233	245	4.9
3	291	293	0.7
4	377	469	19.6
5	687	704	2.4

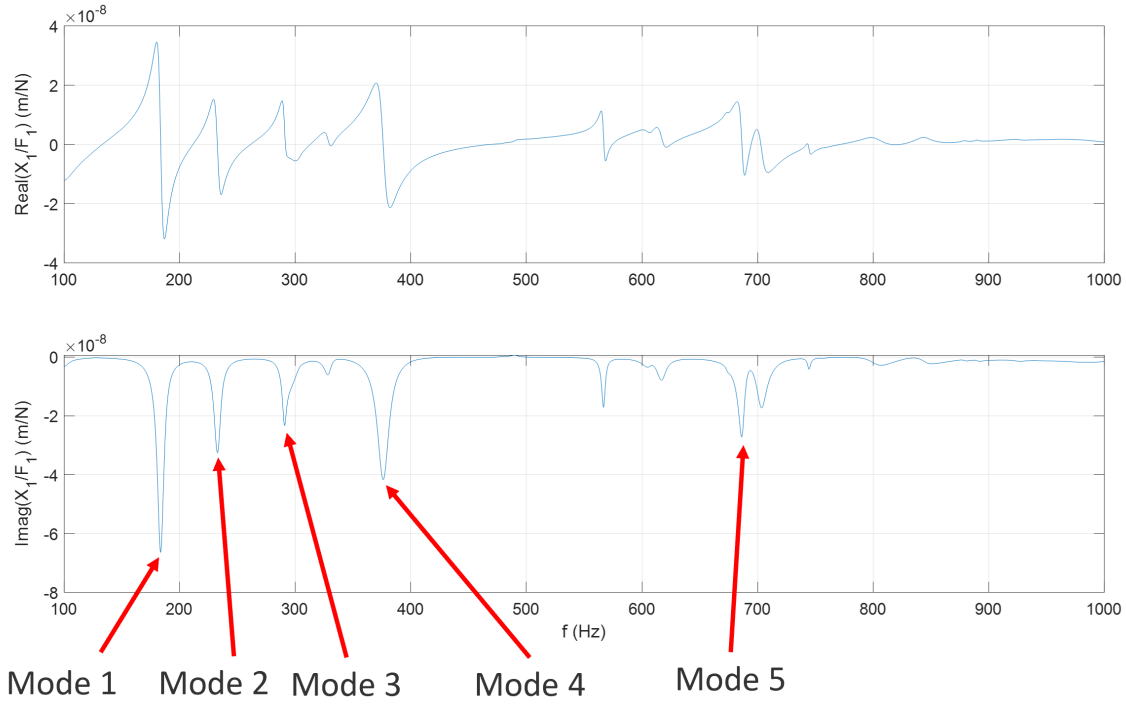

Figure 5.54: Real and imaginary FRF plots of (1,1) from the bottom face with the five identified modes of interest.

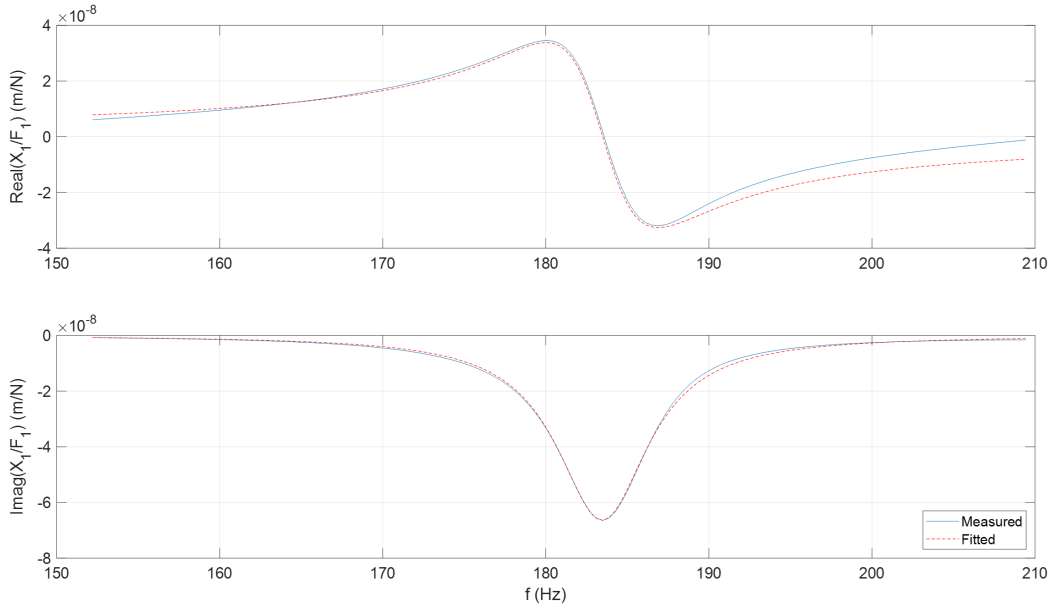

Figure 5.55: Real and imaginary FRF plots of mode 1 of (1,1) from the bottom face with a superimposed plot of the calculated real and imaginary plots.

calculated damping ratios and stiffness values for mode shapes of the bottom face are shown in Table 5.12. The superposition of the calculated real and imaginary plots are shown in Figure 5.56.

5.3.2 Front face

To find the five modes with the largest amplitudes for the front face, the real and imaginary FRF plots of the top row of points in Figure 5.30 were plotted together in TXF. By looking at the amplitudes of the imaginary plot, the most flexible modes were chosen as shown in Figure 5.57. The mode shape frequencies for the front face that were compared were 480, 486, 566, 610, and 674 Hz. These values were extracted through peak-picking and finding the corresponding frequencies.

The approach for finding the mode shapes for the front surface of the WAAM cross beam is the same as finding the mode shapes of the bottom surface. The same sequence of tables and figures is shown in the same order shown for the front face of the weldment. Tables 5.13 through 5.17 show the plotted points of the peak-picked values. Figures 5.58 through 5.67 showcase the plotted mode shapes of the front face in MATLAB as well as the FEA simulated mode shapes. The result is that the mode shapes that were from the tap testing match that of the FEA simulations. This again validates the FEA model that has been used for the frequency simulations. Table 5.18 provides the frequencies of the peak picking and simulated mode shape frequencies. The percent difference in the table was calculated with Equation 3.5. The result was that the largest percent difference was 9

Peak-picking of the mode shapes was also used to find the damping ratio and stiffness values of the five mode shapes of the front face of the WAAM cross beam. The real and imaginary plot of (1,2) shown in Figure 5.68 highlights the same five dynamic modes of interest. Using Equations 3.6 and 3.7, the modal damping ratio and modal stiffness of each peak were able to be calculated. The calculated values were then re-plotted as real and imaginary plots that were superimposed on top of

Table 5.12: Calculated damping ratio and stiffness values from the five modes of the bottom face through peak-picking

Mode	Peak-picking frequency [Hz]	Damping ratio [-]	Stiffness [N/m]
1	184	0.019	4.00×10^8
2	233	0.014	1.10×10^9
3	291	0.006	3.50×10^9
4	377	0.016	7.40×10^8
5	687	0.005	3.70×10^9

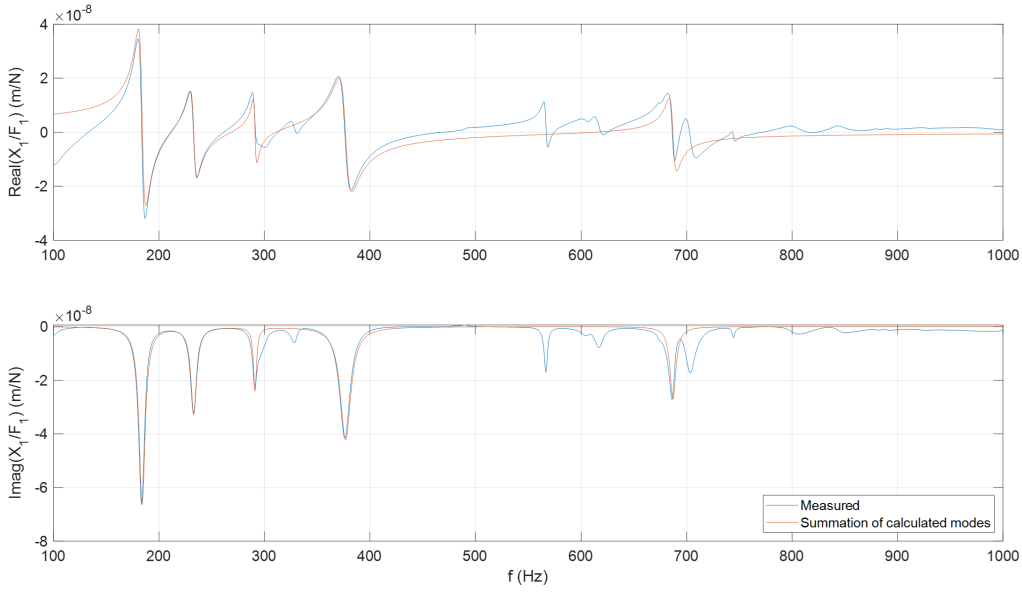

Figure 5.56: Real and imaginary FRF plots (1,1) from the bottom face with a superimposed plot of all the calculated real and imaginary plots summed.

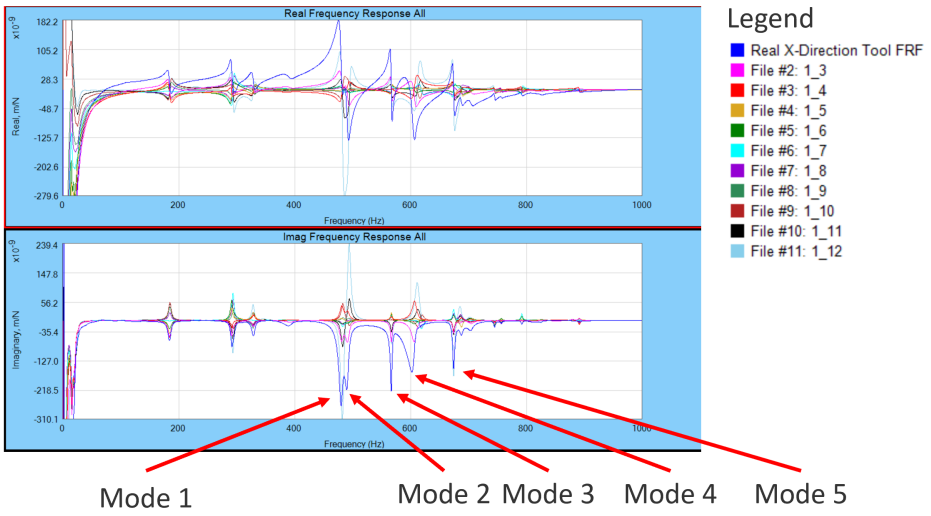

Figure 5.57: Overlay of the real and imaginary plots from the top row of points of the front face (1,2) - (1,12) with the chosen five most flexible modes.

Table 5.13: Peak picked values of Mode 1 at 483 Hz at each location of the front face normalized to (1,2) and scaled by 50.80

Row \ Column	1	2	3	4	5	6	7	8	9	10	11	12	13
1		50.80	14.49	-10.15	-1.24	2.66	5.05	3.30	-2.12	-13.77	21.14	73.98	
2	69.04	45.66	13.18	-9.05	-1.13	2.72	5.28	3.51	-1.66	-11.89	17.65	61.10	77.52
3	56.04	36.70	8.41	-7.96	-0.94	2.80	5.38	3.58	-1.42	-10.36	11.86	44.49	68.55
4	38.50	21.86	4.13	-6.83	-0.80	2.80	5.58	3.73	-1.03	-8.58	4.61	23.80	38.96
5	11.72	5.66	-1.26	-5.96	-0.49	3.12	5.74	3.68	-0.25	-7.22	0.25	11.25	11.75

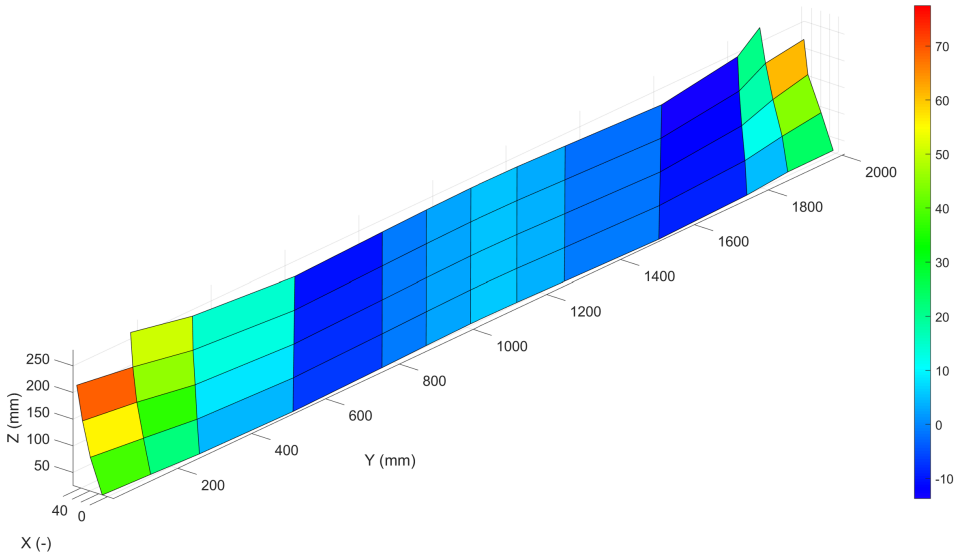

Figure 5.58: Plot of peak picked values of Mode 1 at 483 Hz at each location of the front face normalized to (1,2) and scaled by 50.80.

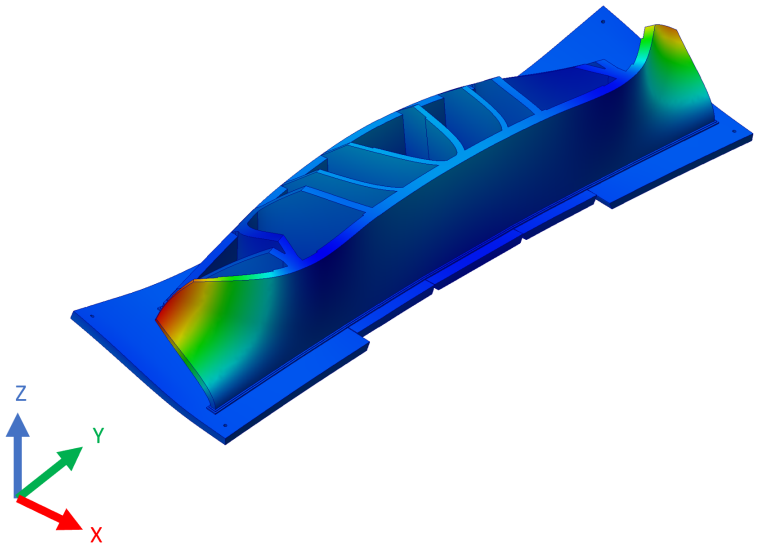

Figure 5.59: FEA simulation of WAAM print at 481 Hz which shows a similar mode shape as found in impact testing for mode 1 where the amplitude is only shown in the X-axis.

Table 5.14: Peak picked values of Mode 2 at 486 Hz at each location of the front face normalized to (1,2) and scaled by 50.80

Row \ Column	1	2	3	4	5	6	7	8	9	10	11	12	13
1		50.80	13.13	-6.89	-0.19	2.10	2.77	1.70	-1.31	-5.70	6.49	14.65	
2	70.77	44.49	11.91	-5.93	-0.10	2.16	2.89	1.61	-1.18	-5.41	5.93	12.85	6.67
3	56.74	34.57	8.00	-5.08	0.06	2.21	3.03	1.73	-1.17	-5.10	4.70	10.63	12.88
4	36.66	19.66	4.23	-4.24	0.18	2.21	3.08	1.67	-1.00	-4.54	1.95	7.10	9.65
5	10.10	5.07	-0.87	-3.62	0.42	2.32	3.19	1.54	-0.58	-4.11	0.21	4.64	4.60

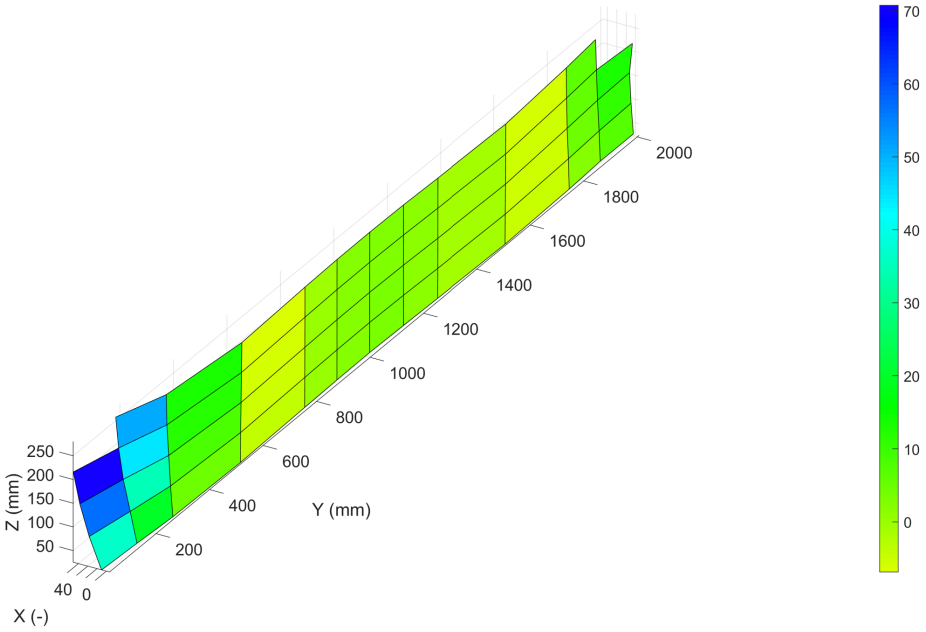

Figure 5.60: Plot of peak picked values of Mode 2 at 486 Hz at each location of the front face normalized to (1,2) and scaled by 50.80.

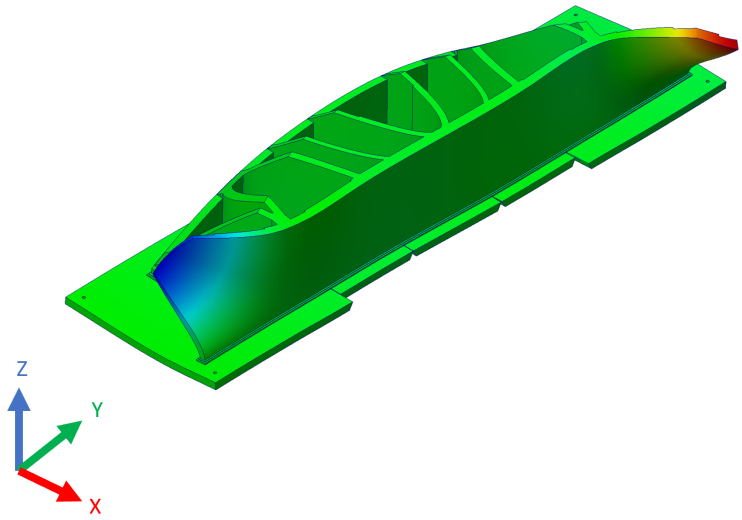

Figure 5.61: FEA simulation of WAAM print at 483 Hz which shows a similar mode shape as found in impact testing for mode 2 where the amplitude is only shown in the X-axis.

Table 5.15: Peak picked values of Mode 3 at 566 Hz at each location of the front face normalized to (1,2) and scaled by -76.20.

Row \ Column	1	2	3	4	5	6	7	8	9	10	11	12	13
1		-76.20	-23.27	4.29	8.52	7.43	5.11	4.90	6.66	0.78	-12.48	-26.12	
2	-87.51	-55.27	-17.41	5.22	5.56	2.25	-0.18	1.15	4.49	2.06	-8.29	-17.15	-28.86
3	-51.54	-29.88	-8.05	7.29	4.71	-3.20	-3.64	-2.08	2.73	4.05	-3.76	-8.32	-13.19
4	-18.61	-9.65	-1.03	9.05	0.96	-7.35	-9.11	-5.84	1.41	6.19	0.81	-0.47	-0.96
5	2.96	3.82	5.95	10.08	-3.36	-14.98	-14.92	-9.68	-2.32	8.09	3.67	2.77	3.71

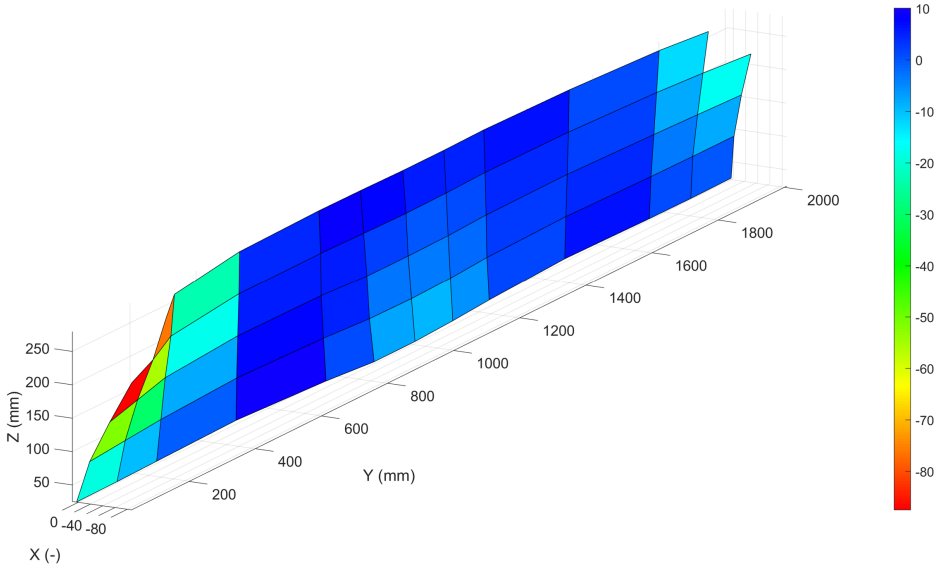

Figure 5.62: Plot of peak picked values of Mode 3 at 566 Hz at each location of the front face normalized to (1,2) and scaled by -76.20.

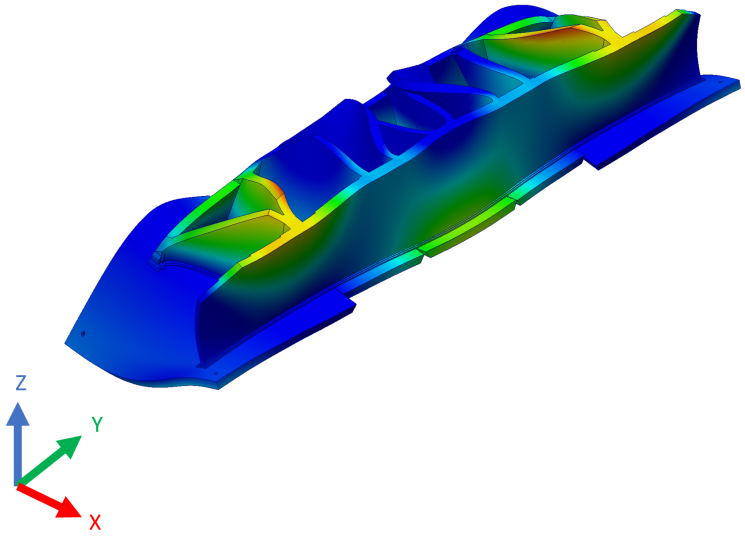

Figure 5.63: FEA simulation of WAAM print at 625 Hz which shows a similar mode shape as found in impact testing for mode 3 where the amplitude is only shown in the X-axis.

Table 5.16: Peak picked values of Mode 4 at 610 Hz at each location of the front face normalized to (1,2) and scaled by -50.80.

Row \ Column	1	2	3	4	5	6	7	8	9	10	11	12	13
1		-50.80	-21.00	18.93	1.87	-3.58	-8.28	-6.75	-1.78	-5.84	10.56	36.90	
2	-52.79	-46.41	-17.99	14.71	1.43	-2.62	-5.36	-4.25	0.79	5.84	7.77	27.31	35.71
3	-43.50	-34.21	-10.66	10.53	1.63	-1.55	-4.03	-1.66	2.44	4.68	4.63	15.03	23.85
4	-24.24	-15.19	-4.50	6.20	0.85	-0.83	-1.15	0.98	3.18	4.94	-1.40	3.55	5.02
5	0.95	-2.63	-2.94	-0.79	-0.44	0.70	2.26	4.59	6.91	4.49	-2.45	-4.34	-6.89

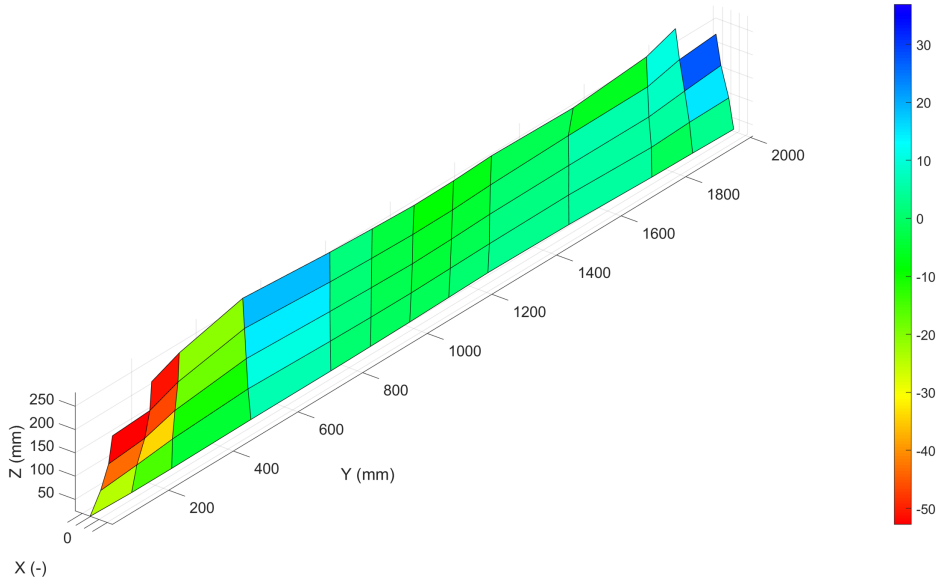

Figure 5.64: Plot of peak picked values of Mode 4 at 610 Hz at each location of the front face normalized to (1,2) and scaled by -50.80.

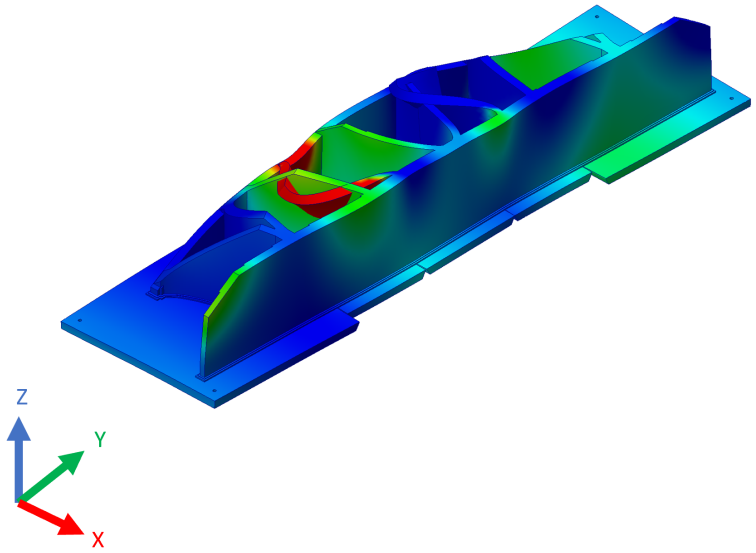

Figure 5.65: FEA simulation of WAAM print at 666 Hz which shows a similar mode shape as found in impact testing for mode 4 where the amplitude is only shown in the X-axis.

Table 5.17: Peak picked values of Mode 5 at 674 Hz at each location of the front face normalized to (1,2) and scaled by 50.80.

Row \ Column	1	2	3	4	5	6	7	8	9	10	11	12	13
1		50.80	13.42	11.95	10.46	-5.72	-11.67	-7.18	10.53	10.62	14.99	58.55	
2	60.75	36.33	9.34	11.15	11.13	-4.26	-10.25	-5.46	11.53	10.71	8.54	39.33	55.06
3	31.13	17.19	2.16	11.49	10.36	-2.60	-9.98	-3.25	12.37	10.86	0.91	15.93	30.33
4	3.41	-1.51	-3.56	11.44	11.52	-1.56	-8.71	-1.43	12.42	11.95	-6.56	-6.36	-4.76
5	-18.33	-12.94	-6.96	10.69	12.13	-0.24	-6.37	1.84	13.36	12.14	-11.25	-16.95	-25.37

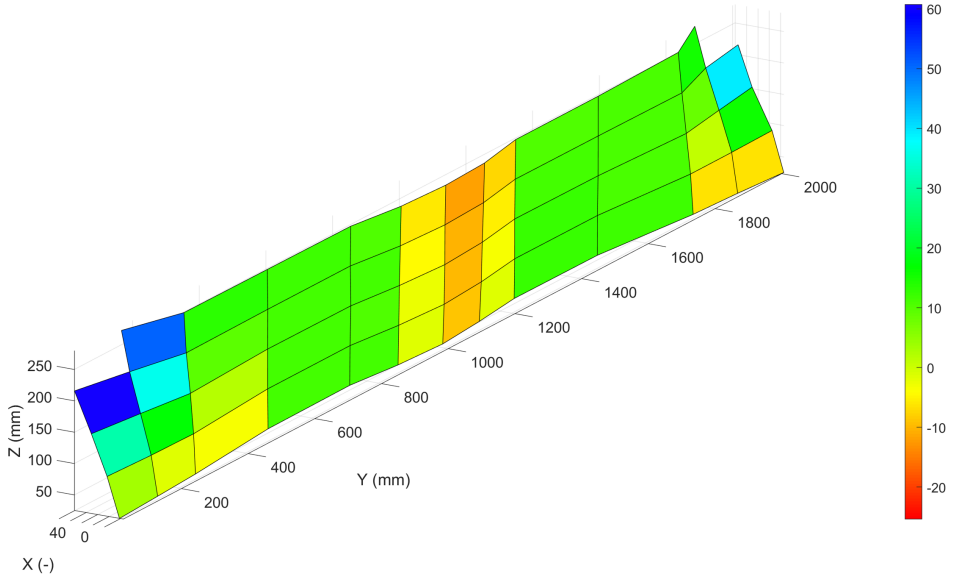

Figure 5.66: Plot of peak picked values of Mode 5 at 674 Hz at each location of the front face normalized to (1,2) and scaled by 50.80.

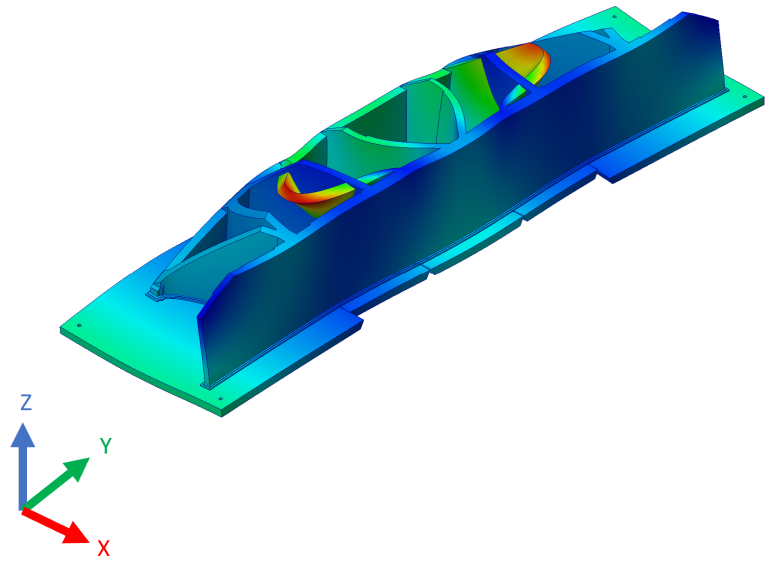

Figure 5.67: FEA simulation of WAAM print at 677 Hz which shows a similar mode shape as found in impact testing for mode 5 where the amplitude is only shown in the X-axis.

Table 5.18: Dynamic mode frequencies from peak-picking and FEA of modes 1-5 for the front face of the WAAM print in addition to the percent difference

Mode shape	Peak-picking [Hz]	FEA [Hz]	Percent difference [%]
1	483	481	-0.4
2	486	483	-0.6
3	566	625	9.4
4	610	666	8.4
5	674	677	0.4

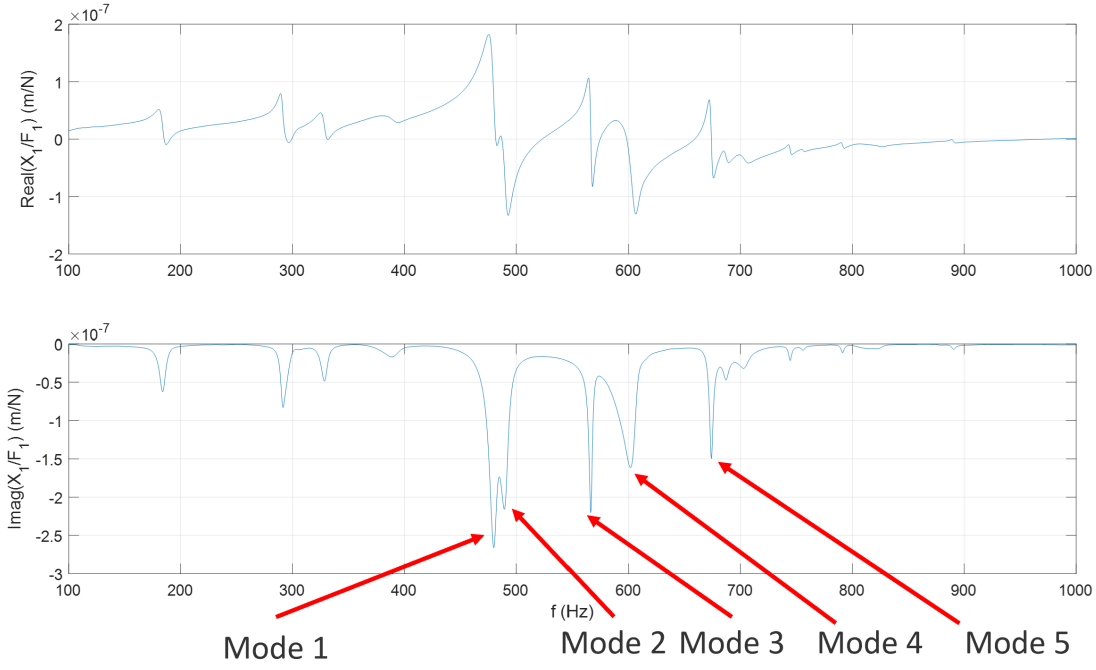

Figure 5.68: Real and imaginary FRF plots of (1,2) from the front face with the five identified modes of interest.

the measured data as demonstrated in Figure 5.69 which is of mode 1 and mode 2. The resulting calculated damping ratios and stiffness values for mode shapes of the front face are shown in Table 5.19. The superposition of the calculated real and imaginary plots are shown in Figure 5.70.

5.4 Comparison of damping ratios for weldment and mBAAM cross beam

The damping ratio, ζ, is used to describe the behavior of damped systems [45]. Tables 5.20 and 5.21 present the calculated damping ratios for the weldment's and WAAM cross beam's bottom and front faces. A higher damping ratio indicates a higher vibrational decay rate and a lower damping ratio indicates a lower decay rate.

The damping ratios from the bottom face of the weldment range from 0.004 to 0.007 with an average of 0.004. The damping ratios from the bottom face for the WAAM cross beam range from 0.005 to 0.019 with an average of 0.012. When comparing the bottom faces of the two structures, the WAAM cross beam has a higher damping ratio average. This indicates that the WAAM cross beam's bottom face dissipates vibrational energy more efficiently.

The damping ratios from the front face of the weldment range from 0.003 to 0.007 with an average of 0.004. The damping ratios from the bottom face for the WAAM cross beam range from 0.003 to 0.015 with an average of 0.008. When comparing the front faces of the two structures, the WAAM cross beam also has a higher damping ratio average. This indicates that the WAAM cross beam's front face also dissipates vibrational energy more efficiently.

Although the WAAM print was incomplete, impact testing of the printed structure provides some insight into the WAAM structure's material and design properties. Damping ratios are difficult to calculate and are best obtained through experimental testing. The impact testing of the WAAM print provided a method to retrieve the

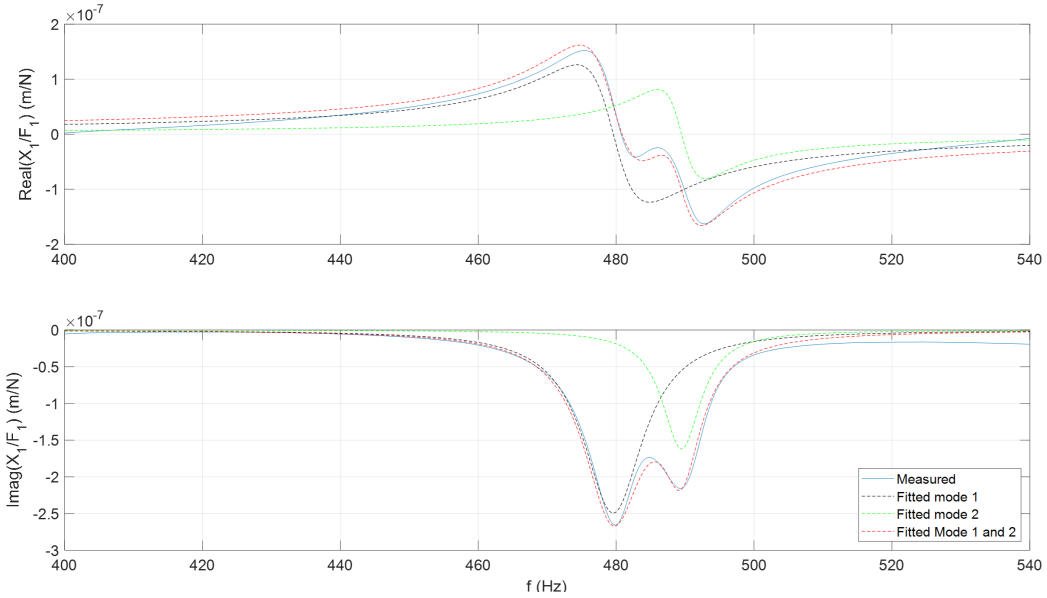

Figure 5.69: Real and imaginary FRF plots of mode 1 and mode 2 of (1,2) from the front face with a superimposed plot of the calculated real and imaginary plots.

Table 5.19: Calculated damping ratio and stiffness values from the five modes of the front face through peak-picking

Mode	Peak-picking frequency [Hz]	Damping ratio [-]	Stiffness [N/m]
1	483	0.011	1.82×10^8
2	486	0.007	4.40×10^8
3	566	0.003	7.90×10^8
4	610	0.015	2.09×10^8
5	674	0.003	1.15×10^9

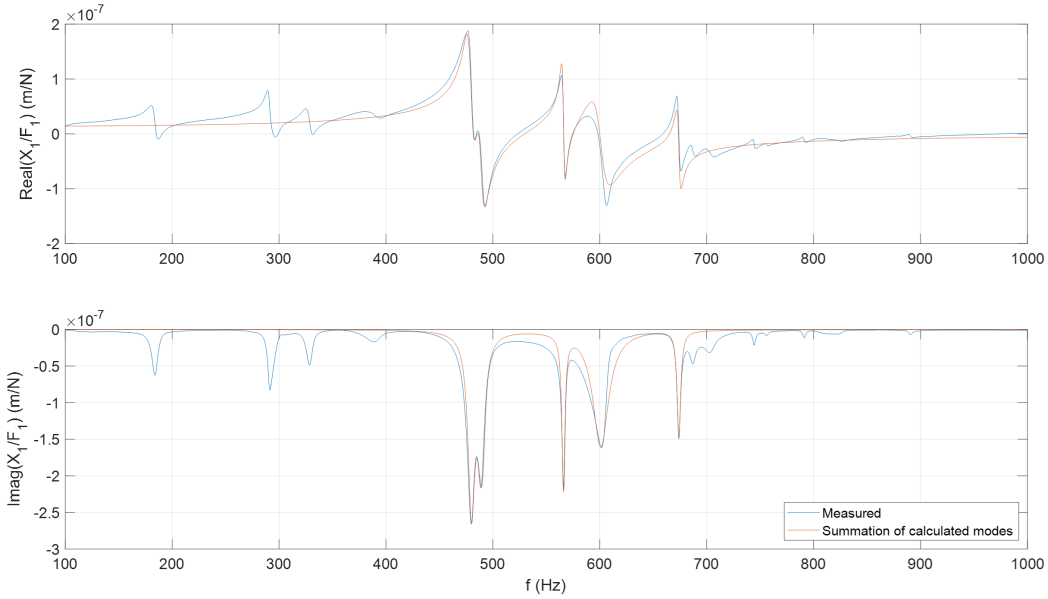

Figure 5.70: Real and imaginary FRF plots (1,2) from the front face with a superimposed plot of all the calculated real and imaginary plots summed.

Table 5.20: Frequencies and damping ratios of the bottom faces of the weldment and WAAM cross beam

Cross beam	Mode number	Frequency [Hz]	Damping ratio [-]
Weldment	1	209	0.006
	2	373	0.004
	3	377	0.006
	4	413	0.007
	5	545	0.005
WAAM	1	184	0.019
	2	233	0.014
	3	291	0.006
	4	377	0.016
	5	687	0.005

Table 5.21: Frequencies and damping ratios of the front faces of the weldment and WAAM cross beam

Cross beam	Mode number	Frequency [Hz]	Damping ratio [-]
Weldment	1	209	0.007
	2	375	0.005
	3	529	0.005
	4	546	0.004
	5	833	0.003
WAAM	1	483	0.011
	2	486	0.007
	3	566	0.003
	4	610	0.015
	5	674	0.003

damping ratios for the most flexible modes of the bottom and front faces of both structures. The damping ratios from the weldment were more consistent compared to those from the WAAM cross beam.

The damping ratios for the two structures are not definitive metrics to deem one design better than the other. For machine tools, the mode shape deflection of the structure is more important at the operational frequency of the machine tool. Machine tools generally operate at higher frequencies compared to the structural modes of the machine. The weldment and WAAM cross beam were tested in free-free states which allowed for accurate simulation results. However when in use, the structures will never be in free-free states.

The damping ratios for the two structures are not definitive metrics to deem one design better than the other. For machine tools, the static and dynamic stiffness values are critical for the machine tool performance. Because damping contributes to the dynamics stiffness, however, it is an important consideration. The weldment and WAAM cross beam were tested in free-free states which allowed for accurate simulation results. However when in use, the structures will never be in free-free states.

Chapter 6

Conclusions and recommendations

Machine tool design requires that the many variables that contribute to the structure's performance are considered simultaneously. A method for assessing the redesign of a machine tool structure was presented in this thesis. FEA was used to give insight into the deflection profile of a machine tool structure. Sampling the extreme deflection states from the large family of potential machine configurations was used to understand the weldment's deflection behavior and serve as a design metric. The deflection profile and capabilities/limitations of the MedUSA system served as guides that resulted in the final design. These metrics enabled assessments that reduced the number of design iterations.

The final design was acceptable to be manufactured with the MedUSA system, had a similar deflection profile to the weldment, and had less mass than the weldment. The WAAM design either matched or had less deflection in 67 out of 72 points on the weldment. Features of the final design were implemented to be manufactured through the WAAM process and avoided supports and overhangs, while also implementing features that reduced the mass of the structure. The mass of the final WAAM design was 4% less than the weldment. Features from the final design can also be implemented in other mBAAM structures.

The mode shapes for the weldment and the WAAM print were compared using FEA simulation and modal analysis through impact testing. With accurate FEA models, simulations of both structures were able to yield the natural frequencies and mode shapes of the structures. Modal analysis of the physical structures validated the simulation accuracy. Of the 20 mode shapes found in this study, the variation in the mode shape's simulated natural frequency versus the peak-picked methods had less than 20% difference.

The WAAM cross beam print revealed problems with mBAAM technology. The deformation of the WAAM part caused the print to stop. The final design was the second largest part that the ORNL WAAM team had attempted. Distortion of the part could have been caused by various factors such as the method in which the build plate was secured. More experiments need to be carried out to print large-scale parts. Experiments could include dynamic clamping or different print paths. The desire for mBAAM parts will not subside and the technology needs to be further improved to print successful large-scale parts.

Although the WAAM cross beam was not completed, the implementation of the design, manufacturing, and testing processes provides a methodology for future mBAAM projects. Before another mABAAM part is printed, the internal stress and deformation of WAAM prints should be better understood and resolved. This can be done through smaller-scaled prints and experimentation that focus on the factors that contribute to severe thermal distortion. However, 77% of the print was able to be printed. With what was printed, the results were promising and indicated that large-scale WAAM prints are possible and the technology was close to making the final design.

Bibliography

[1] HAAS. Desktop mill | training mill | compact CNC | vertical mills – haas CNC machines. [Online]. Available: https://www.haascnc.com/machines/vertical-mills/desktop-mill.html xiv, 4

[2] K\&M. Large CNC machining equipment (hor., vert., lathe). [Online]. Available: https://www.k-mm.com/large-machining/ xiv, 4

[3] Emerging technology center annex. [Online]. Available: https://www.imts.com/show/etcAnnex.cfm? xiv, 6

[4] Lightweight & speed - big CNC - EEW-PROTEC GmbH | EEW-PROTEC GmbH. [Online]. Available: https://www.eew-protec.de/ xiv, 11

[5] MAP machine tools. [Online]. Available: https://map-wzm.de/entwicklung/ xiv, 11

[6] MIG vs TIG | welding types, materials, and applications - a guide. Section: Uncategorized. [Online]. Available: https://www.technoxmachine.com/blog/mig-vs-tig-welding/ xiv, 14

[7] C. M. Greer, "Design of replacement structural components for fabrication using metal big area additive manufacturing," accepted: 2017-06-07T17:49:37Z Publisher: Georgia Institute of Technology. [Online]. Available: https://smartech.gatech.edu/handle/1853/58338 xiv, 19, 20

[8] T. L. Schmitz and K. S. Smith, "Modal analysis," in *Machining Dynamics: Frequency Response to Improved Productivity*, T. L. Schmitz and K. S. Smith, Eds. Springer International Publishing, pp. 7–66. [Online]. Available: https://doi.org/10.1007/978-3-319-93707-6_2 xiv, xv, 21, 22, 23, 27, 28, 29

[9] ——, "Model development by modal analysis," in *Mechanical Vibrations: Modeling and Measurement*, T. L. Schmitz and K. S. Smith, Eds. Springer US, pp. 199–247. [Online]. Available: https://doi.org/10.1007/978-1-4614-0460-6_6 xv, 32

[10] W. J. McCarthy and J. A. McGeough. Machine tool. [Online]. Available: https://www.britannica.com/technology/machine-tool 3

[11] B. Carlsson, "The development and use of machine tools in historical perspective," vol. 5, no. 1, pp. 91–114. [Online]. Available: https://www.sciencedirect.com/science/article/pii/0167268184900283 3

[12] Britannica. Milling machine | britannica. [Online]. Available: https://www.britannica.com/technology/milling-machine 3

[13] J. L. West, E. D. Betters, T. L. Schmitz, S. Smith, A. Roschli, D. Nuttall, J. Lindahl, and L. Love, "Rethinking production of machine tool bases: Polymer additive manufacturing and concrete," vol. 31, pp. 33–35. [Online]. Available: https://www.sciencedirect.com/science/article/pii/S2213846321000377 5, 34

[14] E. D. Betters, J. West, M. Noakes, A. Nycz, S. Smith, and T. L. Schmitz, "Dynamic stiffness modification by internal features in additive manufacturing," vol. 66, pp. 125–134. [Online]. Available: https://www.sciencedirect.com/science/article/pii/S014163591930933X 5

[15] H. Sugishita, H. Nishiyama, O. Nagayasu, T. Shin-nou, H. Sato, and M. O-hori, "Development of concrete machining center and identification of the dynamic and

the thermal structural behavior," vol. 37, no. 1, pp. 377–380. [Online]. Available: https://www.sciencedirect.com/science/article/pii/S0007850607616588 5

[16] A. H. Slocum, *Precision Machine Design*. Society of Manufacturing Engineers, google-Books-ID: 4GH_AwAAQBAJ. 7, 126

[17] J. D. Suh, D. G. Lee, and R. Kegg, "Composite machine tool structures for high speed milling machines," vol. 51, no. 1, pp. 285–288. [Online]. Available: https://www.sciencedirect.com/science/article/pii/S0007850607615182 7

[18] H. C. Möhring, "Composites in production machines," vol. 66, pp. 2–9. [Online]. Available: https://www.sciencedirect.com/science/article/pii/S2212827117305218 10

[19] D. G. Lee, S. H. Chang, and H. S. Kim, "Damping improvement of machine tool columns with polymer matrix fiber composite material," vol. 43, no. 2, pp. 155–163. [Online]. Available: https://www.sciencedirect.com/science/article/pii/S0263822398001068 10

[20] Z. Zhu, V. Dhokia, A. Nassehi, and S. Newman, "A review of hybrid manufacturing processes – state of the art and future perspectives," vol. 26, no. 7, pp. 596–615, publisher: Taylor & Francis _eprint: https://doi.org/10.1080/0951192X.2012.749530. [Online]. Available: https://doi.org/10.1080/0951192X.2012.749530 10

[21] I. Gibson, D. Rosen, B. Stucker, and M. Khorasani, "Introduction and basic principles," in *Additive Manufacturing Technologies*, I. Gibson, D. Rosen, B. Stucker, and M. Khorasani, Eds. Springer International Publishing, pp. 1–21. [Online]. Available: https://doi.org/10.1007/978-3-030-56127-7_1 10

[22] T. Grimm, *User's Guide to Rapid Prototyping*. Society of Manufacturing Engineers, google-Books-ID: o2B7OmABPNUC. 10

[23] I. Gibson, D. Rosen, B. Stucker, and M. Khorasani, "Generalized additive manufacturing process chain," in *Additive Manufacturing Technologies*, I. Gibson, D. Rosen, B. Stucker, and M. Khorasani, Eds. Springer International Publishing, pp. 53–76. [Online]. Available: https://doi.org/10.1007/978-3-030-56127-7_3 12

[24] M. Pérez, D. Carou, E. Rubio, and R. Teti, "Current advances in additive manufacturing," vol. 88, pp. 439–444. 12

[25] A. A. Hassen, M. Noakes, P. Nandwana, S. Kim, V. Kunc, U. Vaidya, L. Love, and A. Nycz, "Scaling up metal additive manufacturing process to fabricate molds for composite manufacturing," vol. 32, p. 101093. [Online]. Available: https://www.sciencedirect.com/science/article/pii/S2214860419303008 12, 15

[26] I. Gibson, D. Rosen, B. Stucker, and M. Khorasani, "Directed energy deposition," in *Additive Manufacturing Technologies*, I. Gibson, D. Rosen, B. Stucker, and M. Khorasani, Eds. Springer International Publishing, pp. 285–318. [Online]. Available: https://doi.org/10.1007/978-3-030-56127-7_10 12

[27] N. A. Rosli, M. R. Alkahari, M. F. b. Abdollah, S. Maidin, F. R. Ramli, and S. G. Herawan, "Review on effect of heat input for wire arc additive manufacturing process," vol. 11, pp. 2127–2145. [Online]. Available: https://www.sciencedirect.com/science/article/pii/S2238785421001289 13

[28] K. Weman and G. Lindén, *Mig Welding Guide*. Woodhead Publishing, google-Books-ID: mr5QAwAAQBAJ. 13

[29] National lab takes on manufacturing techniques. [Online]. Available: https://www.afcea.org/signal-media/national-lab-takes-manufacturing-techniques 15

[30] Breaking the toolhead barrier with MedUSA fabbaloo. [Online]. Available: https://www.fabbaloo.com/news/breaking-the-toolhead-barrier-with-medusa 19

[31] C. Greer, A. Nycz, M. Noakes, B. Richardson, B. Post, T. Kurfess, and L. Love, "Introduction to the design rules for metal big area additive manufacturing," vol. 27, pp. 159–166. [Online]. Available: https://linkinghub.elsevier.com/retrieve/pii/S2214860418309345 19

[32] N.-H. Kim, B. V. Sankar, and A. V. Kumar, *Introduction to Finite Element Analysis and Design*. John Wiley & Sons, google-Books-ID: ti9dDwAAQBAJ. 19, 21

[33] T. L. Schmitz and K. S. Smith, "Introduction," in *Machining Dynamics: Frequency Response to Improved Productivity*, T. L. Schmitz and K. S. Smith, Eds. Springer International Publishing, pp. 1–6. [Online]. Available: https://doi.org/10.1007/978-3-319-93707-6_1 21

[34] ——, *Machining Dynamics: Frequency Response to Improved Productivity*. Springer International Publishing. [Online]. Available: http://link.springer.com/10.1007/978-3-319-93707-6 21

[35] ——, "Introduction," in *Mechanical Vibrations: Modeling and Measurement*, T. L. Schmitz and K. S. Smith, Eds. Springer US, pp. 1–24. [Online]. Available: https://doi.org/10.1007/978-1-4614-0460-6_1 21

[36] ——, "Measurement techniques," in *Mechanical Vibrations: Modeling and Measurement*, T. L. Schmitz and K. S. Smith, Eds. Springer US, pp. 249–277. [Online]. Available: https://doi.org/10.1007/978-1-4614-0460-6_7 30

[37] ——, "Milling dynamics," in *Machining Dynamics: Frequency Response to Improved Productivity*, T. L. Schmitz and K. S. Smith, Eds. Springer International Publishing, pp. 129–212. [Online]. Available: https://doi.org/10.1007/978-3-319-93707-6_4 57

[38] J. Tlusty, *Manufacturing Processes and Equipment*. Prentice Hall, google-Books-ID: xTBvQgAACAAJ. 59

[39] Component interaction PropertyManager - 2021 - SOLIDWORKS help. [Online]. Available: https://help.solidworks.com/2021/english/SolidWorks/cworks/ID_HELP_WELDS_CONTACT.htm?id=8924b541815348608a32b9fb83508165Pg063

[40] MetalMAX kit. [Online]. Available: http://mfg-labs.weebly.com/store/p2/MetalMAX_Kit.html 80

[41] T. L. Schmitz, J. C. Ziegert, J. S. Canning, and R. Zapata, "Case study: A comparison of error sources in high-speed milling," vol. 32, no. 2, pp. 126–133. [Online]. Available: https://www.sciencedirect.com/science/article/pii/S0141635907000748 127

[42] T. L. Schmitz and K. S. Smith, "Turning dynamics," in *Machining Dynamics: Frequency Response to Improved Productivity*, T. L. Schmitz and K. S. Smith, Eds. Springer International Publishing, pp. 67–128. [Online]. Available: https://doi.org/10.1007/978-3-319-93707-6_3 127

[43] SuperArc® LA-100. [Online]. Available: https://www.lincolnelectric.com/en/products/superarcla100_gmaw 129

[44] D. Nikolić, "Catenary arch of finite thickness as the optimal arch shape," vol. 60, no. 5, pp. 1957–1966. [Online]. Available: https://doi.org/10.1007/s00158-019-02304-9 134

[45] T. L. Schmitz and K. S. Smith, "Single degree of freedom free vibration," in *Mechanical Vibrations: Modeling and Measurement*, T. L. Schmitz and K. S. Smith, Eds. Springer US, pp. 25–81. [Online]. Available: https://doi.org/10.1007/978-1-4614-0460-6_2 218

Appendix

Appendix A

Drawings for weldment cross beam

The following drawings were used to construct the cross beam weldment.

NO REPRESENTATION OR WARRANTY, EXPRESSED OR IMPLIED, IS MADE AS TO THE ACCURACY, COMPLETENESS OR USEFULNESS OF THE INFORMATION OR STATEMENTS CONTAINED IN THESE DRAWINGS, OR THAT THE DISCLOSURE OF ANY INFORMATION, APPARATUS, METHOD OR PROCESS DISCLOSED MAY NOT INFRINGE PRIVATE RIGHTS OF OTHERS. NO LIABILITY IS ASSUMED WITH RESPECT TO THE USE OF, OR FOR DAMAGES RESULTING FROM THE USE OF, ANY INFORMATION, APPARATUS, METHOD OR PROCESS DISCLOSED IN THESE DRAWINGS. DRAWINGS MADE AVAILABLE FOR INFORMATION TO BIDDER ARE NOT TO BE USED FOR OTHER PURPOSES AND ARE TO BE RETURNED UPON REQUEST OF THE FORWARDING CONTRACTOR.

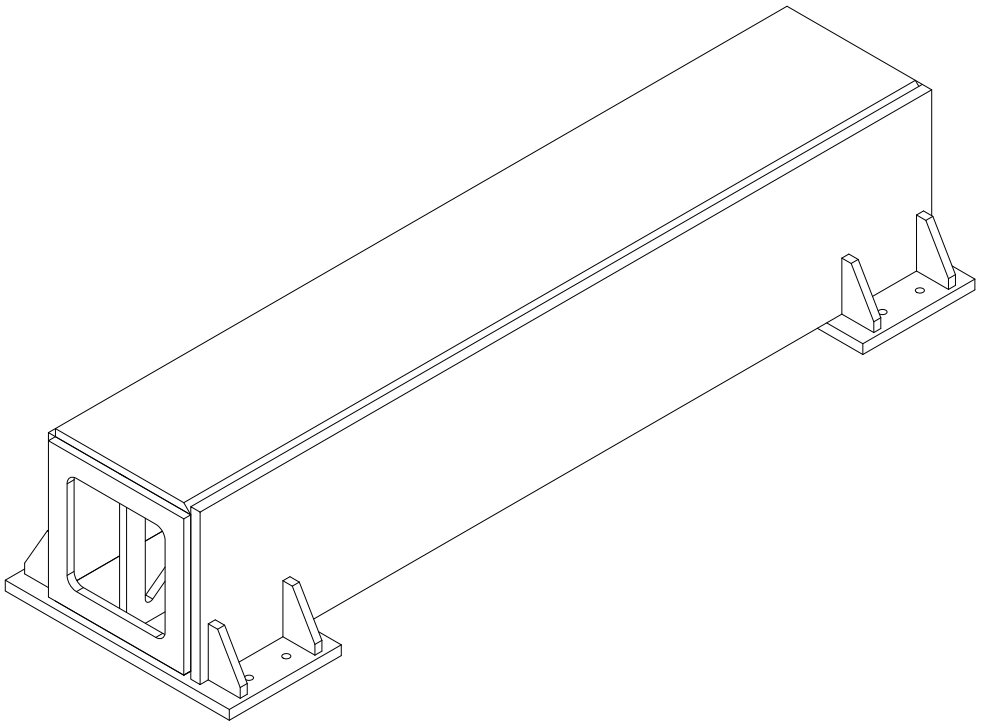

THIRD-ANGLE PROJECTION	APPROVALS		DATE
	DES	E. BETTERS	12/15/2022
UNLESS OTHERWISE NOTED DIMENSIONS ARE IN IN INTERPRET DIMENSIONS AND TOLERANCES PER ASME Y14.5M BREAK SHARP CORNERS AND REMOVE ALL BURRS	DRW	E. BETTERS	1/3/2023
	CHK	J. WEST	7/1/2020
DEFAULT TOLERANCES LINEAR ANGULAR X ± ±3.0 ±5° X.X ± ±0.50 ±2° X.XX ± ±0.125 ±1°	QUANTITY	1	
	MATERIAL	A36 OR EQUIVALENT	
DO NOT SCALE DRAWING	THIS DRAWING PRODUCED USING SolidWorks		

THIS DRAWING IS THE PROPERTY OF
OAK RIDGE NATIONAL LABORATORY
OPERATED FOR THE U.S. DEPARTMENT OF ENERGY UNDER CONTRACT DE-AC05-00OR22725 OAK RIDGE, TN

MACHINING AND MACHINE TOOL RESEARCH GROUP

CROSSBEAM WELDMENT

SIZE	PROJECT	DWG NO.	REV
D	MDF VMC-A	CB-A-M-01	A
SCALE 1:4	CAD FILE Crossbeam_r2	SHEET 1 of 4	

DWG NO. CB-A-M-01 1 of 4

SOLIDWORKS Educational Product. For Instructional Use Only.

ITEM NO.	PartNo	DESCRIPTION	QTY.
1	CB-M-04	CROSSBEAM BACK PLATE	1
2	CB-M-05	CROSSBEAM TOP-BOTTOM	2
3	CB-M-03	CROSSBEAM FRONT PLATE	1
4	CB-M-07	CROSSBEAM END PLATE	2
5	CB-M-01	MOUNTING PLATE	2
6	CB-M-02	CROSSBEAM GUSSET	8
7	CB-M-08	CROSSBEAM CENTER	1

NO REPRESENTATION OR WARRANTY, EXPRESSED OR IMPLIED, IS MADE AS TO THE ACCURACY, COMPLETENESS OR USEFULNESS OF THE INFORMATION OR STATEMENTS CONTAINED IN THESE DRAWINGS, OR THAT THE DISCLOSURE OF ANY INFORMATION, APPARATUS, METHOD OR PROCESS DISCLOSED MAY NOT INFRINGE PRIVATE RIGHTS OF OTHERS. NO LIABILITY IS ASSUMED WITH RESPECT TO THE USE OF, OR FOR DAMAGES RESULTING FROM THE USE OF, ANY INFORMATION, APPARATUS, METHOD OR PROCESS DISCLOSED IN THESE DRAWINGS. DRAWINGS MADE AVAILABLE FOR INFORMATION TO BIDDER ARE NOT TO BE USED FOR OTHER PURPOSES AND ARE TO BE RETURNED UPON REQUEST OF THE FORWARDING CONTRACTOR.

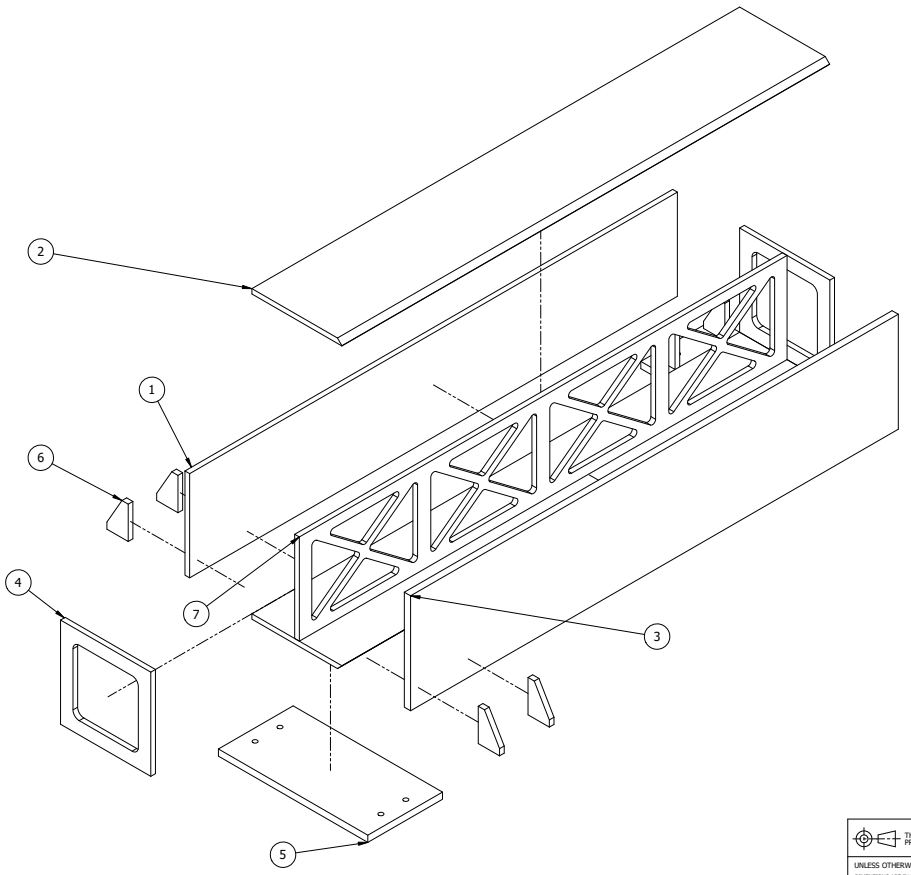

NOTE: SOME COMPONENTS HIDDEN FOR CLARITY

	APPROVALS	DATE
DES	E. BETTERS	12/15/2022
DRW	E. BETTERS	1/3/2023
CHK	J. WEST	

THIRD-ANGLE PROJECTION

UNLESS OTHERWISE NOTED
DIMENSIONS ARE IN IN
INTERPRET DIMENSIONS AND TOLERANCES PER ASME Y14.5M
BREAK SHARP CORNERS AND REMOVE ALL BURRS

DEFAULT TOLERANCES
LINEAR: X ± ±3.0, X.X ± ±0.50, X.XX ± ±0.125
ANGULAR: ±5°, ±2°, ±1°

DO NOT SCALE DRAWING

QUANTITY: 1
MATERIAL: A36 OR EQUIVALENT
THIS DRAWING PRODUCED USING SolidWorks

THIS DRAWING IS THE PROPERTY OF
OAK RIDGE NATIONAL LABORATORY
OPERATED FOR THE U.S. DEPARTMENT OF ENERGY UNDER CONTRACT DE-AC05-00OR22725 OAK RIDGE, TN

MACHINING AND MACHINE TOOL RESEARCH GROUP

CROSSBEAM WELDMENT

SIZE	PROJECT	DWG NO.	REV
D	MDF VMC-A	CB-A-M-01	A

SCALE 1:6 | CAD FILE Crossbeam_r2 | SHEET 2 of 4

DWG NO. CB-A-M-01 2 of 4

SOLIDWORKS Educational Product. For Instructional Use Only.

NO REPRESENTATION OR WARRANTY, EXPRESSED OR IMPLIED, IS MADE AS TO THE ACCURACY, COMPLETENESS OR USEFULNESS OF THE INFORMATION OR STATEMENTS CONTAINED IN THESE DRAWINGS, OR THAT THE USE/DISCLOSURE OF ANY INFORMATION, APPARATUS, METHOD OR PROCESS DISCLOSED MAY NOT INFRINGE PRIVATE RIGHTS OF OTHERS. NO LIABILITY IS ASSUMED WITH RESPECT TO THE USE OF, OR FOR DAMAGES RESULTING FROM THE USE OF, ANY INFORMATION, APPARATUS, METHOD OR PROCESS DISCLOSED IN THESE DRAWINGS. DRAWINGS MADE AVAILABLE FOR INFORMATION TO BIDDER ARE NOT TO BE USED FOR OTHER PURPOSES AND ARE TO BE RETURNED UPON REQUEST OF THE FORWARDING CONTRACTOR.

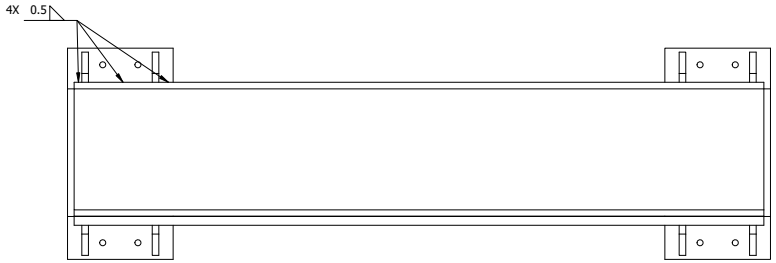

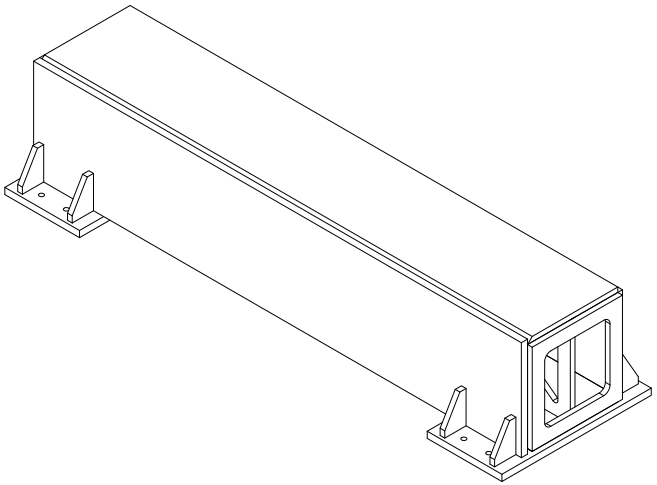

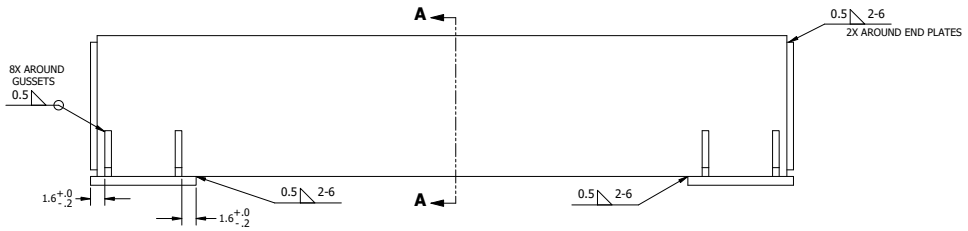

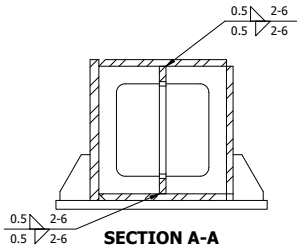

SECTION A-A

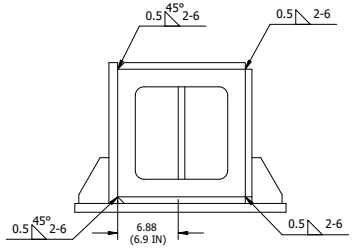

NOTE: ALL WELD NOTES IN INCHES

THIRD-ANGLE PROJECTION	APPROVALS		DATE
	DES	E. BETTERS	12/15/2022
UNLESS OTHERWISE NOTED DIMENSIONS ARE IN IN INTERPRET DIMENSIONS AND TOLERANCES PER ASME Y14.5M BREAK SHARP CORNERS AND REMOVE ALL BURRS	DRW	E. BETTERS	1/3/2023
	CHK	J. WEST	7/1/2020
DEFAULT TOLERANCES LINEAR ANGULAR X ± ±3.0 ±5° X.X ± ±1.00 ±2° X.XX ± ±0.125 ±1°	QUANTITY	1	
	MATERIAL	A36 OR EQUIVALENT	
DO NOT SCALE DRAWING	THIS DRAWING PRODUCED USING SolidWorks		

THIS DRAWING IS THE PROPERTY OF
OAK RIDGE NATIONAL LABORATORY
OPERATED FOR THE U.S. DEPARTMENT OF ENERGY UNDER CONTRACT DE-AC05-00OR22725 OAK RIDGE, TN

MACHINING AND MACHINE TOOL RESEARCH GROUP

CROSSBEAM WELDMENT

SIZE	PROJECT	DWG NO.	REV
D	MDF VMC-A	CB-A-M-01	A
SCALE 1:6	CAD FILE Crossbeam_r2	SHEET 3 of 4	

DWG NO. CB-A-M-01 3 of 4

SOLIDWORKS Educational Product. For Instructional Use Only.

NO REPRESENTATION OR WARRANTY, EXPRESSED OR IMPLIED, IS MADE AS TO THE ACCURACY, COMPLETENESS OR USEFULNESS OF THE INFORMATION OR STATEMENTS CONTAINED IN THESE DRAWINGS, OR THAT THE DISCLOSURE OF ANY INFORMATION, APPARATUS, METHOD OR PROCESS DISCLOSED MAY NOT INFRINGE PRIVATE RIGHTS OF OTHERS. NO LIABILITY IS ASSUMED WITH RESPECT TO THE USE OF, OR FOR DAMAGES RESULTING FROM THE USE OF, ANY INFORMATION, APPARATUS, METHOD OR PROCESS DISCLOSED IN THESE DRAWINGS. DRAWINGS MADE AVAILABLE FOR INFORMATION TO BIDDER ARE NOT TO BE USED FOR OTHER PURPOSES AND ARE TO BE RETURNED UPON REQUEST OF THE FORWARDING CONTRACTOR.

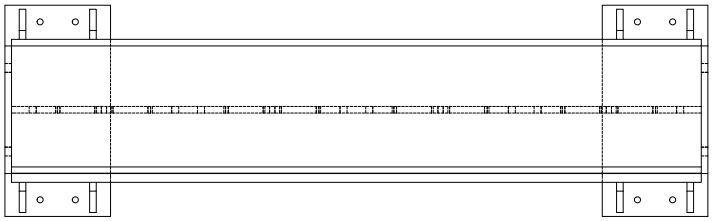

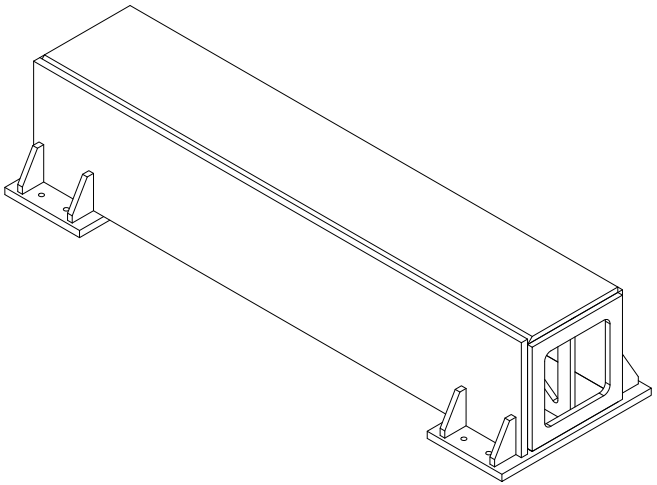

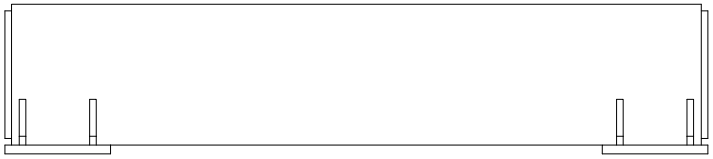

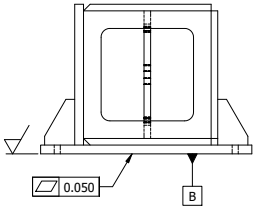

NOTES:
DEFAULT SURFACE FINISH Ra 3.2µm
WHEN NOTED

ALL MACHINING POST WELD

DWG NO. CB-A-M-01 4 of 4

THIRD-ANGLE PROJECTION	APPROVALS		DATE
	DES	E. BETTERS	12/15/2022
UNLESS OTHERWISE NOTED DIMENSIONS ARE IN IN INTERPRET DIMENSIONS AND TOLERANCES PER ASME Y14.5M BREAK SHARP CORNERS AND REMOVE ALL BURRS	DRW	E. BETTERS	1/3/2023
	CHK	J. WEST	7/1/2020
DEFAULT TOLERANCES LINEAR: X ± ±1.0, X.X ± ±0.125, X.XX ± ±0.05 ANGULAR: ±5°, ±2°, ±1°	QUANTITY	1	
	MATERIAL	A36 OR EQUIVALENT	
DO NOT SCALE DRAWING	THIS DRAWING PRODUCED USING SolidWorks		

THIS DRAWING IS THE PROPERTY OF
OAK RIDGE NATIONAL LABORATORY
OPERATED FOR THE U.S. DEPARTMENT OF ENERGY UNDER CONTRACT DE-AC05-00OR22725 OAK RIDGE, TN

MACHINING AND MACHINE TOOL RESEARCH GROUP

CROSSBEAM WELDMENT

SIZE	PROJECT	DWG NO.	REV
D	MDF VMC-A	CB-A-M-01	A
SCALE 1:6	CAD FILE Crossbeam_r2	SHEET 4 of 4	

SOLIDWORKS Educational Product. For Instructional Use Only.

NO REPRESENTATION OR WARRANTY, EXPRESSED OR IMPLIED, IS MADE AS TO THE ACCURACY, COMPLETENESS OR USEFULNESS OF THE INFORMATION OR STATEMENTS CONTAINED IN THESE DRAWINGS, OR THAT THE DISCLOSURE OF ANY INFORMATION, APPARATUS, METHOD OR PROCESS DISCLOSED MAY NOT INFRINGE PRIVATE RIGHTS OF OTHERS. NO LIABILITY IS ASSUMED WITH RESPECT TO THE USE OF, OR FOR DAMAGES RESULTING FROM THE USE OF, ANY INFORMATION, APPARATUS, METHOD OR PROCESS DISCLOSED IN THESE DRAWINGS. DRAWINGS MADE AVAILABLE FOR INFORMATION TO BIDDER ARE NOT TO BE USED FOR OTHER PURPOSES AND ARE TO BE RETURNED UPON REQUEST OF THE FORWARDING CONTRACTOR.

REVISIONS

REV	DESCRIPTION	BY	DATE	BY	APPROVED

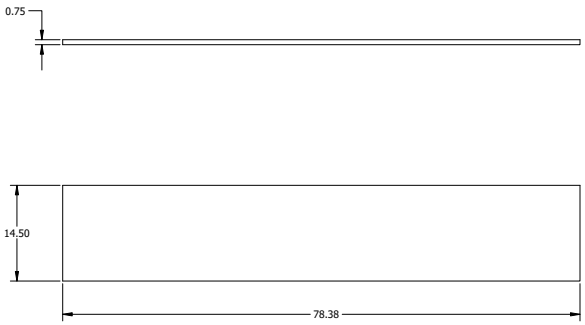

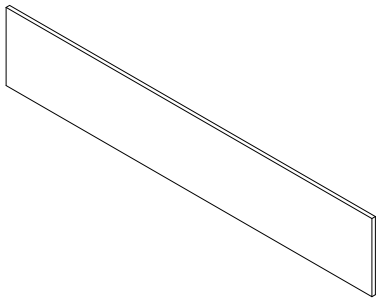

THIRD-ANGLE PROJECTION	APPROVALS		DATE
	DES	E. BETTERS	12/15/2022
UNLESS OTHERWISE NOTED DIMENSIONS ARE IN INCHES INTERPRET DIMENSIONS AND TOLERANCES PER ASME Y14.5M BREAK SHARP CORNERS AND REMOVE ALL BURRS	DRW	E. BETTERS	1/3/2023
	CHK	J. WEST	6/29/2020
DEFAULT TOLERANCES LINEAR ANGULAR X.X ± ±0.125 ±1° X.XX ± ±0.020 ±2' X.XXX ± ±0.005 ±1'	QUANTITY	1	
	MATERIAL	A36 OR EQUIVALENT	
DO NOT SCALE DRAWING	THIS DRAWING PRODUCED USING SolidWorks		

THIS DRAWING IS THE PROPERTY OF
OAK RIDGE NATIONAL LABORATORY
OPERATED FOR THE U.S. DEPARTMENT OF ENERGY UNDER CONTRACT DE-AC05-00OR22725 OAK RIDGE, TN

MACHINING AND MACHINE TOOL RESEARCH GROUP

CROSSBEAM BACK PLATE

SIZE	PROJECT	DWG NO.	REV
D	MDF VMC-A	CB-M-04	A
SCALE 1:8	CAD FILE Crossbeam_r2	SHEET 1 of 1	

DWG NO. CB-M-04 1 of 1

SOLIDWORKS Educational Product. For Instructional Use Only.

NO REPRESENTATION OR WARRANTY, EXPRESSED OR IMPLIED, IS MADE AS TO THE ACCURACY, COMPLETENESS OR USEFULNESS OF THE INFORMATION OR STATEMENTS CONTAINED IN THESE DRAWINGS, OR THAT THE DISCLOSURE OF ANY INFORMATION, APPARATUS, METHOD OR PROCESS DISCLOSED MAY NOT INFRINGE PRIVATE RIGHTS OF OTHERS. NO LIABILITY IS ASSUMED WITH RESPECT TO THE USE OF, OR FOR DAMAGES RESULTING FROM THE USE OF, ANY INFORMATION, APPARATUS, METHOD OR PROCESS DISCLOSED IN THESE DRAWINGS. DRAWINGS MADE AVAILABLE FOR INFORMATION TO BIDDER ARE NOT TO BE USED FOR OTHER PURPOSES AND ARE TO BE RETURNED UPON REQUEST OF THE FORWARDING CONTRACTOR.

REVISIONS

REV	DESCRIPTION	BY	DATE	BY	APPROVED

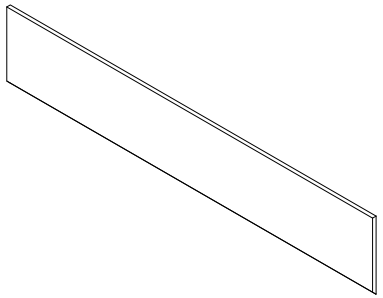

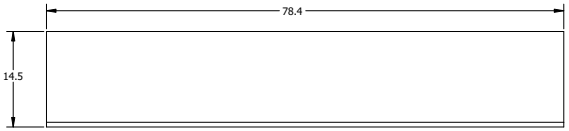

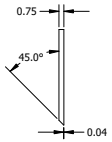

		APPROVALS	DATE
THIRD-ANGLE PROJECTION	DES	E. BETTERS	12/15/2022
UNLESS OTHERWISE NOTED			
DIMENSIONS ARE IN IN	DRW	E. BETTERS	1/3/2023
INTERPRET DIMENSIONS AND TOLERANCES PER ASME Y14.5M	CHK	J. WEST	6/29/2020
BREAK SHARP CORNERS AND REMOVE ALL BURRS			
DEFAULT TOLERANCES	QUANTITY	2	
LINEAR ANGULAR X.X ± ±0.05 ±1° X.XX ± ±0.01 ±.5° X.XXX ± ±0.005 ±.1°	MATERIAL	A36 OR EQUIVALENT	
DO NOT SCALE DRAWING	THIS DRAWING PRODUCED USING SolidWorks		

THIS DRAWING IS THE PROPERTY OF
OAK RIDGE NATIONAL LABORATORY
OPERATED FOR THE U.S. DEPARTMENT OF ENERGY UNDER CONTRACT DE-AC05-00OR22725 OAK RIDGE, TN

MACHINING AND MACHINE TOOL RESEARCH GROUP

CROSSBEAM TOP-BOTTOM

SIZE	PROJECT	DWG NO.	REV
D	MDF VMC-A	CB-M-05	A

SCALE 1:8 | CAD FILE Crossbeam_r2 | SHEET 1 of 1

DWG NO.

SOLIDWORKS Educational Product. For Instructional Use Only.

NO REPRESENTATION OR WARRANTY, EXPRESSED OR IMPLIED, IS MADE AS TO THE ACCURACY, COMPLETENESS OR USEFULNESS OF THE INFORMATION OR STATEMENTS CONTAINED IN THESE DRAWINGS, OR THAT THE DISCLOSURE OF ANY INFORMATION, APPARATUS, METHOD OR PROCESS DISCLOSED MAY NOT INFRINGE PRIVATE RIGHTS OF OTHERS. NO LIABILITY IS ASSUMED WITH RESPECT TO THE USE OF, OR FOR DAMAGES RESULTING FROM THE USE OF, ANY INFORMATION, APPARATUS, METHOD OR PROCESS DISCLOSED IN THESE DRAWINGS. DRAWINGS MADE AVAILABLE FOR INFORMATION TO BIDDER ARE NOT TO BE USED FOR OTHER PURPOSES AND ARE TO BE RETURNED UPON REQUEST OF THE FORWARDING CONTRACTOR.

REVISIONS

REV	DESCRIPTION	BY	DATE	BY	APPROVED

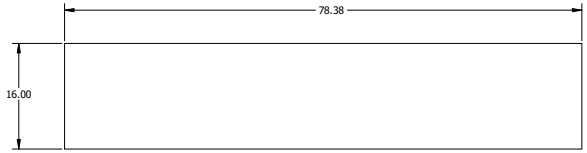

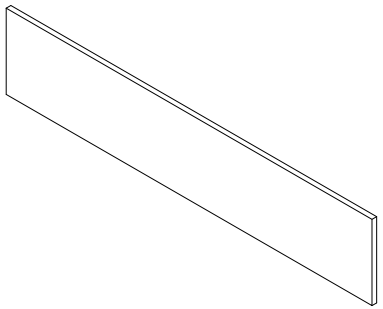

NOTE:
STOCK DIMENSIONS ONLY
ALL MACHINING AFTER WELDING

THIRD-ANGLE PROJECTION	APPROVALS		DATE
	DES	E. BETTERS	12/15/2022
UNLESS OTHERWISE NOTED DIMENSIONS ARE IN INCHES INTERPRET DIMENSIONS AND TOLERANCES PER ASME Y14.5M BREAK SHARP CORNERS AND REMOVE ALL BURRS	DRW	E. BETTERS	1/3/2023
	CHK	J. WEST	6/29/2020
DEFAULT TOLERANCES LINEAR ANGULAR X.X ± ±0.125 ±5° X.XX ± ±0.020 ±2° X.XXX ± ±0.005 ±1°	QUANTITY	1	
	MATERIAL	A36 OR EQUIVALENT	
DO NOT SCALE DRAWING	THIS DRAWING PRODUCED USING SolidWorks		

THIS DRAWING IS THE PROPERTY OF
OAK RIDGE NATIONAL LABORATORY
OPERATED FOR THE U.S. DEPARTMENT OF ENERGY UNDER CONTRACT DE-AC05-00OR22725 OAK RIDGE, TN

MACHINING AND MACHINE TOOL RESEARCH GROUP

CROSSBEAM FRONT PLATE

SIZE	PROJECT	DWG NO.	REV
D	MDF VMC-A	CB-M-03	A
SCALE 1:8	CAD FILE Crossbeam_r2	SHEET 1 of 1	

DWG NO. CB-M-03 1 of 1

SOLIDWORKS Educational Product. For Instructional Use Only.

NO REPRESENTATION OR WARRANTY, EXPRESSED OR IMPLIED, IS MADE AS TO THE ACCURACY, COMPLETENESS OR USEFULNESS OF THE INFORMATION OR STATEMENTS CONTAINED IN THESE DRAWINGS, OR THAT THE DISCLOSURE OF ANY INFORMATION, APPARATUS, METHOD OR PROCESS DISCLOSED MAY NOT INFRINGE PRIVATE RIGHTS OF OTHERS. NO LIABILITY IS ASSUMED WITH RESPECT TO THE USE OF, OR FOR DAMAGES RESULTING FROM THE USE OF, ANY INFORMATION, APPARATUS, METHOD OR PROCESS DISCLOSED IN THESE DRAWINGS. DRAWINGS MADE AVAILABLE FOR INFORMATION TO BIDDER ARE NOT TO BE USED FOR OTHER PURPOSES AND ARE TO BE RETURNED UPON REQUEST OF THE FORWARDING CONTRACTOR.

REVISIONS

REV	DESCRIPTION	BY	DATE	BY	APPROVED

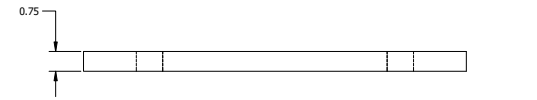

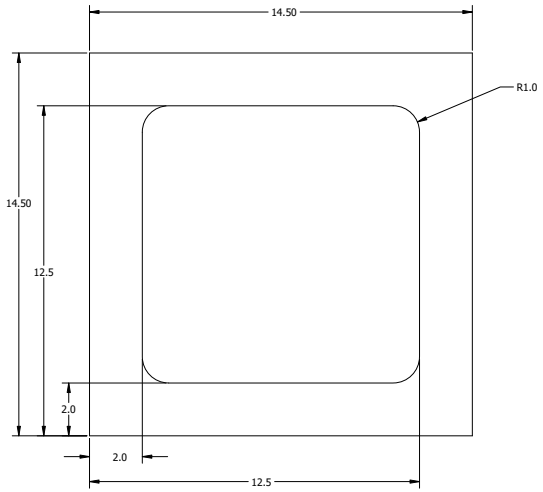

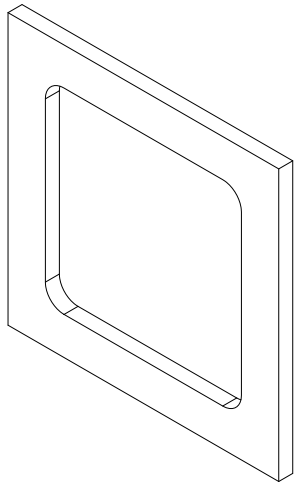

THIRD-ANGLE PROJECTION	APPROVALS		DATE
	DES	E. BETTERS	12/15/2022
UNLESS OTHERWISE NOTED DIMENSIONS ARE IN IN INTERPRET DIMENSIONS AND TOLERANCES PER ASME Y14.5M BREAK SHARP CORNERS AND REMOVE ALL BURRS	DRW	E. BETTERS	1/3/2023
	CHK	J. WEST	6/29/2020
DEFAULT TOLERANCES LINEAR ANGULAR X.X ± ±0.05 ±1° X.XX ± ±0.01 ±2° X.XXX ± ±0.005 ±1'	QUANTITY	2	
	MATERIAL	A36 OR EQUIVALENT	
DO NOT SCALE DRAWING	THIS DRAWING PRODUCED USING SolidWorks		

THIS DRAWING IS THE PROPERTY OF
OAK RIDGE NATIONAL LABORATORY
OPERATED FOR THE U.S. DEPARTMENT OF ENERGY UNDER CONTRACT DE-AC05-00OR22725 OAK RIDGE, TN

MACHINING AND MACHINE TOOL RESEARCH GROUP

CROSSBEAM END PLATE

SIZE	PROJECT	DWG NO.	REV
D	MDF VMC-A	CB-M-07	A
SCALE 1:2	CAD FILE Crossbeam_end_plate	SHEET 1 of 1	

DWG NO.

SOLIDWORKS Educational Product. For Instructional Use Only.

NO REPRESENTATION OR WARRANTY, EXPRESSED OR IMPLIED, IS MADE AS TO THE ACCURACY, COMPLETENESS OR USEFULNESS OF THE INFORMATION OR STATEMENTS CONTAINED IN THESE DRAWINGS, OR THAT THE DISCLOSURE OF ANY INFORMATION, APPARATUS, METHOD OR PROCESS DISCLOSED MAY NOT INFRINGE PRIVATE RIGHTS OF OTHERS. NO LIABILITY IS ASSUMED WITH RESPECT TO THE USE OF, OR FOR DAMAGES RESULTING FROM THE USE OF, ANY INFORMATION, APPARATUS, METHOD OR PROCESS DISCLOSED IN THESE DRAWINGS. DRAWINGS MADE AVAILABLE FOR INFORMATION TO BIDDER ARE NOT TO BE USED FOR OTHER PURPOSES AND ARE TO BE RETURNED UPON REQUEST OF THE FORWARDING CONTRACTOR.

REVISIONS

REV	DESCRIPTION	BY	DATE	BY	APPROVED

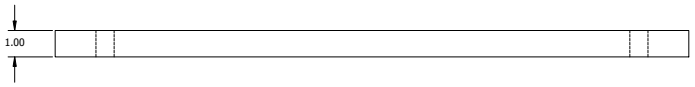

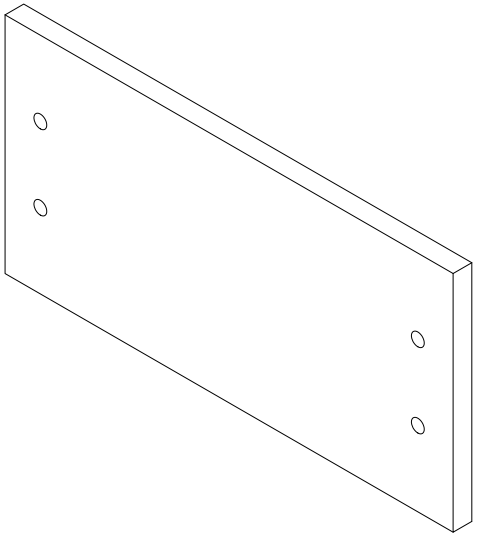

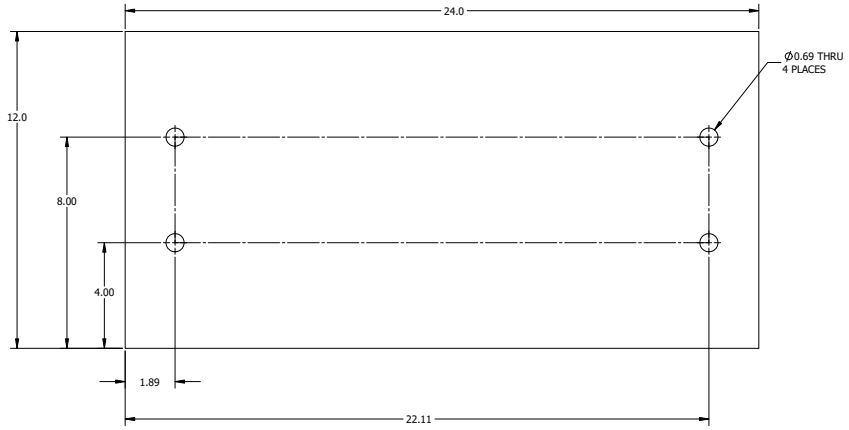

	APPROVALS	DATE
DES	E. BETTERS	11/10/2022
DRW	E. BETTERS	1/3/2023
CHK	J. WEST	6/29/2020

THIRD-ANGLE PROJECTION

UNLESS OTHERWISE NOTED
DIMENSIONS ARE IN IN
INTERPRET DIMENSIONS AND TOLERANCES PER ASME Y14.5M
BREAK SHARP CORNERS AND REMOVE ALL BURRS

DEFAULT TOLERANCES
LINEAR: X.X ± 0.05; X.XX ± 0.01; X.XXX ± 0.005
ANGULAR: ± 1°

DO NOT SCALE DRAWING

QUANTITY: 2
MATERIAL: A36 OR EQUIVALENT

THIS DRAWING PRODUCED USING SolidWorks

THIS DRAWING IS THE PROPERTY OF
OAK RIDGE NATIONAL LABORATORY
OPERATED FOR THE U.S. DEPARTMENT OF ENERGY UNDER CONTRACT DE-AC05-00OR22725 OAK RIDGE, TN

MACHINING AND MACHINE TOOL RESEARCH GROUP

MOUNTING PLATE

SIZE	PROJECT	DWG NO.	REV
D	MDF VMC-A	CB-M-01	A

SCALE 1:2 | CAD FILE MOUNTING PLATE | SHEET 1 of 1

DWG NO.

SOLIDWORKS Educational Product. For Instructional Use Only.

NO REPRESENTATION OR WARRANTY, EXPRESSED OR IMPLIED, IS MADE AS TO THE ACCURACY, COMPLETENESS OR USEFULNESS OF THE INFORMATION OR STATEMENTS CONTAINED IN THESE DRAWINGS, OR THAT THE DISCLOSURE OF ANY INFORMATION, APPARATUS, METHOD OR PROCESS DISCLOSED MAY NOT INFRINGE PRIVATE RIGHTS OF OTHERS. NO LIABILITY IS ASSUMED WITH RESPECT TO THE USE OF, OR FOR DAMAGES RESULTING FROM THE USE OF, ANY INFORMATION, APPARATUS, METHOD OR PROCESS DISCLOSED IN THESE DRAWINGS. DRAWINGS MADE AVAILABLE FOR INFORMATION TO BIDDER ARE NOT TO BE USED FOR OTHER PURPOSES AND ARE TO BE RETURNED UPON REQUEST OF THE FORWARDING CONTRACTOR.

REVISIONS

REV	DESCRIPTION	BY	DATE	BY	APPROVED

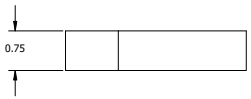

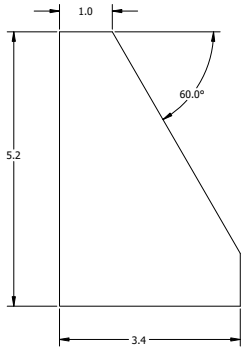

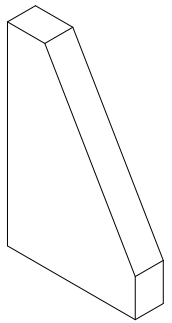

	APPROVALS	DATE
DES	E. BETTERS	11/10/2022
DRW	E. BETTERS	1/3/2023
CHK	J. WEST	6/29/2020

THIRD-ANGLE PROJECTION

UNLESS OTHERWISE NOTED
DIMENSIONS ARE IN IN
INTERPRET DIMENSIONS AND TOLERANCES PER ASME Y14.5M
BREAK SHARP CORNERS AND REMOVE ALL BURRS

DEFAULT TOLERANCES

LINEAR: X.X ± 0.05, X.XX ± 0.01, X.XXX ± 0.005
ANGULAR: ±1°

DO NOT SCALE DRAWING

QUANTITY: 8
MATERIAL: A36 OR EQUIVALENT

THIS DRAWING PRODUCED USING SolidWorks

THIS DRAWING IS THE PROPERTY OF
OAK RIDGE NATIONAL LABORATORY
OPERATED FOR THE U.S. DEPARTMENT OF ENERGY UNDER CONTRACT DE-AC05-00OR22725 OAK RIDGE, TN

MACHINING AND MACHINE TOOL RESEARCH GROUP

CROSSBEAM GUSSET

SIZE	PROJECT	DWG NO.	REV
D	MDF VMC-A	CB-M-02	A

SCALE 1:1 | CAD FILE CROSSBEAM GUSSET | SHEET 1 of 1

DWG NO.

SOLIDWORKS Educational Product. For Instructional Use Only.

NO REPRESENTATION OR WARRANTY, EXPRESSED OR IMPLIED, IS MADE AS TO THE ACCURACY, COMPLETENESS OR USEFULNESS OF THE INFORMATION OR STATEMENTS CONTAINED IN THESE DRAWINGS, OR THAT THE DISCLOSURE OF ANY INFORMATION, APPARATUS, METHOD OR PROCESS DISCLOSED MAY NOT INFRINGE PRIVATE RIGHTS OF OTHERS. NO LIABILITY IS ASSUMED WITH RESPECT TO THE USE OF, OR FOR DAMAGES RESULTING FROM THE USE OF, ANY INFORMATION, APPARATUS, METHOD OR PROCESS DISCLOSED IN THESE DRAWINGS. DRAWINGS MADE AVAILABLE FOR INFORMATION TO BIDDER ARE NOT TO BE USED FOR OTHER PURPOSES AND ARE TO BE RETURNED UPON REQUEST OF THE FORWARDING CONTRACTOR.

REVISIONS

REV	DESCRIPTION	BY	DATE	BY	APPROVED

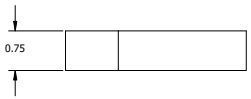

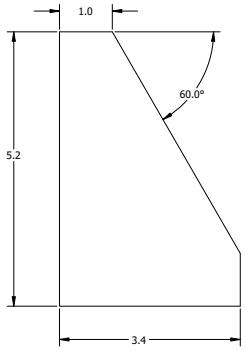

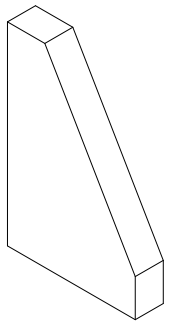

	APPROVALS	DATE
DES	E. BETTERS	11/10/2022
DRW	E. BETTERS	1/3/2023
CHK	J. WEST	6/29/2020

THIRD-ANGLE PROJECTION

UNLESS OTHERWISE NOTED
DIMENSIONS ARE IN IN
INTERPRET DIMENSIONS AND TOLERANCES PER ASME Y14.5M
BREAK SHARP CORNERS AND REMOVE ALL BURRS

DEFAULT TOLERANCES

LINEAR: X.X ± 0.05, X.XX ± 0.01, X.XXX ± 0.005
ANGULAR: ±1°

DO NOT SCALE DRAWING

QUANTITY: 8
MATERIAL: A36 OR EQUIVALENT

THIS DRAWING PRODUCED USING SolidWorks

THIS DRAWING IS THE PROPERTY OF
OAK RIDGE NATIONAL LABORATORY
OPERATED FOR THE U.S. DEPARTMENT OF ENERGY UNDER CONTRACT DE-AC05-00OR22725 OAK RIDGE, TN

MACHINING AND MACHINE TOOL RESEARCH GROUP

CROSSBEAM GUSSET

SIZE	PROJECT	DWG NO.	REV
D	MDF VMC-A	CB-M-02	A

SCALE 1:1 | CAD FILE CROSSBEAM GUSSET | SHEET 1 of 1

DWG NO.

SOLIDWORKS Educational Product. For Instructional Use Only.

NO REPRESENTATION OR WARRANTY, EXPRESSED OR IMPLIED, IS MADE AS TO THE ACCURACY, COMPLETENESS OR USEFULNESS OF THE INFORMATION OR STATEMENTS CONTAINED IN THESE DRAWINGS, OR THAT THE USE/DISCLOSURE OF ANY INFORMATION, APPARATUS, METHOD OR PROCESS DISCLOSED MAY NOT INFRINGE PRIVATE RIGHTS OF OTHERS. NO LIABILITY IS ASSUMED WITH RESPECT TO THE USE OF, OR FOR DAMAGES RESULTING FROM THE USE OF, ANY INFORMATION, APPARATUS, METHOD OR PROCESS DISCLOSED IN THESE DRAWINGS. DRAWINGS MADE AVAILABLE FOR INFORMATION TO BIDDER ARE NOT TO BE USED FOR OTHER PURPOSES AND ARE TO BE RETURNED UPON REQUEST OF THE FORWARDING CONTRACTOR.

REVISIONS

REV	DESCRIPTION	BY	DATE	BY	APPROVED

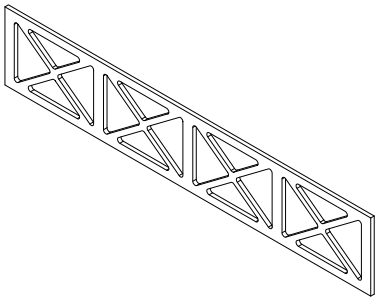

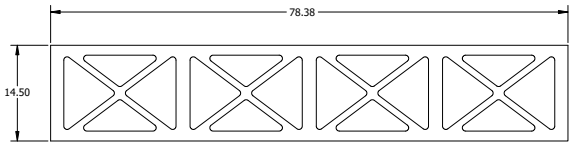

NOTE:
STOCK DIMENSIONS GIVEN
SEE CAD MODEL FOR AWJ PROFILE

		APPROVALS	DATE
THIRD-ANGLE PROJECTION	DES	E. BETTERS	12/15/2022
UNLESS OTHERWISE NOTED DIMENSIONS ARE IN INCHES INTERPRET DIMENSIONS AND TOLERANCES PER ASME Y14.5M BREAK SHARP CORNERS AND REMOVE ALL BURRS	DRW	E. BETTERS	1/3/2023
	CHK	J. WEST	6/29/2020
DEFAULT TOLERANCES LINEAR: X.X = ±0.125, X.XX = ±0.020, X.XXX = ±0.005 ANGULAR: ±5°, ±2°, ±1°	QUANTITY	1	
	MATERIAL	A36 OR EQUIVALENT	
DO NOT SCALE DRAWING	THIS DRAWING PRODUCED USING SolidWorks		

THIS DRAWING IS THE PROPERTY OF
OAK RIDGE NATIONAL LABORATORY
OPERATED FOR THE U.S. DEPARTMENT OF ENERGY UNDER CONTRACT DE-AC05-00OR22725 OAK RIDGE, TN

MACHINING AND MACHINE TOOL RESEARCH GROUP

CROSSBEAM CENTER

SIZE	PROJECT	DWG NO.	REV
D	MDF VMC-A	CB-M-08	A
SCALE 1:8	CAD FILE Crossbeam_r2	SHEET 1 of 1	

DWG NO. CB-M-08 1 of 1

SOLIDWORKS Educational Product. For Instructional Use Only.

Vita

Tyler Poon was born in New York but grew up in Florida. He had a small intermission, from the ages of seven to ten, when he lived in China with his younger sister. It wasn't until he was in high school and joined robotics, FIRST Robotics Competition (FRC), that he learned the fundamental concepts of robotics, engineering, and design. The robotics team also provided him with an engineering family and learned the value of teamwork and lifelong friendships. His passion for engineering was then fostered at the University of Florida (UF).

Tyler's first year at UF allowed him to join the college's robotics club which was the beginning of his mechanical engineering pursuit. The rest of his college experience was focused on the Design for Manufacturing Lab taught by Michael Braddock which opened the door to manufacturing and design. His work and experience led him to an internship with Parametric Solutions Inc. where he worked with Pratt and Whitney. After graduating with his Bachelor of Science in Mechanical Engineering degree, he took up a cooperative (Co-op) opportunity with Edward's Lifesciences in California where he took on the role of research and design in the biomedical field.

After his Co-op, he went to the University of Tennessee, Knoxville to earn his Masters in mechanical engineering. Under the guidance of Dr. Tony Schmitz, Emma Betters, Justin West, his fellow graduate students, and Oak Ridge National Lab, he was able to complete his thesis focused on machine tool design with metal big area additive manufacturing. His next step in life is to join the private industry and follow his passion for engineering and continue to learn and make a difference in the world.